UNIVERSIDADE DE LISBOA

INSTITUTO SUPERIOR TÉCNICO

Numerical and experimental models for vibration attenuation using cork composite materials

Hugo Filipe Diniz Policarpo

Supervisor: Doctor Miguel António Lopes de Matos Neves
Co-Supervisor: Doctor Nuno Manuel Mendes Maia

Thesis approved in public session to obtain the PhD Degree in
Mechanical Engineering
Jury final classification: Pass with distinction

Jury

Chairperson: Chairman of the IST Scientific Board

Members of the Committee:

Doctor Manuel José Moreira de Freitas, Professor Catedrático Aposentado do Instituto Superior Técnico, da Universidade de Lisboa

Doctor Nuno Manuel Mendes Maia, Professor Associado (com Agregação) do Instituto Superior Técnico, da Universidade de Lisboa

Doctor José Fernando Dias Rodrigues, Professor Associado da Faculdade de Engenharia, da Universidade do Porto

Doctor António Paulo Vale Urgueira, Professor Associado da Faculdade de Ciências e Tecnologia, da Universidade Nova de Lisboa

Doctor Luís Filipe Galrão Reis, Professor Associado do Instituto Superior Técnico, da Universidade de Lisboa

Doctor Miguel António Lopes de Matos Neves, Professor Auxiliar do Instituto Superior Técnico, da Universidade de Lisboa

2013

Aos meus pais e avós,

à Rita e a todos os que me ajudaram.

"If I have seen further it is by standing on the shoulders of giants."
Isaac Newton
(Letter to Robert Hooke on February 15, 1676 of the Gregorian calendar)

Abstract

This document proposes a novel analytical-experimental hybrid methodology for the determination of the longitudinal and shear dynamic moduli, in which the longitudinal modulus was compared with the Dynamic Mechanical Analysis (DMA) results for several Cork Composite Materials (CCMs). Symbolic computation was intensively used to achieve a simple equation for the storage modulus and the Rational Fraction Polynomial method was used to determine the natural frequency and its respective loss factor.

Such methodology allowed the development of validated numerical models of Phononic-inspired Vibration Isolators (PIVIs) in the frequency domain. The CCMs have been proposed by the author to achieve significant vibration attenuations at low and wide frequency ranges within reasonable lengths of the PIVIs. A test with a compressor motor illustrates the potential of those devices combined with a spring.

The author also proposes validated numerical models in the frequency domain for metallic panels using CCMs for Surface Damping Treatments (SDTs), to study whether they are a low density alternative to the conventional damping materials.

Topology optimization has been applied to PIVIs and SDTs to improve their performance.

This study was performed to contribute for innovative applications using CCMs under dynamic loading, where the dynamic moduli is now of simpler assessment.

Keywords: Passive vibration isolation, Dynamic modulus, Cork composite, Resonant method, Material property identification, Model validation, Phononic device, Surface damping treatments, Structural optimization, Inverse problem.

Resumo

Este documento propõe uma nova metodologia híbrida analítico-experimental para determinação dos módulos de elasticidade dinâmicos longitudinal e de distorção, cujos resultados no caso longitudinal foram comparados através de Análise Mecânica Dinâmica em vários Compósitos de Cortiça (CCM). Utilizando computação simbólica intensiva obteve-se uma equação simples de cálculo dos módulos dinâmicos, recorrendo ao método polinomial em fracções racionais para identificação da frequência natural e factor de perda.

Esta metodologia permitiu o desenvolvimento de modelos numéricos validados de Isoladores de Vibração Inspirados em Estruturas Fonónicas (PIVIs) no domínio da frequência. Os CCMs propostos pelo autor visam alcançar regiões de atenuação significativas em gamas de baixas frequências e comprimentos razoáveis dos PIVIs. Um teste com um motor de compressor ilustra o potencial destes dispositivos combinados com uma mola.

O autor propõe modelos numéricos validados no domínio da frequência de painéis metálicos utilizando CCMs nos tratamentos de amortecimento (SDT) para estudar se estes são alternativa de baixa densidade aos materiais convencionais de amortecimento.

Optimização topológica foi aplicada aos PIVIs e SDTs para melhorar o desempenho destes.

Este estudo visa contribuir para o desenvolvimento de aplicações inovadoras que utilizam CCMs sob solicitações dinâmicas, onde o módulo dinâmico das CCMs é agora de avaliação mais simples.

Palavras-chave: Isolamento passivo de vibrações, Módulo dinâmico, Compósitos de cortiça, Método ressonante, Identificação de propriedades do material, Validação de modelos, Dispositivo fonónico, Tratamentos superficiais, Optimização estrutural, Problema inverso.

Acknowledgments

To my friend some of which school colleagues namely, Yoann Lage, Tiago Silva and Pedro Jorge for their availability, all the support and incentive given, with particular emphasis in the accomplishment of the experimental tasks which without them would have been time consuming and of difficult execution.

At last, to my family, and in a very special way to my parents, grandparents and Rita for all the support given in all situations.

Agradecimentos

Table of Contents

List of Figures

List of Tables

Publications

In the following are listed the author's publications, in scientific journals and conference proceedings that are directly related with the research work developed in this thesis.

Scientific journals

➢ 2013

- Policarpo H., Neves M.M. and Maia N.M.M., On a hybrid analytical-experimental technique to assess the storage modulus of resilient materials using symbolic computation. Journal of Symbolic Computation **61-62** 31-52 (2014) (Available online on 16/10/2013).

- Policarpo H., Neves M.M. and Maia N.M.M., A simple method for the determination of the complex modulus of resilient materials using a longitudinally vibrating three-layer specimen, Journal of Sound and Vibration **332** (2) 246-263 (2013).

➢ 2010

- Policarpo H., Neves M.M. and Ribeiro A.M.R., Dynamical response of a multi-laminated periodic bar: Analytical, numerical and experimental study, Shock and Vibration **17** (4-5) 521-535 (2010).

- Policarpo H., Neves M.M., and Ribeiro A.R., An Experimental Characterization of Cork Storage Modulus for Cork-Steel Applications in Vibration Attenuation, Materials Science Forum **636-637** 1199-1205 (2010).

Conference Proceedings

➢ 2013

- Policarpo H., Furukava M., Neves M.M., Maia N.M.M., Silva O.M. and Gerges S.N.Y., A methodology for the performance evaluation of different surface damping treatments, IRF'2013 – 4th International Conference on Integrity, Reliability and Failure, Funchal, Portugal, June 23-27 (2013).

- Policarpo H., Diogo A.C., Neves M.M. and Maia N.M.M., A note on the estimation of cork composite elasto-dynamic properties and their frequency dependence, ICEDyn'2013 – International Conference on Structural Engineering Dynamics, Ericeira, Portugal, June 17-18 (2013).

➢ 2012

- Policarpo H., Neves M.M., Maia N.M.M. and Urgueira A.P.V., On using composition cork damping layer for surface damping treatments, ISMA 2012 – International conference on Noise & Vibration Engineering, Leuven, Belgium, September 17-19 (2012).

- Policarpo H., Neves M.M., Maia N.M.M and Urgueira A.P.V., Estimation of Complex Longitudinal and Shear Moduli of Composition Cork Materials, ICEM15 – 15th International Conference on Experimental Mechanics, Porto, Portugal, July 22-27 (2012).

- Jorge P., Policarpo H., Neves M.M. and Maia N.M.M., Cork composition Layer to reduce vibrations, ICEM15 – 15th International Congress Experimental Mechanics, Porto, Portugal, July 22-27 (2012).

- Policarpo H., A steel-composition cork phononic device for low frequency vibration attenuation, II LAETA Young Researchers Meeting 2012, FEUP, Porto, Portugal, April 10-11 (2012).
- Policarpo H., Neves M.M. and Maia N.M.M., On a hybrid analytical-experimental technique to assess the storage modulus of resilient materials using symbolic computation. CSEI2012 – First National Conference on Symbolic Computation in Education and Research, Lisbon, Portugal, April 2-3, (2012).

➢ 2011

- Maia N.M.M., Policarpo H., Neves M.M., Furukava M., Silva O.M., Gerges S.N.Y and Carli S., A Finite Element Model to Improve Unconstrained Layer Damping Treatments on a Simplified Passenger Car Body in White Model. ICSV 18 – 18th International Congress on Sound and Vibration, Rio de Janeiro, Brazil, July 10-14, (2011).
- Policarpo H., Neves M.M. and Maia N.M.M., On the Determination of Storage and Loss Modulli for Cork Composition Materials, ICEDyn'2011 – International Conference on Structural Dynamics, Tavira, Portugal, June 20-22 (2011).
- Neves M.M., Silva O.M., Policarpo H. and Cartaxo A.G., Using classical FEM to predict the dynamical response of periodic devices in acoustic and vibration applications, Phononics 2011 – First International Conference on Phononic Crystals, Metamaterials and Optomechanic, Santa Fe, New Mexico, USA, May 29 – June 2 (2011).

➢ 2010

- Policarpo H., Neves M.M., Maia N.M.M., Coelho J.L.B., Gerges S.N.Y and Viveiros E., On the Determination of Dynamic Properties of Resilient Materials using a Multi-Laminated Periodic Specimen, ICSV 17 – 17th International Congress on Sound and Vibration, Cairo, Egypt, July 18-22 (2010).

Acronyms and abbreviations

1D	One-Dimensional
2D	Two-Dimensional
3D	Three-Dimensional
AIAA	American Institute of Aeronautics and Astronautics
ASME	American Society of Mechanical Engineers
AR	Attenuation Region
BIW	Body in White
CLD	Constrained Layer Damping
CCM	Cork Composite Material
CVI	Commercial Vibration Isolator
DMA	Dynamic Mechanical Analysis
DOF	Degree-of-Freedom
FAAC	Frequency Amplitude Assurance Criterion
FE	Finite Element
FEM	Finite Element Method
FLD	Free Layer Damping
FRAC	Frequency Response Assurance Criterion
FRF	Frequency Response Function
KL	Kirchhoff-Love
MDOF	Multi Degree-of-Freedom
PIVI	Phononic-inspired Vibration Isolator
PMMA	Polymethyl Methacrylate
RFP	Rational Fraction Polynomial method
RM	Reissner-Mindlin
SDT	Surface Damping Treatment
SDOF	Single Degree-of-Freedom
SIMP	Solid Isotropic Material with Penalization
SQP	Sequential Quadratic Programming
TTS	Time-Temperature Superposition principle

Note: an acronym or abbreviations ending with small s indicates the plural, e.g., FEs.

Notation

A general list of the common notation adopted and used in this thesis is here presented. Note that in few particular cases, identical notation is used to define different and punctual entities (that are properly specified in the context) and for this reason are not listed here. Furthermore, all scalar quantities are represented by an italic (slopping) letter symbol whereas, vectors, matrices and tensors use upright bold, except where noted.

a	Characteristic dimension of the cross-section of the bar
	Length
a_T	Temperature shift factor
A	Area
b	Length
$\mathbf{B}$	Partial derivative vector/matrix of shape functions
c	Viscous damping factor
	Wave phase velocity
c_{Mat_α}	Wave phase velocity in material type α
c_{Mat_1}	Wave phase velocity in material type 1
c_{Mat_2}	Wave phase velocity in material type 2
$\mathbf{C}$	Viscous damping matrix
d	Hysteretic damping factor
dx	Infinitesimal length
D	Flexural rigidity vector
$\mathbf{D}$	Hysteretic damping matrix
	Nodal displacement
$\mathbf{D}_{\mathrm{RM}}$	Flexural rigidity matrix (Reissner-Mindlin)
e	Thickness
E^*	Longitudinal dynamic modulus
$E^{'}$	Longitudinal storage modulus
$E^{''}$	Longitudinal loss modulus
$E^{'}_{\mathrm{Mat}_\alpha}$	Longitudinal storage modulus of material type α
$E^{'}_{\mathrm{Mat}_1}$	Longitudinal storage modulus of material type 1
$E^{'}_{\mathrm{Mat}_2}$	Longitudinal storage modulus of material type 2
$E^{''}_{\mathrm{Mat}_2}$	Longitudinal loss modulus of material type 2

f	Body forces
	Frequency
f_0	Corner frequency
f_1	First natural frequency
f_d	Damped natural frequency
$f_{\min}$	Minimum frequency of the attenuation region
$f_{\max}$	Maximum frequency of the attenuation region
f_{lower}	Lower bound frequency of the designed attenuation region
f_{upper}	Upper bound frequency of the designed attenuation region
$\mathbf{F}$	Load vector
G^*	Shear dynamic modulus
G	Shear storage modulus
G'_{Mat_α}	Shear storage modulus of material type α
G'_{Mat_1}	Shear storage modulus of material type 1
G'_{Mat_2}	Shear storage modulus of material type 2
G''_{Mat_2}	Shear loss modulus of material type 2
h	Thickness of the plate
H	Apparent activation energy
$\mathbf{H}$	Receptance FRF matrix
$|\mathbf{H}|$	Magnitude of the receptance FRF matrix
$\angle\mathbf{H}$	Phase of the receptance FRF matrix
$\mathbf{H}_1$	FRF matrix estimator
$\mathbf{H}_2$	FRF matrix estimator
i	Imaginary unit $\left(\mathrm{i}=\sqrt{-1}\right)$
J_p	Polar moment of the cross-section with respect to the centroid
J_t	Saint-Venant torsion constant
k	Stiffness
	Wave number
k^*	Complex stiffness
k_{Mat_α}	Wave number of material type α
$\mathbf{K}$	Stiffness matrix

l	Length
L	Length
L_T	Total length of the structure
L_{Mat_α}	Length of the layer of material type α
L_{Mat_1}	Length of the layer of material type 1
L_{Mat_2}	Length of the layer of material type 2
$L_{\mathrm{Mat}_{\alpha\,\min}}$	Minimum length of the layer of material type α
$L_{\mathrm{Mat}_{1\,\min}}$	Minimum length of the layer of material type 1
$L_{\mathrm{Mat}_{2\,\min}}$	Minimum length of the layer of material type 2
$L_{\mathrm{Mat}_{\alpha\,\max}}$	Maximum length of the layer of material type α
$L_{\mathrm{Mat}_{1\,\max}}$	Maximum length of the layer of material type 1
$L_{\mathrm{Mat}_{2\,\max}}$	Maximum length of the layer of material type 2
$L_{\mathrm{T}_{\min}}$	Minimum total length of the cell
$L_{\mathrm{T}_{\max}}$	Maximum total length of the cell
m	Mass
$\mathbf{M}$	Mass matrix
M	Moment
Mat_α	Material type α
Mat_1	Material type 1
Mat_2	Material type 2
n	Unit vector normal to the surface
N	Shape functions
$\mathbf{N}$	Shape functions vector/matrix
N_{elem}	Number of elements
N_{cel}	Number of unit cells
p	Updating parameter Design variable
R	Universal gas constant
S	Surface
$\mathbf{S}$	Sensitivity matrix
t	Time

T	Surface force
	Traction vector
T_r	Transmissibility
T	Temperature
u	Displacement field
u_{Mat_α}	Displacement of material type α
$\dot{u}$	Velocity
$\ddot{u}$	Acceleration
V	Volume
w	Deflection of the mid-surface of the plate
W	Weight
X_{st}	Static deflection (displacement)
$\mathbf{Z}$	Dynamic stiffness matrix

Greek alphabet symbols

α	Phase angle
β	Phase angle
	Frequency ratio
Γ	Boundary surface
γ	Shear strain
δ	Phase lag (stress-strain)
$\delta\varepsilon$	Virtual strains
δu	Virtual displacements
ε	Strain
$\mathbf{\Delta p}$	Updating parameter change vector
η	Loss factor
	Modal loss factor
η_1	Modal loss factor of the first natural frequency
$\eta_{\mathrm{Mat}_\alpha}$	Loss factor of the layer of material type α
η_{Mat_1}	Loss factor of the layer of material type 1
η_{Mat_2}	Loss factor of the layer of material type 2
$\theta_{\mathrm{Mat}_\alpha}$	Torsional displacement of material type α
$\mathbf{\kappa}_{\mathrm{RM}}$	Curvature vector (Reissner-Mindlin)

K^*	Dynamic bulk modulus
K'_{Mat_2}	Storage bulk modulus of material type 2
ν	Poisson's ratio
ν_{Mat_2}	Poisson's ratio of material type 2
ξ	Damping ratio Modal damping ratio
ξ_1	Damping ratio of the first natural frequency
λ	Wavelength Eigenvalues $\left(\lambda = \omega^2 \right)$
ρ	Volumetric mass density
$\rho_{\mathrm{Mat}_\alpha}$	Mass density of material type α
ρ_{Mat_1}	Mass density of material type 1
ρ_{Mat_2}	Mass density of material type 2
σ	Normal stress
τ	Shear stress
ϕ	Modal vector
ψ	Infinitesimal rotations
Ψ	Natural vibration mode shapes
ω	Angular frequency
ω'	Shifted frequency
ω_1	First natural frequency
Ω	Space domain of the body or structure Geometry

Note: a partial derivative of u_i with respect to coordinate x_j is indicated by a comma, e.g., $u_{i,j} = \partial u_i / \partial x_j$. Furthermore, a superposed dot denotes partial differentiation in respect to time, e.g., $\ddot{u}$ and $\dot{u}$ are the displacement's second and first order derivatives, respectively, with respect to time.

Chapter 1

Introduction and motivation

This thesis presents a study on the development of numerical and experimental dynamic models for the characterization of the dynamic moduli of resilient materials, with emphasis on Cork Composite Materials (CCMs), allowing for numerical model validation and structural optimization. Furthermore, it presents methodologies developed to simulate the dynamic behavior of the two types of resilient layer structures, here considered, for passive vibration attenuation under steady-state conditions. Namely, a one-dimensional (1D) two-material Phononic-inspired Vibration Isolator (PIVI) and metallic panels subject to the constrained and unconstrained Surface Damping Treatments (SDTs).

The first part of this study consists of the characterization of the dynamic longitudinal and shear moduli of CCMs. Even though, it might be considered to be somewhat off-topic for a mechanical engineer, the fact that the dynamic properties of CCMs are usually inaccessible to the engineer (in spite of their proven success in dynamic applications), motivated one of the main topic of this thesis. It is noted that, considerable part of the time available for this thesis was dedicated to an accurate characterization of the dynamic moduli of the materials, which is essential to validate the numerical models used to simulate the dynamic behavior of the two types of layer structures analyzed in this study. A new experimental method (and specimen) is proposed making use of the inverse problem formulations associated with analytical models.

The second part of this study consists of structural analysis, experimental testing, model validation and optimization of the numerical models of the two types of resilient layer structures here studied.

The first type of structure studied is a 1D two-material PIVI that attenuates vibrations in the direction of the stacked layers. The fact that traditional vibration isolators may lack a satisfactory performance in a wide service frequency range motivates the development of the PIVI as an alternative solution, since it can be designed to present significant wider frequency gaps, designated as Attenuation Regions (ARs), between adjacent frequencies. The PIVI is a finite repetitive device and so it does not present a stopband, i.e., a frequency band in which waves are not allowed to propagate, but in its place a strong AR.

The second structure studied is a metallic panel that is subject to SDTs, free layer damping (FLD) or constrained layer damping (CLD), to reduce the vibration of the panel. The properties, location and thickness of the materials used in these treatments dictate the efficiency of the treatment. Usually, synthetic polymers are used in SDTs. However, their efficiency is often reduced if not lost at sufficiently higher temperatures, e.g., > 100ºC.

Motivated by this lack of efficiency and by the increasing concern regarding the comfort of the passengers in vehicles, in this study, the use of CCMs are considered as alternative materials in SDTs. Furthermore, an original methodology to optimize the application of SDTs in panels is developed and presented.

A brief background revision that support the development of this study in the areas of structural dynamics with layer structures applied to vibration isolation/attenuation follows.

1.1. Background and previous works

Vibration control is still a recurrent problem in structural dynamics. Vibrations may be controlled essentially by using passive methods, active methods or a combination of both usually designated as hybrid methods [1]. Active vibration control systems consist essentially of sensors and actuators, which are driven by external power, that measure and actuate directly on the vibrating system in order to control it. On the other hand, passive vibration control systems do not need external power and are usually less expensive when compared to the active systems. Passive vibration control usually involves adjustment of the stiffness and/or mass and/or damping of the vibrating structure. In [2], Mead describes four different methods for passive vibration control: structural design; localized additions; added damping; and resilient isolation. For context purposes, a brief summary of these four methods follows.

Passive vibration control by structural design is usually applied if severe or excessive vibration is expected at the design stage or is encountered in a prototype. Hence, it is common to analyze how the different response quantities depend in different ways on the fundamental structural properties of mass, stiffness and damping [3]. Passive vibration control by localized additions consist in the insertion of additional devices and/or material, usually categorized as localized additions, damping systems, isolation systems, e.g., a lumped mass that changes a troublesome frequency (which may or may not be a resonance) of a system usually designated as vibration absorber [4]. Passive vibration control by added damping consists of increasing the damping properties of the vibrating system. This is usually achieved by applying highly damped polymeric materials at strategic location within the structure where the added damped material is responsible for dissipating as much energy as possible [5]. Passive vibration control by resilient isolation consists of improving the vibration transmissibility between the "source" and the "receiver" at one or more connection points by making them sufficiently soft or resilient [6], e.g., using rubber pads and/or springs in the path between the "source" and the "receiver".

The mechanical characterization of resilient materials, i.e., viscoelastic materials intended to reduce the transmission of vibration, shock or noise [7], is of major importance for proper development and the characterization of new materials dedicated to sound and vibration control. Ferry [8] and Nashif et al. [9], state that the dynamic properties of linear viscoelastic isotropic materials can be represented by any two of the following parameters, namely the storage modulus $E^{'}$, loss modulus $E^{''}$ and loss factor $\eta = E^{''}/E^{'}$, i.e., the dynamic modulus $E^{*} = E^{'} + \mathrm{i}\, E^{''}$ (where i is the imaginary unit).

The idea of measuring the dynamic modulus from vibration tests that require solving an inverse problem [10], in which experimental measurement data is used to infer values of the parameters that characterize the system, dates back to the 1950s, where abundant literature may be found on the subject.

In 1957, Schlägel [11] described the methods successfully used at the time for measuring the dynamic modulus and divided them into: resonant and non-resonant methods. This division depends on whether the dynamic modulus is determined at a resonant frequency or in a range of non-resonant frequencies.

Resonant methods based on the response of a bar specimen subjected to different types of dynamic loads and frequencies have been extensively researched. For e.g., Norris and Young [12] and Madigosky and Lee [13] evaluated the dynamic modulus at the resonance frequencies from the measured accelerations at both ends of a bar specimen subjected to a harmonic load at one end.

In the context of resonant methods, the works of Pritz (see [14]-[16]) are considered of major importance. The transfer function method was used to evaluate the dynamic modulus of resilient acoustic materials by exciting, longitudinal and transversally, a cylindrical or prismatic specimen at one end, the other end being loaded with different masses, and by modeling the specimen with lumped mechanical elements. These works, among a few others (see e.g., [13]), have led to standardization of resonant method procedures to determine the dynamic modulus of viscoelastic materials (see, e.g., ISO 18437-2:2005 [7]). Other resonant methods involving vibrating beams with unconstrained viscoelastic layer were presented by Oberst and Frankenfeld [17] and more recently by Liao and Wells [18].

Non-resonant methods, for which the dynamic stiffness is determined from the response of a rod specimen subjected to different types of dynamic loads, are used to determine the dynamic modulus as for e.g., in the work of Gade et al. [19]. Among the non-resonant methods is the Dynamic Mechanical Analysis (DMA), for which the experimental setup apparatus and equipment is commerciality available [20]. In DMA the specimens are relatively small (less than a few square centimeters) and excited at relatively low frequencies (usually at a few hertz) inside a temperature controlled chamber. From the DMA results, the dynamic modulus and other properties such as creep and relaxation functions are estimated (see, e.g., [21]). Another non-resonant method is the wave propagation method. It consists of determining the dynamic modulus on the basis of strains that are known at three or more points on a longitudinal impacted bar specimen. Among these, some methods are based on the measurement of one wave at a time [22]-[23] and other methods allow the overlapping of waves at instrumented points of the bar specimen [24]-[27]. With the exception of DMA and the wave propagation method, which are considered well suited for broad frequency ranges, the methods previously mentioned are best suited for a narrower frequency range.

It should be noted that, each of these methods relates the response to the perturbation field with the dynamic modulus through a complementary method of analysis. By considering the precise boundary conditions, the analysis should give a rigorous solution to the field equations. However, in practice, to overcome the inherent technical difficulties it is usually necessary to introduce

approximations that may affect the equations just as the boundary conditions do. Thus, some experimental methods may be considered better conceived than others and, as a general rule, a simple method is considered more desirable than a more complex one since it allows these technical difficulties to be simplified or eliminated.

Nevertheless, the methods previously referred are perhaps the most common methods to determine the dynamic modulus of viscoelastic materials. Some relevant reviews describing in more detail several of these methods may be found in [8], [21] and [28].

Polymeric viscoelastic materials are conceivably the most common materials used to passively control the vibration response of structures, e.g., SDTs, with low cost and acceptable reliability [29]. Nevertheless, for applications that are subjected to a wide or high range of temperatures, like in the proximity of exhaust systems, engine parts, automotive panels, etc., the success of these materials is often reduced.

The use of cork and CCMs, which is the designation adopted along this text, are also referred to as cork agglomerate(s), cork-rubber(s) or composition cork(s), among other descriptions, may be foreseen as an alternative solution providing a damping capacity over a wide temperature range (e.g., -60ºC to 150ºC) with the additional characteristics of a low mass density and thermal and acoustic insulation [30]. CCMs are available in the market in a wide range of material compositions varying in cork and/or agglomerate, density, grain size and binder resin material [31]-[33]. Reference to the composition and/or to the properties of cork and CCMs are usually not available in the literature or in material databases. Thus, it is interesting to note that in spite of the widespread use of these materials, e.g., in gaskets (see e.g., [34] and [35]), practically no detailed information on their dynamic properties is usually found. This might be due to the recent use of these types of materials under dynamic conditions, for which (and surprisingly enough) the usually denoted static properties are often misused, as stated by the author and other researchers [36]. Furthermore, it may not be easy to warrant these dynamic properties as they may be affected by environmental condition changes (e.g., temperature, humidity, etc.).

As previously referred, and among others, the rod apparatus and the DMA methods that are usually used in the characterization of the dynamic properties of polymeric viscoelastic materials are also used to identify the dynamic properties of cork and CCMs. As contributions to the knowledge of the dynamic properties of cork and CCMs and as examples of the use of non-resonant vibrating methods, among few others, are the works developed Diogo [37], who conducted a preliminary study of the application of dynamic mechanical techniques to biological polymers, namely cork, by Mano [38], who investigates the viscoelastic properties of cork using DMA, and by Moreira et al. [39], who presents a static and dynamic characterization method, using transfer functions, for sandwich beams with CCM cores.

In previous works (see [40]-[41]), the author has used different approaches in his progression to estimate the storage and loss modulus of CCMs. In the above-mentioned paper [40], a study on the design of ARs concluded that by using CCMs it was possible to lower the frequencies of the frequency range of the ARs to a value of interest for several mechanical applications. However, and not to drift

away from the objectives of the work at that time (in which the test specimen was the periodic or repetitive bar for which the material properties were needed), the storage modulus of the CCMs was approximated by trial and error and based on a visual comparison of the experimental Frequency Response Function (FRF) and Finite Element Method (FEM) results. In [41] a Lagrangian finite element (FE) was used to estimate the storage modulus of CCMs. Initially, a FE undamped free vibration analysis was conducted, where the unknown variable, the storage modulus, was initially considered of unitary value, i.e., $E'_{\text{FEM}} = 1$ Pa. Afterwards, the square ratio of the experimental and FEM first natural frequencies was used to estimate the storage modulus, $\left(\dfrac{\omega_{\text{EXP}}}{\omega_{\text{FEM}}}\right)^2 = E'_{\text{estimated}} \approx E'$

where $\omega^2 = \dfrac{\phi^T \mathbf{K}\, \phi}{\phi^T \mathbf{M}\, \phi}$ and ω_{FEM} obtained with $E'_{\text{FEM}} = 1$ Pa. This was then verified by a structural harmonic analysis to obtain the FRF curve, which was then compared to the one obtained experimentally. As expected, it was verified that in order to obtain an acceptable accuracy some care should be considered with respect to the number of Lagrangian FEs used per wavelength of the vibration wave $\lambda = c/f$ where c is the magnitude of the phase velocity and f is the frequency of the wave (see, e.g. [42] for a detailed discussion on the numerical aspects involved).

From that work, the author understood the need for a more rigorous method to characterize the storage and loss modulus of CCMs. Thus, a hybrid analytical-experimental methodology, which is addressed in this thesis, was developed [43] allowing the validation of the FE models that simulate the dynamic behavior of the two types of resilient layer structures, studied here, for passive vibration isolation.

The first type of resilient layer structure consists of a PIVI, see Figure 1.1, that was first introduced by the author in his MSc dissertation [44].

Figure 1.1 – 1D two-material phononic-inspired device for longitudinal vibration attenuation.

The concept of a phononic device can be considered parallel to that of a photonic device since the main difference is the type of waves involved, i.e., phononics deals with elastic waves whereas photonics deals with electromagnetic waves.

One example of the simplest forms of a photonic crystal is illustrated in Figure 1.2. This photonic crystal is a block of silica with a regular grid of holes [45]. The difference in refractive index between the silica and the air in each hole means that light is scattered at the boundary. If the distance between the holes is similar to the wavelength of the incident light, the scattered photons interfere destructively and a photonic bandgap, i.e., forbidden band of wavelengths in which photons do not propagate, is created.
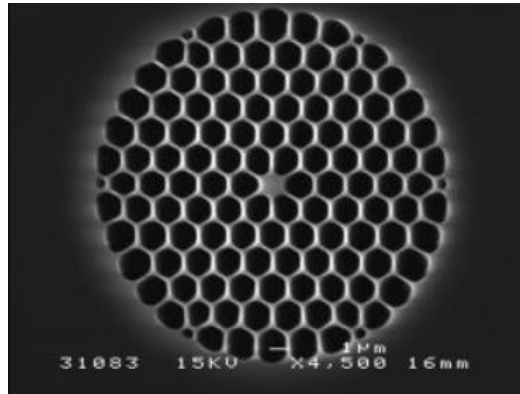
Figure 1.2 – Photograph of a cross-section of a silica photonic crystal fiber. (Image reproduced from [45]).

An unexpected breakthrough took place in 1995 between photonics scientist, Meseguer, and acoustics scientist, Llinares. The scientists realized that if these structures were scaled up to the corresponding wavelength of sound then, it might be possible to create an acoustic analogue of a photonic crystal. In this sense, inside the phononic crystal sound waves should bounce off the "atoms" in such a way that the waves interfere destructively, cancelling out the oscillations in the air creating a phononic bandgap, i.e., a forbidden band of wavelengths in which phonons do not propagate.

The scientists suspected that some form of phononic structure might already exist. Indeed, a great illustration of the phononic properties of a periodic structure was provided by Meseguer and co-workers when the acoustic characteristics of a minimalist sculpture by Eusebio Sempere (a Spanish sculptor, painter and graphic artist), illustrated by Figure 1.3, was studied.

Figure 1.3 – Photograph of a kinematic sculpture by Eusebio Sempere consisting of a periodic array of hollow stainless-steel cylinders, each 30 mm in diameter and arranged on a square 100 mm lattice (spacing) forming a structure with 4 m in diameter. (Image reproduced from [46]).

In addition to being visually appealing, the researchers question themselves about the possibility that the sculpture possess a phononic bandgap. Thus, measurements of the acoustic transmission as a function of frequency and direction were conducted on the sculpture. It was found that sound travelling perpendicular to the axes of the cylinders was strongly attenuated after a frequency of 1670 Hz. This provided the first experimental evidence for the existence of phononic bandgaps in periodic structures [47].

To gather additional data, the researchers decided to build their own minimalist sculpture (see, Figure 1.4) by hanging cylinders of stainless steel from a frame mounted in an acoustic chamber [48].
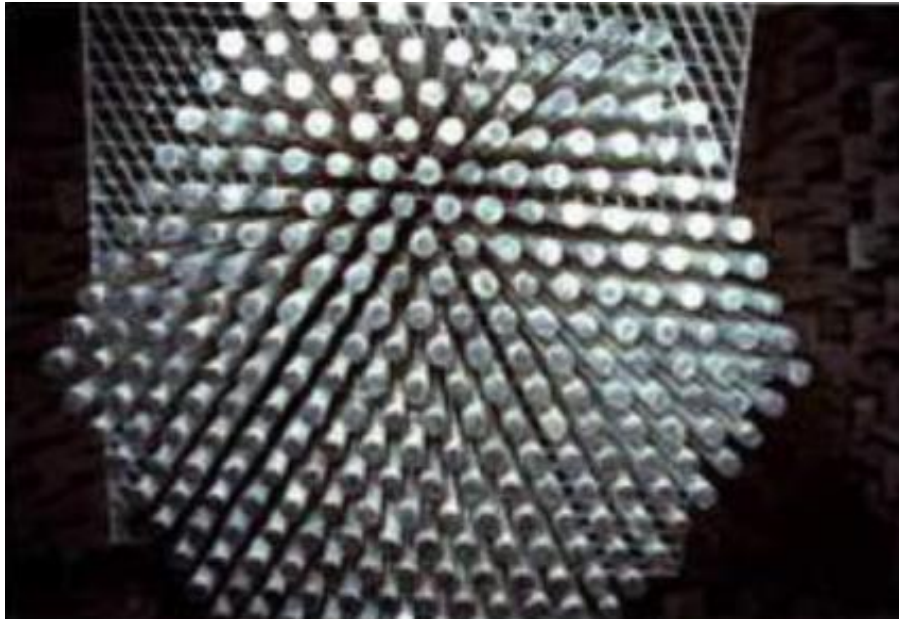
Figure 1.4 – Photograph of a bottom view of a triangular metal bar lattice used to demonstrate an acoustic bandgap. (Image reproduced from [48]).

Results revealed that the structure strongly suppressed sound waves in the audible range, at frequencies between 1400 and 1700 Hz. Similar tests were also conducted in the author's research group where Cartaxo [49] and Cartaxo et al. [50]-[51] studied the wave propagation through an array of metallic cylinders obtaining suppressed sound waves of approximately 25 dB at frequencies between 1250 and 1750 Hz. There was clear evidence of a phononic structure.

Phononic crystals were further used to build a structure that can block seismic waves in the ground. In [52], Meseguer and his colleagues drilled two vertical lattices, one honeycomb-shaped and the other triangular in a bed of marble, see Figure 1.5. Each hole in these lattices was 60 mm across, 1600 mm deep and separated from its neighbors by 140 mm.

Vibrations were created by dropping a steel ball bearing onto the marble floor, and sensors were used to measure how the vibrations were transmitted through the lattices. It was verified that both lattices significantly attenuated the vibrations. Nevertheless, to protect against real seismic waves, the holes would have to be hundreds of meters across and at least a kilometer deep [52].

<div align="center">a)   b)</div>
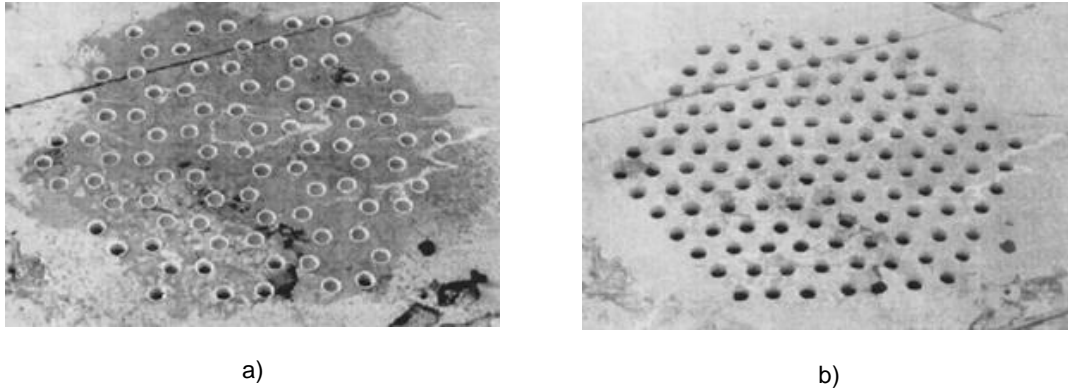
Figure 1.5 – Photographs of: a) the honeycomb; b) the triangular arrangements of cylindrical holes drilled on the surface of marble. (Images reproduced from [52]).

Sánchez-Dehesa confesses that such proposal is not feasible yet, however, you can protect an isolated building [52].

The concepts of phononic crystals described above and more specifically the 1D phononic crystal and its dispersion relations motivated the author to initiate his research in this field. One of the main objectives of the research was, and continues to be, to explore the concept and the design phononic structures for vibration isolation in several mechanical applications [44].

The research began with the basics, i.e.: Bloch's theorem [53] for the characterization of longitudinal waves, in structures with infinite periodicity repetition [54]-[55], leading to the corresponding dispersion relation [56]; and for structures build with finite periodic repetition, which was the case, a description of the basics was found in, e.g., [57]-[59].

Soon after, a study on the dynamical characterization of passive attenuation of longitudinal vibrations through two-material periodic structures, see Figure 1.6, was presented in [40] and [44]. One of the main contributions of these works (within the project entitled *Bloch* wave techniques applied to design periodic structures, see [60]) was to lower the frequencies were the first AR is verified to values of interest for several mechanical applications.
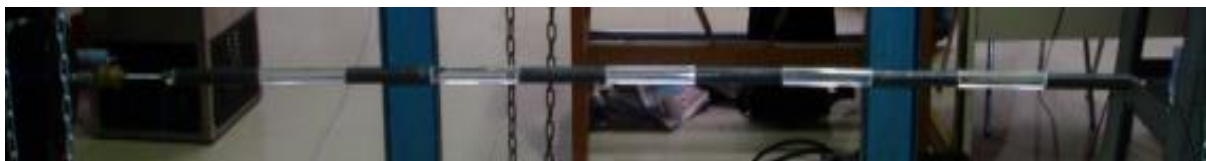
Figure 1.6 – Photograph of the experimental setup used to test a 5.5 cell steel-Polymethyl Methacrylate (PMMA) periodic cylindrical bar with a uniform diameter of 0.020m, composed of six steel and five PMMA half-cells each with a length of 0.135m [44].

However, the structure is approximately 1.5 meters long, presenting an AR initiating at approximately 1840 Hz. In spite of not being the most suitable solution for vibration isolation in mechanical applications, experimental evidence of the existence of phononic bandgaps in 1D two-material periodic structures was obtained with this device.

From these early studies, a patent [61] of a 1D two-material periodic structure for vibration isolation was submitted and conceded in 2009, see Figure 1.7.
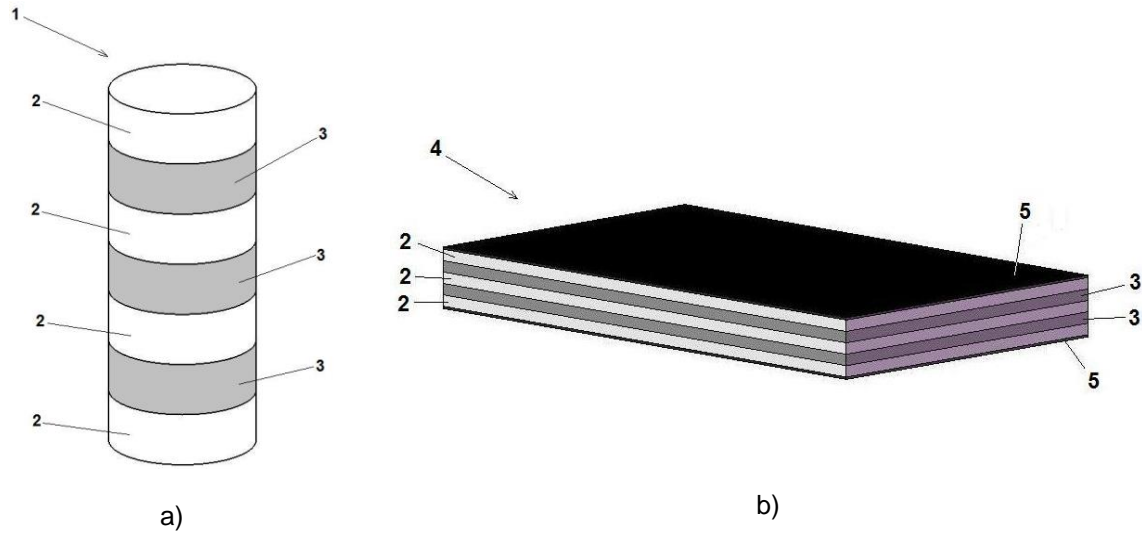
Figure 1.7 – Images of the two-material periodic structure vibration isolator in the published patent [61]: a) cylindrical shaped structure; b) rectangular shaped structure. Legend of the figures: 1) cylindrical shaped structure; 2) steel layer; 3) resilient material; 4) rectangular shaped structure; 5) anti-slip material.

Note that it was not until 2011, that the first international conference on phononic crystals (Phononics 2011) took place in New Mexico where interesting works reporting recent research and developments in the field were presented. For instance, the prediction and experimental validation of the dynamical response and tailoring of wave propagation filters for practical frequency ranges using periodic devices of finite length considering: periodic distribution of materials; addition of masses to a tube; and periodic curvatures [62]. Other examples such as: topology optimization methods for wave propagation of nonlinear wave devices [63]; as well as phononic metamaterials comprising structural framework of a stiff material and a more compliant material that can dissipate energy [64] were addressed.

With reinforced inspiration from the novel potential of phononic structures and based on the author's initial research ([40] and [44]), the author continued his research foreseeing the need to use materials with high contrast in the wave phase velocity (or impedance) between the two-material periodic structure. By doing so, the structure would present a reasonable dimension (i.e., in the centimeters range) as well as a considerable AR in a frequency range of practical use for vibration isolation of mechanical devices.

The materials selected and proposed to fulfill such requirements were steel and CCMs. Steel due to the fact that it may be the material that presents the highest wave phase velocity at the lowest cost. CCMs because they presents relatively low wave phase velocity at an affordable cost. Additionally, it is available in the market in a wide range of compositions. It is as if you can almost select a CCM that meets your requirements. Furthermore, it is of easy access in the market, and in particular at the author's country.

The author's easy access to CCMs and to their dynamic moduli, by means of the hybrid analytical-experimental characterization methodology presented by the author in this thesis, additionally motivated its study on the application for SDTs on metallic panels, where in most cases, polymeric viscoelastic damping material layers are used. As previously referred, for applications subjected to a wide range of temperatures like nearby engine parts, exhaust systems, automotive panels, etc., the use of CCMs as damping layers may be seen as an alternative low mass density, thermal and acoustic insulation solution which provides a damping capacity over a wide temperature range (e.g., -60ºC to 150ºC) [30].

SDTs for noise and vibration reduction of structures (usually associated to sheet metal structure) by means of passive techniques [2] and [29], are used in several areas such as automotive [65]-[67], railway [68] and aerospace engineering [65] and [69]. Such treatments are commonly classified according to whether the damping material is subjected to predominantly extensional or shear deformation and are referred to as extensional, unconstrained or FLD and as shear or constrained CLD treatments, respectively [9].

Considering the automobile as an example, it is consensual that there are several sources (e.g., motor) and paths (e.g., bolts) of vibration transmission to the different components (e.g., panels) of the vehicle that may cause discomfort to the passengers. To improve it, FLD treatments are currently applied in the industry. In Figure 1.8 is illustrated a typical layout of FLD treatments in an automobile.
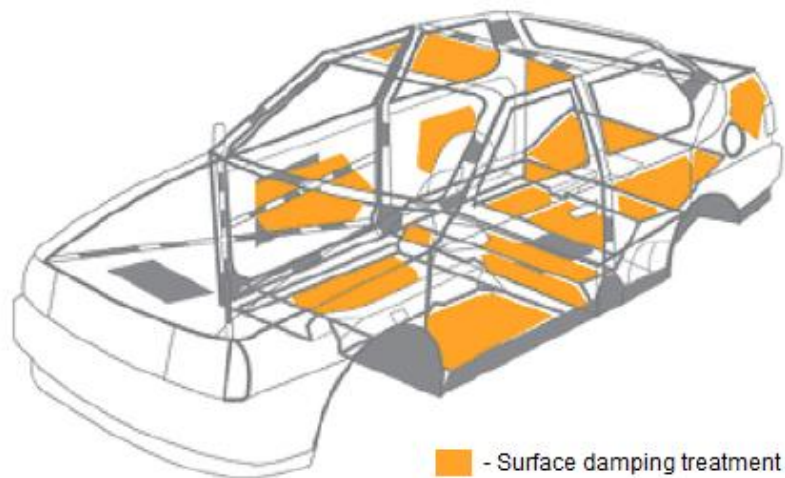
Figure 1.8 – Topology of usual SDTs applied to an automobile. (Image reproduced from [70]).

Amongst the several panels where SDTs may be applied, one that stands out due to the high amount of area treated is the bottom of the vehicle, see Figure 1.8. In fact, the corresponding weight of the materials commonly used in the FLD treatments in this area alone is approximately 10 kg [70].

In Figure 1.9 is illustrated the interior front view of an automobile with specific areas subject to FLD treatments. These FLD treatments are applied using viscoelastic material sheets, e.g., asphaltic melt sheet (with a mass density varying between 1200 kg m^{-3} and 1600 kg m^{-3} [70]) or liquid sprays designated as liquid applied sprayable damper (with a mass density of approximately 1000 kg m^{-3} [70]).

Figure 1.9 – Interior view of the front of an automobile with an FLD SDT applied. (Image reproduced from [70]).

It is clear that the benefits of the SDTs must be paid in terms of additional mass, resulting in additional fuel consumption. In this context, one challenge is to balance the comfort with the need to reduce mass and cost. Thus, in this thesis, the author studies the use of CCM sheets, which have a mass density of approximately 200 kg m^{-3}, in FLD and CLD treatments, see Figure 1.10 a) and Figure 1.10 b), respectively.

a)

b)
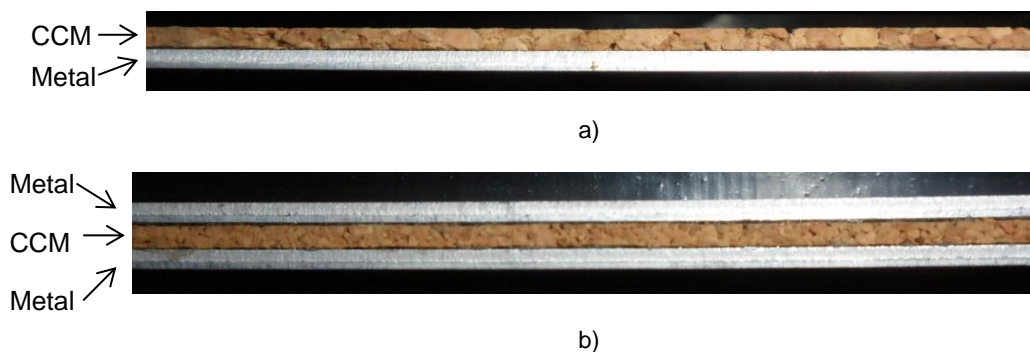
Figure 1.10 – Cross-section view (on black background) of SDTs using a CCM: a) FDL; b) CLD. (Each layer has a thickness of 2 mm).

In the SDTs area, it is quite consensual that FLD treatments are the most common due to their application simplicity using auto-adhesive viscoelastic layers and sprays [65]-[70]. However, there are automobiles in which the typical metallic panels are replaced by CLD panels [71]. Even though, the CLD treatments are generally more efficient than the FLD treatment, for a given weight of damping material, they may present considerable complication in both analysis and application [69].

In this context, and in spite of the type of damping treatment, it is desirable to optimize the spatial distribution of damping treatment in the structure. Numerous reported approaches can be found in the scientific literature to fully automate optimization procedures of SDTs.

For example, Eschenauer and Wodtke [72], Yildiz and Stevens [73] and Lumsdaine and Scott [74] considered the thickness of the damping layer as a design variable and used different optimization methods to vary the individual thickness of each damping layer. Bandini et al. [75] used a different approach by considering a constant thickness of the damping treatment on the structure where a genetic algorithm was used to control the evolution and a FEM was used to evaluate the performance of the configurations. Lin and Scott [76] optimized the shape of a damping layer for both constrained and unconstrained beams. Alvelid [77] proposed a modified gradient method to find "allowable positions" of damping materials to reduce noise and vibration. Zheng et al. [78] used topology optimization with the method of the moving asymptotes approach to optimally design damping treatment by maximizing the attenuation effect. In [79], the author presents a structural topology optimization scheme in which commercial FEM software was used to evaluate the performance of a FLD treatment with constant thickness. The properties of the material (used in the damping treatment) follow the Solid Isotropic Material with Penalization (SIMP) idea [80], where material properties are assumed constant within each element used to discretize the design domain and in which the stiffness is proportional to density in the power n (greater than one). In [81], the author extended a similar optimization scheme to the CLD treatments and to the use of CCMs as the damping layer material. This subject will be further discussed later in this thesis.

From the previous brief on optimization of SDTs, it quite consensual to mention that FEMs were and continue to be responsible for fostering the improvement of these treatments in more or less complex structures.

Note that, until the late 1940s, vibration analyses of even the most complex engineering systems were modeled using simple approximated methods and considering a few Degrees-of-Freedom (DOFs). Nowadays, and due to the development of the FEM it is possible to consider thousands of DOFs to approximate practical problems in a wide variety of areas. Information on FEM basics and other advanced topics may be found in Bathe [82], Zienkiewicz and Taylor [83]-[85], Cook et al. [86], and Reddy [87].

The FEM involves dividing the actual physical system into small subdomains or elements. Each element is a simple unit, the behavior of which can readily be analyzed using approximation of displacement or stress fields by shape functions. Thus, the resulting mathematical model is a set of equations that represent the actual structure with more or less accuracy. The inaccuracies or uncertainties that may be represent in FE models need to be assessed and when required, minimized. This allows adjusting (updating) the FE models so that their results match the experimental vibration test results of structures, at least in certain parameters' domains.

Modal testing has been a fast developing technique in the experimental evaluation of the dynamic properties. It consists of data acquisition and data analysis for the identification of modal parameters such as natural frequencies, mode shapes, damping ratios, etc. [88]. This area has been extensively

developed where for e.g., various techniques for identifying modal models from FRF data have been proposed. Further details of the theoretical and practical aspects of vibration measurement techniques are given by Maia et al. [88], Broch [89], Ewins [90] and McConnell [91].

Like other methods, modal testing possesses several limitations such as: a limited number of measurement locations; a limited number of identified modes which is defined by the frequency range; difficulty in establishing some boundary conditions, e.g., fixed or clamped; and noise in the measured data; among others.

For various reasons, to elaborate later on, the numerical predictions and experimental results often collaborate to disagree. So being, the scene is set to improve the numerical predictions using the experimental results. This improvement is possible, e.g., by modifying the modeling assumptions and/or parameters until the correlation of numerical predictions and experimental results satisfies practical requirements.

Initially, model updating was accomplished by a trial and error approach, which is normally time consuming and/or not be feasible in some cases. However, computational methodologies have been developed and numerous updating algorithms that use test data to update the parameters of the numerical models have been developed and presented. Particularly, modal data (natural frequencies and mode shapes) determined from measured frequency responses have wide application as a target or model parameter adjustment, see Mottershead and Friswell [92]-[93] and Mottershead et al. [94] for a detailed description. Surveys may be found in review articles of Hatke [95] and Imregun and Visser [96].

More recently, model updating has been developed into an established technology successfully applied to the correction of industrial scale FE models. Essentially, at this level, model updating is a process of adjusting a set of predefined parameters of the FE model. Usually, it is required the application of considerable physical insight in the choice of parameters to update and in the arrangement of the constraints, force inputs and response measurements in the experimental vibration test.

Developing sophisticated physics based models does not necessarily guarantee accuracy and predictability. The aim of structural analyses to predict the structural response can be achieved if the modeling errors are minimized with respect to the given purpose of the structural analysis. Models that contemplate these requirements are usually designated as validated models [96].

1.2. Problem description, main objectives, motivation and achievements

This thesis presents a study on the development of numerical and experimental models for structural vibration attenuation of two types of resilient layer structures under steady-state conditions using cork composite materials. Namely, phononic-inspired one-dimensional two material periodic vibration isolators and metallic panels subject to the unconstrained and constrained SDTs. The main objectives of this study are to formulate and develop theoretical, numerical and experimental models to:

- characterize the dynamic longitudinal and shear moduli of resilient materials, e.g., CCMs;

- validate the numerical models that simulate the dynamic behavior of these layer structures in a given frequency range and under steady-state conditions.

In this sense, and for presentation purposes, this study is divided into two main topics.

The first topic of this study regards the determination of the dynamic moduli of the resilient materials that in this study are mainly CCMs. This is motivated by the lack of technical data supplied by the manufactures regarding the dynamic modulus. Thus, one of the objectives of this study is to develop a methodology that allows obtaining these dynamic material properties on-site, i.e. with the common equipment available to an experimental vibration analyst in a vibration laboratory (which usually consists of an impact hammer and/or shaker, force transducers and accelerometers). In this sense, a novel hybrid analytical-experimental methodology for the determination of the dynamic moduli of resilient materials is developed and presented. Note that considerable part of the time available for this thesis was dedicated to an accurate characterization of the materials dynamic moduli, which is essential to validate the numerical models.

The second topic of this study regards the structural analysis, experimental testing, validation and optimization of the numerical models that simulate the dynamic behavior of the two types of resilient layer structures studied here.

The first type of structure consists of a structurally inspired phononic resilient layer vibration isolator that was introduced by the author in his MSc dissertation [44]. This vibration isolator may be used to control in a passive form longitudinal vibration in specific frequency ranges for which it was designed. The objective is to present a design methodology for these devices, which is based on a new perspective given by the *Bloch* wave theory of and conduct a rigorous evaluation of the pros and cons as well as the limitations of this methodology. This is motivated by the fact that traditional vibration isolators do not always provide a satisfactory performance in a wide service frequency range, since they present natural frequencies in the service frequency spectrum, originating unwanted vibration and possible acoustic discomfort, for frequencies nearby the resonances. These resilient layer vibration isolators are here introduced and studied as an alternative solution since they can be designed to present significant wider ARs between two adjacent frequencies and for certain frequency ranges, relatively to the traditional commercial vibration isolators.

The second type of structure consists of a metallic panel that is subject to SDTs. These treatments are a way for vibration reduction, usually associated with sheet metal structure vibration, by means of passive techniques. The usefulness of damping treatments depends upon its material properties, location and thickness of the treatment. The objective is to develop adequate rigorous numerical models to deal with the problem of finding the optimized spatial distributions of the damping material used in the SDTs of panels. This is motivated by an increasing concern on the comfort of the passengers. Therefore, SDTs and its materials have to be developed and optimized to balance the comfort of the passengers with the need to reduce the mass and cost of the vehicle.

The main achievements and contributions of this study are:

- The novel analytical-experimental hybrid methodology that allows for the successful determination of the dynamic moduli of resilient materials, with special emphasis to cork and CCMs;

- Experimental and validated numerical models of PIVIs composed of steel and CCMs, which present satisfactory performance in a low and wide service frequency range;

- Experimental and validated numerical models illustrating the potential use of CCMs in surface damping which presents an alternative low mass density damping solution to the conventional polymeric materials;

- topology optimization procedures improving the material disposition and consequently the performance of both PIVIs and SDTs.

This thesis resides in a linkage amongst different areas of science and engineering. In particular, symbolic computation, numerical methods, structural analysis, theoretical and experimental modal analysis of vibrations, rheology, materials characterization, prototyping and in more recent areas such as phononics.

It should be noted that this study adds value and knowledge to applications with CCMs, whose importance for the Portuguese industry has been evidenced though innovative international projects, e.g., Amorim Cork Composites LIFE project [97]. Apart from the quality of the scientific component, the use of CCMs is an additional contribute to the development of the cork sector of which Portugal is considered a leader in production, processing, research, development and innovation.

It is expected that this study will have a high impact, especially amongst the cork and CCMs environments, manufactures and research and development institutes and groups, since these materials are capable of new and innovative applications even when subject to dynamic solicitations, where the dynamic moduli are now of simpler determination using the proposed analytical-experimental hybrid methodology.

To conclude this introductory chapter, next is presented the layout of this thesis.

1.3. Layout of the thesis

This document is composed of six main chapters. The first is an introductory chapter where the theme is introduced justifying the importance and motivation of this study in terms of engineering and particularly in the structural vibrations field. Then, a non-exhaustive careful review of some of the most relevant research works that supports the development of this study is presented. This is followed by asserting the problem here addressed, its motivation, the main objectives and the methodologies adopted and proposed for fulfillment.

The second chapter introduces some of the most relevant fundaments regarding physical laws and/or mathematical concepts that support the study developed in this thesis. The equilibrium and constitutive equations, types of analysis, definitions, properties and characteristics used, are presented in this chapter. Furthermore, a general description of both modal testing and FEM is presented. Validation, correlation analysis and model updating concepts are then introduced. The formulation of the optimization problem and a brief introduction on vibration isolation and attenuation

mechanisms is followed by a brief introduction to the inverse problem formulation that conclude this chapter.

In the following chapters all the contents, except when referenced to the respective authors, are original contributions of this study.

Hence, the third chapter regards the characterization of the dynamic modulus. The proposed new analytical-experimental hybrid method is presented to characterize first the dynamic longitudinal modulus and then adapted to characterize the dynamic shear modulus. The analytical formulation, its numerical implementation, the construction of the test specimens and the experimental setups used in the proposed methodology are presented. Then, follows a brief description of DMA (that is used to characterize the longitudinal dynamic modulus), the Time-Temperature-Superposition (TTS) principle, the methodology, and the experimental setup adopted in this study. The main results from each method are presented and then compared and discussed. For a quick guidance of the main result relative to this third chapter, see the following list below at the indicated pages.

The presentation of the main contributions and conclusions complete this chapter.

In the fourth chapter, are first presented the analytical, numerical and experimental models of the proposed PIVI. The selection of the pair of materials, the design, structural improvement and optimization of the PIVI for several mechanical applications follow. An experimental comparison, in terms of force transmissibility, between two Commercial Vibration Isolators (CVIs) and some of the proposed PIVI is also presented. Then, PIVIs are applied in an industrial application to a motor of a hermetic compressor. Following are presented the main results and their discussion. For a quick guidance of the main result relative to this fourth chapter, see the following list below at the indicated pages.

To conclude this chapter, the respective contributions and conclusions are presented.

The fifth chapter regards the SDTs. First, a brief introduction to the FLD and CLD treatments is presented. Then, FE modeling and analysis of SDTs are presented and followed by the structural

optimization method developed. Following are presented the experimental setup and specimens used. Then, are presented the main results and respective discussion. For a quick guidance of the main result relative to this fifth chapter, see the following list below at the indicated pages.

The respective contributions and conclusions complete this chapter.

In the sixth and final chapter, entitled, "Contributions, conclusions and future works" are presented the main original contributions and conclusions of this thesis as well as some suggestions for future works.

Chapter 2

Fundaments

Fundamental concepts used in this thesis are presented at this chapter in a summarized format to introduce existing knowledge, from a broad range of physical laws and mathematical concepts, as a starting point of this study. In this sense, the proposed idea, methods and original contributions are presented in the following chapters.

Since it is not possible, even if intended, to cover all subjects in detail it is preferable that some of the most relevant references regarding each topic are specified to further guide the reader. Nevertheless, and before proceeding to an overview of the fundaments that support this thesis, three basic assumptions, that will be taken as given throughout this thesis, are now established: i) the structures studied are assumed as linear systems whose dynamic behavior may be described by a set of second order differential equations; ii) the structure obeys the reciprocal theorem associated with the names of Maxwell, Betti, and Rayleigh and; iii) steady-state conditions are assumed.

2.1. Equilibrium and constitutive equations

The theory of continuum mechanics regards matter as continuum that remains continuous in the sense that it pays no attention to the molecular or microstructure of a material. Thus, in this idealization matter may be indefinitely divisible into infinitesimal volumes of continuum matter to study the motion and the mechanical behavior of materials and structures.

The mechanical behavior of continuum materials is generally defined by constitutive stress-strain relations expressing the stress as a function of the strain, strain rate, strain history, temperature, and material properties. In this study, a brief introduction to linear theory of elasticity is presented, boarding the necessary concepts and formulations.

Thus, consider a closed sub-domain Ω with volume V and surface S within a continuum body in elastic equilibrium. The region has a general distribution surface forces T on the boundary surface Γ and body forces f in the volume Ω as illustrated in Figure 2.1.

After applying the loads, the body (or the material points of the body) changes its position from the initial or undeformed configuration to the current or deformed configuration. The displacement u of the body is defined by the difference of these two positions vectors [98].
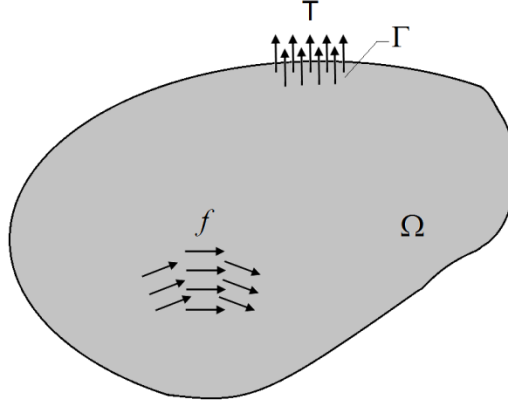
Figure 2.1 – Body Ω with surface forces T acting on arbitrary portion of its boundary Γ and volume forces f acting on an arbitrary volume Ω .

The infinitesimal strain tensor neglects the nonlinear terms of the *Green* strain tensor and may be written as

$$\varepsilon_{ij} = \frac{1}{2}\left(u_{i,j} + u_{j,i}\right), \qquad i \text{ and } j = 1, 2, 3 \tag{2.1}$$

where, $u_{i,j} = \partial u_i / \partial x_j$ (a partial derivative of the u_i component of u with respect to the coordinate x_j is indicated by a comma) with i and $j =$1, 2, 3 where i and j are notation indices with respect to directions in the space. In the above, and in the sequel is adopted the convention that repeated indices in a term are summed over the range of the index.

The *Cauchy* stress tensor at the boundary is defined by the traction vector T_i on the boundary surface Γ characterized by a unit vector, n_j, normal to the surface at each point expressed by

$$T_i = \sigma_{ij} n_j \tag{2.2}$$

The principle of linear momentum, states the rate of change of the linear momentum of a body is equal to the sum of the forces acting on the body.

Hence, it may be written in the weak form as

$$\int_{\Gamma} T_i \, d\Gamma + \int_V f_i \, dV = \int_V \rho \, \ddot{u}_i \, dV + \int_V c \, \dot{u}_i \, dV. \tag{2.3}$$

where, ρ is the mass density, c is a constant that takes into account the velocity dependent damping forces, i.e., the viscous damping constant, and $\ddot{u}$ and $\dot{u}$ are the displacement's second and first order derivatives, respectively, with respect to time (a superposed dot denotes partial differentiation in respect to time).

Eq. (2.3) may be rewritten using Eq. (2.2) as

$$\int_{\Gamma} \sigma_{ij} n_i \, d\Gamma + \int_V f_i \, dV = \int_V \rho \, \ddot{u}_i \, dV + \int_V c \, \dot{u}_i \, dV. \tag{2.4}$$

Using the Divergence theorem of *Gauss* Eq. (2.4) becomes

$$\int_V \left(\sigma_{ij,i} \, n_i + f_i \right) dV = \int_V \left(\rho \, \ddot{u}_i + c \, \dot{u}_i \right) \, dV. \tag{2.5}$$

Since Ω is of arbitrary volume, Eq. (2.5) may be rewritten in the strong form as

$$\sigma_{ij,i} n_i + f_i = \rho \, \ddot{u}_i + c \, \dot{u}_i \tag{2.6}$$

To obtain a solution to Eq. (2.6) it is necessary to assume the material behavior (constitutive laws), the initial conditions for a given reference instant t_0 and the boundary conditions. The problem discretization follows the path of the parabolic problem [99] obtaining a system of second order differential equations that in matrix notation for a Multiple-Degree-Of-Freedom (MDOF) system with N DOF may be expressed as

$$\mathbf{M} \, \ddot{\mathbf{u}} + \mathbf{C} \, \dot{\mathbf{u}} + \mathbf{K} \, \mathbf{u} = \mathbf{F}, \tag{2.7}$$

where $\mathbf{M}$, $\mathbf{C}$ and $\mathbf{K}$ are the $N \times N$ mass, damping and stiffness matrices, respectively and $\mathbf{F}$ is the $N \times 1$ applied load vector.

2.1.1. Stress-strain relations

The linear elastic dynamic properties of continuum solid materials may be characterized in the frequency domain by the dynamic modulus E^*, see [8]. The dynamic modulus is also referred to as the complex modulus of elasticity, the dynamic modulus of elasticity, among other designations.

For an applied harmonic force, it relates the amplitudes of the stress $\sigma(t) = \sigma_0 \, e^{\mathrm{i} \, \omega_{ap} t}$ and of strain $\varepsilon(t) = \varepsilon_0 \, e^{\mathrm{i} \, (\omega_{ap} t - \delta)} = \bar{\varepsilon}_0 \, e^{\mathrm{i} \, \omega_{ap} t}$ where $\bar{\varepsilon}_0 = \varepsilon_0 \, e^{-\mathrm{i} \, \delta}$, as

$$E^* = \frac{\sigma_0}{\bar{\varepsilon}_0} = \frac{\sigma_0}{\varepsilon_0} e^{\mathrm{i} \, \delta} \tag{2.8}$$

where $\mathrm{i} = \sqrt{-1}$ is the imaginary unit, ω_{ap} is the applied excitation angular frequency, t is the time variable and δ is the phase lag between the stress and the strain, as illustrated by Figure 2.2 a).
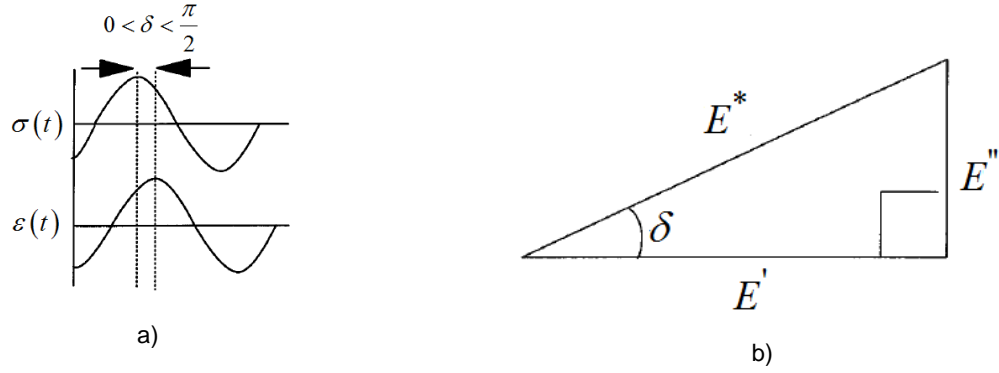
Figure 2.2 – a) Stress-strain curves and phase lag δ (where t relates to the angle); b) Geometric relations involved in E^*.

The elasticity moduli E must therefore be redefined using complex quantities to include this time dependence. A geometric relation of these quantities is illustrated in Figure 2.2 b). Thus, the dynamic modulus of elasticity is defined as

$$E^* = \frac{\sigma_0}{\varepsilon_0} e^{i\,\delta} \longrightarrow \begin{cases} E^{'} = \dfrac{\sigma_0}{\varepsilon_0}\cos\delta \\[2mm] E^{''} = \dfrac{\sigma_0}{\varepsilon_0}\sin\delta \end{cases} \xrightarrow{\;yields\;} E^* = E^{'} + i\,E^{''}, \tag{2.9}$$

where $E^{'}$ is the storage modulus (the real component of E^*), and is a measure of the energy stored elastically and $E^{''}$ is the loss modulus (the imaginary component of E^*), which is a measure of the energy lost, e.g. as heat or sound. The loss factor η is defined as

$$\eta = tg\delta = E^{''}\big/E^{'}. \tag{2.10}$$

The definition of the dynamic modulus expressed in Eq. (2.8) presents no restrictions on the type of deformation such as shear, bulk, tensile, etc. Therefore, E^* may represent the complex form of any dynamic modulus of elasticity.

The phase lag between the stress and the strain δ, see Figure 2.2, may serve to determine the type of material behavior. Hence, if $\delta = \pi/2$ the material is said to present a purely linear viscous elastic behavior. If $0 < \delta < \pi/2$ the material is said to present a linear viscoelastic behavior. Whereas, if $\delta = 0$ the material is said to present a purely linear elastic behavior.

In the last case ($\delta = 0$), the dynamic modulus Eq. (2.9) is simplified and may be expressed as

$$E^* = \frac{\sigma_0}{\varepsilon_0} = E^{'} = E, \tag{2.11}$$

where, E is the *Young's* modulus also known as the tensile or longitudinal elastic modulus, among other designations. Note that the *Young's* modulus can be determined by a static or quasi-static experimental test. Most structural metals are nearly linear elastic under small strain at ambient temperature and follow a constitutive law based on *Hooke's* law, i.e., $\sigma = E\,\varepsilon$.

Besides the *Young's* modulus, there are other elastic moduli such as the shear modulus and bulk modulus. Hence, for a material that presents a purely linear elastic behavior (δ =0) the shear modulus G may be obtained similarly to Eq. (2.11) and expressed as

$$G^* = \frac{\tau_0}{\gamma_0} = G' = G, \tag{2.12}$$

where G^* is the dynamic shear modulus, τ_0 and γ_0 are the amplitudes of the shear stresses and strains, respectively and G' is the shear storage modulus. The bulk modulus K that measures the response of the material to uniform pressure may be expressed by relating the *Young's* and shear moduli, see Eq.(2.11) and Eq. (2.12), as

$$K^* = K' = K = \frac{E\,G}{3(3G - E)}. \tag{2.13}$$

where K^* and K' are the dynamic and storage bulk moduli, respectively.

Furthermore, it is also common to measure the *Poisson* effect, i.e., the expansion/contraction of the material in one or more directions when subject to a compression or traction in a different perpendicular direction. For this, the Poisson's ratio is defined as the negative of the ratio of the expansion (contraction) strain divided by the fraction of compression (traction) strain. Similarly to the bulk modulus and for a material that presents a purely linear elastic behavior (δ =0), the *Poisson's* ratio may be expressed by relating the *Young's* and shear moduli, see Eq.(2.11) and Eq. (2.12), as

$$\nu = \frac{E}{2G} - 1. \tag{2.14}$$

2.2.   Types of structural analysis

Once the material behavior is known (or assumed) it is possible to evaluate the effects of loads on the body (structure). This type of evaluation is usually referred to as structural analysis. In this study, three types of structural analyses are considered: i) static analysis, which is used to determine the effects of steady loading conditions on a structure, while neglecting inertia and damping effects, such as those caused by time-varying loads; ii) free vibration analysis, which is used to determine the vibration characteristics (natural frequencies and mode shapes) of a structure; iii) and steady state forced vibration analysis, which is used to determine the steady state response of a structure to time-varying loads.

2.2.1. Static analysis

The static analysis consists of solving Eq. (2.7) in which the inertia and damping effects, such as those caused by time-varying loads are not considered (since they do not induce significant effects), i.e.: $\ddot{\mathbf{u}} = \dot{\mathbf{u}} = \mathbf{0}$ and $\mathbf{F}(t) = \mathbf{F}$, where $\mathbf{F}$ is a constant vector. It is obtained a linear force-displacement law expressed by Eq. (2.15), which is rewritten here for demonstration purposes, as

$$\mathbf{K}\,\mathbf{u} = \mathbf{F}. \tag{2.15}$$

In this study, whenever static loading and response conditions are considered, it means that the loads and the response of the structure to those loads are assumed as static.

2.2.2. Free vibration analysis

The free vibration analysis consists of calculating the natural vibration frequencies ω of the structure considering that external forces vanish ($\mathbf{F} = \mathbf{0}$) after an initial perturbation. Assuming that

$$\mathbf{u} = \bar{\mathbf{u}}_0\, e^{\mathrm{i}\omega t}, \tag{2.16}$$

where $\bar{\mathbf{u}}_0 = \mathbf{u}_0\, e^{-\mathrm{i}\,\alpha}$ is the amplitude of the displacement and α is the phase angle of the harmonic motion, by substituting Eq. (2.16) and its derivatives with respect to time in Eq. (2.7), after some mathematical manipulation one obtains

$$\left(-\omega^2\mathbf{M} + \mathrm{i}\,\omega\,\mathbf{C} + \mathbf{K}\right)\bar{\mathbf{u}} = \mathbf{0}. \tag{2.17}$$

In the general case, where damping is non-proportional, one is faced with a quadratic problem and one can recur to e.g., the state-space analysis to solve Eq. (2.17), see [88] for more details.

In the case of proportional damping, i.e., when the viscous damping matrix $\mathbf{C}$ is directly proportional to the stiffness matrix, mass matrix or to a linear combination of both as

$$\mathbf{C} = \bar{\alpha}\mathbf{K} + \bar{\beta}\mathbf{M}, \tag{2.18}$$

where $\bar{\alpha}$ and $\bar{\beta}$ are constants, one is faced with a set of N uncoupled damped Single Degree-of-Freedom (SDOF) equations and one may recur e.g., to the Laplace domain [88] to solve Eq. (2.17).

For the undamped case, Eq. (2.17) is a homogeneous system of equations with non-zero solution when

$$\det\left(\mathbf{K} - \omega^2\mathbf{M}\right) = 0. \tag{2.19}$$

Solving this equation leads to the characteristic equation, and the left-hand side is called the characteristic polynomial. When expanded, this gives a polynomial equation in $\lambda_r\left(= \omega_r^2\right)$. For a large number or DOFs other numerical methods may be preferable to solve this type of problem [100].

2.2.3. Forced steady state vibration analysis

Whenever external energy is supplied, through either dynamic applied forces or displacements to a structural system, it is said to undergo forced vibration. The dynamical applied forces and displacements may be classified as: periodic harmonic or periodic non-harmonic; non-periodic; with long or short duration; or random in nature. The dynamical response of a system to a harmonic excitation is called harmonic response. In this study, it is considered a harmonic excitation that may be presented in the complex form as

$$\mathbf{F} = \bar{\mathbf{F}}_0 e^{\mathrm{i}\omega t}, \tag{2.20}$$

where $\bar{\mathbf{F}}_0 = \mathbf{F}_0\, e^{-\mathrm{i}\beta}$ is the force amplitude and β is the phase angle of the harmonic excitation. For an excitation frequency coincident to the natural frequency, the response of the system will be large, tending to infinite if there is no damping. This is known as resonance and is generally avoided to prevent system failure. However, in some particular cases the resonance phenomenon is used, e.g., in the design of atomic probes for microscopes, see [101].

The steady-state solution will be given by substituting Eq. (2.16) and its derivatives with respect to time and Eq. (2.20) in Eq. (2.7), obtaining

$$\left(-\omega^2 \mathbf{M} + \mathrm{i}\,\omega\,\mathbf{C} + \mathbf{K}\right)\bar{\mathbf{u}}_0 = \bar{\mathbf{F}}_0. \tag{2.21}$$

Note that for each given ω, the only unknown is the respective $\bar{\mathbf{u}}_0$.

2.3. Receptance frequency response function

The ratio between the displacement response due to the excitation force, as a function of frequency is designated as the receptance (compliance) FRF [88] which can be expressed by the matrix of the frequency response functions as

$$\mathbf{H}(\omega) = \left(-\omega^2 \mathbf{M} + \mathrm{i}\omega\,\mathbf{C} + \mathbf{K}\right)^{-1} = \mathbf{Z}^{-1}(\omega). \tag{2.22}$$

Note that its inverse is usually designated as the dynamic stiffness and represented by $\mathbf{Z}(\omega)$. The receptance FRF is a complex function with magnitude $\left|\mathbf{H}(\omega)\right|$ and phase $\sphericalangle\,\mathbf{H}(\omega)$ illustrated in Figure 2.3 a) and Figure 2.3 b), respectively.

The physical interpretation of the FRF is that a sinusoidal input force, at a frequency ω, will produce in the time domain a sinusoidal output motion at the same frequency with an amplitude multiplied by $\left|\mathbf{H}(\omega)\right|$, and a phase shifted by $\sphericalangle\,\mathbf{H}(\omega)$.

Since the dynamic properties of a system may be expressed in terms of any convenient response characteristic, i.e., displacement, velocity or acceleration that are mathematically interrelated response quantities, knowledge of an FRF in terms of any one of the motion parameters allows for derivation of

the other FRF form. In this sense, FRFs may be referred to as receptance, mobility or accelerance when the response characteristic is displacement, velocity or acceleration, respectively. It is usual to use the receptance FRF for modeling and the accelerance FRF for measurements, since the most common motion transducer is the accelerometer.

a)

b)
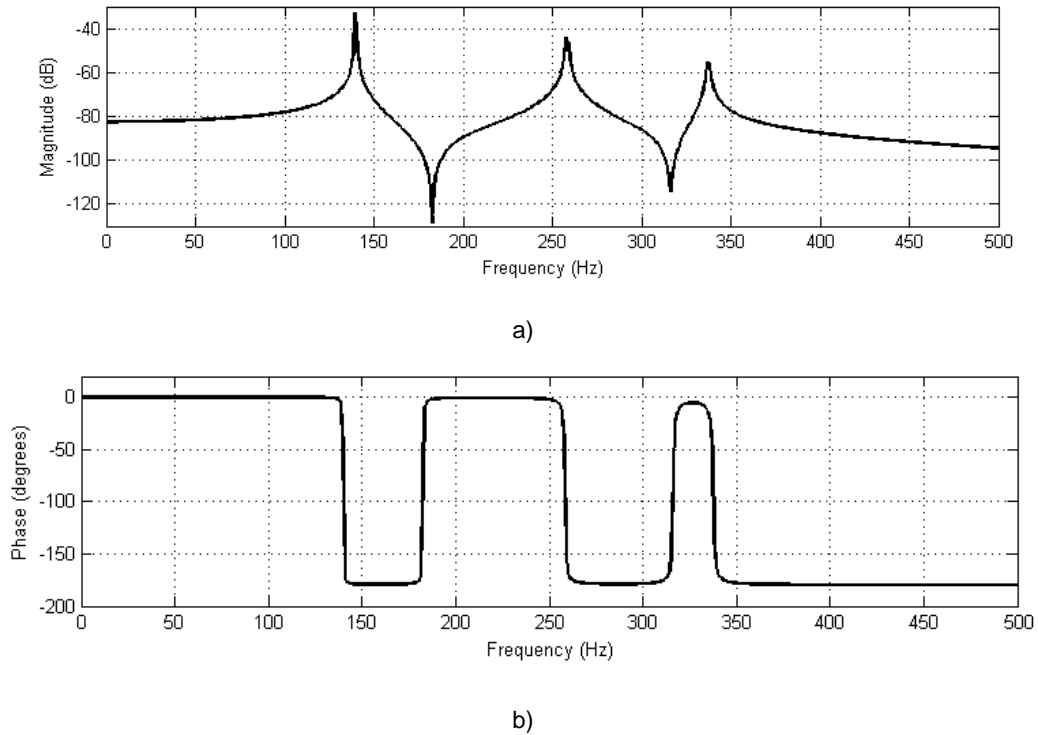
Figure 2.3 – Receptance FRF curve: a) magnitude; b) phase.

In general, the FRF curves may be estimated: analytically (at least for simple systems and up to certain frequencies); numerically using the FEM to model and solve more complex systems and; experimentally by modal testing of the real structure.

2.4. Modal testing

One may say that there is no single right way to perform an experimental modal test. In almost every case, the support, the excitation equipment or the transducers will influence the dynamic behavior of the structure under test. In experimental modal testing one has to realize that these influences exist, understand them, and then design the test to minimize their effects on the dynamic behavior of the structure. In many aspects, experimental modal testing can be considered as part art and part science in the sense that the validity and accuracy of the experimental results may strongly depend on the knowledge and experience of the user.

In this study, one of the objectives of experimental modal testing is to acquire sets of FRFs that are sufficiently extensive and accurate to enable analysis and extraction of the properties for the required modes of the structure. However, the frequency domain extent of experimental measurements will be dictated by the capabilities of the hardware equipment (transducers, data processing equipment, etc.) used in the measurements.

In experimental modal testing, the measurement chain can be divided into three main sub-sets [88]: i) the excitation components; ii) the sensing components and; iii) the data acquisition and processing components. However, in the author's opinion a fourth sub-set regarding the supporting/linking components, i.e., the components that support/link: the structure under test (e.g., rubber springs); the excitation system (e.g., metallic chains) and the sensing components (e.g., beeswax), should also be considered in the measurement chain. A brief introduction to these topics is presented next.

2.4.1. Excitation of the test structure

The excitation mechanism provides the input solicitation, generally in the form of a driving force applied to the structure under analysis. There are some variants for this mechanism depending on the desired input, accessibility and properties of the test structure. The most popular are the exciter, also referred to as shaker and the impact hammer.

The shaker is usually an electromagnetic vibrator capable of transmitting different excitation signals (generated by a signal generator and then amplified by a power amplifier), e.g., stepped-sine, swept-sine, random, etc., to the structure under test.

This excitation mechanism requires physical contact with the structure, see Figure 2.4 a). The objective is to transmit controlled excitation to the structure in a given direction and, simultaneously, to impose as small restraint on the structure as possible in all other directions. A push-rod (drive-rod or stinger) is usually used to form a link between the shaker and the structure under test. The push-rod is designed so that it is highly stiff axially and relatively flexible to lateral and rotational motions.

A popular alternative to the shaker is the impact hammer, which consists of a hammer with a force transducer attached to its head and a rubber, plastic or metallic tip, see Figure 2.4 b). The hammer itself is the excitation mechanism, which exempts the signal generator and the power amplifier. Furthermore, its use avoids structure restraint and mass loading on the test structure.
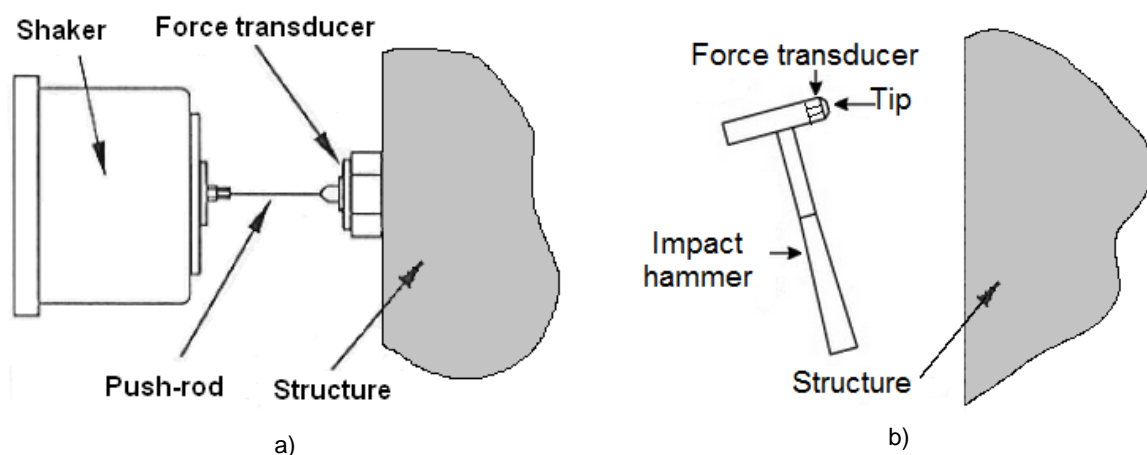
Figure 2.4 – Excitation mechanism of the test structure: a) vibration transmissibility between the shaker and the structure through a push-rod; b) impact or impulse hammer.

One may state that, without prior knowledge of the dynamic characteristics of a structure or its model, the best location of the excitation and response measurement points is a matter of trial and error coupled with experience and engineering judgement. Here, the use of numerical models is expected to be of great help.

2.4.2. Sensing transducers

The technology developed in measurement equipment allows the direct measurement of physical quantities that characterize movement like displacement, velocity and acceleration. Thus, for measuring displacements the most common instruments are potentiometers (of simple conception), while for measuring velocities, laser equipment (using the *Doppler's* effect) is probably the most popular option. Relatively to acceleration measurements transducers, usually designated as accelerometers, they can be piezoelectric, piezoresistive, capacitive or force balanced.
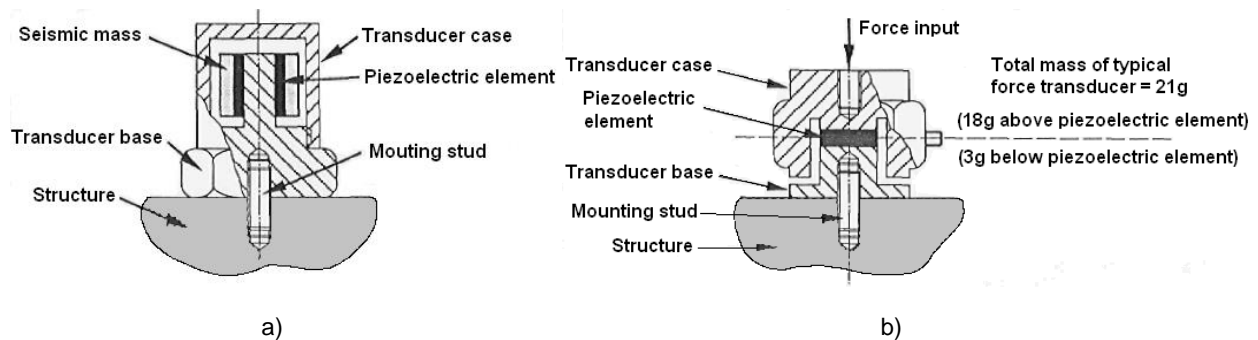
Figure 2.5 – Technical drawings of sensing transducers [88]: a) partial cut of a piezoelectric accelerometer; b) partial cut of a piezoelectric force transducer.

A partial cut of a typical piezoelectric accelerometer is illustrated in Figure 2.5 a). There are four basic components: a base and case, a center post, an annular section of piezoelectric ceramic and an annular seismic mass element. The base of the accelerometer moves with the motion structure to which is attached, and to cause equivalent motion of the seismic mass, a force must be applied. This force is transmitted through the piezoelectric crystal that deforms slightly as a consequence. The deformation produces a charge in the piezoelectric crystal that is proportional to the deformation and hence, ultimately, to the acceleration of the seismic mass and structure. These devices operate well over a fairly wide frequency range, but they are not generally well suited to low frequency applications [88], i.e., less than approximately 10 Hz, depending on the accelerometer.

The most common type of force transducers (see Figure 2.5 b)), works on the principle that the deformation of a piezoelectric crystal produces a charge output proportional to the force acting on that crystal (same principle as described for the piezoelectric accelerometer). In Figure 2.5 b) it is illustrated the cross-section of a typical piezoelectric force transducer from which is possible to identify two constitutive masses: one below the piezoelectric element ("base-side" mass) with ≈3 grams; and the other above the piezoelectric element ("live-side" mass) with ≈18g [88]. The "live-side" mass of the force transducer is kept small minimizing the modification to the structure. For a typical force

transducer, the "base-side" is only ≈3 grams. In reference [88] it is discussed the importance and influence of the active and total mass of the force transducers in experimental work.

Furthermore, there are also "dummy" sensing transducers that have similar mass properties to the real transducers [88]. These are normally used in cases where there are not sufficient real transducers available. Hence, the dummy transducers may be systematically and temporarily replaced by real transducers until all the intended measurements locations have been covered. Note that the results obtained from tests that use these types of transducers should be the same as if a complete set of real transducers had been attached to the structure.

2.4.3. Data acquisition and processing components

These components are used to acquire and process the signals developed by the sensing components, e.g., magnitudes and phases of the excitation forces and its responses. Signal conditioning, power amplifiers, generators and analyzers are an example of types of these components. Nowadays, this information is transmitted to a digital computer, in which specific software, e.g. Pulse Labshop (Brüel & Kjaer), processes the acquired data.

2.4.4. Supporting components

Considerations of the support of the structure under test as well as the excitation system and sensing components is an import part of the setup of the test. The support conditions must be well defined and experimentally repeatable if the results of the dynamic measurements are to reflect the properties of the test structure.

For laboratory testing of structures usually free boundary conditions are employed since they are achieved with relative ease by recurring to flexible suspensions (e.g., soft springs) so that the resonance frequency of the mass of the structure on the stiffness of the suspensions or devices are low and distant from the frequency range of interest.

Even though, the support of the excitation system is less important it should still be considered. It is common to support a shaker on a hoist due to its convenience for positioning and alignment with the test structure. However, the shaker on a hoist is a dynamic system and will move as a result of the internal force generated. This movement may cause problems at low frequencies where the modes of the suspensions of the shaker can be excited.

The attachment of sensing transducers to the test structure will necessarily have more or less inertial loading effects on the structure. When necessary, these effects should be considered at an early stage of the setup. One other aspect is that the stiffness of attachment has to be sufficiently high throughout the frequency range of interest so that the motion of the transducer is identical to that of the attachment point of the structure. For low frequency measurements it is common to use beeswax. However, for high frequency measurements the sensing transducers have to be firmly bolted/cemented to the structure.

2.4.5. Estimation of frequency response functions

In addition to the previous mentioned aspects that may affect the dynamics of the test structure there are other aspects that one faces in practice and that have to be considered when estimating an FRF. Apart from low-level electrical noise, dynamic processes (e.g., machines, wind, footsteps etc.) may result in mechanical noise that produces vibration in the test structure. This is typically referred to as noise in the measured output signal in the sense that the response signal contains the response due to the measured excitation and external random excitations.

The least squares principle may be used to minimize the effect of noise at the output as [88]

$$\mathbf{H}_1(\omega) = \frac{\sum \mathbf{F}^\bullet \cdot \mathbf{X}}{\sum \mathbf{F}^\bullet \cdot \mathbf{F}}, \tag{2.23}$$

where the superscript $\bullet$ indicates the complex conjugate. $\mathbf{H}_1(\omega)$ may be seen as the ratio of the cross spectrum, between the response $\mathbf{X}$ and force $\mathbf{F}$, divided by the autospectrum of the force. This FRF estimator removes the random noise in the output during the averaging process of the cross spectrum and converges to the true $\mathbf{H}(\omega)$ as the number of averages is increased.

Another noise source may appear when a vibration exciter is used. At its natural frequencies, the structure becomes highly compliant resulting in high vibration amplitudes. The exciter may then use all the available energy to accelerate its own mechanical components, leaving no force to drive the structure. The signal-level of the force may then drop towards the normal noise-level in the instrumentation, in contrast to the response that is at a maximum and likely to obscure any noise. This is typically referred to as having noise at the input. An estimator that minimizes this input signal noise effect is expressed as [88]

$$\mathbf{H}_2(\omega) = \frac{\sum \mathbf{X}^\bullet \cdot \mathbf{X}}{\sum \mathbf{X}^\bullet \cdot \mathbf{F}}. \tag{2.24}$$

By using the $\mathbf{H}_2(\omega)$ FRF estimator, the input noise is removed from the cross spectrum during the averaging process. As the number of averages is increased, $\mathbf{H}_2(\omega)$ converges to the true $\mathbf{H}(\omega)$. In cases where noise is present at both output and input, $\mathbf{H}_1(\omega)$ and $\mathbf{H}_2(\omega)$ generally form the confidence interval for the true $\mathbf{H}(\omega)$.

To conclude the brief introduction on FRF estimators and measurement errors, two rules of thumb may be established depending on whether the structure is subject to a random or an impact excitation. Thus, for random excitations, $\mathbf{H}_2(\omega)$ is preferable since it cancels noise at the input being a better estimator at resonances and for impact excitations both $\mathbf{H}_1(\omega)$ and $\mathbf{H}_2(\omega)$ will generally be equal at

the resonances. However, $\mathbf{H}_1(\omega)$ is preferred since it cancels noise at the output being a better estimator at anti-resonances.

Besides these estimators, that filter output and input signal noise, the quality of the FRFs are affected by many other parameters. Identifying and introducing every single one of these parameters is beyond this study. However, a few of the most relevant are: the weighting function also known as the window; the frequency resolution; and the frequency and spatial truncation, among many others.

Thus, the modal parameters, i.e., natural frequencies, damping ratios, modal constants and their phases that characterize the FRF are also affected by these parameters.

To identify the modal parameters of an FRF or a set of FRFs it is common to recur to modal identification methods. Whether in the time or frequency domains, various direct (based on the general matrix equation of dynamic equilibrium) and indirect (based on the modal parameters) modal identification methods have been developed for both SDOF and MDOF systems. A detailed review of the most widely known methods may be found in [88].

2.4.6. Rational fraction polynomial method for modal identification

In this study, an indirect frequency domain identification curve fitting method based on the Rational Fraction Polynomial method is used (see [102] for a detailed discussion and [103] for the online link to a MATLAB® implementation code). From references [88] and [102], the receptance FRF for a linear system with N DOFs and viscous damping may be expressed in the rational fraction form as

$$\mathrm{H}(\omega) = \left. \frac{\sum\limits_{k=0}^{2N-1} a_k s^k}{\sum\limits_{k=0}^{2N} b_k s^k} \right|_{s=\mathrm{i}\omega} , \qquad (2.25)$$

and in the partial fraction form as

$$\mathrm{H}(\omega) = \sum\limits_{k=1}^{N} \left[\frac{r_k}{s - p_k} + \frac{r_k^*}{s - p_k^*} \right]_{s=\mathrm{i}\omega} , \qquad (2.26)$$

where a_k and b_k are the coefficients of the polynomial of the numerator and of the polynomial of the denominator, respectively; r_k is the residue of the kth pole; $p_k = \sigma_k + \mathrm{i}\omega_k$ is the kth pole where σ_k, $\sigma_k = \left(-\xi\omega_n \right)_k$, and $\left(\mathrm{i}\omega_k \right)$ are the axes in the s-plane known as the damping and frequency axes, respectively; ω_k and ω_n $\left(\omega_k = \omega_n\sqrt{1-\xi^2} \right)$ are the damped and undamped natural frequencies, respectively, and ξ is the modal damping ratio. This RFP method fits the analytical expression Eq. (2.25), by finding the unknown coefficients a_k, $k = 1, \ldots, 2N-1$ and

b_k, $k = 1, \ldots, 2N$, as described in [102], to the experimental FRF measurement in a least-squared error sense. Once the coefficients are known, it is a straightforward process to obtain the modal properties of the FRF. The natural frequency ω_n of each pole p_k is

$$\omega_n(p_k) = |p_k| = \sqrt{\sigma_k^2 + \omega_k^2}, \tag{2.27}$$

and the correspondent modal damping ratio is

$$\xi(p_k) = -\frac{\sigma_k}{|p_k|}. \tag{2.28}$$

Note that the RFP method is developed considering the viscous damping model ([88] and [102]). In this study, i.e., for the materials and frequency range studied and tested, the modal loss factor η is successfully approximated by $\eta \approx 2\xi$, as the results show.

The RFP method may also be applied to FRFs obtained using the FEM.

2.5.   Finite element method

The FEM is a method for numerical solutions of field problems, which require determining the spatial distribution of one more dependent variables. Mathematically, field problems may be described by either differential or integral equations to formulate FEs that can be visualized as small pieces of a structure. The field quantity in each FE is restricted to simple spatial variations described, e.g., by second order polynomials. FEs are connected at points designated as nodes and the union of FEs (designated as a mesh) is the FE structure. The FE mesh is represented by a system of algebraic equations to be solved for nodal unknowns. The assumed field in an element combined with the solution of nodal quantities determines the spatial variation field in that element. Hence, the field quantity over the entire structure is approximated element by element and can be improved by using more elements to represent the structure.

The mathematical formulation of the FEM [86] can be presented as a variational problem with an element-wise *Rayleigh-Ritz* treatment and shape function discretization. Alternatively the FE equations may be obtained directly from the differential equations using a *Galerkin* approach weighted by the element's shape functions.

A variational (weak) form of Eq. (2.6) that yields the virtual work equations may be expressed as

$$\int_V \delta u_j \rho \, \ddot{u}_j dV + \int_V \delta u_j c \, \dot{u}_j dV + \int_V \delta \varepsilon_{ij} \sigma_{ij} dV - \int_\Gamma \delta u_j t_j d\Gamma - \int_V \delta u_j f_j dV = 0, \tag{2.29}$$

where the virtual strains $\delta \varepsilon$ are related to virtual displacements (kinematically admissible) δu as $\delta \varepsilon_{ij} = \frac{1}{2}\left(\delta u_{i,j} + \delta u_{j,i}\right)$. Furthermore and as previously defined in sub-chapter 2.1, V is the volume of a closed sub-domain with a boundary surface Γ, ρ is the mass density, c is a constant that takes

into account the velocity dependent damping forces, i.e., the viscous damping constant, σ_{ij} are the components of the *Cauchy* stress tensor, t_j are the components traction vector, f_j are the components of the body forces, and $\ddot{u}$ and $\dot{u}$ are the displacement's second and first order derivatives, respectively, with respect to time.

In Eq. (2.29) the terms one to five indicate the virtual work associated with: the inertia forces, the damping forces, the internal elastic forces, the boundary contact forces; and the volume forces, respectively.

The FE custom notation provides

$$\mathbf{u} = \mathbf{N}\,\mathbf{d} \ ; \ \dot{\mathbf{u}} = \mathbf{N}\,\dot{\mathbf{d}} \ ; \ \ddot{\mathbf{u}} = \mathbf{N}\,\ddot{\mathbf{d}} \ ; \ \boldsymbol{\varepsilon} = \mathbf{B}\,\mathbf{d}, \tag{2.30}$$

where interpolating shape functions $\mathbf{N}$ are function of space x while nodal DOFs $\mathbf{d}$ may or not be function of time, depending on the type of problem. Furthermore, $\mathbf{B}$ is the matrix containing the partial derivatives of the shape functions, i.e., $\mathbf{B} = \partial\mathbf{N} = \left[\partial\mathbf{N}_j/\partial x, \partial\mathbf{N}_j/\partial y, \partial\mathbf{N}_j/\partial z \right], \ j = 1,\ldots,n$.

By substituting the terms expressed in Eq. (2.30) in Eq. (2.29) one obtains in matrix notation that

$$\delta\mathbf{d}^T \left[\int_V \rho\,\mathbf{N}^T\mathbf{N}\,d\mathsf{V}\,\ddot{\mathbf{d}} + \int_V c\,\mathbf{N}^T\mathbf{N}\,d\mathsf{V}\,\dot{\mathbf{d}} + \int_V \mathbf{B}^T\boldsymbol{\sigma}\,d\mathsf{V} - \int_\Gamma \mathbf{N}^T\mathbf{t}\,d\Gamma - \int_V \mathbf{N}^T\mathbf{f}\,d\mathsf{V} \right] = 0. \tag{2.31}$$

The first two integrals in Eq. (2.31) are the element's mass $\mathbf{M}^{\mathrm{el}}$ and damping $\mathbf{C}^{\mathrm{el}}$ matrices, respectively, expressed as

$$\mathbf{M}^{\mathrm{el}} = \int_V \rho\,\mathbf{N}^T\mathbf{N}\,d\mathsf{V} \ ; \quad \mathbf{C}^{\mathrm{el}} = \int_V c\,\mathbf{N}^T\mathbf{N}\,d\mathsf{V}. \tag{2.32}$$

The third integral in Eq. (2.31) is related with the strain energy. If the material is linear elastic, then the loads associated with the element's stresses are $\mathbf{K}^{\mathrm{el}}\,\mathbf{d} = \int_V \mathbf{B}^T\boldsymbol{\sigma}\,d\mathsf{V} = \int_V \mathbf{B}^T\mathbf{E}\,\mathbf{B}\,d\mathsf{V}\,\mathbf{d}$ where $\mathbf{E}$ is the elasticity matrix and $\mathbf{K}^{\mathrm{el}}$ is the conventional element's stiffness matrix expressed as

$$\mathbf{K}^{\mathrm{el}} = \int_V \mathbf{B}^T\mathbf{E}\,\mathbf{B}\,d\mathsf{V}. \tag{2.33}$$

Note that sometimes proportional (*Rayleigh*) damping defined as $\mathbf{C}^{\mathrm{el}} = \bar{\alpha}\mathbf{K}^{\mathrm{el}} + \bar{\beta}\mathbf{M}^{\mathrm{el}}$ where $\bar{\alpha}$ and $\bar{\beta}$ are the proportional stiffness and mass constants, respectively, is used. The last two integrals in Eq. (2.31) express the volume and surface loads (forces and/or moments) which are then applied to the nodes as equivalent loads on the element and adding nodal external forces $\mathbf{F}_i$ may be expressed as

$$\mathbf{F}^{\text{el}} = \int_{\Gamma} \mathbf{N}^T \mathbf{t} \, d\Gamma + \int_{V} \mathbf{N}^T \mathbf{f} \, dV + \sum \mathbf{F}_i. \tag{2.34}$$

By substituting Eq. (2.32) - Eq. (2.34), and vanishing the left $\delta\mathbf{d}$ which is true for an arbitrary kinetically admissible $\delta\mathbf{d}$, Eq. (2.31) of a multi-element structure after assembly becomes

$$\mathbf{M}\ddot{\mathbf{D}} + \mathbf{C}\dot{\mathbf{D}} + \mathbf{K}\,\mathbf{D} = \mathbf{F}. \tag{2.35}$$

Note that Eq. (2.35) is a system of coupled, second order differential equations in time. The nodal vector $\mathbf{D}$ consists on discrete functions of space but continuous functions of time.

2.5.1. Basic steps in finite element method

The basic steps involved in most FE analysis are: preprocessing; solution; and post-processing. For a more detailed description, see e.g. Cook et al. [86]. The pre-processing step is quite generally described as defining the model, i.e.: the geometric domain of the problem; the element types to be used (bar, plate); the material properties of the elements ($E^{'}, \rho, c, \text{etc.}$); the geometric properties of the elements (length, section properties); the element connectivities (mesh of the model); and the physical constraints (boundary and loading conditions). The preprocessing step is critical since even a perfectly computed FE solution is of absolutely no value if it corresponds to a different problem.

To initialize the solution step, first the analysis type is chosen, i.e.: static; free vibration; or forced harmonic vibration. Then, the governing algebraic equations are assembled in the matrix form and the unknown values (usually displacements) are computed. The computed values are then used to compute additional derived variables, such as reaction forces, element stresses, etc.

Post-processing is commonly referred to as analysis and evaluation of the solution results and may be divided into generic post-processing (static and free vibration) and time-history post-processing (forced harmonic vibration). The objective is to present adequately the results obtained from the numerical solution given by the solver.

2.5.2. Type and geometry of the finite element

In general, the geometry of the FE is defined by the location of the nodal points and the interpolation functions. Most elements used in practice have simple geometries: 1D elements are usually straight lines or curved segments; 2D elements are of triangular or quadrilateral shape; and 3D elements are of three common shapes, i.e., tetrahedral, pentahedral (also called prisms) and hexahedra (also called bricks). Furthermore, there are also single node elements used to model concentrated masses and massless longitudinal two-node spring and damper dashpot elements that provide a variety of element formulations that may be used individually or in combination.

2.5.2.1. Point mass finite element

The structural mass element is a point element defined by a single node, concentrated mass components in the element coordinate directions, and rotary inertias about the element coordinate

axes having up to six degrees of freedom: translations in the nodal x, y, and z directions and rotations about the nodal x-, y-, and z-axes, see Figure 2.6. Note that a different mass and rotary inertia may be assigned to each exiting coordinate direction. This element does not account for any stiffness or damping capabilities, only adds corresponding entries to the mass matrix.
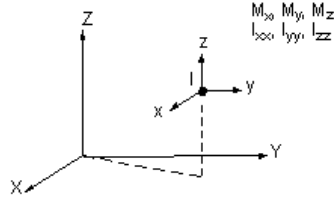
Figure 2.6 – Discrete mass finite element coordinate system.

2.5.2.2. Longitudinal linear elastic spring finite element

The longitudinal elastic spring element is a two nodes 1D tension-compression massless linear elastic spring with a spring constant k, see Figure 2.7,
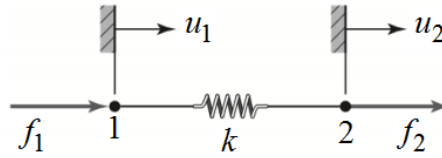
Figure 2.7 – Discrete two-node linear elastic spring finite element model.

The deformation, assuming that the nodal displacements are zero when the spring is not deformed, may be expressed as $\Delta u = (u_2 - u_1)$ and the resultant axial force in the spring as $f = k(u_2 - u_1)$. In equilibrium $f_1 = -f_2$, then terms of the applied nodal forces can be expressed in matrix form as

$$\underbrace{\begin{bmatrix} k & -k \\ -k & k \end{bmatrix}}_{\mathbf{K}^{el}} \underbrace{\begin{Bmatrix} u_1 \\ u_2 \end{Bmatrix}}_{\mathbf{u}} = \underbrace{\begin{Bmatrix} f_1 \\ f_2 \end{Bmatrix}}_{\mathbf{F}^{el}}, \tag{2.36}$$

where $\mathbf{K}^{el}$ is the element stiffness matrix in the element coordinate system, $\mathbf{u}$ is the nodal displacements vector and $\mathbf{F}^{el}$ is the element's nodal forces vector. Note that this element does not account for any damping capabilities or inertia effects.

2.5.2.3. Longitudinal linear elastic damper finite element

Similar to the spring, the longitudinal damper element is a massless two nodes 1D tension-compression massless element used to represent the energy dissipation observed in structures. For linear elastic materials, two types of damping are commonly used: viscous and hysteretic (also commonly referred to as structural) damping. The viscous damping force is proportional to velocity

$f = c\,\dot{u}$ and hysteretic damping force is proportional to displacement $f = d\,u$ where c and d are the viscous and hysteretic damping factors, respectively.

As in the case of the longitudinal linear elastic spring, a similar line of thought may be applied to the viscous and hysteretic damping models where the elements viscous and hysteretic damping matrices may be expressed as

$$\mathbf{C}^{\text{el}} = \begin{bmatrix} c & -c \\ -c & c \end{bmatrix} \text{ and } \mathbf{D}^{\text{el}} = \begin{bmatrix} d & -d \\ -d & d \end{bmatrix}. \tag{2.37}$$

The hysteretic damping model is justified by the fact that rubber and other viscoelastic materials exhibit frequency dependence, usually less pronounced than that associated with a viscous damper and, over a limited range of frequencies, the properties may often be assumed constant. Thus, a hysteretic damper model opposes the relative motion between its ends with a force that is proportional to the displacement and not to the velocity (though still in phase with the velocity) is apparently required. This is equivalent to using a viscous damper with a viscous damping rate that varies inversely with frequency, i.e., $c = d/\omega$ where $d = \eta\,k$ and η is the loss factor. In this case, it is common to define a dynamic stiffness k^{*} as

$$k^{*} = k(1 + \mathrm{i}\eta). \tag{2.38}$$

The hysteretic damping model has the advantage of not only describing more closely the energy dissipation mechanism exhibited by several real structures, but also provides a much simpler analysis by considering the use of dynamic moduli, e.g., Eq. (2.9), i.e., $E^{*} = E'(1 + \mathrm{i}\eta)$, in the analysis of complex systems.

2.5.2.4. One-dimensional bar finite element for dynamic linear elasticity

The bar (truss/link) FE is also a two-node element. For it, consider a material body with cross sectional area A with the axis aligned in the lengthwise direction x. It is assumed that the material of the body is homogeneous, i.e., the material properties are independent of the position. Considering that one isolates from the body a small element with length dx, see Figure 2.8, the internal efforts at the cut faces are axial and symmetrically positioned with respect to the geometric centroid of the cross-section. Note that they represent the summation of the internal efforts of all material points along the cut surfaces. Then the axial stress σ_x, i.e., force per unit area, in the member, except near the points of load application (see *Saint-Venant's* principle), will be uniform in the transversal section. Such members are usually designated as bars and if cylindrical as rods.
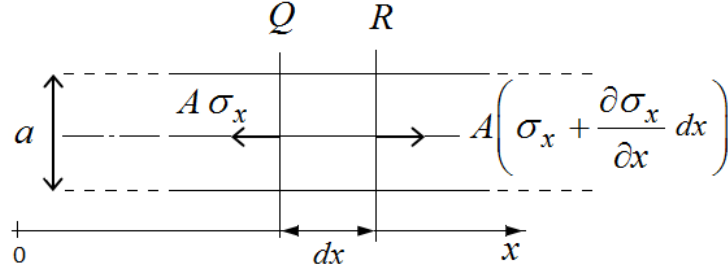
Figure 2.8 – Forces acting on a small element with length dx of a slender bar in the longitudinal direction x.

The governing equations of bars can be derived from *Newton's* second law applied to a small element of the bar QR with length dx. In the absence of distributed (volume) forces, the summation of the internal forces along the element with length dx results in $A\dfrac{\partial \sigma_x}{\partial x} dx$, as illustrated by Figure 2.8, competing with the inertial force $\rho A \dfrac{\partial^2 u}{\partial t^2} dx$ as

$$A\frac{\partial \sigma_x}{\partial x} d_x - \rho A\, d_x \frac{\partial^2 u}{\partial t^2} = 0, \tag{2.39}$$

i.e.,

$$\frac{\partial \sigma_x}{\partial x} - \rho \frac{\partial^2 u}{\partial t^2} = 0, \tag{2.40}$$

where ρ is the mass density of the material; $u = u(x,t)$ is the displacement response at the longitudinal coordinate x and at time t.

Using *Newton's* second law applied to an element of the body, see [86], and $\sigma_x = E\,\varepsilon_x = E\dfrac{\partial u}{\partial x}$, the forced harmonic longitudinal vibrations are locally governed by the following second order hyperbolic partial differential equation (also known as stress wave equation) as

$$\frac{\partial^2 u}{\partial t^2} - c^2 \frac{\partial^2 u}{\partial x^2} = 0, \tag{2.41}$$

with *Neumann* boundary conditions, i.e., an applied harmonic force in the axial direction expressed as $F(t) = \mathbf{F_0} e^{i(\omega t + \beta)}$, where $\mathbf{F_0}$ is the force amplitude and β is the phase angle of the harmonic excitation, $c = \sqrt{E/\rho}$ is the longitudinal wave phase velocity in the bar material, which is independent of the frequency. Rigorously, this frequency independence assumption is only valid for waves with a

wavelength λ large ($\lambda/a > 10$) compared with the characteristic dimension of the cross-section of the bar a, see [104] for more details.

Hence, consider a two node (nodes 1 and 2 of Figure 2.9 which corresponds to points Q and R of Figure 2.8) 1D uniform prismatic elastic bar FE of length L, with cross-sectional area A, a characteristic dimension of the cross-section of the bar a, elastic modulus E and mass density ρ, as illustrated in Figure 2.9.
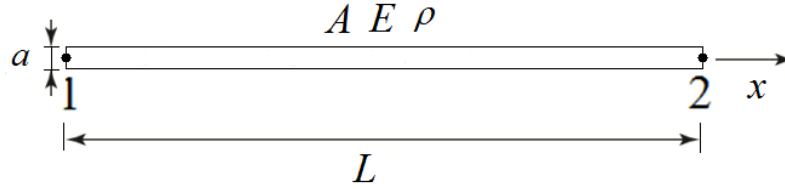
Figure 2.9 – Two-node bar finite element.

By considering the nodal displacements $u(0) = u_1$, $u(L) = u_2$, the displacement field $u = u_1 N_1 + u_2 N_2$ and the shape functions $N_1 = (L-x)/L$ and $N_2 = x/L$, the element matrices may now be obtained using Eq. (2.32) and Eq. (2.33) as

$$\mathbf{M}^{el} = \frac{1}{2} \rho A L \begin{bmatrix} 1 & 0 \\ 0 & 1 \end{bmatrix} \text{ and } \mathbf{K}^{el} = \frac{EA}{L} \begin{bmatrix} 1 & -1 \\ -1 & 1 \end{bmatrix}. \tag{2.42}$$

The stress wave equation for torsional vibrations, i.e. the equivalent of Eq. (2.41) for torsion, may be obtained and expressed as

$$\frac{\partial^2 \theta}{\partial t^2} - c_\theta^2 \frac{\partial^2 \theta}{\partial x^2} = 0, \tag{2.43}$$

where θ is the torsional (angular) displacement response and c_θ is the wave phase velocity in torsional vibrations expressed as

$$c_\theta = \sqrt{G' J_t / (\rho J_p)}, \tag{2.44}$$

where G' is the shear storage modulus of elasticity; J_t is the torsional constant; and J_p is the polar moment of the cross-section with respect to the centroid. Note that for circular cross-sections of radius r, $J_t = \pi r^4 / 2$ and $J_p = J_t$ whereas, for square cross-section with a side length a, $J_t = 2.25a^4$ and $J_p = a^4 / 12$ [98].

Hence, for both longitudinal and torsional vibrations the model presents similar equations with different parameters and displacement fields. Nevertheless, in both cases it is assumed uniform properties ($E, G, A, L, \rho, J_t, J_p$) along each element.

2.5.2.5. Plate finite element

Regarding the 2D FEs, perhaps the most common is the plate element. For it, the Kirchhoff-Love (KL) and Reissner-Mindlin (RM) plate theories that are often used to formulate plate elements [105] are introduced in this sub-chapter. The difference between the two theories consist essentially in the fact that KL plate theory does not account for transverse shear stresses and rotational inertia while RM plate theory take into account the shear stress distribution over the thickness as well as rotational inertia. Consequently, the KL plate elements may underestimate deformation especially for thick plates while, the RM plate elements typically demonstrate a softer deformation behavior due to the presence of shear stresses. A brief summary on the RM and KL plate theories are presented next.

In this sense, consider the RM plate theory and a plate of thickness h with a mid-surface (located in the xy plane at $z = 0$) at $h/2$ from each lateral surface as illustrated in Figure 2.10 a). It is assumed that a straight line normal to the mid-surface remains straight but not necessarily normal to the deformed mid-surface when a load is applied. Furthermore, for small rotation of this straight line, see Figure 2.10 b), with components ψ_x and ψ_y, and small displacements $u = -z\,\psi_x$ and $v = -z\,\psi_y$ of a point (out of the mid-surface) in the x and y directions, respectively, the strains (normal ε and shear γ) may be expressed as

$$\varepsilon_x = -z\,\psi_{x,x};\ \varepsilon_y = -z\,\psi_{y,y};\ \gamma_{xy} = -z\left(\psi_{x,y} + \psi_{y,x}\right);\ \gamma_{yz} = w_{,y} - \psi_y;\ \gamma_{zx} = -w_{,x} - \psi_x, \qquad (2.45)$$

where w is the deflection of the mid-surface in the z direction. The normal strain term ε_z is left undefined in the plate element to avoid ill conditioning due to small thickness.

a)   b)
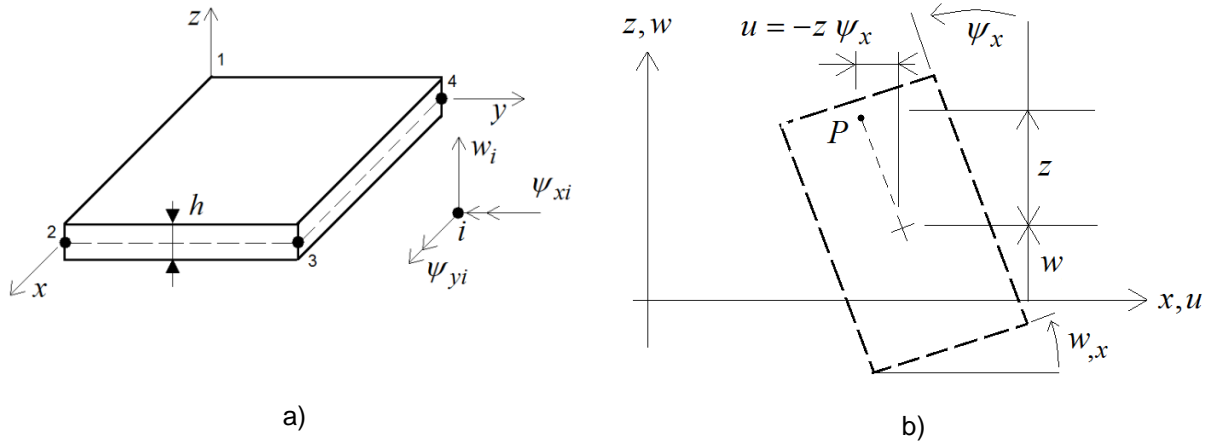
Figure 2.10 – A plate element: a) with corner nodes illustrating the typical DOF ($w_i, \psi_{xi}, \psi_{yi}$); b) with deformed cross section, viewed in the + y direction.

Usually, the stresses (normal σ and shear τ) are associate with moments M and forces Q (per unit of length) in the xy plane as

$$M_x = \int_{-h/2}^{h/2} \sigma_y\, z\, dz; M_y = \int_{-h/2}^{h/2} \sigma_x\, z\, dz; M_{xy} = \int_{-h/2}^{h/2} \tau_{xz}\, z\, dz; Q_x = \int_{-h/2}^{h/2} \tau_{zx}\, dz; Q_y = \int_{-h/2}^{h/2} \tau_{yz}\, dz, \tag{2.46}$$

To describe the state of deformation and stress in a plate it is required that three independent fields (w, ψ_x and ψ_y) are each expressed in terms of x and y. Thus, the moment curvature relations for a homogeneous, isotropic and linear elastic RM plate may be expressed as

$$\begin{Bmatrix} M_x \\ M_y \\ M_{xy} \\ Q_x \\ Q_y \end{Bmatrix} = -\underbrace{\begin{bmatrix} D & vD & 0 & 0 & 0 \\ vD & D & 0 & 0 & 0 \\ 0 & 0 & \dfrac{(1-v)D}{2} & 0 & 0 \\ 0 & 0 & 0 & kGh & 0 \\ 0 & 0 & 0 & 0 & kGh \end{bmatrix}}_{\mathbf{D}_{RM}} \left(\underbrace{\begin{Bmatrix} \psi_{x,x} \\ \psi_{y,y} \\ \psi_{x,y} + \psi_{y,x} \\ \psi_x - w_{,x} \\ \psi_y - w_{,y} \end{Bmatrix}}_{\mathbf{\kappa}_{RM}} - \{\kappa_0\} \right), \tag{2.47}$$

where $D = Eh^3 / \left(12\left(1-v^2\right)\right)$ is the flexural rigidity, $\mathbf{D}_{RM}$ is the flexural rigidity matrix, $\mathbf{\kappa}_{RM}$ is the curvature vector, $\{\kappa_0\}$ is the initial curvature vector and k is a shear correction factor (with a value of 5/6 for homogeneous plates with uniform thickness [105]) that accounts for the parabolic z direction variation of the shear stress.

Note that in the KL plate theory, shear deformation is not considered, thus $w_{,x} = \psi_x$ and $w_{,y} = \psi_y$ and consequently the strains expressed by Eq. (2.45) may be rewritten as

$$\varepsilon_x = -z\, w_{,xx}; \varepsilon_y = -z\, w_{,yy}; \gamma_{xy} = -2z\, w_{,xy}. \tag{2.48}$$

Furthermore, in the KL plate theory the terms of forces Q in Eq. (2.46) are zero. Thus, the moment curvature relations of Eq. (2.47) may be simplified as

$$\begin{Bmatrix} M_x \\ M_y \\ M_{xy} \end{Bmatrix} = -\underbrace{\begin{bmatrix} D & vD & 0 \\ vD & D & 0 \\ 0 & 0 & \dfrac{(1-v)D}{2} \end{bmatrix}}_{\mathbf{D}_{KL}} \left(\underbrace{\begin{Bmatrix} w_{,xx} \\ w_{,yy} \\ 2w_{,xy} \end{Bmatrix}}_{\mathbf{\kappa}_{KL}} - \{\kappa_0\} \right). \tag{2.49}$$

Returning to the RM plate theory, the lateral displacements and rotations fields of a RM plate having n nodes can be expressed as

$$\begin{Bmatrix} w \\ \psi_x \\ \psi_y \end{Bmatrix} = \sum_{i=1}^{n} \underbrace{\begin{bmatrix} N_i & 0 & 0 \\ 0 & N_i & 0 \\ 0 & 0 & N_i \end{bmatrix}}_{\mathbf{N}} \underbrace{\begin{Bmatrix} w_i \\ \psi_{xi} \\ \psi_{yi} \end{Bmatrix}}_{\mathbf{d}}. \qquad (2.50)$$

The curvature term (transverse and shear) κ_{RM} of Eq. (2.47) may be expressed as

$$\kappa_{\mathrm{RM}} = \begin{bmatrix} \partial \end{bmatrix} \mathbf{u} \text{ where } \begin{bmatrix} \partial \end{bmatrix} = \begin{bmatrix} 0 & \partial/\partial x & 0 \\ 0 & 0 & \partial/\partial y \\ 0 & \partial/\partial y & -\partial/\partial x \\ -\partial/\partial x & 1 & 0 \\ -\partial/\partial y & 0 & 1 \end{bmatrix}. \qquad (2.51)$$

By substituting Eq. (2.50) in Eq. (2.51) one obtains for an element with n nodes

$$\kappa_{\mathrm{RM}} = \mathbf{B}_{RM}\,\mathbf{d} \text{ where } \mathbf{B}_{RM} = \begin{bmatrix} \partial \end{bmatrix}\mathbf{N}, \qquad (2.52)$$

In general, isoparametric coordinates ξ and η are used in the mid-surface which for a four node element the shape functions N are expressed as

$$N_1 = \frac{1}{4}(1-\xi)(1-\eta); N_2 = \frac{1}{4}(1+\xi)(1-\eta); N_3 = \frac{1}{4}(1+\xi)(1+\eta); N_4 = \frac{1}{4}(1-\xi)(1+\eta). \qquad (2.53)$$

Then, similarly to Eq. (2.33) the element stiffness matrix may expressed as

$$\mathbf{K}^{\mathrm{el}} = \int_A \mathbf{B}_{\mathrm{RM}}^T \mathbf{D}\, \mathbf{B}_{\mathrm{RM}}\; d\mathrm{A}. \qquad (2.54)$$

It should be noted that the inclusion of the transverse shear strains in the RM plate theory may present computational difficulties when the side to the thickness ratio of the plate is large, i.e., for thin plates. In this case, the transverse shear strains are negligible and consequently the element stiffness matrix becomes stiff yielding erroneous results for the generalized displacements. This occurrence is known as shear locking [105]. To overcome this, reduced integration is used to evaluate the stiffness coefficients involving the transverse shear terms. Thus, when a four node rectangular element is used, the one-point Gauss rule may be used to evaluate the shear energy terms while, the two-point Gauss rule may be used for all the other terms.

2.5.3. Matrix equations for structural analysis

The structural analysis presented in this sub-chapter, even though similar to those presented in sub-chapter 2.2, are formulated via the FEM [86] and after the respective matrices assemblage, are expressed by Eq. (2.35). Similarly, to Eq. (2.15) the static analysis to obtain the static displacement may be expressed as

$$\mathbf{K}\,\mathbf{D} = \mathbf{F},\tag{2.55}$$

with given boundary conditions. Usually, the unknowns are the displacements $\mathbf{D}$ at the nodes, which once known may be used to obtain results like element forces, strains, and stresses on an element-by-element basis.

For the free vibration analysis, similar to Eq.(2.17), to obtain the eigenfrequencies and eigenmodes the matrix equations are in the form

$$\left(-\omega^2\mathbf{M} + \mathrm{i}\,\omega\,\mathbf{C} + \mathbf{K}\right)\boldsymbol{\psi} = \mathbf{0}.\tag{2.56}$$

where, $\boldsymbol{\psi}$ is the eigenvector associated with the respective eigenfrequency ω.

The non-trivial solutions are the singular values of the system matrix, commonly referred to as eigenvalues. For a FE model with N DOFs, there are $2N$ eigenvalues. For vibrating structures, these always occur in complex conjugate pairs. Therefore, there are N pairs of eigenvalues:

$$\lambda_j = \sigma_j + \mathrm{i}\omega_j;\ \lambda_j^* = \sigma_j\text{-}\mathrm{i}\omega_j,\quad\text{for } j = 1,\ldots,N\tag{2.57}$$

where, σ_j is the modal damping and the value ω_j is the damped natural frequency for mode j. Corresponding to each eigenvalue is a real eigenvector $\boldsymbol{\psi}_j$. Each pair of eigenvalues and corresponding eigenvector represents, mathematically, a free vibration mode of the structure.

For the steady-state analysis, similar to Eq.(2.21), to obtain the frequency response one uses the following matrix equation

$$\left(-\omega_{ap}^2\mathbf{M} + \mathrm{i}\,\omega_{ap}\,\mathbf{C} + \mathbf{K}\right)\mathbf{D} = \mathbf{F}_{\omega_{ap}},\tag{2.58}$$

where ω_{ap} is the applied force excitation frequency, $\mathbf{D}$ and $\mathbf{F}_{\omega_{ap}}$ are the magnitudes and phases of the displacement and applied force vectors, respectively.

2.6. Model validation

Having introduced both experimental modal FE analyses, see sub-chapter 2.4 and sub-chapter 2.5, respectively, a critical issue that usually arises immediately is how to assess confidence between the numerical and experimental models. It must somehow be accessed that the many assumptions involved in the successive steps of idealization, discretization, modeling and experimentation yield satisfactory predictions.

This results in a concept that numerical models can be validated. Model validation is the assessment of the accuracy of a numerical simulation by comparison with experimental data for a range of parameters. In model validation, the relationship between the numerical and the real world is the issue. Model validation should not be expected to result in a perfect model, since the perfect

model would be the real system itself and by definition, any model is a simplification of reality. Then, the validated model should be accurate enough, which depends on the goal of the model.

The American Institute of Aeronautics and Astronautics (AIAA) and the American Society of Mechanical Engineers (ASME) define validation as *"the process of determining the degree to which a model is an accurate representation of the real world from the perspective of its intended uses"* [106].

To do this, several steps must be taken (see, [107] and [108]) and often recurring to an iterative process as that illustrated by Figure 2.11.
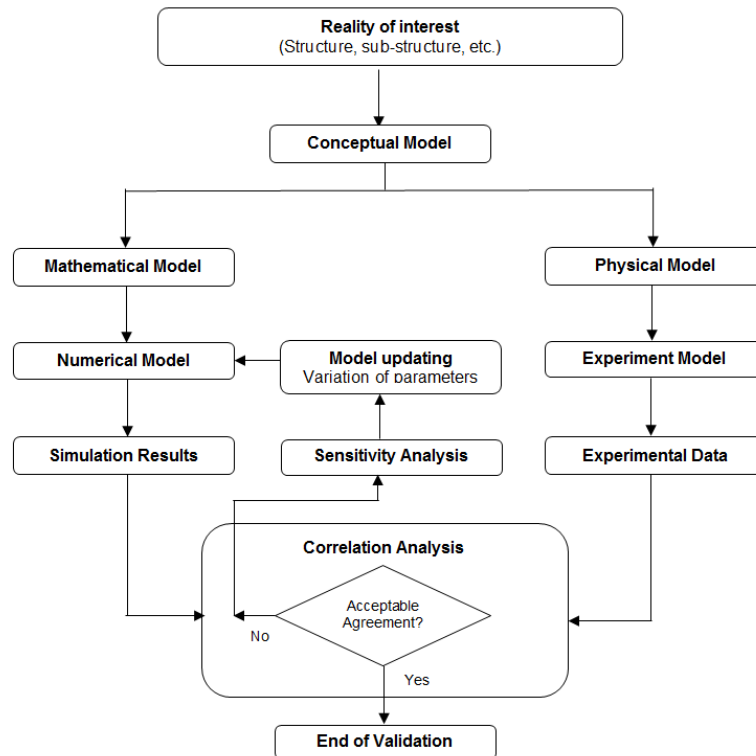
Figure 2.11 – Model validation flowchart. (Adapted from [107]).

The model validation process begins by creating a conceptual model of the reality of interest taking into account the domain of interest, physical processes and assumptions, system-response quantities and the intended use of the model so that the relevant physics are included in both the model and the experiments conducted to validate the model.

From the conceptual model, two branches derive. In the left branch it is common to start off by building a mathematical interpretation of the conceptual model that results in a mathematical model which is a set of equations e.g., governing and constitutive equations, and both initial and boundary conditions that describe physical reality. Then a numerical model is built, e.g., a FE model, for solving the equations prescribed by the mathematical model providing the simulation results, which are post-processed to generate response features for comparison with experimental data.

In the right branch experiments are conducted via the physical modeling, where the conceptual model is physically designed from which, the experimental model is conceived accounting for locations

of sensor positioning, boundary conditions, types of measurements, among others. When necessary, the experimental results may be post-processed into other experimental features that are more useful for direct comparison with the numerical data, i.e., a correlation analysis.

2.6.1. Correlation analysis and frequency response function correlations

Correlation analysis is a technique to quantitatively and qualitatively examine the correspondences and differences between numerically and experimentally obtained modal parameters (resonance frequencies, damping and mode shapes), which characterize the linear dynamics of the structure. Different levels of correlation analysis exist. They range from visual comparison of the mode shapes, global and local correlation, and FRFs.

The use of FRFs for correlation instead of mode shapes might be considered advantageous in some cases, e.g., when the data is noisy and/or significant modal damping is present, as it becomes difficult to extract the modes shapes accurately. Furthermore, the experimental FRFs are easier to obtain than mode shapes, which require post-processing analyses of numerous FRFs.

In this study, two local assurance criteria are used to determine the level of assurance between the analytical and the experimental FRF, ranging from 0 to 1 (where 0 and 1 indicate 0% and 100% correlation, respectively), and evaluated at each frequency point ω_q.

The first is the Frequency Response Assurance Criterion (FRAC) (see [109]-[110]) which is somewhat analogous to the Coordinate Modal Assurance Criterion (COMAC) (see e.g., [111]) since it contains information about a specific measuring point for a given excitation point. It is a measure of the shape correlation of the FRFs thus, is most sensitive to changes in mass and stiffness. For a given DOF, it is expressed as

$$\mathrm{FRAC}\left(\omega_q\right) = \frac{\left|\mathbf{H}_A^{\mathrm{H}}\left(\omega_q\right)\mathbf{H}_M\left(\omega_q\right)\right|^2}{\left(\mathbf{H}_A^{\mathrm{H}}\left(\omega_q\right)\mathbf{H}_A\left(\omega_q\right)\right)\left(\mathbf{H}_M^{\mathrm{H}}\left(\omega_q\right)\mathbf{H}_M\left(\omega_q\right)\right)}, \qquad q = 1, 2, \ldots, N_{\mathrm{freq}} \qquad (2.59)$$

where, $\mathbf{H}_A$ and $\mathbf{H}_M$ are the estimated FRFs (analytical or numerical) and the measured FRFs vectors of each DOF, respectively, the superscript $^{\mathrm{H}}$ indicates the *Hermitian* transpose and N_{freq} is the number of frequency points used in the frequency range to discretize it.

Since the FRF is not only defined by its shape, but also by amplitude a second assurance criterion also of COMAC type is used. It is designated as the Frequency Assurance Amplitude Criterion (FAAC) (see [109]-[110]) which is a measure of the FRFs amplitude discrepancies. Thus, it is more sensitive to deviations in damping modeling. It is expressed as

$$\mathrm{FAAC}\left(\omega_q\right) = \frac{2\left|\mathbf{H}_A^{\mathrm{H}}\left(\omega_q\right)\mathbf{H}_M\left(\omega_q\right)\right|}{\left(\mathbf{H}_A^{\mathrm{H}}\left(\omega_q\right)\mathbf{H}_A\left(\omega_q\right)\right) + \left(\mathbf{H}_M^{\mathrm{H}}\left(\omega_q\right)\mathbf{H}_M\left(\omega_q\right)\right)}, \qquad q = 1, 2, \ldots, N_{\mathrm{freq}} \qquad (2.60)$$

Note, that the diamond symbol in the previous flowchart (see Figure 2.11) provides a decision point for the need of test improvements in the numerical model (even though, in some cases it may be necessary to return to the mathematical model or even to the conceptual model to initiate the proper improvements).

When satisfactory results and assurance values are obtained it is common to state that the model is validated [112].

2.6.2. Sensitivity analysis in model validation

However, for several reasons the numerical estimates and experimental results often disagree. So being, all is set to use the experimental results to improve the numerical estimates by modifying the modeling assumptions and parameters until the correlation of numerical estimates and experimental results satisfies the intended requirements.

Sensitivity analysis is a technique that determines how the structural responses of a model are influenced by modifying one or more parameters p used to model the real structure [94]. These parameters can be a material property, plate thickness, lumped mass, joint stiffness or any other physical property for which uncertainty exist or that is used to compensate errors due to geometrical simplification.

The sensitivity matrix $\mathbf{S}$ represents the slope of the response R_j with respect to a set of parameters p_k, computed at a given state of the parameter as

$$\mathbf{S} = S_{jk} \frac{\partial R_j}{\partial p_k},$$ (2.61)

where, $j = 1, \ldots, n$ responses and $k = 1, \ldots, m$ parameters.

The FRF sensitivities may be derived by considering the following identity

$$\frac{\partial \mathbf{H}}{\partial p} = \frac{\partial (\mathbf{H}\,\mathbf{I})}{\partial p} = \frac{\partial (\mathbf{H}\,\mathbf{Z}\,\mathbf{H})}{\partial p},$$ (2.62)

where, $\mathbf{H}$, $\mathbf{Z}$ and $\mathbf{I}$ are the receptance (see, Eq. (2.22)), dynamic stiffness (see, Eq. (2.22)) and identity matrices, respectively. Then, one obtains

$$\frac{\partial \mathbf{H}}{\partial p} = \frac{\partial \mathbf{H}}{\partial p}\,\mathbf{Z}\,\mathbf{H} + \mathbf{H}\,\frac{\partial \mathbf{Z}}{\partial p}\,\mathbf{H} + \mathbf{H}\,\mathbf{Z}\,\frac{\partial \mathbf{H}}{\partial p}.$$ (2.63)

Since $\mathbf{H}\,\mathbf{Z} = \mathbf{I}$, Eq. (2.63) may be simplified as

$$\frac{\partial \mathbf{H}}{\partial p} = 2\frac{\partial \mathbf{H}}{\partial p} + \mathbf{H}\,\frac{\partial \mathbf{Z}}{\partial p}\,\mathbf{H} = -\mathbf{H}\,\frac{\partial \mathbf{Z}}{\partial p}\,\mathbf{H}.$$ (2.64)

The correlation sensitivity coefficients for FRF correlation function FRAC and FAAC are obtained by deriving Eq. (2.59) and Eq. (2.60) with respect to the parameter p. In the general case of a damped structure, the sensitivities are functions of the numerical $\mathbf{H}_A$ and experimental $\mathbf{H}_M$ FRFs but also of the real $\mathrm{Re}(\mathbf{H}_A)$ and imaginary $\mathrm{Im}(\mathbf{H}_A)$ parts of the numerical FRFs as

$$
\begin{aligned}
\frac{\partial \mathrm{FRAC}(\omega_q)}{\partial p} &= f\left(\mathbf{H}_M, \mathbf{H}_A, \frac{\partial \mathrm{Re}(\mathbf{H}_A)}{\partial p}, \frac{\partial \mathrm{Imag}(\mathbf{H}_A)}{\partial p}\right) \\
\frac{\partial \mathrm{FAAC}(\omega_q)}{\partial p} &= f\left(\mathbf{H}_M, \mathbf{H}_A, \frac{\partial \mathrm{Re}(\mathbf{H}_A)}{\partial p}, \frac{\partial \mathrm{Imag}(\mathbf{H}_A)}{\partial p}\right).
\end{aligned}
\tag{2.65}
$$

2.6.3. Model updating

In this study, an iterative sensitivity method that improves the correlation between analytical and experimental FRFs over a given frequency range in terms FRF correlation functions FRAC and FAAC is used.

The updating task may be expressed as

$$
\begin{Bmatrix} 1 - \mathrm{FRAC}(\omega_q) \\ 1 - \mathrm{FAAC}(\omega_q) \end{Bmatrix} = \mathbf{S}\,\Delta\mathbf{p} = \begin{Bmatrix} \dfrac{\partial \mathrm{FRAC}(\omega_q)}{\partial p} \\[2mm] \dfrac{\partial \mathrm{FAAC}(\omega_q)}{\partial p} \end{Bmatrix} \Delta\mathbf{p},
\tag{2.66}
$$

where, $\mathbf{S}$ is the sensitivity matrix, p is the selected updating parameter and $\Delta\mathbf{p}$ is parameter change vector.

Once the improvements to one or more sets of parameters originates an acceptable agreement between the sets of numerical and experimental data then, the numerical models can be said to have been validated and are fit to be used for further analysis.

2.7.   Optimization

Optimization is an important tool in decision science and in the design of physical systems. To make use of its tools, it is necessary to first identify some objective function of the involved parameters that quantitatively measure of the performance of the system under study. The objective depends on certain characteristics of the system, called variables or unknowns. The goal is to find values of the variables that optimize the objective. Often the variables are restricted, or constrained, in some way. The process of identifying objective, variables, and constraints for a given problem is known as formulating the optimization problem.

Construction of an appropriate model is the first step, sometimes the most important step, in the optimization process. Once the model has been built and the optimization problem formulated, an

optimization algorithm can be used to find its solution. Note that there is no universal optimization algorithm but rather a collection of algorithms. If the optimality conditions are not satisfied, they may give useful information on how the current estimate of the solution can be improved. The model may be improved by applying techniques such as sensitivity analysis revealing the sensitivity of the solution to changes in the model and data. Interpretation of the solution in terms of the application may also suggest ways in which the model can be refined or improved. If any changes are made to the model, a new the optimization problem is solved, and the process repeats.

Mathematically speaking, optimization is the minimization or maximization of a function subject (or not) to constraints on its variables. For a more detailed description see for e.g., Arora [113]. The optimization problem is usually formulated as

$$
\begin{aligned}
&\min_{\mathbf{x} \in \Re^n} F_{\mathrm{obj}}(\mathbf{x}) \\
&\text{subject to:} \\
&g_i(\mathbf{x}) = 0, \, i \in \alpha, \\
&h_i(\mathbf{x}) \geq 0, \, i \in \beta,
\end{aligned}
\tag{2.67}
$$

where F_{obj} is the objective function, $\mathbf{x}$ is the vector of design variables, also referred to as unknowns or parameters, g_i and h_i are equality and inequality constraint functions, which are scalar functions of $\mathbf{x}$ that define certain restrictions that the unknown vector $\mathbf{x}$ must satisfy and α and β are sets of indices for equality and inequality constraints, respectively.

In this study, a constrained nonlinear optimization methodology, a Sequential Quadratic Programming (SQP) algorithm, is used (see [113] for more details) in which, a sequence of quadratic problems are solved. The second order derivatives are determined using a *quasi-Newton* method whereas, the gradients of the objective function are obtained by an adaptive finite difference method.

2.8. Vibration isolation/attenuation mechanisms

Nowadays, a great amount of mechanisms dedicated to vibrations reduction (some of which can be tuned and/or optimized) are commercially available. Perhaps the most common are the vibration isolators, vibration absorbers [4] and SDTs. Even though the isolator and absorber as well as the absorber and SDTs may seem similar in the way they reduce vibrations, they are in fact quite different. The isolator and absorber dissipate energy depending on their location on the vibrating structure whereas, the absorber depends on the local displacement of the structure and the SDTs depend on the surface strains.

Due to the interest for this study, a brief summary on the isolator and absorber is presented next whereas, the SDTs will be addressed in chapter 5.

Common isolators are composed of springs and/or dashpot and/or rubber mounts for isolating machinery. For example, the isolator at Figure 2.12 a), provides stiffness k and damping c to the

system of mass m through their physical connections with the surroundings. On the other hand, the absorber at Figure 2.12 b), is an auxiliary mass m_A connected to the system.

a)   b)
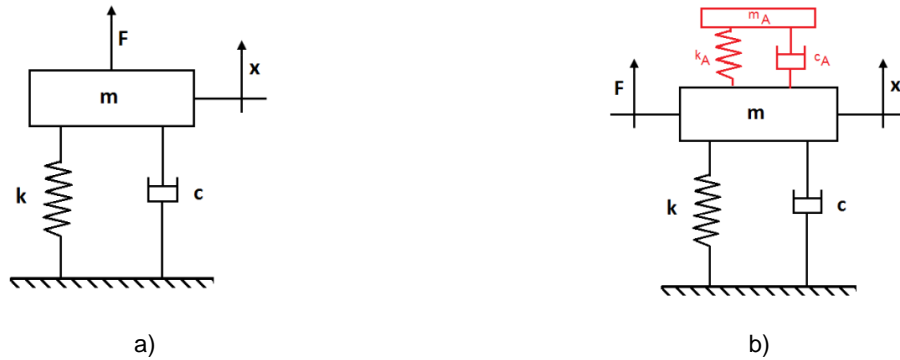
Figure 2.12 – Vibration isolation/attenuation mechanisms: a) vibration isolator; b) vibration absorber.

If the connection of the auxiliary mass has stiffness k_A and little damping c_A it is classified as a dynamic absorber, which can be tuned to "absorb" (neutralize) the vibration amplitude at a specific troublesome frequency (which may or may not be a resonance), in which case it acts like a "notch" filter. Often the "troublesome frequency" is indeed the resonant frequency. In that case the absorber is tuned so that its natural frequency matches the natural frequency of the main system. Hence, the absorber exerts a force on the main system that is equal and opposite of the excitation force, reducing vibration at the resonant frequency. The fact that the motion of the absorber is finite at this resonant frequency, even though there is none or little damping involved is justified by the fact that the system has changed to a 2-DOF system and now it has two resonance frequencies, neither of which equals the original resonance frequency of the main system or absorber.

However, if the connection of the auxiliary mass presents significant damping c_A, it is classified as a damped dynamic absorber, which can be tuned to "absorb" (damp) the vibration amplitude at a specific troublesome frequency over a wider band of excitation frequencies. For optimal behavior the absorber minimizes the maximum amplitude of the two resonance frequencies. This may be achieved by increasing the damping of the absorber until the optimal value for which the amplitudes of the resonance frequencies coincide with the "fixed-points" frequencies, i.e., frequencies at which the response amplitude of the main system is independent of the absorbers damping (the response of the main system passes through them regardless the value of the damping). A further increase in damping causes the amplitude to increase beyond the minimum value.

Hence, a common and significant difference between the absorber and isolator is their location on the vibrating structure. The absorber should be placed at the nearest possible location of the highest vibration of the system to reduce vibrations whereas, the isolator should be located in the transmission path between the disturbance source and the equipment or between the equipment and its support to isolate and filter unwanted vibrations above a certain frequency (depending on the stiffness of the isolator).

When subjected to steady-state sinusoidal force F or displacement x solicitation, the performance of these devices may be measured by the transmissibility concept.

In general, transmissibility T_r is defined as being the ratio between the magnitude of the output and input entities (force, displacement, velocity or acceleration). If the ratio is greater than one, the entity is amplified, and if the ratio is less than one, the entity is reduced, isolated or attenuated and, may be defined for the case of forces as

$$T_r = \frac{F_{\text{output}}}{F_{\text{input}}} \, .$$

(2.68)

Note that these ratios are equivalent for 1D linear systems [114]. For MDOF systems see chapter 6 of Maia et al. [115] and the respective references, as well as Lage et al. [116].

Particularizing for the case of the vibration isolator (see, e.g. [2] for the case of the absorber), considering that the support base is fixed or is stiff or massive enough that its displacement may be taken to be zero, the force transmissibility may be given by the same expression as the motion transmissibility, i.e.,

$$T_r = \sqrt{\frac{1+(2\xi\beta)^2}{(1-\beta^2)^2+(2\xi\beta)^2}} \, ,$$

(2.69)

where, $\xi = c/c_c$ is the ratio of the system's viscous damping coefficient c to its critical damping coefficient $c_c = 4\pi f_0 m$ (beyond which the system will not vibrate), $\beta = f/f_0$ is the ratio of the excitation frequency $f = \omega/2\pi$ to the undamped natural frequency f_0, also designated as corner frequency or mount frequency of the system, expressed as

$$f_0 = \frac{1}{2\pi}\sqrt{\frac{k}{m}} \, ,$$

(2.70)

or alternatively as

$$f_0 = \frac{1}{2\pi}\sqrt{\frac{k\,g}{W}} = \frac{1}{2\pi}\sqrt{\frac{g}{X_{st}}} \, ,$$

(2.71)

where, g denotes the acceleration of gravity and X_{st} is the static deflection of the spring due to the weight W associated with the mass m. Recall that, the relation $X_{st} = k/W$ is only valid for linear systems, i.e., where the slope of the force-deflection curve is constant.

Note that in the presence of damping, if $\xi < 1$, the system will oscillate at its damped natural frequency expressed as

$$f_d = f_0\sqrt{1-\xi^2} \; . \tag{2.72}$$

However, if $\xi > 1$, the system will not vibrate when disturbed, i.e., the system when disturbed from its equilibrium position will return to its equilibrium position without vibrating.

In Figure 2.13 are illustrated the transmissibility curves, see Eq. (2.69), of a SDOF isolator, see Figure 2.12 a), as a function of the frequency ratio β for different values of the damping ratio ξ .
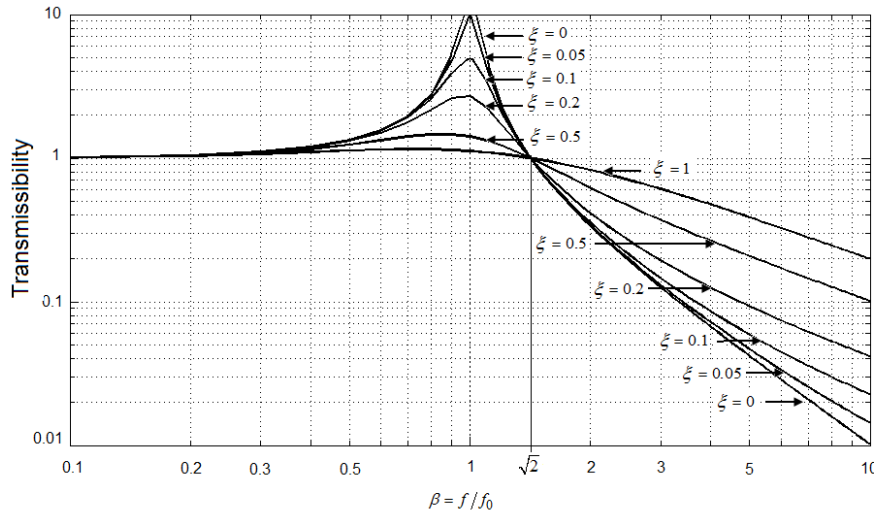
Figure 2.13 – Vibration isolator transmissibility curves as a function of the frequency ratio β considering different values of the damping ratio ξ .

From Figure 2.13 it becomes clearer that, besides the stiffness and/or damping, the frequency ratio also becomes important when analyzing the transmissibility of a system. For disturbances at frequencies above $\sqrt{2}f_0$, the transmissibility is less than unity and vibration isolation occurs whereas, for disturbance at frequencies less than $\sqrt{2}f_0$, vibration amplification occurs. For disturbance frequencies much lower than the corner frequency f_0 , the transmissibility is of unitary value. However, when the disturbance frequency approaches the natural frequency of the system, a resonant condition occurs and the transmissibility is unbounded if no damping is present in the isolator.

Since the isolator operates when the disturbance frequency is greater than $\sqrt{2}f_0$, the corner frequency f_0 of the isolator should be minimized as much as possible. However, there is a limit on the value of the corner frequency and the limit is determined by the static displacement X_{st} of the isolator when the system is subjected to a static loading. Therefore, the isolator must support the equipment under static loading and must also be compliant so that disturbances are not transmitted to the equipment.

Another design constraint for the isolator is the amount of damping present in the isolator. If damping is not present, the absolute transmissibility will be theoretically unbounded when the

disturbance frequency approaches the natural frequency of the system. If damping is present, the transmissibility will no longer approach infinity at the resonant condition but will be finite. However, the transmissibility at disturbance frequencies greater than $\sqrt{2}f_0$ will be amplified due to the isolators damping which is counterproductive from the isolation point of view.

2.8.1. Helical springs and elastomeric mounts for vibration isolation

Perhaps, the first vibration isolating devices that come to mind are coil springs or alternatively some type of elastomeric mount. In most datasheets, it is common to find data tables and/or figures, e.g., see Table 2.1 and Figure 2.14, indicating the vibration transmissibility of these devices (or their efficiency) in isolating vibrations as a function of the equipment's working frequency f (usually given in RPM) and the required static deflection X_{st} which is directly related to the undammed natural frequency f_0, see Eq. (2.71), or damped natural frequency f_d, see Eq. (2.72).

Equipment speed (RPM)	Vibration Transmission				
	99.5%	99%	$\cdots$	85%	60%
f	Static deflection required for isolator X_{st} (mm)				
3600	0.55	0.27	$\cdots$	0.02	0.01
2400	1.2	0.62	$\cdots$	0.05	0.02
$\vdots$	$\vdots$	$\vdots$	$\cdots$	$\vdots$	$\vdots$
300	-	-	$\cdots$	3.0	1.4
250	-	-	$\cdots$	4.3	2.0

Table 2.1 – Example of a table usually found in datasheets of vibration isolation devices indicating the transmissibility as a function of the excitation frequency f and the static deflection X_{st}.
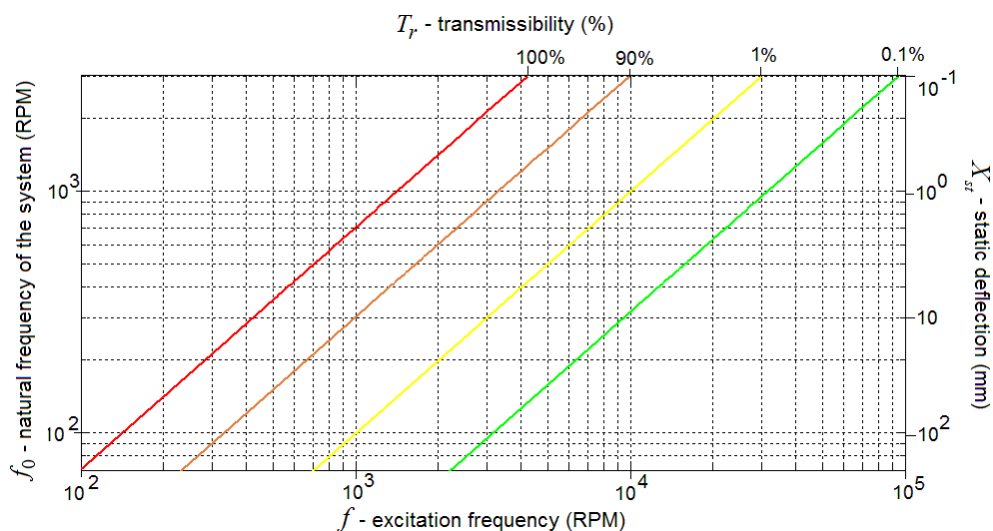
Figure 2.14 – Example figure usually found in vibration isolation devices datasheets indicating the transmissibility as a function of: excitation frequency f; natural frequency of the system f_0; and static deflection X_{st}.

From Figure 2.14 and Table 2.1, it is possible to observe that low transmissibility implies a higher static deflection X_{st} (i.e., reduced stiffness) of the vibration isolator. Thus, by operating at a higher excitation frequency it is possible to improve (lower) the transmissibility.

A reduced stiffness of the vibration isolator is not always compatible with the high stiffness required to meet the performance of the isolated object. Even so, the vibration isolators may be subject to optimization and with it obtain an optimal solution that satisfies the requirements.

In this thesis, the vibration isolator concept will be addressed when developing periodic bars with parallel alternating layers of two materials (metallic and resilient) to isolate vibrations in specific frequency ranges.

Under dynamic solicitations, solid materials present in practice elastic and damping properties that are dependent to a greater or lesser extent of: the operational conditions, e.g., frequency; and the existing environmental conditions, e.g., temperature and humidity (which in this study are not considered). Knowledge of the dynamic properties of the materials involved are essential in the design of these mechanisms, especially if one intends to obtain a validated model.

Nevertheless, the dynamic properties of some material, e.g., CCMs are usually not available and/or known. Hence, one way to determine the dynamic properties of these materials is to solve the inverse problem where, observed measurements are converted into information about the system of interest and consequently to the materials dynamic properties.

2.9. Inverse problem

Formally, a generic inverse problem may be stated as a counterpart to the definition of the direct problem [10], which may be described as the calculation of the responses (like displacements u, natural frequency ω, etc.) in a specific body defined by its domain (geometry) Ω, material properties K, physical model (operator Z) and boundary conditions like imposed values of u (*Dirichlet* boundary conditions) and forces F (*Neumann* boundary conditions) as

$$Z(\mathrm{K}, \omega)u = F \quad \text{on } \Omega. \tag{2.73}$$

where, the nature of the unknowns (which in this study are related to the material properties, i.e., some parameters characterizing K) yields different classifications for the inverse problems (see e.g., Kubo [117]). Namely, domain/boundary inverse problems, governing equation inverse problems, boundary value/initial value inverse problems, force inverse problems, and material properties inverse problems.

Usually, inverse problems are not easy to solve due to their common ill-posed nature. Note that a well-posed mathematical problem must satisfy the existence, uniqueness and stability requirements [10]. The existence requirement may really not be an issue in many realistic situations since the physical reality is itself a solution. Nevertheless, due to noisy and/or insufficient measurement data, an accurate solution to the problem may not exist. On the other hand, a major difficulty is to find a unique solution especially when solving a parameter identification problem for which, different combinations of

parameter values (including boundaries and boundary conditions) may lead to similar solutions. The stability requirement is perhaps the most delicate where inevitable measurement and round-off errors can be amplified by large factors and turn the computed solution useless. For more details on this topic see, e.g., Tarantola [10].

As previously stated, in this study one deals with the material properties inverse problems for which the unknowns are some parameters characterizing K. Thus, in order to determine these unknown parameters, supplementary information has to be provided, in the form of experimental measurements of u (and/or F) made on accessible points of the domain or boundary of the structure.

In this sense, in the next chapter is proposed a new hybrid analytical-experimental methodology in which, an inverse problem (based on the analytical model and experimental data) is solved to determine the dynamic modulus of resilient materials.

Chapter 3

Characterization of the dynamic modulus of resilient materials

3.1. Introduction

The dynamic modulus is a material property concept commonly used in the frequency domain [118] to characterize the elasto-dynamic properties of viscoelastic materials. This concept allows regarding the elastic moduli (longitudinal, shear, bulk, etc.) of a solid material, whether isotropic or anisotropic, as a complex quantity [119]. The knowledge of the dynamic modulus is of major importance for proper and efficient development and characterization of novel materials and applications in many scientific areas, e.g., viscoelastic materials intended to reduce the transmission of vibration, shock or noise for sound and vibration control.

Even though several methods have been developed, studied and applied to characterize the dynamic modulus of viscoelastic materials, information regarding their values, limitations and precision is not often found in the literature. The same applies to the sources of discrepancies between different experimental methods.

In this study, two methods, a proposed new analytical-experimental hybrid method and the Dynamic Mechanical Analysis (DMA), are used to characterize the longitudinal dynamic modulus of CCMs. A judicious analysis of the results obtained by both methods is presented. The advantages/disadvantages, limitations, sources of error among others are accounted for and discussed in this framework.

The new hybrid analytical-experimental methodology was developed to determine the longitudinal dynamic modulus of resilient materials using a new three-layer specimen created for this test and a simple equation from the analytical model for the longitudinal vibrations of the specimen. This methodology is developed to avoid dealing with geometric constraints in slender specimens, and boundary condition difficulties (e.g., fixation of the structure (see, sub-chapter 2.4.4)) found on other tests, obtaining by this way a simple and more rigorous method. Furthermore, it requires only the basic common equipment of a vibration laboratory, i.e., impact hammer with force transducer, one accelerometer, data acquisition equipment and cables.

A new hybrid analytical-experimental methodology is also proposed to determine the shear dynamic modulus of resilient materials. Even though the experimental specimen is similar to the one used in the longitudinal dynamic modulus characterization, and the fact that the analytical formulation

remains simple (just have to consider the torsion constants) the experimental setup is not equally simple, as will be seen.

Nevertheless, in this study the new analytical-experimental hybrid method is used to characterize both the longitudinal and the shear dynamic moduli of CCMs whereas, DMA tests are only used for the longitudinal dynamic modulus characterization.

To further clarify the advantages of the proposed method and how it was achieved, a brief background and description on the most common methods used for the characterization of the dynamic modulus of viscoelastic materials follows.

Since the 1950s, numerous experimental techniques have been developed to determine the dynamic modulus of viscoelastic materials. These methods may be divided into resonant and non-resonant methods depending on whether the dynamic modulus is determined at a resonant frequency or in a range of non-resonant frequencies, respectively [11]. Some relevant reviews describing several of these methods may be found in [8], [21] and [28].

It should be noted that, each of these methods relates the response to the perturbation field with the dynamic modulus through an auxiliary method of analysis. By considering the exact boundary conditions, these analyses should give the exact solution to the field equations. However, in practice, to overcome the inherent technical difficulties it is usually necessary to introduce approximations that may affect the equations just as the boundary conditions do. Thus, some experimental methods may be considered better conceived than others, and, as a general rule, a simple method is always more desirable than a more complex one when it allows these technical difficulties to be simplified or eliminated.

Following is presented a brief description of the rod apparatus and DMA. Perhaps, two of the most common methods used.

Possibly, one the most popular resonant method which, has led to standardization (see, e.g., ISO 18437-2 (2005) [7]), is the rod apparatus. It is based on the response of a cylindrical or prismatic bar attached to the excitation source (vibration exciter) and subjected to different types of dynamic loads and/or frequencies [12]-[15] at one end, being the other end free or loaded with different masses [16]. The transfer function method is used to evaluate the dynamic modulus where the specimen is modeled with lumped mechanical elements. The fact that it is considered one of the most common methods to determine the dynamic modulus of viscoelastic materials may be due to its simplicity in both theory and experimental setup, even though it depends on specific boundary conditions (e.g., load distribution on the specimen) that may not be easy to obtain in practice.

Probably, one the most common non-resonant method is the DMA, for which the experimental setup apparatus and equipment is commerciality available [20]. In DMA the specimens are relatively small (less than a few square centimeters) and excited at relatively low frequencies (usually at a few hertz) inside a temperature controlled chamber. This method relies on the TTS principle and on the subsequent shift factors required for constructing a master curve over a broad frequency range from the measurements taken at multiple temperatures. DMA is commonly used by material engineers and others to study the rheological and viscoelastic properties of polymers [20].

Polymeric viscoelastic materials are conceivably the most common materials used to passively control the response of structures, e.g., SDTs, with low cost and high reliability [29]. Nevertheless, for applications that are subjected to a wide or high range of temperatures, like in the proximity of exhaust systems, engine parts, automotive panels, etc., the success of these materials is often reduced.

In this sense, in preliminary works (see [40]-[41]), the author has used a finite periodic two-material bar with parallel alternating layers (half-cells) of two-material differing in wave phase velocity under free-free displacement boundary conditions (avoiding the clamped-free displacement boundary conditions of the standardized rod apparatus of ISO 18437-2:2005 [7]) and recurred to different approaches in his progression to estimate the dynamic modulus, i.e., the storage and loss moduli of CCMs. Note that by avoiding the fixed displacement boundary condition that is rigorously more difficult (if not even impossible) to obtain in practice than the free boundary condition, the experimental setup is considerably simplified in the opinion of the author.

In [40], the storage modulus of a commercial CCM was estimated by trial and error which was based on a visual comparison of the experimental FRF and FEM results using a sequence of steel-CCM-steel-CCM-steel-CCM-steel, i.e., a 3.5 cell steel-CCM finite periodic bar. An identical 3.5 cell bar configuration was adopted in [41] where a Lagrangian bar (link) FE is used to estimate the storage modulus of CCM and as expected, it was verified that in order to obtain an acceptable accuracy some care should be considered with respect to the number of Lagrangian FE used per wavelength of the vibration wave [42].

From that work, the author understood the need for a more rigorous method. Thus, in [43], the author proposed the new hybrid analytical-experimental methodology, which is presented here. It estimates the storage modulus having the objective of easing the characterization procedure for resilient materials, in this case with particular interest in CCMs. That is achieved by the developed simple equation from the analytical model of a 1.5 cell (three-layer) specimen test, i.e., steel-CCM-steel lamina sequence. The proposed methodology is validated in this study using correlation criteria for five CCMs. This hybrid methodology although simple, has shown more rigorous due to the introduction of the analytical equation when compared for example with the optional case of using the FEM (in which it is necessary to pay special attention to the number of FEs used per wavelength that increases with frequency).

Furthermore, DMA are conducted to measure the longitudinal dynamic moduli of the same five CCMs tested using the proposed hybrid analytical-experimental methodology. The main objectives are to compare and discuss the experimental data obtained from both methodologies as well as the frequency independency hypothesis often assumed in this framework (for more details see e.g., [120]).

Results show a good agreement between both methodologies for the five CCMs tested presenting deviations less than 0.42% for the storage modulus and 0.86% for the loss factor relative to the results obtained using the proposed hybrid analytical-experimental methodology. Furthermore, it was verified that in the frequency range between 1Hz and ≈10000 Hz the storage and loss moduli present a frequency dependence that may be modeled using a power law model (with power >0). Thus, the

frequency dependence decreases with the increase in frequency, i.e., high frequency dependence at lower frequencies and low frequency dependence at higher frequencies.

Regarding the shear dynamic modulus characterization using the new hybrid analytical-experimental method, the results obtained for the two CCMs tested present correlation values in the interval of 90% and 99.9% thus, validating and demonstrating the potential of the proposed methodology.

Hence, a characterization tool is presented to rigorously estimate the longitudinal and shear dynamic moduli, and with it, the bulk modulus and *Poisson's* ratio (under the assumption of the homogeneous isotropic linear elastic material behavior), of resilient materials, e.g., CCMs.

The author hopes it presents a good contribution to the estimation of the dynamic properties of CCMs.

To conclude this introductory sub-chapter, a brief discretion of its layout follows. Note that except when referenced to the respective authors, all contents are original contributions from this study.

This chapter is composed of eight sub-chapters. This first introductory sub-chapter is followed by a second sub-chapter where a brief review of the dynamic modulus previously introduced in sub-chapter 2.1.1 is presented. In the third sub-chapter is presented the new hybrid analytical-experimental methodology used to characterize the longitudinal dynamic modulus of resilient materials. The analytical formulation of a finite two-material layer bar with uniform cross section is presented and then particularized for the three-layer bar model, which is used in the experimental test. For comparison purposes a two DOF discrete model composed of two rigid masses and one massless spring is introduced. This is followed by a description of: the proposed methodology (an inverse method); the numerical implementation for the storage modulus estimation; the construction of the test specimens; and the experimental setup used to obtain the FRF curves. In the fourth sub-chapter is presented the new analytical-experimental hybrid method now used to characterize the shear dynamic modulus of two CCMs. The experimental specimen is similar to the one used in the longitudinal dynamic modulus characterization and the analytical formulation remains simple (just have to consider the torsion constants). In sub-chapter five is presented a brief description of the DMA used in this study, which includes: TTS principle; the methodology adopted and; the experimental setup. In the sixth sub-chapter are presented the CCMs to be characterized using both methodologies. Then, in the seventh sub-chapter are presented the main results and their discussion. To conclude, an eighth sub-chapter containing the main contributions and conclusions, regarding this chapter, is presented.

3.2. A brief review on the dynamic modulus

The dynamic modulus has been introduced with some detail in sub-chapter 2.1.1. Nevertheless, a brief contextual review on its basics follows.

The dynamic modulus E^{*}, also referred to as the dynamic modulus of elasticity and the complex modulus of elasticity, is a concept used in the frequency domain to characterize the elasto-dynamic properties of viscoelastic materials. By relating the stress and strain amplitudes as expressed by

Eq. (2.8), the dynamic modulus of elasticity is a complex quantity with real (E' - the storage modulus) and imaginary (E'' - the loss modulus) components defined as

$$E^* = E' + \mathrm{i}\ E'',$$ (3.1)

i.e.,

$$E^* = E'\left(1 + \mathrm{i}\ \eta\right),$$ (3.2)

where η is the corresponding loss factor.

Note that the concept of the dynamic modulus presents no restrictions on the type of deformation such as shear, bulk, tensile, etc. Hence, in this study, both longitudinal and shear dynamic moduli are experimentally determined using the new hybrid analytical-experimental methodology proposed.

3.3. Hybrid analytical-experimental methodology

To obtain a simple (in the sense that avoids specific boundary conditions found on other tests) and rigorous (in the sense that avoids the dependence of the number of FEs per wave length) method for the estimation of the storage modulus of the resilient material, an analytical formulation for a finite periodic two-material multi-layer bar is used here to predict the dynamical (harmonic) response of the particular three-layer case of the specimen.

3.3.1. General case of a two-material layer bar subject to longitudinal vibrations

Hence, lets first consider the general case of a 1D bar (rod) with uniform transversal sectional area A, as illustrated in Figure 3.1, with parallel alternating layers of two materials (Mat_α), where index $\alpha = 1$ is used for steel and index $\alpha = 2$ for the resilient material, with longitudinal storage moduli of elasticity E'_{Mat_1} and E'_{Mat_2}, mass densities ρ_{Mat_1} and ρ_{Mat_2} and lengths L_{Mat_1} and L_{Mat_2}, subjected to a longitudinal harmonic force excitation at one extremity.
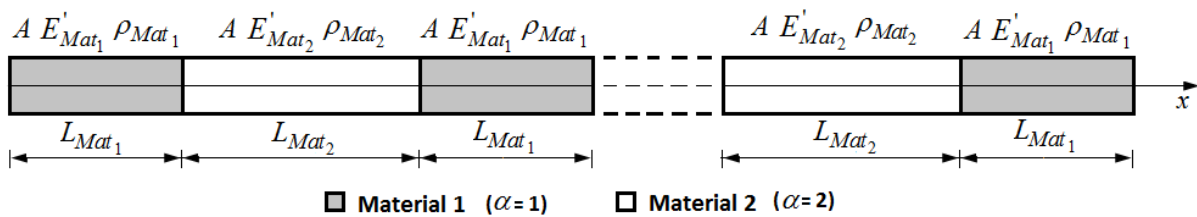
Figure 3.1 – Finite uniform periodic bar composed of two materials.

If the wavelength λ of the stationary waves in the dynamically and longitudinally loaded bar is much longer than the characteristic transverse dimension a of the bar the elementary 1D theory of longitudinal vibrations of bars may be used, see sub-chapter 2.5.2.4 and [104], [121] and [122] for more details.

So being, for a piecewise heterogeneous bar, i.e., material properties are not independent of the position along the axial direction (see Figure 3.1), with constant cross sectional area A, Eq. (2.41) may be rewritten for each material layer Mat_α, where α is layer's type number, as

$$E'_{Mat_\alpha} A \frac{\partial^2 u_{Mat_\alpha}(x,t)}{\partial x^2} - \rho_{Mat_\alpha} A \frac{\partial^2 u_{Mat_\alpha}(x,t)}{\partial t^2} = 0 \qquad \alpha = 1,2. \tag{3.3}$$

where, E'_{Mat_α} is the corresponding longitudinal storage modulus of elasticity, $\rho_{\mathrm{Mat}_\alpha}$ is the corresponding mass density and $u_{\mathrm{Mat}_\alpha}(x,t)$ is the corresponding displacement response at the longitudinal coordinate x and time t.

Note that in Eq. (3.3) the damping term is not included. This is justified as to identify the storage modulus E'_{Mat_α} only an accurate value of the undamped natural frequency is needed. However, this is only valid for frequency independent or weakly frequency dependent materials [88].

For the free longitudinal vibration problem, i.e., when the bar is excited and released to vibrate with no external force, the solution may be developed (assuming that vibrations are harmonic displacements) using the method of the separation of variables and expressed as

$$u_{\mathrm{Mat}_\alpha}(x,t) = U(x)T(t) = \left(B_1 \sin\left(\frac{\omega}{c_{\mathrm{Mat}_\alpha}} x \right) + B_2 \cos\left(\frac{\omega}{c_{\mathrm{Mat}_\alpha}} x \right) \right) \left(B_3 \sin(\omega\,t) + B_4 \cos(\omega\,t) \right), \tag{3.4}$$

where $U(x)$ is the eigenfunction, the constants B_1 and B_2 can be evaluated from the boundary conditions, the function $T(t)$ indicates harmonic motion and the constants B_3 and B_4 can be determined from the initial conditions of the bar, ω is the angular frequency of vibration and

$$c_{\mathrm{Mat}_\alpha} = \left(E'_{\mathrm{Mat}_\alpha} \rho_{\mathrm{Mat}_\alpha}^{-1} \right)^{1/2} \tag{3.5}$$

is the wave phase velocity in the respective material α.

As one is interested in steady-state response and undamped free vibration, neglecting at this step the damping one is dealing with the frequency domain analysis, which is conducted on $U(x)$.

Introducing the wave number $k_{\mathrm{Mat}_\alpha} = \omega\, c_{\mathrm{Mat}_\alpha}^{-1}$, $U(x)$ and its first derivative with respect to space $U,_x$ may expressed as

$$\begin{Bmatrix} U \\ U,_x \end{Bmatrix} = \begin{bmatrix} \sin(k_{\mathrm{Mat}_\alpha} x) & \cos(k_{\mathrm{Mat}_\alpha} x) \\ k_{\mathrm{Mat}_\alpha} \cos(k_{\mathrm{Mat}_\alpha} x) & -k_{\mathrm{Mat}_\alpha} \sin(k_{\mathrm{Mat}_\alpha} x) \end{bmatrix} \begin{Bmatrix} B_1 \\ B_2 \end{Bmatrix}. \tag{3.6}$$
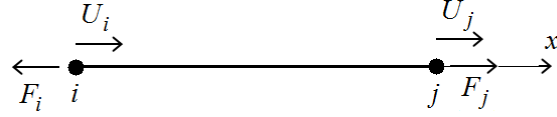
Figure 3.2 – Nodal displacements and forces at the extremity nodes.

For the local referencial with origin at the left node i, the nodal displacement at nodes i $(x=0)$ and j $(x=L_{\text{Mat}_\alpha})$, see Figure 3.2, may be expressed as

$$\underbrace{\begin{Bmatrix} U_i \\ U_j \end{Bmatrix}}_{\mathbf{U}} = \begin{Bmatrix} U|_{x=0} \\ U|_{x=L_{\text{Mat}_\alpha}} \end{Bmatrix} = \underbrace{\begin{bmatrix} 0 & 1 \\ \sin(k_{\text{Mat}_\alpha} L_{\text{Mat}_\alpha}) & \cos(k_{\text{Mat}_\alpha} L_{\text{Mat}_\alpha}) \end{bmatrix}}_{\mathbf{UD}} \underbrace{\begin{Bmatrix} B_1 \\ B_2 \end{Bmatrix}}_{\mathbf{B}}, \tag{3.7}$$

and the nodal forces $F = \sigma A = AE \dfrac{\partial u}{\partial x}$, see Figure 3.2, may be expressed as

$$\underbrace{\begin{Bmatrix} F_i \\ F_j \end{Bmatrix}}_{\mathbf{F}} = A \, E'_{\text{Mat}_\alpha} \begin{Bmatrix} -U,_x|_{x=0} \\ U,_x|_{x=L_{\text{Mat}_\alpha}} \end{Bmatrix} =$$

$$= A \, E'_{\text{Mat}_\alpha} \underbrace{\begin{bmatrix} -k_{\text{Mat}_\alpha} & 0 \\ k_{\text{Mat}_\alpha} \cos(k_{\text{Mat}_\alpha} L_{\text{Mat}_\alpha}) & -k_{\text{Mat}_\alpha} \sin(k_{\text{Mat}_\alpha} L_{\text{Mat}_\alpha}) \end{bmatrix}}_{\mathbf{FD}} \underbrace{\begin{Bmatrix} B_1 \\ B_2 \end{Bmatrix}}_{\mathbf{B}}. \tag{3.8}$$

By replacing constants B_1 and B_2 from Eq. (3.7) into Eq. (3.8) (i.e., taking into account that $\mathbf{U} = \mathbf{UD}\,\mathbf{B}$ and $\mathbf{F} = \mathbf{FD}\,\mathbf{B}$, hence $\mathbf{F} = \mathbf{FD}\,\mathbf{UD^{-1}}\,\mathbf{U}$) one obtains the elementary longitudinal dynamic stiffness matrix $\mathbf{Z} = \mathbf{FD}\,\mathbf{UD^{-1}}$ expressed as

$$\mathbf{Z}(\omega) = A \begin{bmatrix} \varsigma_{\text{Mat}_\alpha} & \gamma_{\text{Mat}_\alpha} \\ \gamma_{\text{Mat}_\alpha} & \varsigma_{\text{Mat}_\alpha} \end{bmatrix}, \tag{3.9}$$

where $\gamma_{\text{Mat}_\alpha} = -E'_{\text{Mat}_\alpha} k_{\text{Mat}_\alpha} \left(\sin(k_{\text{Mat}_\alpha} L_{\text{Mat}_\alpha}) \right)^{-1}$ and $\varsigma_{\text{Mat}_\alpha} = -\gamma_{\text{Mat}_\alpha} \cos(k_{\text{Mat}_\alpha} L_{\text{Mat}_\alpha})$ are considered for $\alpha = 1, \ 2$, i.e., the index of the material type.

Hence, for the general case of a 1D bar (rod) illustrated in Figure 3.1, the global dynamic stiffness matrix is expressed as

$$\mathbf{Z}(\omega) = A \begin{bmatrix} \zeta_{\mathrm{Mat}_1} & \gamma_{\mathrm{Mat}_1} & 0 & \cdots & \cdots & 0 \\ \gamma_{\mathrm{Mat}_1} & \zeta_{\mathrm{Mat}_1} + \zeta_{\mathrm{Mat}_2} & \gamma_{\mathrm{Mat}_2} & 0 & \cdots & 0 \\ 0 & \gamma_{\mathrm{Mat}_2} & \zeta_{\mathrm{Mat}_1} + \zeta_{\mathrm{Mat}_2} & \gamma_{\mathrm{Mat}_1} & 0 & 0 \\ \vdots & 0 & \gamma_{\mathrm{Mat}_1} & \zeta_{\mathrm{Mat}_1} + \zeta_{\mathrm{Mat}_2} & \ddots & 0 \\ \vdots & \vdots & 0 & \ddots & \ddots & \gamma_{\mathrm{Mat}_\alpha} \\ 0 & 0 & 0 & 0 & \gamma_{\mathrm{Mat}_\alpha} & \zeta_{\mathrm{Mat}_\alpha} \end{bmatrix}, \tag{3.10}$$

Usually for the direct problem, the material properties E'_{Mat_α} and $\rho_{\mathrm{Mat}_\alpha}$ are known and the natural frequencies are calculated from the nontrivial solution of the system of linear equations $\mathbf{Z}(\omega)\ \mathbf{U} = \mathbf{0}$, which can be obtained solving the characteristic equation

$$\det \mathbf{Z}(\omega) = 0. \tag{3.11}$$

Hence, for this case, the direct problem that consists of obtaining the dynamic response u for a given bar and harmonic excitation may be formulated as.

Direct problem

Input: Ω, Z, F, K, of

$$Z(\mathrm{K}, \omega)u = F \quad \text{on } \Omega$$

where

geometry Ω: A, L_{Mat_1} and L_{Mat_2};

physical model Z: $E^* = \dfrac{\sigma_0}{\varepsilon_0} e^{\mathrm{i}\,\delta}$

boundary conditions: u (free-free) and F (harmonic)

material properties K: ρ_{Mat_1}, ρ_{Mat_2}, E'_{Mat_1} and E'_{Mat_2}

Output: displacements u; and natural frequencies ω and vibration modes ϕ ($u = \text{constant} \times \phi$)

obtained by solving the characteristic equation $\det \mathbf{Z}(\mathrm{K}, \omega) = 0$ with all K known.

In this study, one deals with the inverse identification problem (see, sub-chapter 2.9 and/or [10] for a detailed discussion), where E'_{Mat_1}, ρ_{Mat_1}, ρ_{Mat_2}, as well as the first natural frequency ω_1 of the specimen, are known. Then, after introducing ω_1 (obtained from the experimental test) the only unknown parameter of K is E'_{Mat_2}.

Hence, for this case, the inverse problem may be formulated as follows.

Input: Ω, Z, u, F, and part of K, of

$$Z(K,\omega)u = F \quad \text{on } \Omega$$

where

geometry Ω : A, L_{Mat_1} and L_{Mat_2}

physical model Z : $E^* = \dfrac{\sigma_0}{\varepsilon_0} e^{i\,\delta}$

boundary conditions: u (free-free) and F (harmonic)

responses: ω_1 known from an experimental test

known part of the material properties K : ρ_{Mat_1}, ρ_{Mat_2} and $E^{'}_{\text{Mat}_1}$

Output: $E^{'}_{\text{Mat}_2}$, the remaining unknown part of K, obtained with the characteristic equation

$$\det \mathbf{Z}(K, \omega_1) = 0 \text{ with } \omega_1 \text{ known.}$$

Thus, Eq. (3.11) may be rewritten as

$$\det \mathbf{Z}(E^{'}_{\text{Mat}_2}, \omega_1) = 0. \tag{3.12}$$

In this case, setting the determinant of the matrix $\mathbf{Z}$ to zero leads to a one variable scalar nonlinear equation, which allows determining the unknown $E^{'}_{\text{Mat}_2}$ once the experimentally identified ω_1 is known and introduced. Hence, once $E^{'}_{\text{Mat}_2}$ is determined, the analytical FRF curve may be obtained by solving the forced harmonic vibration problem. Using the dynamic stiffness matrix, Eq. (3.10), one obtains for each applied frequency ω_{ap} the following system of linear equations

$$\mathbf{Z}(\omega_{\text{ap}}) \ \mathbf{U} = \mathbf{F}_0, \tag{3.13}$$

where $\mathbf{F}_0$ is the amplitude vector of the nodal applied harmonic forces (at same excitation frequency) and $\mathbf{U}$ is the vector that defines the nodal displacement response (steady-state solution).

3.3.2. Identification problem of a three-layer two-material bar subject to longitudinal vibrations

Consider now a three layer bar, as illustrated in Figure 3.3, with the material of the extremity layers differing from the material of the intermediate layer. Recall that this study focuses on the cases where the extremity layers have known elastic properties $E^{'}_{\text{Mat}_1}$ and mass density ρ_{Mat_1}. Regarding the intermediate layer, it is assumed to have a linear viscoelastic behavior and only the mass density

ρ_{Mat_2} is known. Here, for the identification problem the first natural frequency ω_1 of the specimen (previously determined from an experimental test) is known.
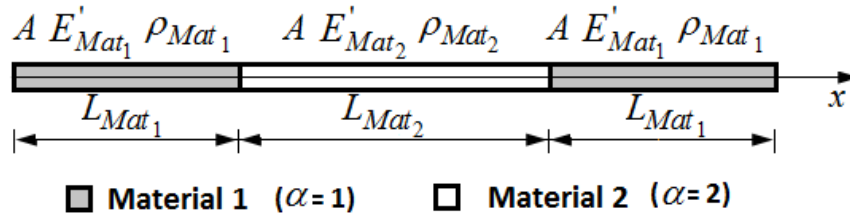
Figure 3.3 – Three layer bar composed of two materials.

Thus, the general dynamic stiffness matrix expressed by Eq. (3.10) may now be particularized for this case and expressed as a function of the only unknown variable E'_{Mat_2} as

$$\mathbf{Z}(E'_{\mathrm{Mat}_2}, \omega_1) = A \begin{bmatrix} \varsigma_{\mathrm{Mat}_1} & \gamma_{\mathrm{Mat}_1} & 0 & 0 \\ \gamma_{\mathrm{Mat}_1} & \varsigma_{\mathrm{Mat}_1} + \varsigma_{\mathrm{Mat}_2} & \gamma_{\mathrm{Mat}_2} & 0 \\ 0 & \gamma_{\mathrm{Mat}_2} & \varsigma_{\mathrm{Mat}_1} + \varsigma_{\mathrm{Mat}_2} & \gamma_{\mathrm{Mat}_1} \\ 0 & 0 & \gamma_{\mathrm{Mat}_1} & \varsigma_{\mathrm{Mat}_1} \end{bmatrix}. \tag{3.14}$$

In this case, the solution of Eq. (3.12), $\det \mathbf{Z}(E'_{\mathrm{Mat}_2}, \omega_1) = 0$, as obtained by the direct calculus of the determinant is expressed as

$$\begin{aligned}
\mathrm{DETZZG} = & (A^4 E_{\mathrm{Mat}_1}{}^4 c_{\mathrm{Mat}_2}{}^2 \omega^4 \cot((L_{\mathrm{Mat}_1}\omega)/c_{\mathrm{Mat}_1})^4 \sin((L_{\mathrm{Mat}_1}\omega)/c_{\mathrm{Mat}_1})^4 \sin((L_{\mathrm{Mat}_2}\omega)/c_{\mathrm{Mat}2})^2 \\
& -2A^4 E_{\mathrm{Mat}_1}{}^4 c_{\mathrm{Mat}_2}{}^2 \omega^4 \cot((L_{\mathrm{Mat}_1}\omega)/c_{\mathrm{Mat}_1})^2 \sin((L_{\mathrm{Mat}_1}\omega)/c_{\mathrm{Mat}_1})^2 \sin((L_{\mathrm{Mat}_2}\omega)/c_{\mathrm{Mat}_2})^2 + A^4 E_{\mathrm{Mat}1}{}^4 \\
& c_{\mathrm{Mat}_2}{}^2 \omega^4 \sin((L_{\mathrm{Mat}_2}\omega)/c_{\mathrm{Mat}_2})^2 + 2A^4 E_{\mathrm{Mat}_1}{}^3 E'_{\mathrm{Mat}_2} c_{\mathrm{Mat}_1} c_{\mathrm{Mat}_2} \omega^4 \cot((L_{\mathrm{Mat}_1}\omega)/c_{\mathrm{Mat}_1})^3 \\
& \cot((L_{\mathrm{Mat}_2}\omega)/c_{\mathrm{Mat}_2}) \sin((L_{\mathrm{Mat}_1}\omega)/c_{\mathrm{Mat}_1})^4 \sin((L_{\mathrm{Mat}_2}\omega)/c_{\mathrm{Mat}_2})^2 - 2A^4 E_{\mathrm{Mat}_1}{}^3 E'_{\mathrm{Mat}_2} c_{\mathrm{Mat}_1} c_{\mathrm{Mat}_2} \omega^4 \\
& \cot((L_{\mathrm{Mat}_1}\omega)/c_{\mathrm{Mat}_1}) \cot((L_{\mathrm{Mat}_2}\omega)/c_{\mathrm{Mat}_2}) \sin((L_{\mathrm{Mat}_1}\omega)/c_{\mathrm{Mat}_1})^2 \sin((L_{\mathrm{Mat}_2}\omega)/c_{\mathrm{Mat}_2})^2 + A^4 E_{\mathrm{Mat}_1}{}^2 \\
& E'_{\mathrm{Mat}_2}{}^2 c_{\mathrm{Mat}_1}{}^2 \omega^4 \cot((L_{\mathrm{Mat}_1}\omega)/c_{\mathrm{Mat}_1})^2 \cot((L_{\mathrm{Mat}_2}\omega)/c_{\mathrm{Mat}_2})^2 \sin((L_{\mathrm{Mat}_1}\omega)/c_{\mathrm{Mat}_1})^4 \\
& \sin((L_{\mathrm{Mat}_2}\omega)/c_{\mathrm{Mat}_2})^2 - A^4 E_{\mathrm{Mat}_1}{}^2 E'_{\mathrm{Mat}_2}{}^2 c_{\mathrm{Mat}_1}{}^2 \omega^4 \cot((L_{\mathrm{Mat}_1}\omega)/c_{\mathrm{Mat}_1})^2 \sin((L_{\mathrm{Mat}_1}\omega)/c_{\mathrm{Mat}_1})^4)/ \\
& (c_{\mathrm{Mat}_1}{}^4 c_{\mathrm{Mat}_2}{}^2 \sin((L_{\mathrm{Mat}_1}\omega)/c_{\mathrm{Mat}_1})^4 \sin((L_{\mathrm{Mat}_2}\omega)/c_{\mathrm{Mat}_2})^2)
\end{aligned} \tag{3.15}$$

The last expression may be considered as relatively complicated in comparison with usual expressions available for these experimental tests. For a detailed description, see Policarpo et al. ([123] and [124]). As result of this, it would be most likely that experimentalists would fully ignore this hybrid analytic-experimental method if present in the form of Eq. (3.15). Note that symbolic computation was here intensively used (see the MATLAB® code in Appendix A.1) to acquire a much simpler equation (i.e., Eq. (3.16)) than the one that is achieved without symbolic computation (i.e., Eq. (3.15)).

$$\Lambda_1 E_{\text{Mat}_2}^{'} + \frac{\Lambda_2 \left(E_{\text{Mat}_2}^{'} \right)^{1/2}}{\tan\left(\Lambda_3 \left(E_{\text{Mat}_2}^{'} \right)^{-1/2} \right)} - \Lambda_4 = 0, \tag{3.16}$$

where:

$$\Lambda_1 = \rho_{\text{Mat}_2} c_{\text{Mat}_1}^2 \beta_1^2 \beta_2^2 ,$$

$$\Lambda_2 = 2 E_{\text{Mat}_1}^{'} c_{\text{Mat}_1} \rho_{\text{Mat}_2}^{1/2} \beta_1 \beta_2^{\,3} ,$$

$$\Lambda_3 = \rho_{\text{Mat}_2}^{1/2} L_{\text{Mat}_2} \omega_1 ,$$

$$\Lambda_4 = E_{\text{Mat}_1}^{'2} \left(\beta_1^2 - 1 \right)^2 ,$$

$$\beta_1 = \cos(\omega_1 L_{\text{Mat}_1} c_{\text{Mat}_1}^{-1}) ,$$

$$\beta_2 = \sin(\omega_1 L_{\text{Mat}_1} c_{\text{Mat}_1}^{-1}) \text{ and }$$

$$c_{\text{Mat}_1} = \left(E_{\text{Mat}_1}^{'} \rho_{\text{Mat}_1}^{-1} \right)^{1/2} .$$

Eq. (3.16) is a one variable scalar nonlinear equation, which allows us to determine $E_{\text{Mat}_2}^{'}$ once the experimentally identified ω_1 is known and introduced.

Fortunately, the actual symbolic computation tools allows for the obtaining Eq. (3.16). It is as simple as the usual formulæ in this field presenting a rigorous and more accurate on hand alternative solution when compared to other actual methods, e.g., 2 DOF discrete model and to the *Lagragian* FE (mention before in relation to [41]), as far as the author is aware and as shown in the results.

Remember that the Lagragian FE strongly depends on the number of FE per wavelength of the vibration wave. The solution proposed here does not suffer from that problem and has also the purpose of avoiding the need for a FE code. However, one has to verify the assumption that the wavelength λ is large (at least, $\lambda/a > 10$) compared with the characteristic dimension of the cross-section of the bar a, see [104] for more details.

In this sense, the simple scalar nonlinear Eq. (3.16) is proposed instead.

3.3.3. Two degrees-of-freedom discrete model

The bar illustrated by Figure 3.3, may alternatively be modeled using two infinitely rigid point masses M_{Mat_1} (see, sub-chapter 2.5.2.1) and one massless spring k_{Mat_2} (see sub-chapter 2.5.2.2.) as illustrated in Figure 3.4. Note that it is the lowest discretization possible (2 DOFs) that allows to

characterize the first natural frequency ω_1 of the three layers with the resilient (intermediate) layer having mass density ρ_{Mat_2} considerably lower than ρ_{Mat_1} so that the mass of this layer may be neglected.
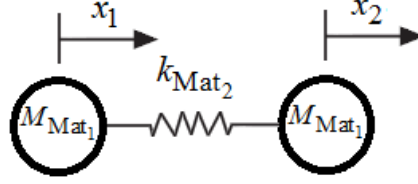
Figure 3.4 – Two DOF discrete model.

Solving Eq. (2.19), (see, appendix A.2. for more details) one obtains the first non-zero natural frequency of the 2 DOFs discrete model, as $\left(f_1 \right)_{\mathrm{2DoF}} = \left(2\pi \right)^{-1} \sqrt{2 k_{\mathrm{Mat}_2} / M_{\mathrm{Mat}_1}}$, where $\omega_1 = 2\pi f_1$, $M_{\mathrm{Mat}_1} = \rho_{\mathrm{Mat}_1} A_{\mathrm{Mat}_1} L_{\mathrm{Mat}_1}$ and $k_{\mathrm{Mat}_2} = E'_{\mathrm{Mat}_2} A_{\mathrm{Mat}_2} / L_{\mathrm{Mat}_2}$ which, when solved in order to the unknown E'_{Mat_2} and considering that $A_{\mathrm{Mat}_1} = A_{\mathrm{Mat}_2} = A$ leads to

$$\left(E'_{\mathrm{Mat}_2} \right)_{\mathrm{2DoF}} = \left(2\pi^2 \rho_{\mathrm{Mat}_1} M_{\mathrm{Mat}_1} L_{\mathrm{Mat}_1} L_{\mathrm{Mat}_2} \right) \left(f_1^2 \right)_{\mathrm{2DoF}}. \tag{3.17}$$

This is an alternative procedure that may be used to obtain E'_{Mat_2} knowing ω_1. Note that Eq. (3.17) may be used to determine the initial guess value of E'_{Mat_2} used to solve Eq. (3.16), see the MATLAB® code presented in Appendix A.3.

3.3.4. Proposed methodology for the inverse method

In this study, a hybrid analytical-experimental methodology is proposed for which an inverse method (see sub-chapter 2.9 and/or [10]) is used to identify the dynamic modulus (storage modulus and modal loss factor) of CCMs.

Figure 3.5 illustrates the main steps of the proposed methodology, which is here described as:

1. Start by building the test specimen (for which the material properties of the extremity layers, i.e., the modulus of elasticity E'_{Mat_1}, mass density ρ_{Mat_1} and modal loss factor $\eta_{\mathrm{Mat}_1} \approx 0$ and mass density ρ_{Mat_2} of the intermediate resilient material are known. The unknown material properties are the storage modulus E'_{Mat_2} and modal loss factor η_{Mat_2} of the resilient material). Conduct an experimental analysis of the test specimen to obtain the experimental FRF curve (as described in sub-chapter 3.3.7);
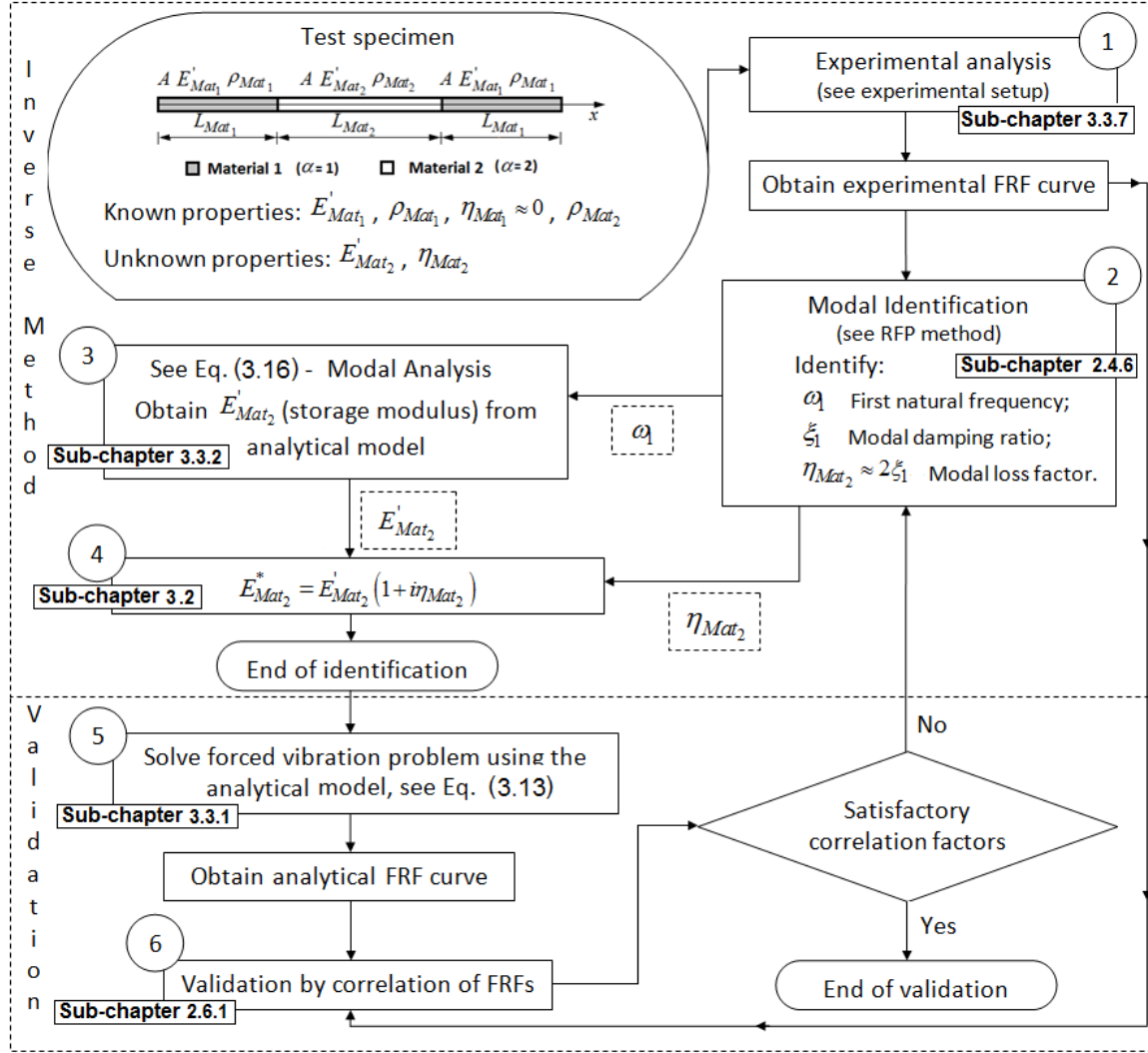
Figure 3.5 – Flowchart of the proposed methodology for determination of the dynamic modulus. The numbers within circles from 1 to 6 underline the steps of the identification procedure, while the sub-chapter of this paper that describes the step is also indicated.

2. Conduct a modal identification analysis using the method RFP (as described in sub-chapter 2.4.6) to identify the first natural frequency ω_1 of the specimen and the correspondent modal damping ratio ξ_1;

3. Introduce the first natural frequency ω_1 into the one variable nonlinear equation Eq. (3.16), obtained from the analytical model (as described in sub-chapter 3.3.2) and use it to estimate the storage modulus E'_{Mat_2};

4. Estimate the dynamic modulus of the resilient layer $E^*_{\text{Mat}_2}$ based on the identified material properties: E'_{Mat_2} and η_{Mat_2} (as described in sub-chapter 3.2). As $E'_{\text{Mat}_1} \gg E'_{\text{Mat}_2}$ i.e., in these cases E'_{Mat_1} is approximately 10^4 order of magnitude greater than E'_{Mat_2} and for the tested

frequency range $\eta_{Mat_1} \approx 2 \times 10^{-4}$, then the modal loss factor of the resilient layer η_{Mat_2} is successfully approximated at the first natural frequency ω_1 by $\eta_{\text{Mat}_2} \approx \eta_1 \approx 2\xi_1$, as the results show. Identification is terminated and if validation is required then follow to step 5.

5. Use the identified material properties (E'_{Mat_2} and η_{Mat_2}) and solve the forced vibration problem Eq. (3.13) using the analytical model of the specimen, to obtain the FRF curve (as described in sub-chapter 2.2.3);

6. Then, conduct a validation analysis, e.g., by correlating the experimental and analytical FRF curves using the FRAC and FAAC assurance criteria (see sub-chapter 2.6.1). If the correlation values are not satisfactory then return to step 2. Otherwise, validation is successful and the identification with validation process is terminated.

The following note is important to clarify the approximation assumed in step 4, i.e., that the modal loss factor of the resilient layer η_{Mat_2} is successfully approximated by $\eta_t \approx \eta_{\text{Mat}_2}$. Note that when springs are connected in series, the total stiffness k_t is determined by $1/k_t = 1/k_{s1} + 1/k_{s2} + \cdots$ (where $k_{s1}, k_{s2}, \ldots$ are the stiffness of the springs one, two and so forth). The longitudinal stiffness of a uniform bar with cross sectional area A and length L may be expressed as $k = \left(E^* A\right)/L$. Therefore, the two-material bar present a total longitudinal stiffness E_t^* which can be estimated as with springs connected in series by the following relation $L_t/\left(E_t^* A\right) = L_{\text{Mat}_1}/\left(E_{\text{Mat}_1}^* A\right) + L_{\text{Mat}_2}/\left(E_{\text{Mat}_2}^* A\right)$. Since $E'_{\text{Mat}_1} \gg E'_{\text{Mat}_2}$ and $\eta_{Mat_1} \approx 2 \times 10^{-4}$, the modal loss factor of the resilient layer η_{Mat_2} is successfully approximated by the total modal loss factor, i.e. $\eta_t \approx \eta_{\text{Mat}_2}$. A detailed description on this is presented in appendix A.4.

3.3.5. Numerical implementation for the storage modulus estimation

The numerical implementation of Eq. (3.16) is considered simple (see the developed code in appendix A.3). Once the values of the input variables (E'_{Mat_1}, ρ_{Mat_1}, ρ_{Mat_2}, L_{Mat_1}, L_{Mat_2} and ω_1) are inserted, the Λ_k with k=1,2,3 and 4 (represented by LAM_ variables in the appendix A.3) are concatenated horizontally using the "horzcat" function to automate the building of the one variable, E'_{Mat_2}, nonlinear Eq. (3.16).

The nontrivial solutions are the roots of the obtained equation or function. Here, the built-in MATLAB® "fzero" function is used. It requires an initial guess or starting point (see initial_guess attribution in appendix A.3. Note that Eq. (3.17) may be and is here used to determine the initial guess value). To do it, the "fzero" function uses a combination of bisection, secant, and inverse quadratic interpolation methods (see the help documentation manual from MATLAB® [125] or the link to

MathWorks$^{®}$ online documentation [126]). By using Eq. (3.17) to determine the initial guess value which is close enough to the solution, one avoids the need to use several starting points to assure the correct solution since "fzero" converges to the nearest zero.

3.3.6. Proposed test specimens

The experimental test specimen proposed by the author consists of a three-layer bar with extremity layers of steel and an intermediate layer of the resilient material to characterize in terms of its dynamic modulus, see Figure 3.6. The construction process of the specimens is described in appendix A.5. In [44], the author present a brief study on the influence of the adhesive layer in the behavior of these structures, which showed to be unnoticed for, thin layers (we considered < 50 μm) of the adhesive. Note that no special cares are required to obtain such a thickness, just the necessary amount of liquid adhesive to cover uniformly the metallic surface to bond is needed.
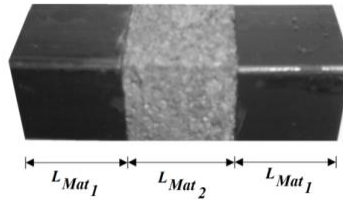
Figure 3.6 – Photograph of the experimental test specimen proposed in this study for measurements of dynamic modulus.

3.3.7. The experimental setup to obtain the frequency response function curve

The experimental setup used in this study to characterize the longitudinal dynamic modulus of resilient materials is illustrated by Figure 3.7. It may be described as: the specimen is suspended from a fix support by two thin elastic nylon strings. In the following, the commercial name of the equipment is indicated within parenthesis. With an impact hammer a longitudinal impact force is applied (a vibration exciter may also be used) to an extremity of the specimen; the force effectively applied to the specimen is measured (input signal) through a force transducer (PCB 208C01). The dynamical deformation propagates throughout the specimen and, at the opposite extremity, an accelerometer (Brüel & Kjaer 4508-B) measures the longitudinal acceleration (output signal).
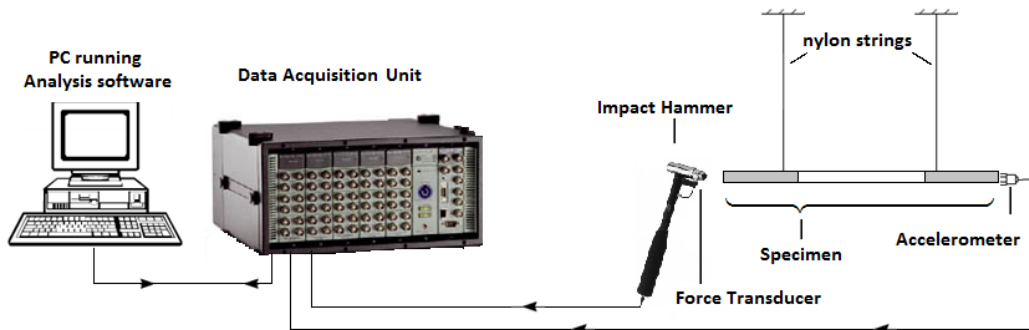
Figure 3.7 – Basic layout of the experimental setup used to identify the first natural frequency ω_1 and the modal loss factor η_{Mat_2} .

The input and output signals are acquired using a data acquisition unit (Brüel & Kjaer 3560D) and analyzed (Bruel & Kjær analysis software PULSE® LabShop Version 6.1.5.65). The FRF curve is obtained allowing identification of the value of the first natural frequency ω_1 and correspondent modal loss factor η_{Mat_2}, using the RFP method (as described in sub-chapter 2.4.6).

3.4. Identification problem of a three-layer two-material bar subject to torsional vibrations

The analytical formulation previously presented in sub-chapter 3.3.1 for the characterization of longitudinal dynamic modulus of elasticity may be similarly applied (using a parallel line of though as in sub-chapter 2.5.2.4) to the shear dynamic modulus of elasticity. For this reason, only the three-layer case will be presented here as the reader can see the work of Policarpo et al. [127] for a detailed discussion on the subject.

Consider a three-layer bar, as illustrated by Figure 3.8 (may or not be the same as the one illustrated by Figure 3.3) with uniform transversal sectional area A, torsional (Saint-Venant) constant J_t and polar moment of the cross-section with respect to the centroid J_p, subjected to a torsional harmonic force excitation at one extremity. The material of the extremity layers differ from the material of the intermediate layer where the extremity layers have known elastic properties G'_{Mat_1} and mass density ρ_{Mat_1}. Regarding the intermediate layer, it is assumed to have a linear viscoelastic behavior and only the mass density ρ_{Mat_2} is known. Here, for the inverse identification problem (see sub-chapter 2.9 and/or [10] for a detailed discussion) the first natural frequency ω_1 of the specimen (previously determined from an experimental test) and the only unknown parameter of K is G'_{Mat_2}.
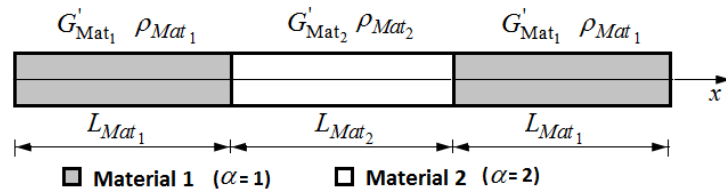
Figure 3.8 – Three layer bar composed of two materials

For this case, the equivalent of Eq. (3.3) written for each material layer Mat_α, where α is layer's type number is

$$c^2_{\mathrm{Mat}_\alpha} \frac{\partial^2 \theta_{\mathrm{Mat}_\alpha}(x,t)}{\partial x^2} - \frac{\partial^2 \theta_{\mathrm{Mat}_\alpha}(x,t)}{\partial t^2} = 0 \qquad \alpha = 1,2. \qquad (3.18)$$

where $\theta_{\mathrm{Mat}_\alpha}(x,t)$ is the torsional displacement response at coordinate x and at time t and c_{Mat_α} is the corresponding wave phase velocity in the respective material α expressed as

$$c_{\text{Mat}_\alpha} = \sqrt{G'_{\text{Mat}_\alpha} J_t \big/ \left(\rho_{\text{Mat}_\alpha} J_p \right)} \qquad (3.19)$$

where G'_{Mat_α} is the corresponding shear storage modulus of elasticity.

The free vibration problem solution, i.e., when the bar is excited and released to vibrate with no external force, may be developed using the method of the separation of variables, see Eq. (3.4). The procedure is similar to the one used in sub-chapter 3.3.1 however: i) instead of the cross transversal sectional area A one considers the torsional constant J_t; ii) instead of the longitudinal storage modulus one considered the shear storage modulus and; iii) the adequate expression of the wave phase velocity, i.e., instead of Eq. (3.5) one considered Eq. (3.19).

Thus, the dynamic stiffness matrix for this case may be expressed as a function of the only unknown variable G'_{Mat_2} as

$$\mathbf{Z}(G'_{\text{Mat}_2}, \omega_1) = J_t \begin{bmatrix} \zeta_{\text{Mat}_1} & \gamma_{\text{Mat}_1} & 0 & 0 \\ \gamma_{\text{Mat}_1} & \zeta_{\text{Mat}_1} + \zeta_{\text{Mat}_2} & \gamma_{\text{Mat}_2} & 0 \\ 0 & \gamma_{\text{Mat}_2} & \zeta_{\text{Mat}_1} + \zeta_{\text{Mat}_2} & \gamma_{\text{Mat}_1} \\ 0 & 0 & \gamma_{\text{Mat}_1} & \zeta_{\text{Mat}_1} \end{bmatrix}. \qquad (3.20)$$

In this case, the solution of $\det \mathbf{Z}(G'_{\text{Mat}_2}, \omega_1) = 0$, may be expressed as

$$\Lambda_1 G'_{\text{Mat}_2} + \frac{\Lambda_2 \left(G'_{\text{Mat}_2} \right)^{1/2}}{\tan \left(\Lambda_3 \left(G'_{\text{Mat}_2} \right)^{1/2} \right)} - \Lambda_4 = 0, \qquad (3.21)$$

where,

$$\Lambda_1 = \rho_{\text{Mat}_2} c_{\text{Mat}_1}^2 \beta_1^2 \beta_2^2,$$

$$\Lambda_2 = 2G'_{\text{Mat}_1} c_{\text{Mat}_1} \rho_{\text{Mat}_2}^{1/2} \beta_1 \beta_2^3,$$

$$\Lambda_3 = \rho_{\text{Mat}_2}^{1/2} L_{\text{Mat}_2} \omega_1,$$

$$\Lambda_4 = G'^2_{\text{Mat}_1} \left(\beta_1^2 - 1 \right)^2,$$

$$\beta_1 = \cos(\omega_1 L_{\text{Mat}_1} c_{\text{Mat}_1}^{-1}),$$

$$\beta_2 = \sin(\omega_1 L_{\text{Mat}_1} c_{\text{Mat}_1}^{-1}) \text{ and}$$

$$c_{\text{Mat}_\alpha} = \sqrt{G'_{\text{Mat}_\alpha} J_t \big/ \left(\rho_{\text{Mat}_\alpha} J_p \right)}.$$

69

Identically to Eq. (3.16), Eq. (3.21) is a one variable scalar nonlinear equation, which allows one to determine G'_{Mat_2}, once ω_1 is experimentally identified and introduced.

The modal identification method, i.e., the hybrid analytical-experimental methodology proposed in sub-chapter 3.3.4, may be used to identify the shear dynamic modulus of elasticity $G^*_{\text{Mat}_2}$ (storage modulus G'_{Mat_2} and the respective modal loss factor η_{Mat_2}) of resilient materials. Additionally, the numerical implementation of Eq. (3.21) is identical to that of Eq. (3.16) which was previously presented in sub-chapter 3.3.5. Furthermore, the experimental test specimen can be the same as the ones proposed in sub-chapter 3.3.6 consisting of a simple three layer bar with extremity layers of steel and a resilient layer of the material to characterize in terms of its dynamic modulus, see Figure 3.6.

However, the experimental setup is different and is presented next.

3.4.1. The experimental setup to obtain the frequency response function curve: Torsion case 1

To characterize the shear dynamic modulus of elasticity $G^*_{\text{Mat}_2}$ the experimental setup illustrated in Figure 3.9 was used (designated as torsion case 1). To create torque on the specimen an auxiliary rod designated as torque rod, see Figure 3.9, is coupled to the specimen. Any lateral motion of the structure may be minimized by using an additional rod mounted on a lubricated puncture made on the torque rod (see point P_2 in Figure 3.9) and fixed at the other extremity.
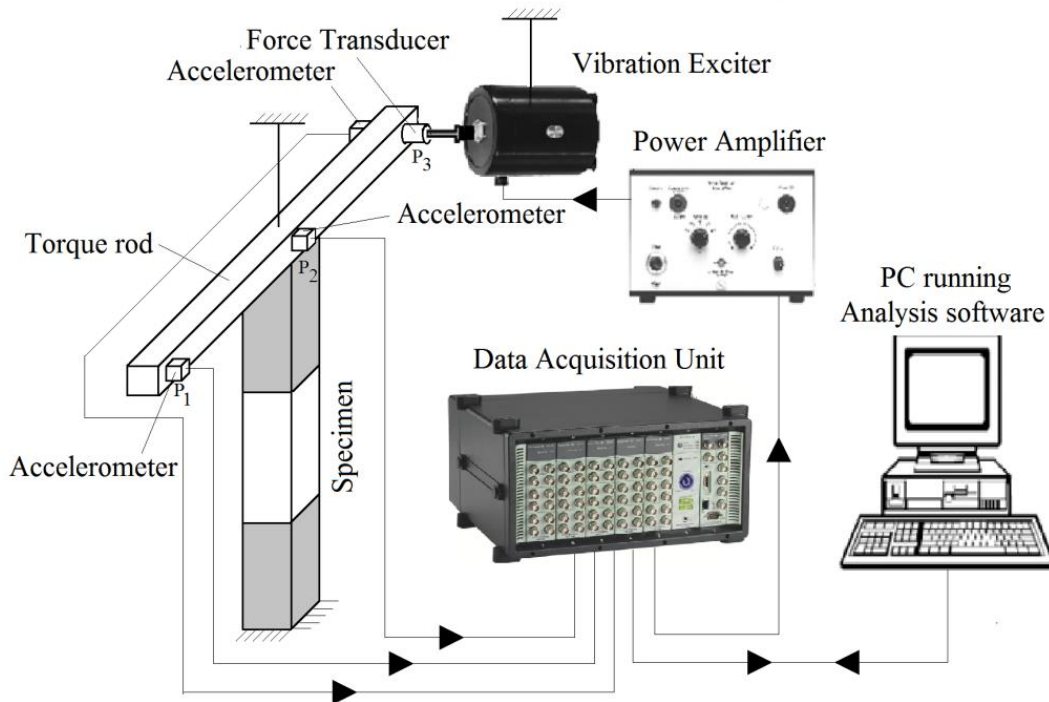
Figure 3.9 – Basic layout of the torsional experimental setup used to identify the first natural frequency ω_1 and modal loss factor η_{Mat_2}.

Using a vibration exciter, see Figure 3.9, a transverse force is applied to an extremity of the torque rod (e.g, point P_3 in Figure 3.9); the force effectively applied to the torque rod is measured through a force transducer (input signal). This force creates a torsional moment (but also some flexural moment, which means no pure torsion) in the specimen, which has an extremity fixed to a rigid support. Three accelerometers mounted on the torque rod measure the transverse accelerations at points P_1, P_2 and P_3 (output signals).

The input and output signals are acquired by a data acquisition unit and processed using analysis software. To experimentally characterize the shear dynamic modulus in a way that the analytical formulation described in sub-chapter 3.3.2 is applicable it is required that: the mass and inertia of the torque rod are accounted for, which does not present any difficulty; and that the specimen is in pure torsion. From the experimental point of view, this last requirement is not easily fulfilled.

Not to drift away from the objective of experimentally characterizing the shear dynamic modulus of the resilient material of the specimen $G_{\mathrm{Mat}_2}^*$, the author decided to apply an approach based on a FE modal analysis see, [40] and [41] for more details. Initially a FE modal analysis was conducted, where the unknown variable, the shear storage modulus $G_{\mathrm{Mat}_2}^{'}$, was initially considered of unitary value, i.e., $G_{\mathrm{FEM}}^{'} = 1\,\mathrm{Pa}$. Afterwards, the square ratio of the experimental and FEM first natural frequencies was used to estimate the shear storage modulus, as

$$\left(\omega_{\mathrm{EXP}}/\omega_{\mathrm{FEM}}\right)^2 \approx G_{\mathrm{Mat}_2}^{'}. \tag{3.22}$$

This is followed by a structural harmonic analysis, see Eq. (3.13), to obtain the FRF curve that is then compared with the one obtained experimentally. Validation by correlating the experimental and numerical FRF curves using the FRAC and the FAAC correlation measures (see sub-chapter 2.6.1) is then conducted.

3.4.2. The numerical equivalent of the experimental setup to obtain the frequency response function curve: Torsion case 2

From the experimental point of view, applying a pure torsion moment to the specimen is not easily fulfilled. Thus, FEs are used to study the FE model of a specimen with free displacement boundary conditions (designated as torsion case 2). In this case, the FE model of the specimen is subjected to a torsional excitation $f(x,t)$ applied at an extremity (see Figure 3.10) and the response is obtained at the opposite extremity.
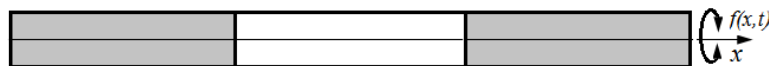
Figure 3.10 – Numerical model, of specimen used in torsion case 2, used to identify the first natural frequency ω_1 and modal loss factor η_{Mat_2} .

Using the shear storage modulus G'_{Mat_2} and modal loss factor η_{Mat_2} determined using the torsion case 1 (see sub-chapter 3.4.1) FE structural harmonic analysis of the specimen is conducted to obtain the frequency response function (FRF) curve which is then compared with the one obtained analytically. The FRF curve is obtained allowing identification of the value of the first natural frequency ω_1 and correspondent modal loss factor η_{Mat_2}, using the RFP method (as described in sub-chapter 2.4.6).

3.5. Dynamic mechanical analysis

Continuing with the longitudinal dynamic modulus estimation, another method used in this study is the DMA.

DMA consists of applying a small oscillating force (or displacement) causing a sinusoidal strain (or stress), in the linear viscoelastic regime, on a material sample and measuring the resulting stress (or strain) response. By measuring both the lag δ between the stress and strain sine waves and the amplitude of the deformation at the peak of the sine wave, quantities like the dynamic modulus E^* may be determined. In this way, with DMA it is possible to obtain the modulus every single time a sine wave is applied. Thus, one can sweep along the temperature T and/or frequency ω range to obtain the modulus as a function of the temperature and/or the frequency, see Figure 3.11.
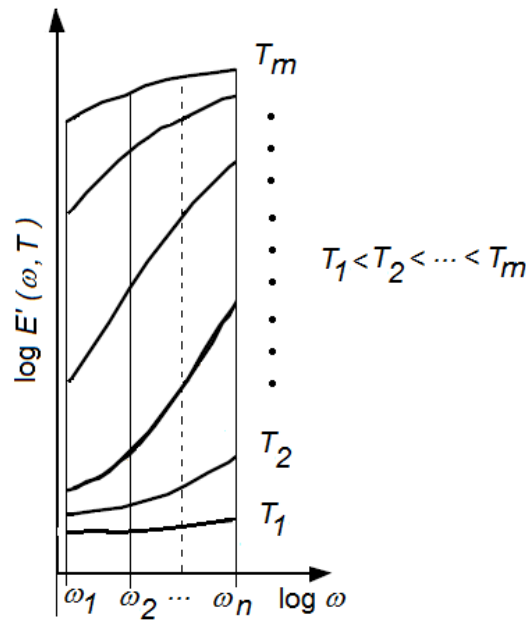
Figure 3.11 – Storage modulus (E') curves obtained by DMA at different temperatures and frequencies.

However, this is easier said than done since experimental data may not be available and/or obtainable. Note that while wide range temperatures measurements may be made with relative ease, it is not as easy to assess for measurements in which changes occur at relative high or low frequencies, i.e., in less than, e.g., a second or in longer than, e.g., an hour.

Nevertheless, a solution arises from the experimental findings that time (or frequency) and temperature dependent processes present equivalent effects on the rheological properties of linear viscoelastic materials [8]. Thus, if the temperature of the material is lowered, the dynamic mechanical responses take longer than they would present at a higher temperature, and the extent of these processes is slowed in proportion to the temperature reduction. On the other hand, elevating the temperature speeds these processes in proportion to the temperature increase.
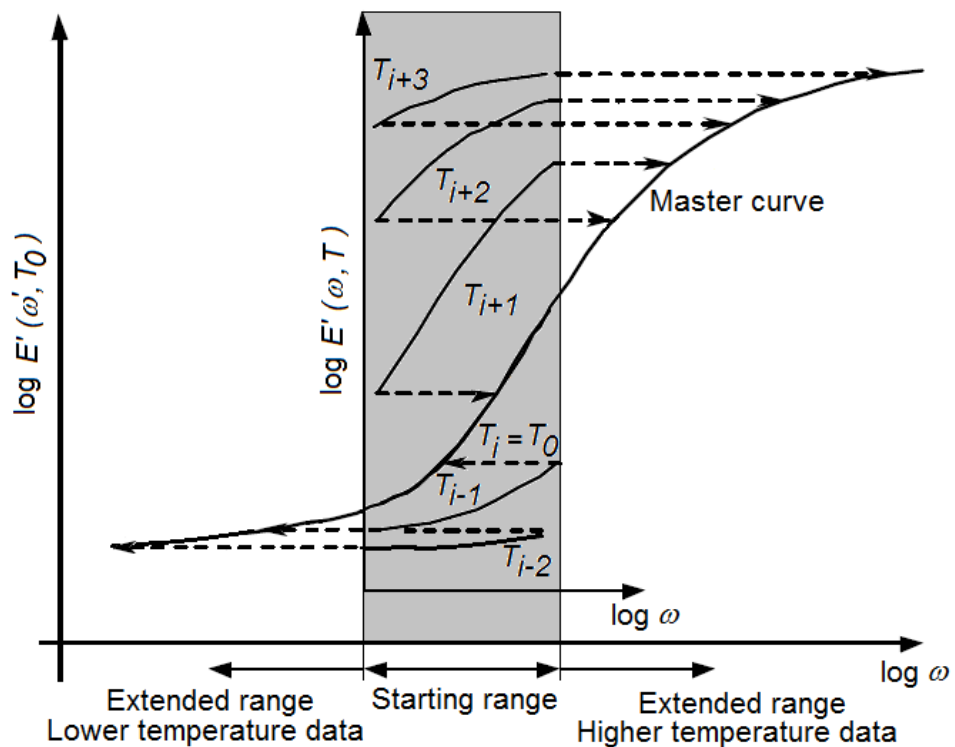
Figure 3.12 – Storage modulus ($E^{'}$) curves measured ($\log \omega$) and the master curve obtained ($\log \omega^{'}$) after

shifting the measured curves where $\omega^{'}$ is the shifted frequency.

Three distinct areas or ranges are illustrated in Figure 3.12. In the shaded area, designated as starting range, the storage modulus curves of Figure 3.11 are represented for different temperatures T and measured frequencies ω. To the left and right hand side of the shaded area are two other areas designated as extended ranges, which contain the data obtained at lower and higher temperatures, respectively.

As illustrated in Figure 3.12, the main effect from the temperature change is the rescale of frequency (or time), i.e., temperature changes shift the viscoelastic functions along the modulus and time (or frequency) scales without changing their shapes. This produces a composite curve called a master curve, which can be generated from a series of curves by overlapping data collected at different temperatures and frequencies, see Figure 3.12. This procedure is usually referred to as time-temperature superposition (TTS) principle as described in e.g., Fesko and Tschoegl [128].

3.5.1. Time-temperature superposition principle

The underlying bases of the TTS principle are: i) that the processes involved in molecular relaxation or rearrangements in viscoelastic materials occur at accelerated rates at higher temperatures and; ii) that there is a direct equivalency between frequency (or time) and temperature. Hence, the time over which these processes occur can be reduced by conducting the measurement at elevated temperatures and transposing (shifting by a factor a_T) the resultant data to lower temperatures. The result of this shifting is a master curve where the material property of interest at a specific temperature can be predicted over a broad frequency scale. A comprehensive discussion on TTS is provided by the text of Ferry [8]. In order to apply the TTS principle it is required that all the relaxation times (or the full relaxation spectrum) must show practically the same temperature dependence. In these conditions, the curves representing the material functions can be superimposed by translation in the time axis (or in the frequency axis, as illustrated by Figure 3.12). In multiphase systems, the relaxation spectrum of every component presents different temperature dependence, so it is expected that for multi-phase systems TTS will not hold [128]. Nevertheless, in circumstances where the contribution of one component is dominant in the involved relaxation processes, TTS may still be useful and provide numerical values rather close to the experimental ones.

Determination of the shift factor by aligning curves taken at multiple temperatures provides shift factor values only for temperatures at which data is known. Often it is useful to be able to shift the master curve to any arbitrary temperature, which requires knowledge of the shift factor as a continuous function of temperature. This is generally accomplished by fitting the empirically obtained shift factors to an appropriate function. One of the most common functions used for this purpose is based on the Arrhenius equation [129]

$$\log a_T = \frac{H}{2.303R} \left(\frac{1}{T} - \frac{1}{T_0} \right), \qquad (3.23)$$

where a_T is the temperature shift factor, H is the apparent activation energy in [kJ/mol], R is the gas constant 8.314 [J/(°K mol)], T is the absolute measurement temperature and T_0 is the absolute reference temperature.

When applied to DMA data, which is the case, TTS relates temperature and frequency rather than temperature and time. Data is measured at multiple frequencies over a range of temperatures, see shaded area in Figure 3.12. The data may then be shifted onto a single master curve by treating frequency as the inverse of time and determining shift factors as described above, see Eq. (3.23), representing the storage modulus as a function of shifted frequency $\omega' = a_T \omega$ at the reference temperature as illustrated by Figure 3.12 . Note that the master curve may be used to predict behavior at frequencies outside the practical limitations of the test equipment.

3.5.2. Methodology

In this study, DMA tests are conducted under dual cantilever clamped conditions as illustrated in Figure 3.13. The DMA dual cantilever clamp measuring system is similar to the typical three-point bending except that in the DMA the ends of the specimen are clamped. The clamping center screws are threaded on the support bar allowing movement of the jaws to clamp/unclamp the specimen to the fixed clamps (that are supported by mounting posts) and to a moveable clamp that is driven by a driveshaft that applies a sinusoidal controlled force/ displacement to the specimen.
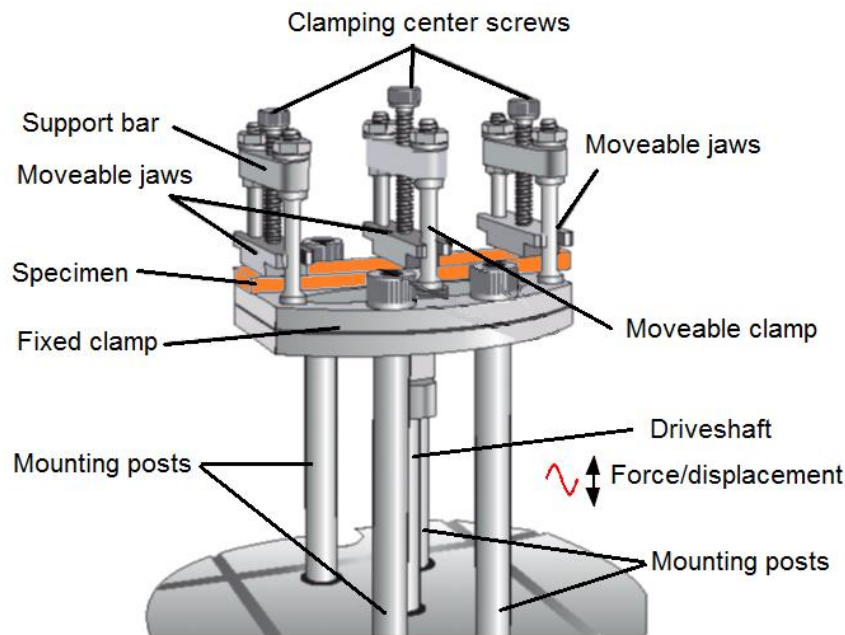
Figure 3.13 – Illustration of the DMA dual cantilever clamp measuring system.

The specimens are tested inside a controlled temperature furnace, which is initially cooled using liquid nitrogen to a specific temperature (e.g., -50ºC) bellow the glass temperature allowing one to register part of the glassy region as well as the glass transition region in order to obtain a characterization in the low frequency range. Recall that temperature changes shift the viscoelastic functions along the modulus and frequency scales as illustrated by Figure 3.12.

When that temperature is reached the specimen in maintained under isothermal conditions for a specific time to ensure thermal and mechanical equilibrium after which, the experiment is initialized. Subsequently, the furnace is heated at a specific rate that should be such that its change per cycle is not significant allowing the specimen to reach thermal equilibrium. The specimen is subject to a control strain at different frequencies and the respective resulting strains are measured. The experiment ends when a specific final temperature is reached.

With this, one obtains the storage modulus $E^{'}$ and loss factor η curves (usually designated as $tg\delta$ in DMA, see Eq. (2.9)), among other data. Using commercial software (TA Instrument Universal Analysis 2000 [130]) the data file format is converted to TTS data format. The TTS analyses are then conducted also using commercial software (TA Instrument Rheology Advantage Data Analysis [131]).

TTS analysis begins by selecting a reference temperature to determine the shift factors that best fit the Arrhenius equation, see Eq. (3.23), leading to the master curves of the storage modulus $E^{'}$ and loss factor η as a function of frequency.

3.5.3. Experimental setup

The experimental apparatus used to conduct the DMA tests is the illustrated in Figure 3.14 and consists of the following: 1 – DMA test equipment referenced as Q800 from TA Instruments to conduct the analyses with a; 2 – dual cantilever clamp system and; 3 – a furnace to control the temperature of the test. Connected to the Q800 is a; 4 – tank containing liquid nitrogen used to lower the temperatures of the tests and; 5 – a computer is used to control define the parameters of the DMA tests as well as record the data obtained.

a)   b)
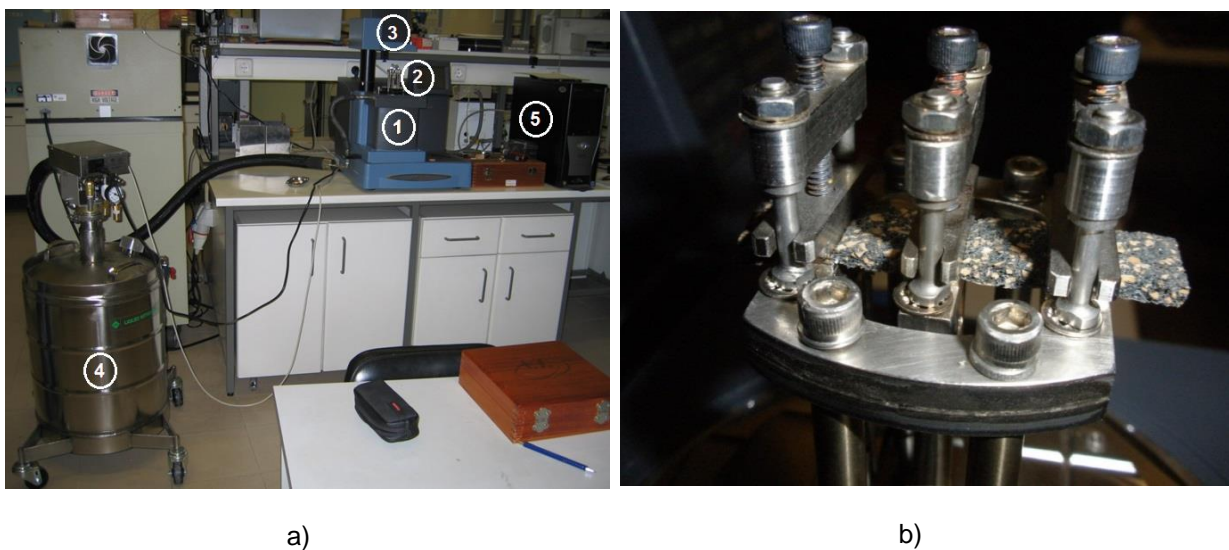
Figure 3.14 – Experimental DMA test apparatus: a) 1–TA Instruments Q800 DMA; 2 – Dual cantilever clamp measuring system; 3 – Furnace; 4 – Liquid nitrogen gas cooling tank; 5 – Computer for data analyses; b) Dual cantilever clamp system.

Once the DMA test data, i.e., $E^{'}$ and $tg\delta$ at different temperatures and for different frequencies, is obtained, commercial TA Instrument software (TA Instrument Universal Analysis 2000 [130] and TA Instrument Rheology Advantage Data Analysis [131]) is used to obtain the master curves.

3.6.   Materials studied

Five different CCMs (illustrated by Figure 3.15), four types of cork-rubber and one type of cork agglomerate are studied. These materials were supplied by a cork composite producer (Amorim Cork Composites [132]) that referenced the cork-rubber materials by the initials VC and the cork agglomerate material by the initials NL. For future reference, these designations will be maintained in this document.
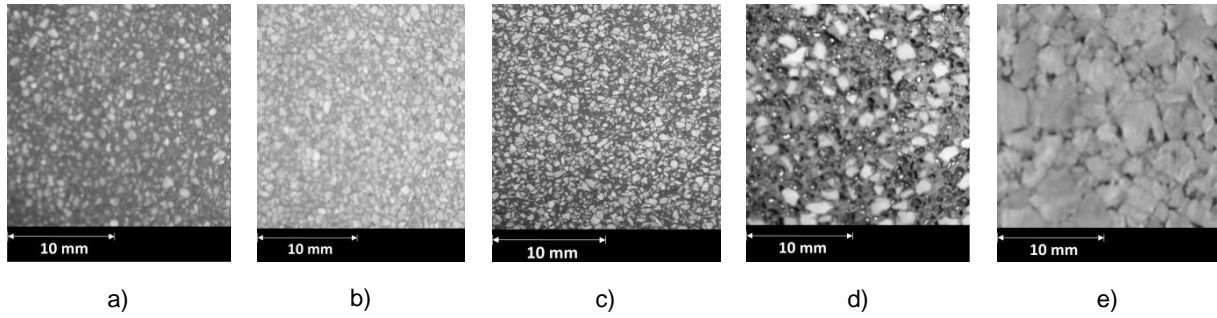
Figure 3.15 – Amplified photograph of the used intermediate resilient materials (Area=40 mm^2): a) VC 6400; b) VC 5200; c) VC 2100; d) VC 1001 (porous); e) NL20.

The mass density ρ_{Mat_2} of each material is estimated by measuring the dimensions and the weight of the material specimen. This is based on $\rho_{\mathrm{Mat}_2} = M_{\mathrm{Mat}_2} \, V_{\mathrm{Mat}_2}^{-1}$, where M_{Mat_2} and V_{Mat_2} are the mass and the volume of the resilient layer, respectively. For each material, ten samples were used, from which the five with the lowest standard deviation (< 10 kg m^{-3}) are considered to determine the arithmetic mean value of the mass density ρ_{Mat_2} of the material as indicated in Table 3.1.

	Steel $\alpha = 1$	VC 6400 $\alpha = 2$	VC 5200 $\alpha = 2$	VC 2100 $\alpha = 2$	VC 1001 $\alpha = 2$	NL20 $\alpha = 2$
$\rho_{\mathrm{Mat}_\alpha}$ (kg m^{-3})	7640 [44]	893	590	836	516	210
E_{Mat_α} (GPa)	205 [44]	To be determined	To be determined	To be determined	To be determined	To be determined
$\eta_{\mathrm{Mat}_\alpha}$	≈ 0	To be determined	To be determined	To be determined	To be determined	To be determined

Table 3.1 – Known and unknown material properties.

3.7. Results and discussion

In this sub-chapter are presented the main results obtained using the proposed analytical-experimental hybrid method to characterize the longitudinal and shear dynamic moduli of the above five CCMs. DMA tests were also conducted to characterize the longitudinal dynamic modulus of the same CCMs. Analyses of the results obtained by both methods are presented and discussed in this framework. Furthermore and to conclude, are presented the results obtained using the proposed analytical-experimental hybrid method to characterize the shear dynamic modulus of elasticity of two CCMs.

3.7.1. Proposed methodology: Analytical-experimental hybrid methodology

Eighteen experimental test specimens (see sub-chapter 3.3.6), three of each type of resilient material, were built and tested using the experimental setup described in sub-chapter 3.3.7. A total of

10 averages were used for each specimen, minimizing the lack of repeatability inherent to impact testing, see sub-chapter 2.4.1.

A transient time weighting function was used for the force signal to improve the signal to noise ratio, and an exponential time weighting function was used for the response signal, to reduce leakage effects and noise. Auto-ranging of the input/output signals for the impulse measurements was conducted to optimize the signal to noise ratio and automatic rejection of "overload" signals was considered. See sub-chapter 2.4 and Maia et.al [88] for more details.

The identification methodology described in sub-chapter 2.4.6 (the indirect frequency domain identification curve fitting method based on the RFP method) was used to determine the poles, the first natural frequency f_1 (where $\omega_1 = 2\pi f_1$), see Eq. (2.27), the correspondent modal damping ratio ξ_1 see Eq. (2.28) (where the modal loss factor may be approximated by $\eta_{\text{Mat}_2} = 2\xi$ as results will show), and the residue. It was considered that the degree of the denominator of Eq. (2.25) was equal to five since, it was the lowest value that produced satisfactory results. The loss modulus was determined by Eq. (2.10), and the storage modulus E'_{Mat_2} was determined as the solution of Eq. (3.16). All these results as well as the longitudinal lengths (L_{Mat_1} and L_{Mat_2}) of the steel and the resilient materials are presented in Table 3.2 and Table 3.3.

For the cases considered in this study, the behavior of $\det \mathbf{Z}(E'_{\text{Mat}_2}, \omega_1)$,i.e., Eq. (3.12), is illustrated by Figure 3.16. It was considered in the Figure 3.16 a) that f_1 =533 Hz and in the Figure 3.16 b) it was considered that E'_{Mat_2} =17.9 MPa. This behavior allows us to use the "fzero" function to determine a solution of Eq. (3.16) (see sub-chapter 3.3.5 and for more detail see, e.g., [125]).
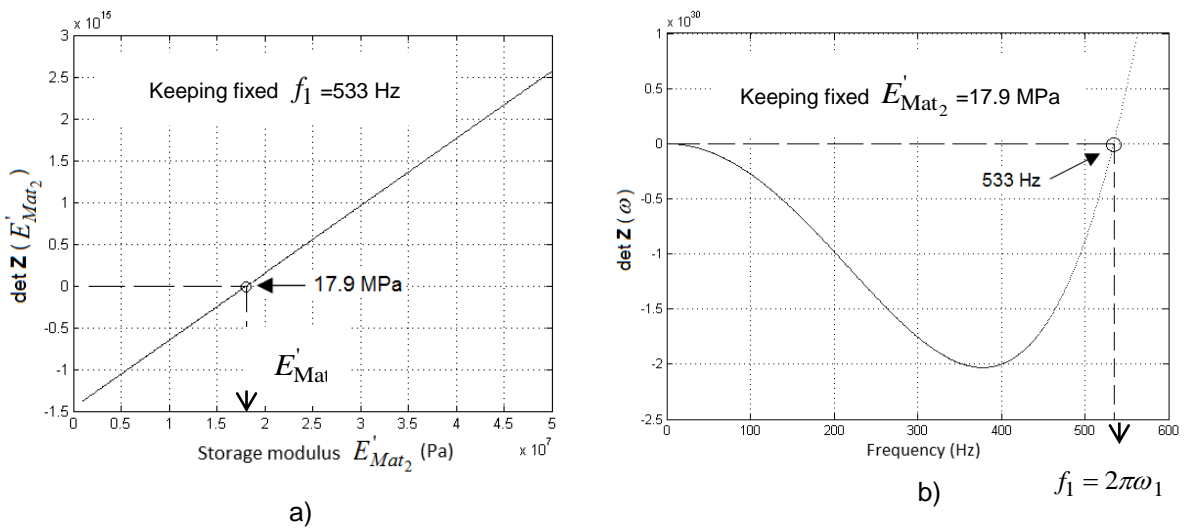
Figure 3.16 – Plot of $\det \mathbf{Z}$ as a function of: a) E'_{Mat_2} and considering f_1 =533 Hz and; b) ω and considering E'_{Mat_2} =17.9 MPa.

Figure 3.17 illustrates the dependence of the first solutions of the nonlinear Eq. (3.16) with respect to the measured natural frequency f_1. It is represented by the lines without dots considering three different steel lengths: $L_{\mathrm{Mat}_1} = 0.0100$ m, $L_{\mathrm{Mat}_1} = 0.0205$ m and $L_{\mathrm{Mat}_1} = 0.0300$ m; and a resilient material (VC6400) layer with fixed length $L_{\mathrm{Mat}_2} = 0.0128$ m, see Table 3.2. The properties of the steel as well as the mass density of the resilient material layer are presented in Table 3.1.

Furthermore, Figure 3.17 also illustrates the solutions of a lumped 2 DOFs semi-definite dynamic system model (represented by the lines with dots), previously described in sub-chapter 3.3.3, in which: the extremity steel layers with a cross-sectional area $A_{\mathrm{Mat}_1} = A = 0.004$ m^2 are modeled as infinitely rigid masses M_{Mat_1}, and the resilient material (VC 6400) layer with a cross-sectional area $A_{\mathrm{Mat}_2} = A = 0.004$ m^2 is modeled as a massless spring. For the two DOF model the equivalent to Eq. (3.16), is represented by Eq. (3.17).
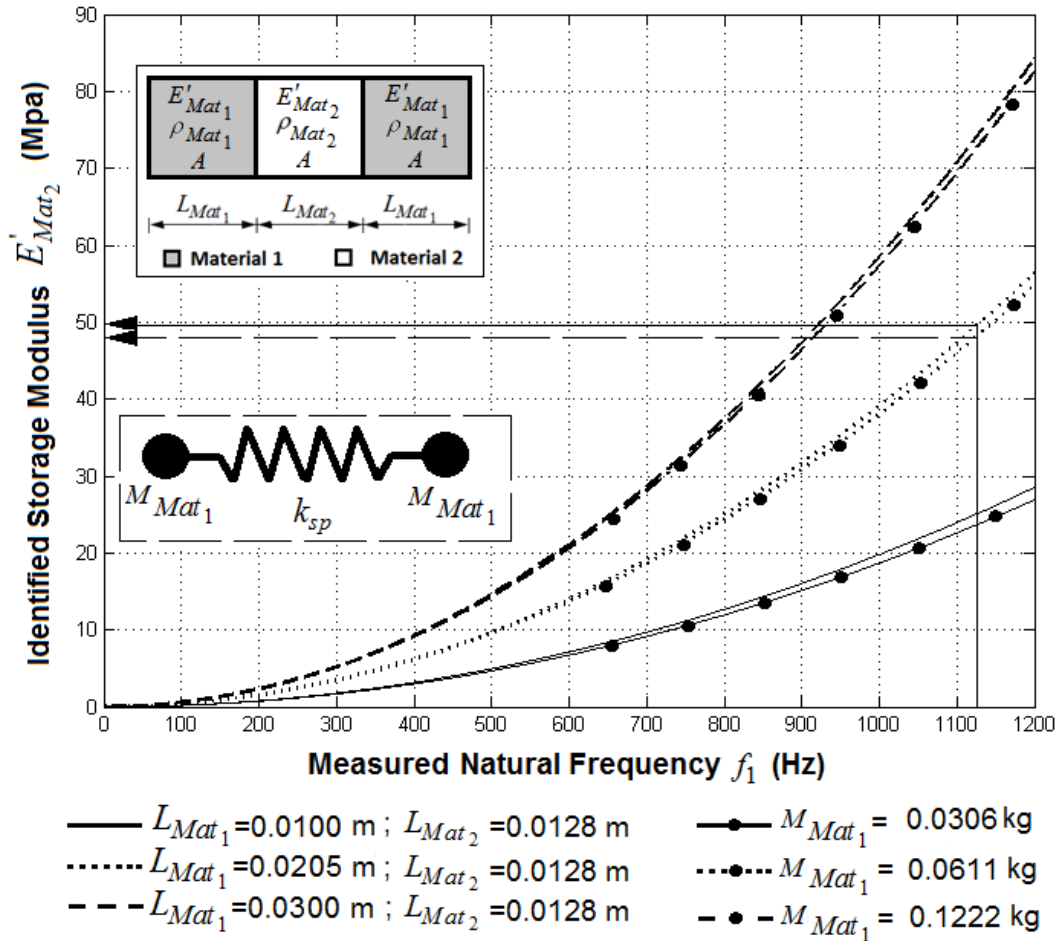
Figure 3.17 – Dependence of the solutions of Eq. (3.16) E'_{Mat_2} on the measured frequency f_1 for three values of steel lengths and a fixed resilient material length (lines without dots); and 2 DOF lumped model (lines with dots).

In Figure 3.17, one may observe that the identified storage moduli E'_{Mat_2} using the 2 DOF lumped model Eq. (3.17) (lines with dots) diverge from the identified storage moduli of the proposed nonlinear Eq. (3.16) (lines without dots), as the identified natural frequency f_1 increases.

As an example, in Figure 3.17 consider a measured natural frequency f_1 of 1124 Hz and a steel length L_{Mat_1} of 0.0205 m, which is equivalent to a mass M_{Mat_1} of 0.061 kg. It is possible to observe that the storage modulus E'_{Mat_2} identified using the 2 DOF lumped model Eq. (3.17) is approximately 48.7 MPa, whereas the storage modulus E'_{Mat_2} identified using the proposed nonlinear Eq. (3.16) is 49.5 MPa. From this example, even though others were verified, one may conclude that the storage moduli identified using the 2 DOF lumped model presents a relative deviation of 1.6%.

Furthermore, based on Figure 3.17, one may conclude that the sensitivity of the identified storage modulus E'_{Mat_2} increases with the identified natural frequency f_1 (in Hz) as well as with the reduction of length L_{Mat_1} of the extremity (steel) layers. Thus, small lengths for the extremity steel layers L_{Mat_1} are advantageous. However, small length of the extremity steel layers lead to higher natural frequencies of the specimen, which is where the proposed nonlinear Eq. (3.16) is considered more accurate than the 2 DOF lumped model.

Additionally, it was verified that Eq. (3.16) presents a relatively low sensitivity regarding the identified natural frequency f_1. Indeed, considering the previous example (i.e., VC 6400 as the resilient material, f_1 of 1124 Hz and a steel length L_{Mat_1} of 0.0205 m) and a perturbation of 0.1 Hz in the identified natural frequency leads to a relative deviation of approximately 0.017% in the identified storage modulus E'_{Mat_2}.

In this study, the lengths of all the resilient materials were kept constant; thus, it was necessary to increase the length of the extremity steel layers in order to characterize the storage modulus for lower frequencies. In this context, the sensitivity regarding the identified natural frequency f_1 using longer extremity steel layers increases, which can be verified by the slope of the curves illustrated in Figure 3.17. Therefore, one may conclude that in these cases (long extremity steel layers) a more precise and accurate frequency measurement is required.

With this in mind, the author tested the cases of extremity steel layers with lengths of: i) L_{Mat_1} of approximately 20.5 mm (for higher frequencies), see Table 3.2 and ii) L_{Mat_1} of 0.976 m (for lower frequencies), see Table 3.3. Hence, the results of Table 3.2 and Table 3.3 are not comparable among each other. The length L_{Mat_2} was fixed at the thickness value available from the CCMs supplied.

Material	L_{Mat_1} (mm)	L_{Mat_2} (mm)	Pole Eq. (2.27)	f_1 (Hz) Eq. (2.27)	η_{Mat_2} Eq. (2.28)	Residue r_k	E'_{Mat_2} (MPa)	E''_{Mat_2} (MPa)
VC 6400	20.5	12.8	-660.0+7030.7i	1123.9	0.187	(1-6i)×10⁻⁴	49.5	9.3
VC 5200	20.5	10.1	-700.0+5690.0i	912.4	0.244	(1-5i)×10⁻⁴	26.2	6.4
VC 2100	20.4	10.0	-1258.4+6960.6i	1125.8	0.356	(1+6i)×10⁻⁴	40.0	14.2
VC 1001	20.7	10.1	-245.4+1989.6i	319.1	0.245	(3+23i)×10⁻⁴	3.1	0.8
NL20	20.5	20.0	-217.7+3343.8i	533.3	0.130	(1+14i)×10⁻⁴	17.9	2.3

Table 3.2 – Poles, first natural frequency of the test specimens, modal loss factor, residue and storage and loss moduli of the resilient materials for $L_{\mathrm{Mat}_1} \approx$20.5 mm.

Material	L_{Mat_1} (mm)	L_{Mat_2} (mm)	Pole Eq. (2.27)	f_1 (Hz) Eq. (2.27)	η_{Mat_2} Eq. (2.28)	Residue r_k	E'_{Mat_2} (MPa)	E''_{Mat_2} (MPa)
VC 6400	976	12.8	-77.7+1000.2i	159.7	0.155	(0+1i)×10⁻⁴	48.8	7.6
VC 5200	976	10.1	-86.5+801.6i	128.3	0.214	(0+1i)×10⁻⁴	24.5	5.3
VC 2100	976	10.0	-161.6-995.3i	160.5	0.321	(0-1i)×10⁻⁴	38.4	12.3
VC 1001	976	10.1	-31.8+280.6i	44.9	0.225	(0+3i)×10⁻⁴	2.9	0.7
NL20	976	20.0	-28.1+480.4i	76.6	0.117	(0+2i)×10⁻⁴	17.3	2.0

Table 3.3 – Poles, first natural frequency of the test specimens, modal loss factor, residue and storage and loss moduli of the resilient materials for L_{Mat_1} =976 mm.

The CCMs tested in this study present considerable damping (see η_{Mat_2} presented in the sixth column, i.e., second shaded column, of Table 3.2 and Table 3.3). This fact justifies the use of the RFP method (see sub-chapter 2.4.6) in the identification process of the modal loss factor η_{Mat_2} and first natural frequency f_1 of the specimen.

Note that in Figure 3.18 and Figure 3.19 the lower and the upper bounds values of the storage modulus E'_{Mat_2} and modal loss factor η_{Mat_2} were determined using test specimens with L_{Mat_1} =976 mm and $L_{\mathrm{Mat}_1} \approx$20.5 mm, respectively.
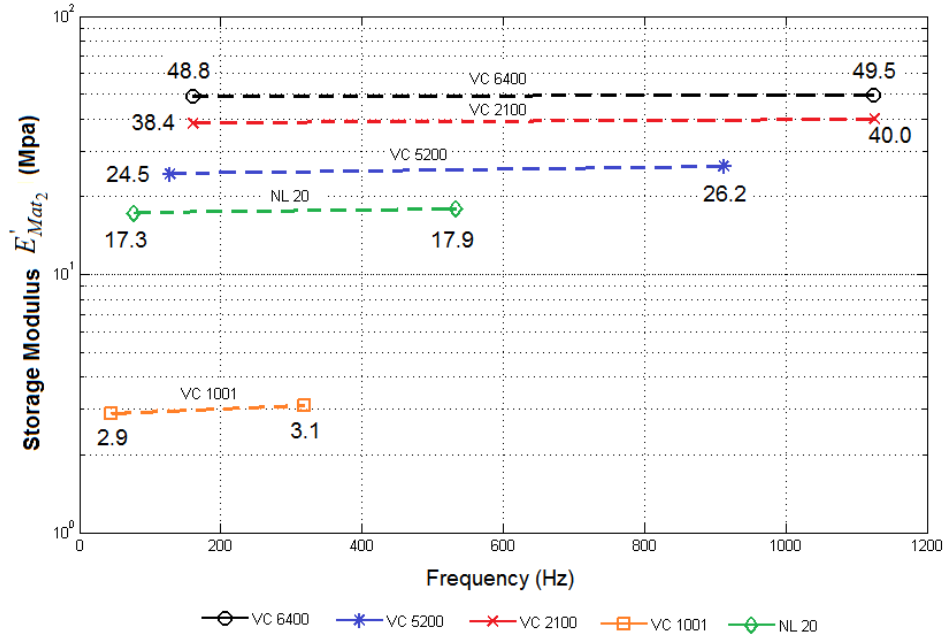
Figure 3.18 – Estimated frequency dependence of the storage modulus E'_{Mat_2} for the tested materials (left points L_{Mat_1} =976 mm and right points L_{Mat_1} =20.5 mm). Each line corresponds to a specific CCM.
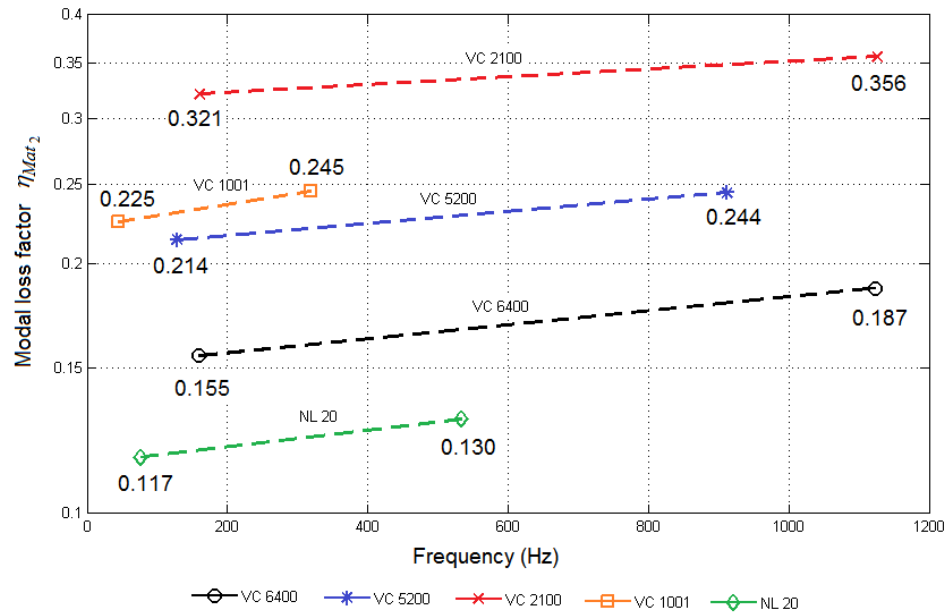
Figure 3.19 – Estimated frequency dependence of the modal loss factor η_{Mat_2} for the tested materials (left points L_{Mat_1} =976 mm and right points L_{Mat_1} =20.5 mm). Each line corresponds to a specific CCM.

In Table 3.4 are presented the frequency dependence of the identified storage modulus E'_{Mat_2} and respective modal loss factor η_{Mat_2} for the tested materials.

	L_{Mat_1} =960 mm			L_{Mat_1} ≈20.5 mm			Slope	
Material	f_1 (Hz)	$E^{'}_{\text{Mat}_2}$ (MPa)	η_{Mat_2}	f_1 (Hz)	$E^{'}_{\text{Mat}_2}$ (MPa)	η_{Mat_2}	$\Delta E^{'}_{\text{Mat}_2}$ (MPa Hz^{-1})	$\Delta \eta_{\text{Mat}_2}$ (Hz^{-1})
VC 6400	159.7	48.8	0.155	1123.9	49.5	0.187	7.26×10^{-4}	3.32×10^{-5}
VC 5200	128.3	24.5	0.214	912.4	26.2	0.244	2.17×10^{-3}	3.83×10^{-5}
VC 2100	160.5	38.4	0.321	1125.8	40.0	0.356	1.66×10^{-3}	3.63×10^{-5}
VC 1001	44.9	2.9	0.225	319.1	3.1	0.245	7.29×10^{-4}	7.29×10^{-5}
NL20	76.6	17.3	0.117	533.3	17.9	0.130	1.31×10^{-3}	2.85×10^{-5}

Table 3.4 – Frequency dependence of the identified storage modulus $E^{'}_{\text{Mat}_2}$ and modal loss factor η_{Mat_2}.

As illustrated by Figure 3.18 and Figure 3.19 and presented in Table 3.4, a low frequency dependence of the identified storage modulus $E^{'}_{\text{Mat}_2}$ and respective modal loss factor η_{Mat_2} is observed for the tested materials. For e.g., $\Delta E^{'}_{\text{Mat}_2}$ =7.26×10^{-4} MPa Hz^{-1} and $\Delta \eta_{\text{Mat}_2}$ =3.32×10^{-5} Hz^{-1} for the VC6400 material.

Tests were conducted at an approximately constant temperature and relative humidity of 20.5 ºC and 40%, respectively. The experimental FRF curves obtained are represented by the dotted-circle line in Figure 3.20 and Figure 3.22.

3.7.2. Validation of the proposed methodology

Having identified the dynamic modulus $E^{*}_{\text{Mat}_2}$, the analytical receptance FRF curves were obtained by solving the forced harmonic vibrations problem, see Eq. (3.13), which was implemented in MATLAB® where the dynamic stiffness matrix $\mathbf{Z}$ is in this case (see Figure 3.3) expressed by Eq. (3.14). The material properties ρ_{Mat_1}, ρ_{Mat_2}, $E^{'}_{\text{Mat}_1}$ and η_{Mat_1} are presented in Table 3.1 whereas, L_{Mat_1}, L_{Mat_2}, $E^{'}_{\text{Mat}_2}$ and η_{Mat_2} are presented in Table 3.2 and Table 3.3.

Even though validation was successfully conducted for all resilient materials, next only are presented the results for the resilient materials VC6400 illustrated by Figure 3.15 a) and VC1001 illustrated by Figure 3.15 d) as they present the main characteristics found in all (see, Appendix A.6 for the other results). The experimental and analytical receptance FRF curves are represented by the dotted-circle and filled lines, respectively, in Figure 3.20 and Figure 3.22. The experimental and analytical receptance FRF curves were then correlated using the FRAC, Eq. (2.59), and the FAAC, Eq. (2.60), assurance criteria and are illustrated by Figure 3.21 and Figure 3.23 by the dotted line and filled lines, respectively.
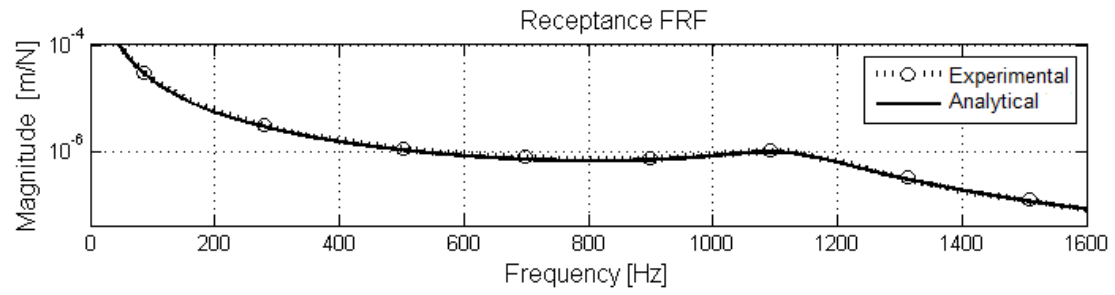
a)
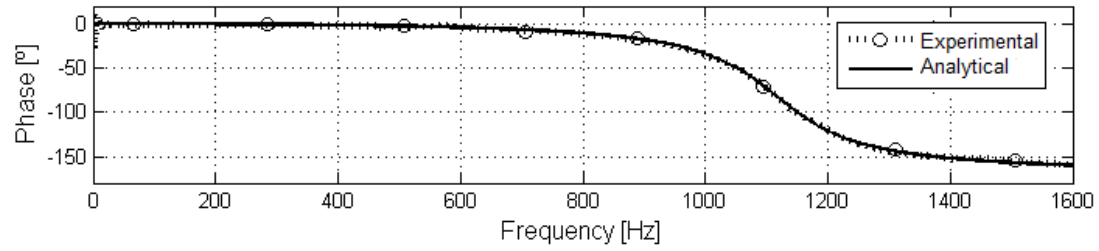
b)

Figure 3.20 – Experimental and analytical FRF curves of test specimen with resilient material VC 6400: a) magnitude; b) phase.
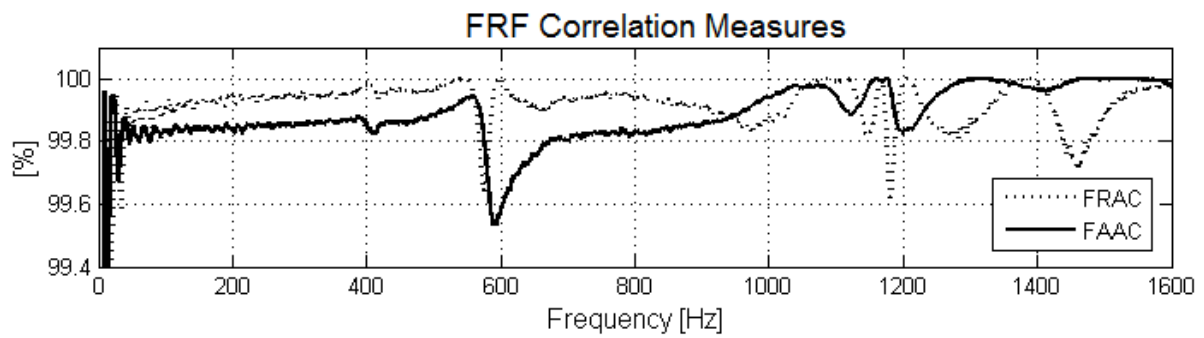
Figure 3.21 – FRF correlation functions curves of test specimen with resilient material VC 6400.

Receptance FRF
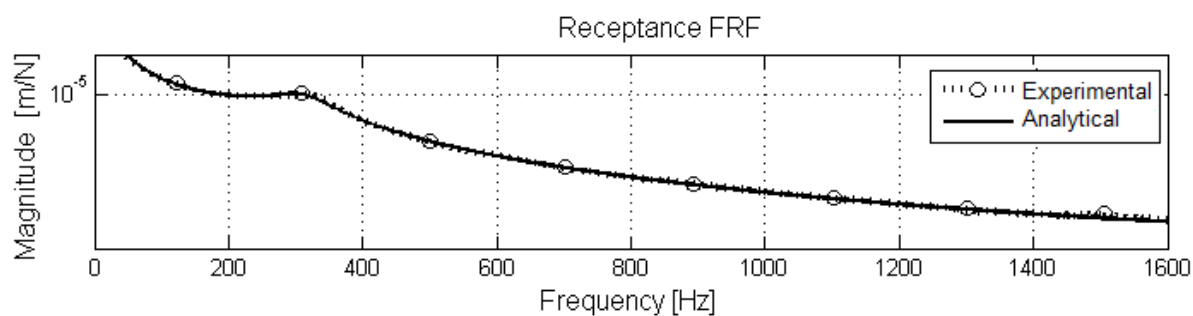
a)
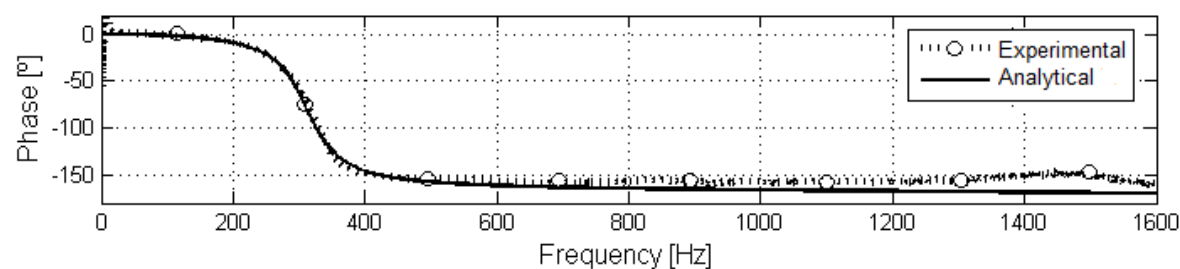
b)

Figure 3.22 – Experimental and analytical FRF curves of test specimen with resilient material VC1001: a) magnitude; b) phase.

FRF Correlation Measures
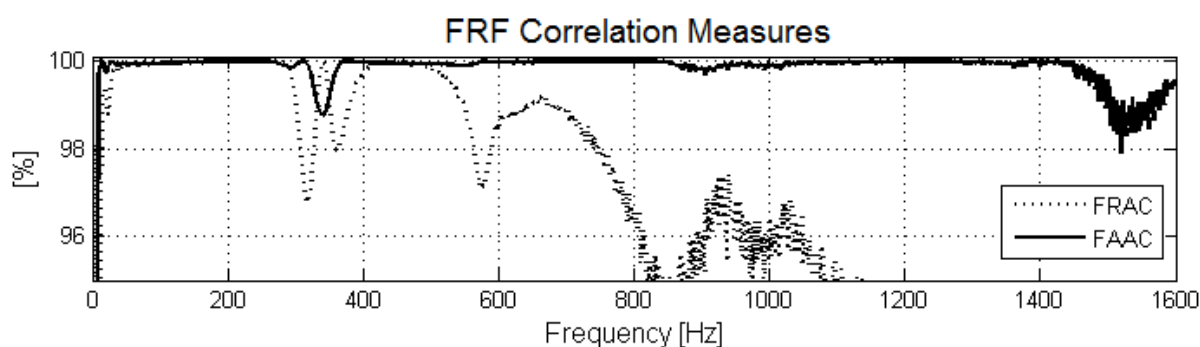
Figure 3.23 – FRF correlation functions curves of test specimen with resilient material VC1001.

The presented analytical and experimental FRF are in a good agreement in terms of magnitude and phase as illustrated by the above figures. Note that similar results have been obtained for the other resilient materials tested. Some discrepancy is noticed for the VC 1001 specimens above 500 Hz, as illustrated by Figure 3.22 and nearby the natural frequency (320 Hz), as illustrated by Figure 3.23. This is justified by the fact that this is a porous CCM, see Figure 3.15 d), that presents more significant storage modulus frequency dependence at higher frequencies (> 500 Hz). Even so, with the proposed methodology it was possible to estimate the dynamic modulus of this porous material. However, and since the dynamic modulus of porous materials is not a topic of this study, reference [133] may be recommended for further details.

The results of the receptance FRF correlation criteria present values above 99.5% and 95% for the FAAC and the FRAC assurance criteria, respectively. The presence of flexural modes is almost

unnoticed in receptance FRF curves. However, their presence is evidentiated by the FRF assurance criteria, e.g., as seen in Figure 3.21 near 600 Hz.

3.7.3. Shear dynamic modulus results

The shear dynamic modulus of elasticity of two CCMs, one cork-rubber VC 6400 illustrated by Figure 3.15 a), and one of cork agglomerate NL20 illustrated Figure 3.15 e) where characterized using the proposed hybrid methodology presented in sub-chapter 3.4. The experimental test specimen is illustrated by Figure 3.6 and consists of a simple three layer bar with extremity layers of steel and an intermediate resilient layer of the material to characterize (in terms of shear dynamic modulus). The extremity layers have known elastic properties E'_{Mat_1} =205 GPa, G'_{Mat_1} =79.2 GPa, and mass density ρ_{Mat_1} =7640 kg m^{-3}. Regarding the resilient layer only the mass density ρ_{Mat_2} are known and are 893 kg m^{-3} and 210 kg m^{-3} for materials VC 6400 and NL20, respectively.

Following the procedures described in sub-chapter 3.4.1 and sub-chapter 3.4.2 for the torsion 1 and torsion 2 cases, respectively, the results presented in Table 3.5 were obtained. For comparison purposes, the values of the longitudinal dynamic modulus (see Table 3.2 and Table 3.3) of the materials subject to shear dynamic modulus characterization, i.e., VC 6400 and NL 20, are also presented.

	Resilient Material	L_{Mat_2} (mm)	f_1 (Hz)	η_{Mat_2}	E'_{Mat_2} (MPa)	G'_{Mat_2} (MPa)	E''_{Mat_2} (MPa)	G''_{Mat_2} (MPa)
Longitudinal	VC 6400	10.0	1123.9	0.187	49.5	-	9.3	-
	NL20	20.0	533.3	0.130	17.9	-	2.3	-
Shear Torsion 1	VC 6400	10.0	106	0.189	-	16.8	-	3.2
	NL20	20.0	57	0.135	-	7.5	-	1.0
Shear Torsion 2	VC 6400	10.0	599	0.189	-	16.9	-	3.2
	NL20	20.0	317	0.135	-	7.6	-	1.0

Table 3.5 – First natural frequency f_1 of the test specimens, modal loss factor η_{Mat_2}, longitudinal storage modulus E'_{Mat_2}, shear storage modulus G'_{Mat_2}, longitudinal loss modulus E''_{Mat_2} and shear loss modulus G''_{Mat_2} of the resilient materials for L_{Mat_1} =20.5 mm.

Having determined the longitudinal E'_{Mat_2} and shear G'_{Mat_2} storage moduli of the resilient materials, see Table 3.5, the bulk storage modulus K'_{Mat_2} (considering an homogeneous isotropic linear elastic material) expressed by Eq. (2.13) and Poisson's ratio ν expressed by Eq. (2.14) were estimated and the respective results obtained are presented in Table 3.5.

Resilient Material	E'_{Mat_2} (MPa)	G'_{Mat_2} (MPa)	ν_{Mat_2} Eq.(2.14)	K'_{Mat_2} (MPa) Eq.(2.14)
VC 6400	49.5	16.8	0.47	308
NL20	17.9	7.5	0.23	11.6

Table 3.6 – Longitudinal E'_{Mat_2}, shear G'_{Mat_2} and bulk K'_{Mat_2} storage moduli and *Poisson's* ratio ν_{Mat_2} of the resilient materials.

The values of the *Poisson's* ratio ν, presented in Table 3.6, are expected in the sense that: VC 6400 is a cork rubber composite material (and the *Poisson's* ratio of rubber is approximately 0.5); NL20 is a cork agglomerate material in which an epoxy resin is used as the agglomerate element (and the *Poisson* ratio of cork is approximately 0).

Having identified the shear dynamic modulus of elasticity $G^*_{\mathrm{Mat}_2}$ (see Table 3.5), the analytical receptance FRF curves were obtained by solving the forced harmonic vibrations problem, see Eq. (3.13), which was implemented in MATLAB® where the dynamic stiffness matrix $\mathbf{Z}$ is in this case (see Figure 3.8) expressed by Eq. (3.20). The material properties ρ_{Mat_1}, ρ_{Mat_2}, and η_{Mat_1} are presented in Table 3.1 whereas, L_{Mat_1}, L_{Mat_2}, G'_{Mat_2} and η_{Mat_2} are presented in Table 3.5 and G'_{Mat_1} =79.2 GPa.

For the torsional case 1 described in sub-chapter 3.4.1, the experimental and numerical receptance FRF curves are represented by the dotted-circle and filled lines, respectively, in Figure 3.24 and Figure 3.26. For the torsional case 2 described in sub-chapter 3.4.2, the numerical and analytical receptance FRF curves are represented by the dotted-circle and filled lines, respectively, in Figure 3.28 and Figure 3.30. The receptance FRF curves were then correlated using the FRAC, Eq. (2.59), and the FAAC, Eq. (2.60), correlation measures and are illustrated by Figure 3.25, Figure 3.27, Figure 3.29 and Figure 3.31 by the dotted and solid lines, respectively.
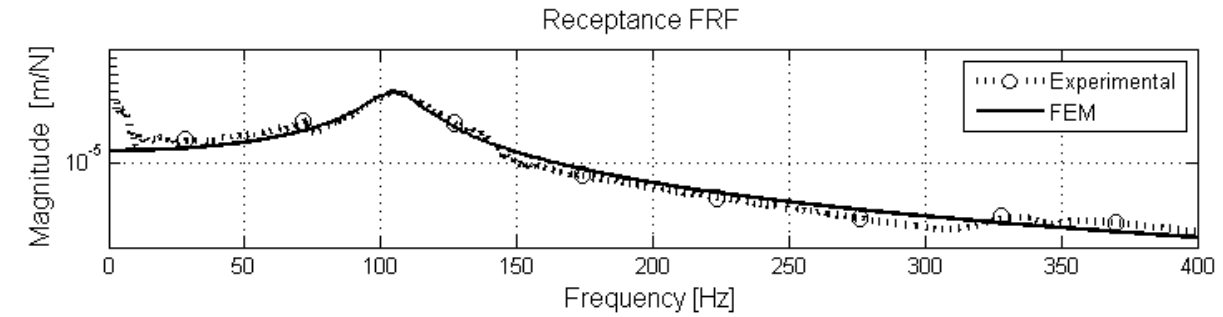
a)
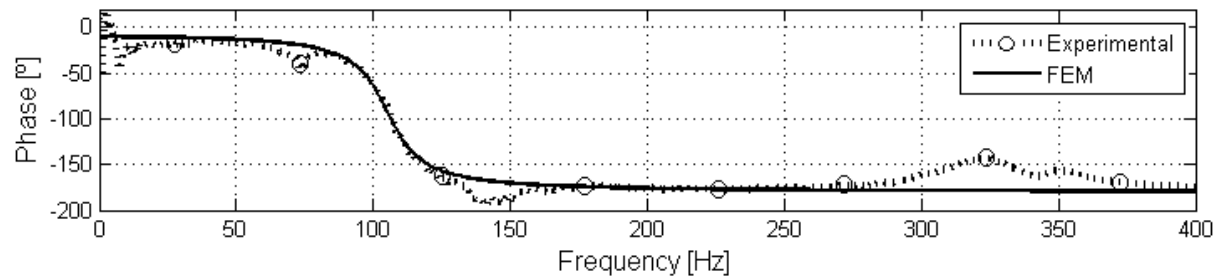
b)

Figure 3.24 – Torsional (case 1) experimental and FE method FRF curves of test specimen with resilient material VC6400: a) magnitude; b) phase.
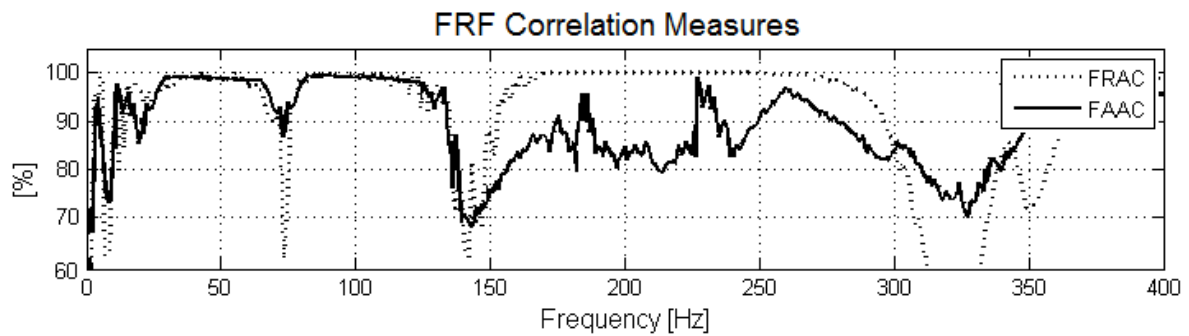
Figure 3.25 – Torsional (case 1) FRF correlation functions curves of test specimen with resilient material VC6400.

a)

b)
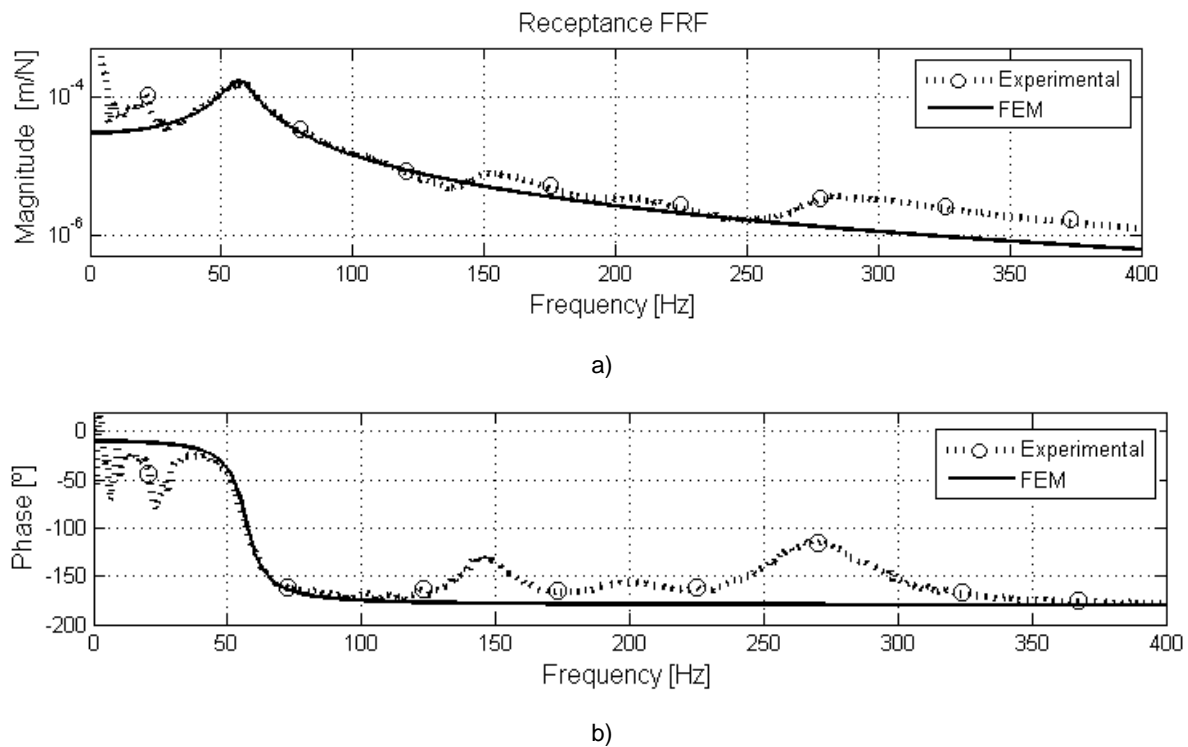
Figure 3.26 – Torsional (case 1) experimental and FE method FRF curves of test specimen with resilient material NL20: a) magnitude; b) phase.
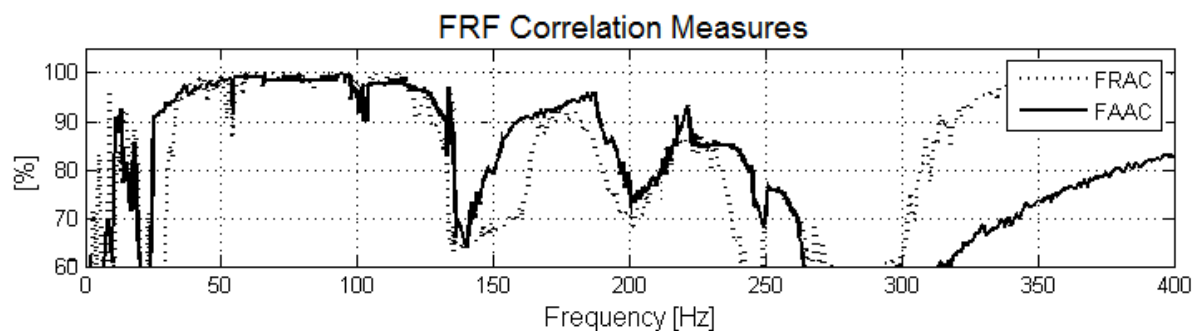
Figure 3.27 – Torsional (case 1) FRF correlation functions curves of test specimen with resilient material NL20.

For the torsional case 1 described in sub-chapter 3.4.1, the FRF curves, see Figure 3.24 and Figure 3.26, illustrate a good agreement in terms of magnitude and phase between the numerical and experimental receptance FRF curves. The results of the receptance FRF correlation functions present mean values above 50% and for the FRAC and the FAAC correlation measures, respectively, in the tested frequency range. However, nearby the resonance values above 90% are obtained for the FRAC and the FAAC correlation measures. The presence of flexural modes are evidentiated by discrepancies in the receptance FRF curves and FRF correlation functions curves, e.g., see Figure 3.25 near 25 Hz and 325 Hz and see Figure 3.27 near 145 Hz and 270 Hz.
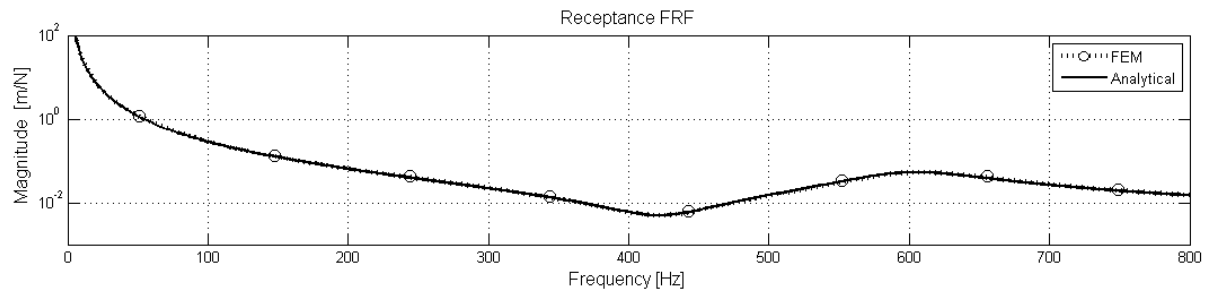
a)
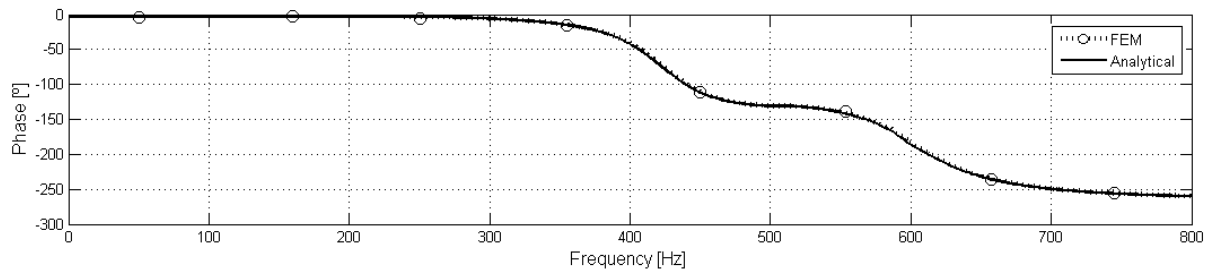
b)

Figure 3.28 – Torsional (case 2) FE method and analytical FRF curves of test specimen with resilient material VC6400: a) magnitude; b) phase.
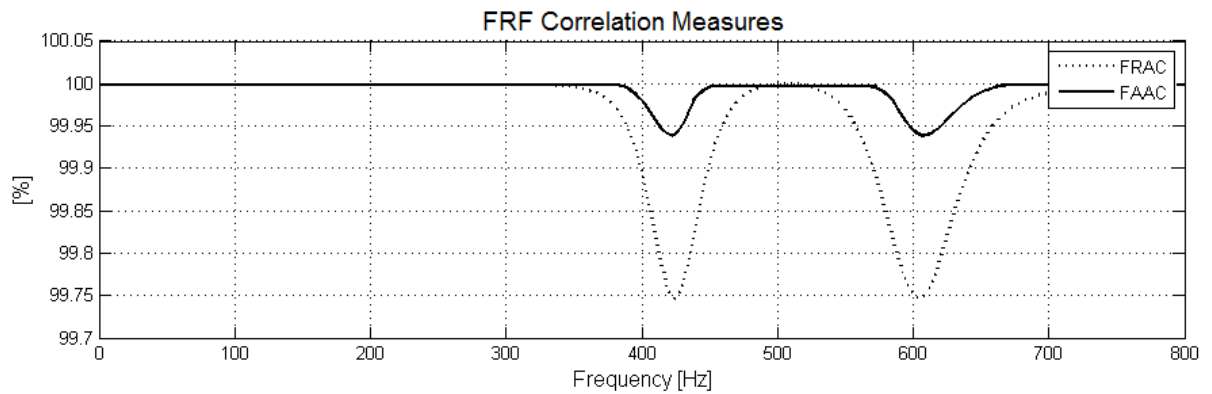
Figure 3.29 – Torsional (case 2) FRF correlation functions curves of test specimen with resilient material VC6400.
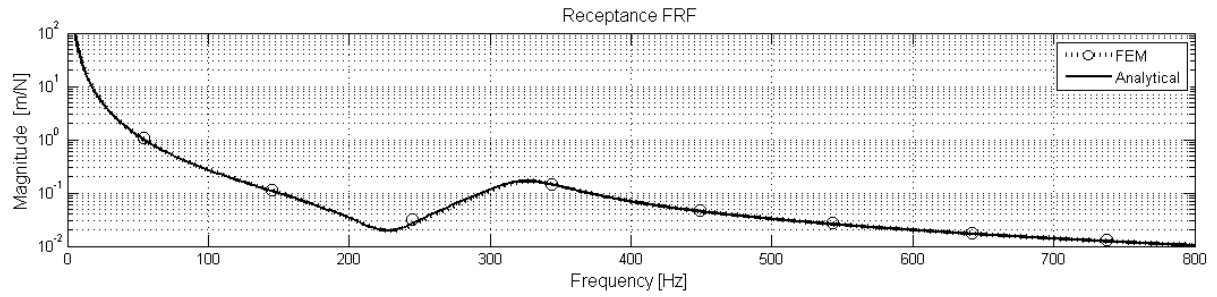
a)
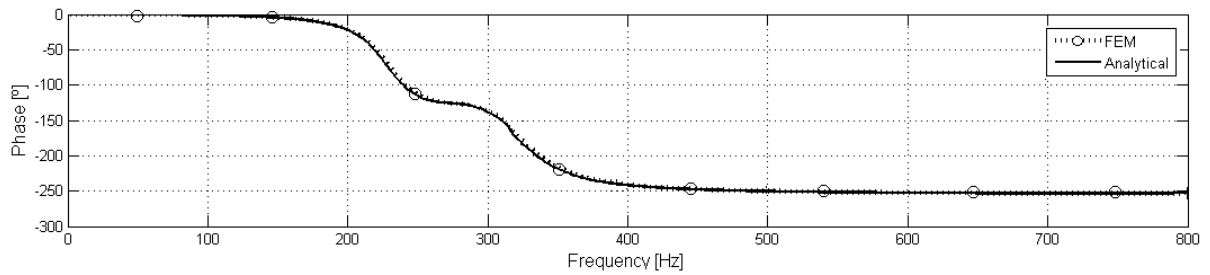
b)

Figure 3.30 – Torsional (case 2) FE method and analytical FRF curves of test specimen with resilient material NL20: a) magnitude; b) phase.
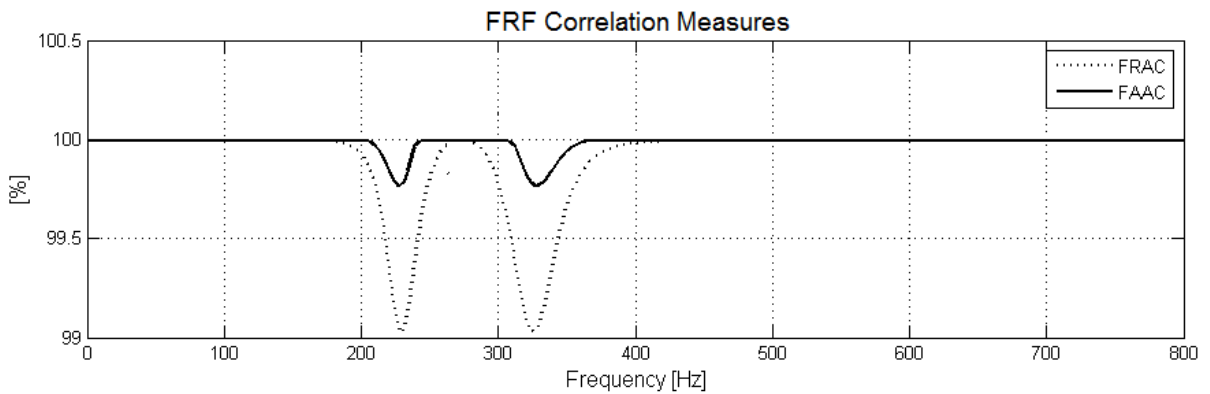
Figure 3.31 – Torsional (case 2) FRF correlation functions curves of test specimen with resilient material NL20.

For the torsional case 2 described in sub-chapter 3.4.2, the FRF plots, see Figure 3.28 and Figure 3.30, illustrate a good agreement in terms of magnitude and phase between the numerical and experimental receptance FRF curves. The results of the receptance FRF correlation functions present values above 99% and 99.9 % for the FRAC and the FAAC correlation measures, respectively. The presence of flexural modes is almost unnoticed in receptance FRF curves.

3.7.4. Dynamic mechanical analysis results

In this study, DMA tests were conducted to simply determine the longitudinal dynamic modulus E^*, i.e., longitudinal storage modulus E' and respective loss factor η, of five CCMs. The DMA test specimens have a rectangular geometry, see Table 3.7 and Figure 3.32, and were tested using the experimental setup described in sub-chapter 3.5.3 for each of the five types of CCMs indicated in sub-chapter 3.6.

Material	VC 6400	VC 5200	VC 2100	VC 1001	NL 20
l_1 (mm)	20.00	20.00	20.00	20.00	20.00
l_2 (mm)	13.95	13.09	14.22	12.58	14.16
h (mm)	3.25	2.22	2.06	3.02	2.03

Table 3.7 – Geometric properties of the DMA test specimens where l_1 is the longer side, l_2 is the shorter side and h is the thickness.

a)   b)   c)   d)   e)
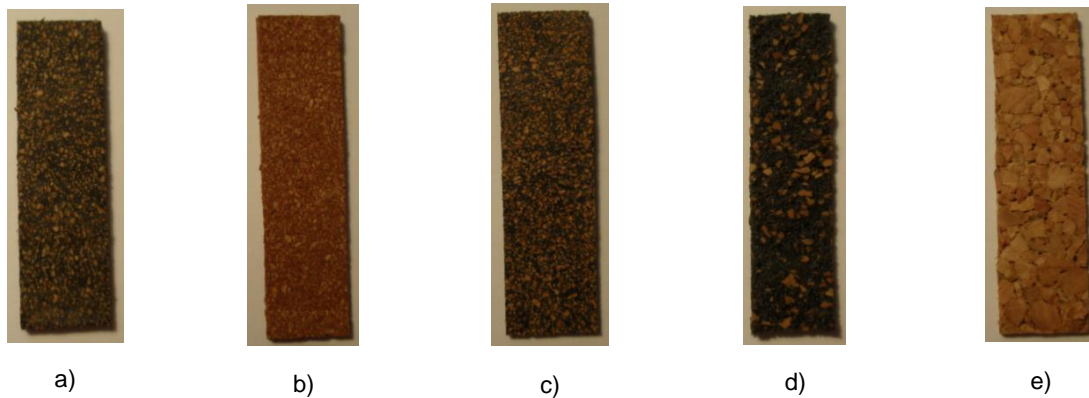
Figure 3.32 – Photographs of the DMA test specimens: a) VC6400; b) VC5200; c) VC2100; d) VC1001; and e) NL20.

The methodology adopted and previously presented in sub-chapter 3.5.2 consists of having a specimen under dual cantilever clamp conditions as illustrated in Figure 3.13 and tested inside a controlled temperature furnace (see label 3 of Figure 3.14), which is initially cooled using liquid nitrogen to a temperature, see Table 3.8, bellow the glass temperature of the material, allowing one to register part of the glassy region and the glass transition region, i.e., to obtain a characterization in the low frequency range.

When that temperature is reached, the specimen is maintained under isothermal conditions for 180 seconds to ensure thermal and mechanical equilibrium after which, the experiment is initialized. Subsequently, the furnace is heated at a rate of 0.05ºC/s that is such that its change per cycle is not significant allowing the specimen to reach thermal equilibrium. The specimen is submitted to an imposed sinusoidal stress, at three different frequencies (1Hz, 3 Hz and 10 Hz). The amplitude of the imposed stress is such that the amplitude of the resultant displacement is about 10μm. The experiment ends when final temperature reaches 150ºC.

Material	VC 6400	VC 5200	VC 2100	VC 1001	NL 20
T_{initial} (ºC)	-80	-70	-50	-80	-50

Table 3.8 – Initial temperatures of the DMA tests for each material specimen.

With this, one obtains the storage modulus $E^{'}$ and loss factor η curves (usually designated as tan delta or $tg\delta$ in DMA), as a function of the temperature, see Figure 3.33 and/or frequency, see Figure 3.34. Even though tests were conducted for all five materials, next are only illustrated the results for the VC 6400 material as it present the main characteristics found in all and avoiding by this way a too extensive illustrated sub-chapter. Nevertheless, further results and illustrations regarding the other materials are presented in Appendix A.7.
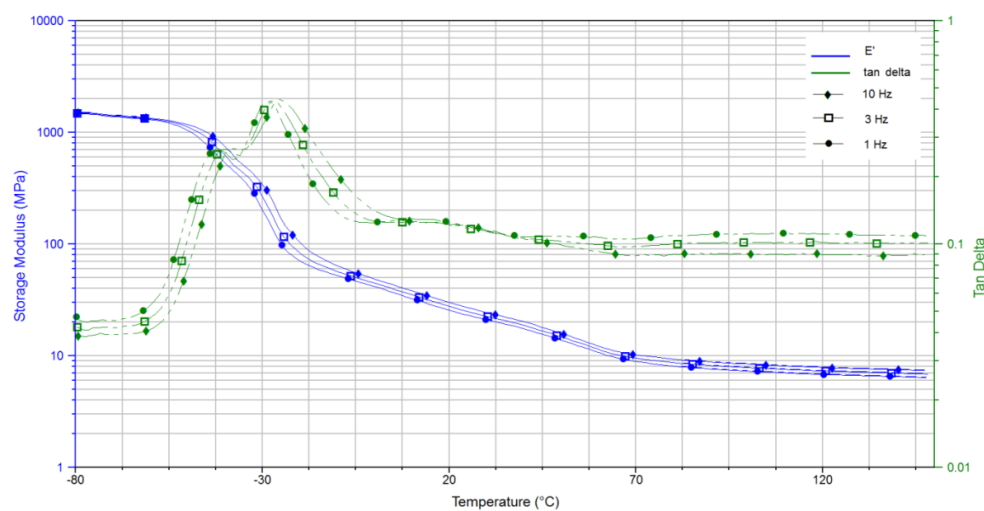
Figure 3.33 – Storage modulus $E^{'}$ and loss factor η curves as a function of the temperature for three different frequencies for material VC 6400 obtained using DMA.
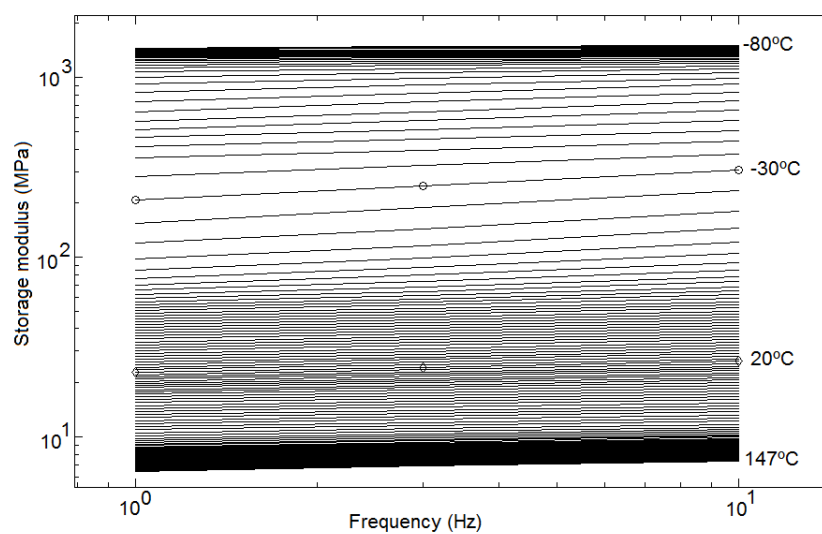
Figure 3.34 – Storage modulus $E^{'}$ as a function of the frequency for different temperatures for material VC 6400.

Using commercial software (TA Instrument Rheology Advantage Data Analysis [131]), the TTS is applied at a reference temperature of 20ºC which, is used to determine the shift factors a_T, see Figure 3.35, that best fit the Arrhenius Equation, see Eq. (3.23), considering an activation energy of H =79.40kJ/mol for the VC6400, leading to the master curves of the storage modulus $E^{'}$ and loss factor η as a function of frequency, as can be seen in Figure 3.36.

It should be noted that the materials tested in this study (CCMs, see Figure 3.15) are essentially two-phase systems (with a polymer and cork matrix) for which the TTS principle does not usually apply. Nevertheless, in this study, the applicability of TTS principle is justified by the fact that the matrix does not undergo significant changes during the DMA test.
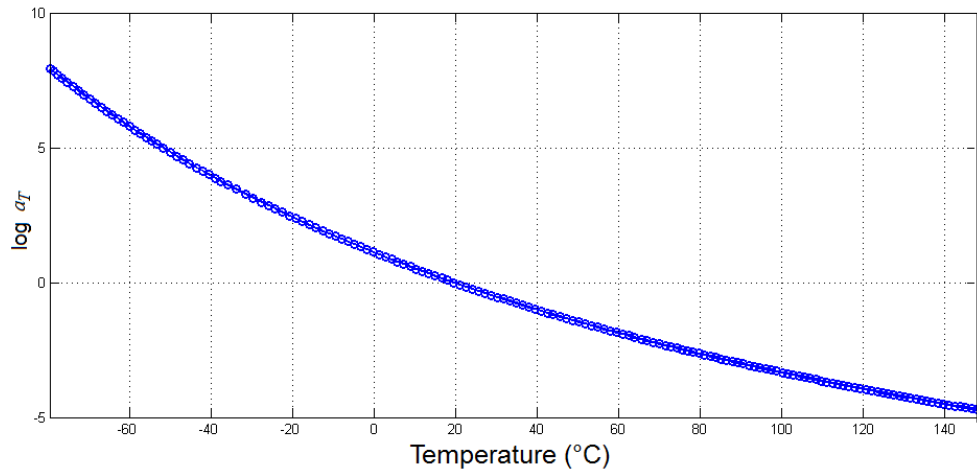
Figure 3.35 – Shift curve as a function of the temperature for material VC 6400.
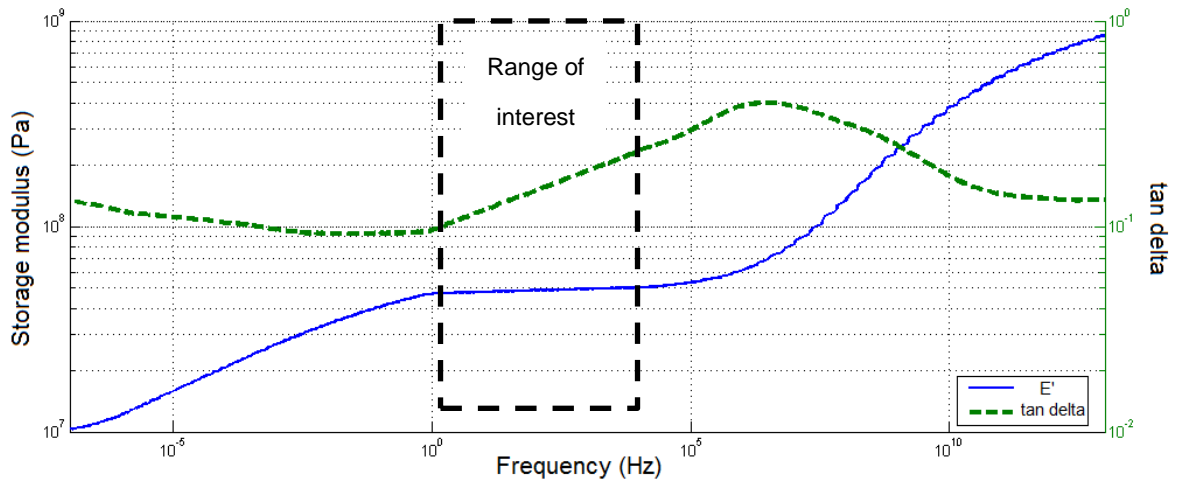
Figure 3.36 – Master curves of the storage modulus $E^{'}$ and loss factor η as a function of the frequency for material VC 6400.

A curve fitting power law with two terms ($y = a\,x^b + c$ where y is the storage modulus $E^{'}$ or loss factor η and x is the frequency) is applied to the curves in the frequency range of interest illustrated

in Figure 3.36 to obtain Figure 3.37 and the analytical expressions, see Table 3.9, that allows determining the storage modulus $E^{'}$ and loss factor η in the interval between 1Hz and 10^4Hz.

For clarification purposes note that Figure 3.36 and Figure 3.37 have different right and left scales. For this reason, in Figure 3.36 the storage modulus $E^{'}$ curve appears bellow the loss factor η curve and in Figure 3.37 it appears above.
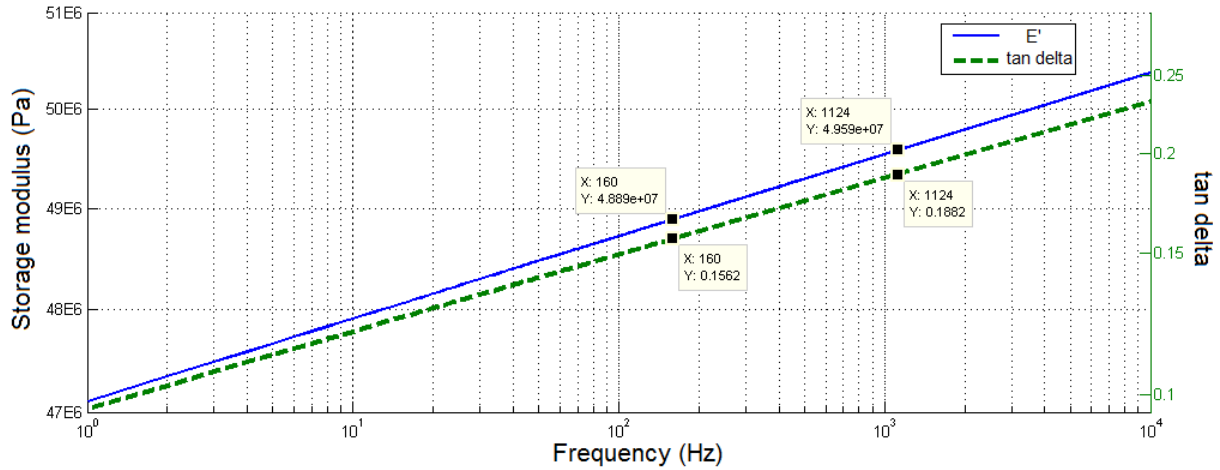
Figure 3.37 – Curve fitting of the master curves of the storage modulus $E^{'}$ and loss factor η as a function of the frequency in the interval between 1Hz and 10^4Hz (on logarithm scale) for material VC 6400.

Figure 3.38 illustrates the same data as Figure 3.37 but in linear scales. Sometimes this is more convenient, e.g., for visualization ease of the frequency dependence of both the storage modulus $E^{'}$ and loss factor η with the increasing frequency.
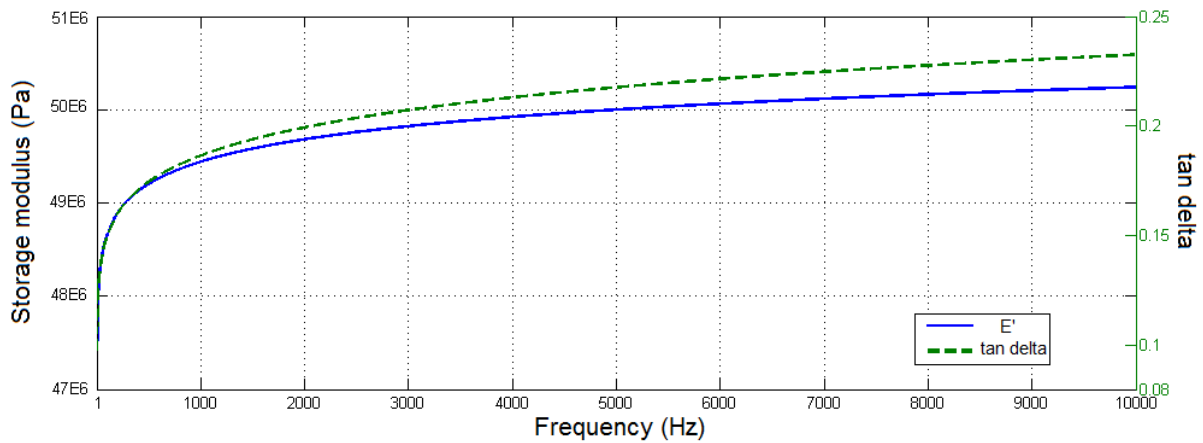
Figure 3.38 – Curve fitting of the master curves of the storage modulus $E^{'}$ and loss factor η as a function of the frequency in the interval between 1Hz and 10^4Hz (on linear scale) for material VC 6400.

As previously stated, only the graphical results for the VC6400 material are presented in the main text as for the remaining materials tested the respective figures are presented in Appendix A.7.

Nevertheless, next are presented the terms of the analytical expression, i.e., the curve fitting power law for the materials tested.

Material	Property	a	b	c	R-square
VC 6400	$E^{'}$	6.871×10^7	4.852×10^{-3}	-2.161×10^7	0.985
	η	0.0996	0.09384	-3.866×10^{-3}	0.998
VC 5200	$E^{'}$	2.124×10^7	0.03348	-4.150×10^5	0.988
	η	0.1748	0.06078	-0.0195	0.995
VC 2100	$E^{'}$	3.296×10^7	0.02547	6.65×10^5	0.985
	η	0.2303	0.05588	0.01603	0.991
VC 1001	$E^{'}$	2.567×10^6	0.03381	-1.076×10^4	0.983
	η	0.1755	0.04648	0.01653	0.989
NL 20	$E^{'}$	1.733×10^6	0.1124	1.447×10^7	0.964
	η	0.09246	0.05423	1.112×10^{-3}	0.961

Table 3.9 – Terms of the analytical expression of the storage modulus $E^{'}$ and loss factor η obtained using a power law $y = a\,x^b + c$ where y is the storage modulus $E^{'}$ or loss factor η and x is the frequency.

By using the analytical expressions of Table 3.9 or by visual observation of Figure 3.37 it is possible to determine the storage modulus $E^{'}$ and loss factor η in the interval between 1Hz and 10^4Hz. Hence, it is now possible to compare these values with those obtained using the proposed analytical-experimental hybrid methodology (see, sub-chapter 3.3).

3.7.5. Result comparison of the identified longitudinal dynamic modulus obtained via dynamic mechanical analysis and via hybrid analytical-experimental methodology

The respective longitudinal dynamic moduli results, i.e., storage moduli $E^{'}$ and loss factors η, of both DMA and the proposed analytical-experimental hybrid methodology for two frequencies (those for which results were obtained using hybrid analytical-experimental methodology) designated as lower and upper frequencies are presented in Table 3.10.

The values of the storage modulus $E^{'}$ and loss factors η (shaded lines of Table 3.10) obtained using DMA were determined by using of the curve fitting power law ($y = a\,x^b + c$ where y is the storage modulus $E^{'}$ or loss factor η, x is the frequency f (second line of Table 3.10) and the constants a, b and c may be found in Table 3.9.

	Material type	VC 6400		VC 5200		VC 2100		VC 1001		NL20	
	Frequency f (Hz)	159.7	1123.9	128.3	912.4	160.5	1125.8	44.9	319.1	76.6	533.3
E' (MPa)	DMA	48.9	49.6	24.6	26.3	38.5	40.1	2.9	3.1	17.3	17.9
	Hybrid M.	48.8	49.5	24.5	26.2	38.4	40	2.9	3.1	17.3	17.9
η	DMA	0.156	0.188	0.215	0.245	0.322	0.357	0.226	0.246	0.118	0.131
	Hybrid M.	0.155	0.187	0.214	0.244	0.321	0.356	0.225	0.245	0.117	0.13
Relative deviations $\left\| \dfrac{y_{\text{DMA}} - y_{HM}}{y_{\text{DMA}}} \right\|$	$y = E'$	0.20%	0.20%	0.41%	0.38%	0.26%	0.25%	0.00%	0.00%	0.00%	0.00%
	$y = \eta$	0.64%	0.53%	0.47%	0.41%	0.31%	0.28%	0.44%	0.41%	0.85%	0.76%

Table 3.10 – Storage modulus E' and loss factor η values obtained via DMA and the proposed hybrid methodology for two frequencies and the respective relative deviations.

Based on the results obtained with the DMA and those obtained using hybrid analytical-experimental methodology, see Table 3.10, Figure 3.39 and Figure 3.40, next are presented the relative deviations of the storage modulus and loss factor, respectively, for the materials tested.
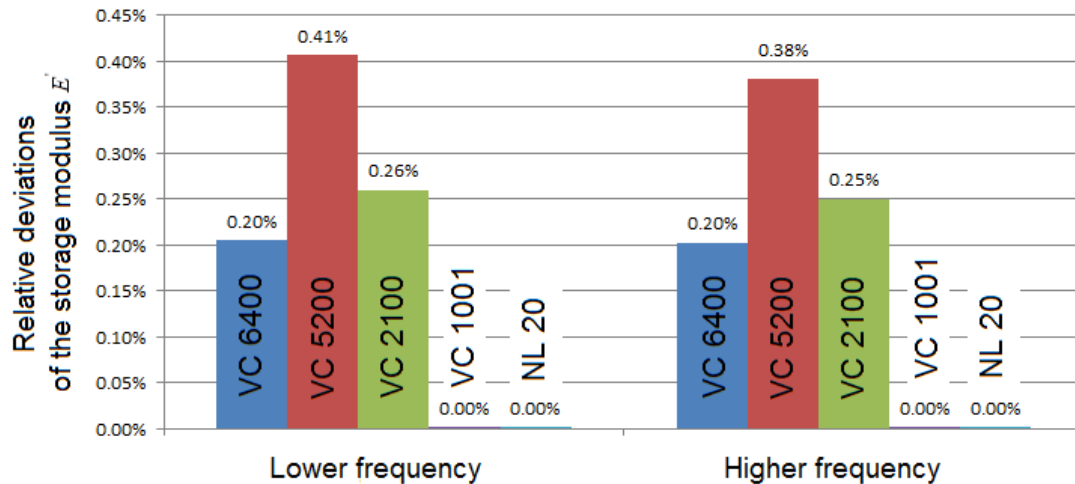
Figure 3.39 – Deviations of the storage modulus obtained via DMA relative to those obtained using the proposed hybrid methodology.
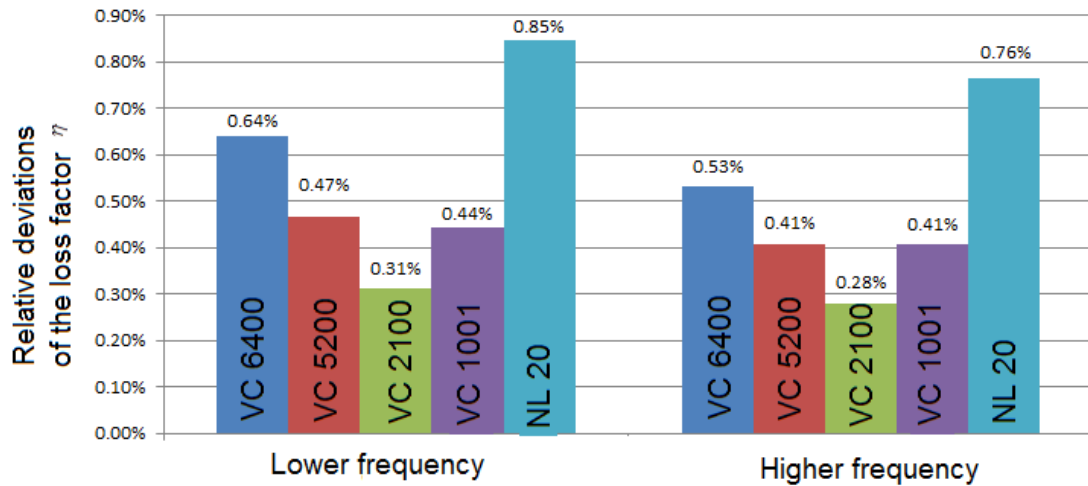
Figure 3.40 – Deviations of the loss factor obtained via DMA relative to those obtained using the proposed hybrid methodology.

As can be seen from Table 3.10, Figure 3.39 and Figure 3.40, the results obtained via DMA are similar to those from hybrid analytical-experimental methodology. The five CCMs tested present deviations less than 0.42% for the storage modulus and 0.86% for the loss factor relative to the results obtained using analytical-experimental hybrid methodology. Thus, the applicability of the TTS procedures may be considered useful under the conditions assumed and for the materials tested in this study.

Based on the R-square values (that measure the goodness of the fit varing between 0 and 1 where 1 is best) of Table 3.9, it is verified in the frequency range between 1Hz and ≈10^4Hz that the storage and loss factor present a frequency dependence which may be modeled using a power law model (with a positive power).

In Table 3.11 are presents the results of the frequency dependence for both the storage modulus E' or loss factor η considering the power law ($y = a\,x^b + c$ where y is the storage modulus E' or loss factor η, x is the frequency f and the constants a, b and c may be found in Table 3.9.

Material type	VC 6400		VC 5200		VC 2100		VC 1001		NL20	
f (Hz)	1	10000	1	10000	1	10000	1	10000	1	10000
E' (MPa)	47.1	50.2	20.8	28.5	33.6	42.3	2.56	3.49	16.2	19.3
η	0.0957	0.233	0.155	0.286	0.246	0.401	0.192	0.286	0.0936	0.153
$\Delta E'$ (MPa Hz^{-1})	3.14×10^{-4}		7.67×10^{-4}		8.72×10^{-4}		9.38×10^{-5}		3.15×10^{-4}	
$\Delta\eta$ (Hz^{-1})	1.37×10^{-5}		1.31×10^{-5}		1.55×10^{-5}		9.38×10^{-6}		5.99×10^{-6}	

Table 3.11 – Frequency dependence of the storage modulus E' and respective loss factor η in the frequency interval between f =1 Hz and f =10^4 Hz.

Thus, and as illustrated by Figure 3.38, the frequency dependence for both the storage modulus $E^{'}$ or loss factor η decreases with the increase in frequency, i.e., high frequency dependence at lower frequencies and low frequency dependence at higher frequencies. Furthermore, in the frequency range between the 1 and 10^4 Hz (see Table 3.11) and for each of the materials tested the storage and loss factor present a low frequency dependence, e.g., $\Delta E^{'}$ =3.14×10^{-4} MPa Hz^{-1} and $\Delta \eta$ =1.37×10^{-5} Hz^{-1} for the VC6400 material.

The results previously presented in Table 3.4, determined using the hybrid analytical-experimental methodology had already indicated for a low frequency dependence for both the storage modulus $E^{'}$ and loss factor η, but in a narrower frequency range than the one now available from DMA tests, i.e., between 1 Hz and 10^4 Hz.

3.8. Conclusions on the characterization of the dynamic modulus

In this sub-chapter are presented the original contributions and main conclusions regarding the characterization of the dynamic modulus conducted on this study.

The first original contribution is the proposed new hybrid analytical-experimental methodology to determine the longitudinal dynamic modulus of resilient materials, e.g., CCMs. It is based on a simple equation from the analytical model of a three-layer specimen (with an intermediate resilient material layer which is the material to be characterized and two steel extremity layers) and on an experimental modal test of the specimen (considering free-free boundary conditions). It also involves the development of a new specimen.

This hybrid methodology has its inherent advantages/disadvantages and limitations as all methodologies do. A list is presented and a brief discussion follows.

Advantages	Disadvantages and limitations
• Simple analytical expression; • Experiment requires only the common equipment found in a vibration laboratory; • Simple experimental setup; • Rigorous results; • Prompt characterization;	• Characterization only at the resonant frequency; • Frequency range limited by the length of the specimens.

This hybrid methodology revealed to be simpler (when compared to other methods) and more rigorous due to the introduction of the analytical equation which, is as simple as the usual formulæ used in this field, presenting a rigorous and more accurate on hand alternative solution when compared to other actual methods, e.g., 2 DOF discrete model and to the Lagragian FE (for which it is necessary to pay special attention to the number of FEs used per wavelength, that increases with frequency).

Note that the modal test requires only the common equipment found in a vibration laboratory, i.e., impact hammer with force transducer, one accelerometer, data acquisition equipment and cables. This is advantageous, as one does not require any special equipment to obtain a prompt dynamic modulus characterization of the materials.

Furthermore, this hybrid methodology avoid geometric constraints, e.g., slender specimens, and boundary condition difficulties, e.g., fixed displacement boundary condition, that is rigorously more difficult (if not even impossible) to obtain in practice than the free boundary condition, found on other tests.

Being this a resonant method, where the characterization is conducted at a resonant frequency, it is possible, by changing the length of the steel extremities, to test and characterize the resilient material at different resonant frequencies. Nevertheless, for higher frequencies (shorter lengths of the steel extremities) it is recommended to use lightweight accelerometers so that their influence (in terms of weight) may be neglected and thus, not accounted for in the model. For low frequencies (long lengths of the steel extremities), the limit is set by the recti-linearity of the specimen.

The second original contribution, and perhaps part of the first, is the development of the hybrid analytical-experimental methodology to determine the shear dynamic modulus of resilient materials. Besides the experimental setup, which is not as simple as in the longitudinal case, the remaining advantages and all the disadvantageous and limitations are verified.

Furthermore, and regarding the shear dynamic modulus characterization, besides DMA techniques, there is a considerable lack of work and development of characterization methodologies in the scientific literature.

DMA test, that requires specific dedicated equipment as well as liquid nitrogen for characterization at low frequencies, were conducted in this study and allowed characterizing the longitudinal dynamic modulus for several frequencies and temperatures per test (reason why it was more time consuming $\approx$ 80 minutes per test).

The results obtained via DMA verify, in the sense that they are in agreement with, the ones obtained using the proposed hybrid analytical-experimental methodology. Furthermore, and as already indicated by the results obtained by the hybrid analytical-experimental methodology but for a narrower frequency range, DMA results show low frequency dependence for both the storage modulus $E^{'}$ and loss factor η, in a wider frequency rage, i.e., between 1 Hz and 10^4 Hz.

Thus, and for all the reasons previously mentioned, the hybrid analytical-experimental method here presented is a tool that allows for a rigorous and prompt characterization of the longitudinal and shear dynamic moduli, and with it, the bulk modulus and *Poisson's* ratio of resilient materials (under the assumption of the homogeneous isotropic linear elastic material behavior, which is a simplification).

It should be noted that even though the temperature and humidity effects were not considered in this study for the proposed hybrid method, the respective values were registered at the time of the tests. Thus, studying how the effect of changes in the temperature, humidity, age of the materials,

amount of overload, among other parameters, influence the dynamic modulus of the materials is suggested for future works.

Altogether, the hybrid analytical-experimental method is one of the main original contributions of this study. Note that it was motivated by the fact that the dynamic properties of CCMs were usually inaccessible in spite of being essential for the development and validation of the numerical models which, simulate the dynamic behavior of structures that in one way or another use these types of materials, e.g., phononic-inspired vibration isolators.

Chapter 4

Phononic-inspired vibration isolator

4.1. Introduction

Similarly to the semiconductor in which electrons can only occupy certain energy bands, and to photons (quantum of electromagnetic energy) in photonic crystals [134] where electromagnetic waves can only propagate in certain frequency ranges, one can also idealized structures in which phonons (quantum of vibrational energy) propagate only in certain frequency ranges that, by analogy with the previous may be designated as phononic crystals. It uses the characteristics of the dispersive medium relatively to elastic waves. Hence, the frequency range where the phonons are not allowed to propagate is usually designated as a bandgap (also referred to as a stopband) which, is formed due to periodical change in the mass density and/or elastic constants of the materials, i.e., due to the periodical changes in wave phase velocity in the structure.

Phononic structures are raising nowadays a considerable interest and expectation in many promising areas of science and in particular for engineering applications. Namely, in wireless communications by developing frequency sensors [135]; semiconductor to control the thermal transport at the nano-scale [136]-[137], in the vibration isolation of systems of micro-electro-mechanical components [138] or in buildings [139]; in acoustics with the development of an acoustic shield to block radar signals and sonar [140], and in opto-mechanics with the development of invisible and silent materials [141], among others.

Within this context and in this chapter (in which all contents are original contributions from this study except when referenced to the respective authors), is presented a study in which the analysis, design, prototyping and experiments of 1D PIVI, previously introduced as (phononic-inspired vibration isolator) with alternating layers of two materials (where each two successive layers can be regarded as a cell) with a significant contrast in the wave phase velocity. Such a contrast associated with the adequate length of the cell (thickness of the layers) allows for vibration isolation in a relatively low and wide frequency range that is of high interest for several mechanical applications, and which up to date and to the knowledge of the author has not yet been sufficiently explored in the field of phononics.

To determine the location and width of the bandgaps, a computational component is explored to develop the analytical and numerical models used in simulation, which revealed to be strategic for prototyping and experimentation. Furthermore, the computational component is also essential when recurring to the *Bloch* wave theory [53], in which the dispersion equations are used to determine the

location and width of the bandgaps in frequency for structures with infinite periodicity (infinite periodic structures), and allowing extrapolating for the particular case of finite periodicity (finite repetitive structures). For the finite structure, it is verified that with only two or three cells (depending on materials) relatively strong ARs were obtained instead of bandgaps [142]-[143] at the same frequency ranges. Thus, it is possible to numerically predict the location and width of the ARs in frequency, which in this study is validated with the subsequent application to finite repetitive structures.

Similarly to the bandgaps, the ARs are formed due to the abrupt change in the wave phase velocity of the two materials that comprise the structure. Thus, an algorithm is developed for selection of the pair of material and for their optimal proportion within the cell to obtain a finite repetitive phononic-inspired structure with the intended width and location (in frequency) of the AR.

From an abundant material diversity, the selection of the pair of materials and the respective proportions in the cell (each pair is a cell) is made taking into account the following requirements: 1) solid materials; 2) materials which have a high contrast in the wave phase velocity, allowing obtaining ARs in frequency ranges that are useful for several mechanical applications; 3) materials which allow for periodic structures in the range of centimeters, to simplify the construction of the prototypes and the execution of experimental tests and; 4) materials easily accessible both in terms of logistics and monetary cost.

Thus, the pairs of selected materials are steel and CCMs such as cork-rubbers and cork agglomerates. However, with the choice of CCMs emanates a new and unexpected challenge. Despite the high diversity of CCMs in the market, differing in mass density of cork and/or agglomerate, grain size and binder resin [32], it is noted that their dynamic properties are rarely known, in which (and surprisingly enough) the static properties are often misused, as stated by the author and other researchers [34].

Since cork presents a viscoelastic behavior [38] the dynamic modulus of elasticity differs from the static modulus, which is usual for these kind of materials. The dynamic modulus is a complex quantity [8], in which the real component is designated as the storage modulus (accounts for the elastic energy stored), and an imaginary term, designated as the loss modulus (accounts for the dissipated energy), see sub-chapter 2.1.1.

There are several methods available to characterize the dynamic properties of viscoelastic materials, see sub-chapter 3.1. However, when dealing with CCMs there are some difficulties in meeting the specifications related to the experimental clamped boundary condition due to the low density and stiffness of some of the CCMs.

To avoid these difficulties, the author proposed in chapter 3 a new hybrid analytical-experimental methodology for the characterization of the dynamic modulus for these types of CCMs (although it can also apply to other materials), see sub-chapter 3.3 for more details. The method consists of experimental testing of a specimen (under free-free boundary conditions, avoiding difficulties associated with the boundary conditions used in other methods), in the numerical implementation of a numerical method for modal identification in the frequency domain, see sub-chapter 2.4.6, and solving an equation to identify the dynamic modulus.

Once the dynamic modulus of the chosen materials that form the periodic structure are known, the study of the PIVI for the isolation of vibrations in frequency ranges of interest can be conducted.

The results obtained in this study verify the validity of the extrapolation of the infinite periodic to the finite repetitive medium considering three or more cells as previously verified by Jensen and Pedersen in [144]-[145]. Through the algorithm developed for the selection of the pair of materials and the optimization of their proportions (thickness of the layers) it was possible to obtain a solution that contemplates the use of different pairs of steel and CCMs. Using the hybrid analytical-experimental method it was possible to characterize the longitudinal and shear dynamic moduli of various CCMs.

Through the interconnection between the symbolic and numeric computation with numerical methods, optimization techniques and the experimental modal analysis, reside the main tools used in this study to design several PIVIs with ARs situated in different frequency ranges of interest.

Furthermore, a practical application regarding the suspension of the motors used in hermetic compressors is addressed. Originally, helical spring are used as supports. However, these may present undesirable vibration transmissibility to the carcass at certain frequencies, and consequently undesirable noise to the environment. The aim is to test the application of a PIVI, as presented here. Additionally, the possibility of combining these isolators with the spring in order to maintain the flexibility of the support in which the PIVI acts as a filter, is also presented

4.2. Phononic devices

Phononic crystals may be conceptualized as (micro) structures composed of numerous cells (composed of two materials) arranged accurately (or with some defects) and repeatable in space, leading to some ideal order and symmetry as illustrated by Figure 4.1. Due to the periodical change in mass density and/or elastic constants (i.e., on the wave phase velocity through the cells in the crystal) and making use of the fundamental properties of waves (namely, scattering and interference), it is possible to create in a periodic structure/media forbidden bands (also referred to as bandgaps and stopband), i.e., ranges of frequencies within which the phonons (mechanical waves) do not propagate.

1D   2D   3D

a)   b)   c)
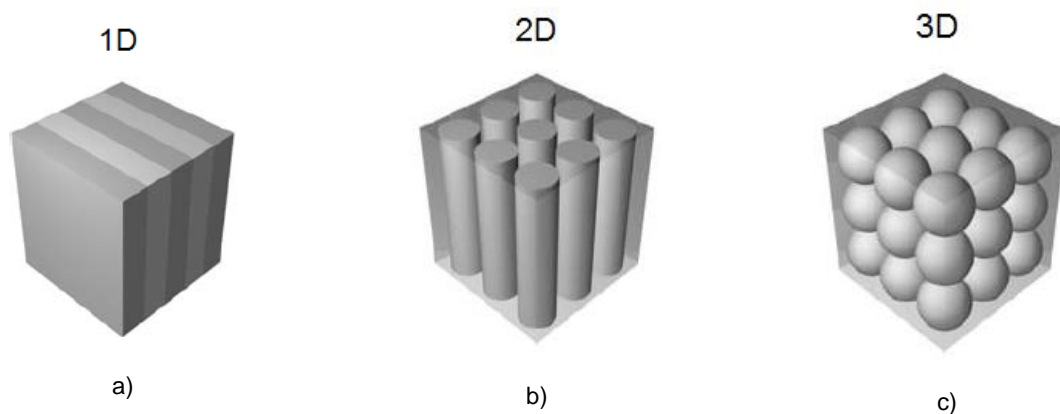
Figure 4.1 – Examples of phononic crystals with one, two and three dimension periodicities: a) 1D crystal consisting of alternating layers of two materials with different mechanical properties; b) 2D crystal consisting of parallel cylinders of a material inserted in another material with different mechanical properties; c) 3D crystal consisting of one material spheres embedded in another material with different mechanical properties [134].

Note that one of the differences between mechanical waves and electromagnetic waves is the fact that mechanical waves cannot propagate in a vacuum thus necessitating a medium for propagation.

The propagation of 1D longitudinal mechanical waves is typically described by a dispersion relation that relates the frequency ω and wavenumber k. For the homogeneous case this relationship is expressed by

$$k = \omega \, c^{-1} \tag{4.1}$$

where c is the wave phase velocity in the medium. However, the dispersion relations for materials that are not homogeneous, such as phononic crystals (see Figure 4.1), are not so simple as will be shown.

4.3. Bloch wave analytical model for structural analysis

Hence, consider a piecewise heterogeneous bar, i.e., material properties are dependent of the position along the axial direction as illustrated by Figure 4.2. The bar has a uniform transversal sectional area A and parallel alternating layers of two materials, with longitudinal dynamic moduli of elasticity $E^*_{\mathrm{Mat}_1}$ and $E^*_{\mathrm{Mat}_2}$, mass densities ρ_{Mat_1} and ρ_{Mat_2} and lengths L_{Mat_1} and L_{Mat_2}.
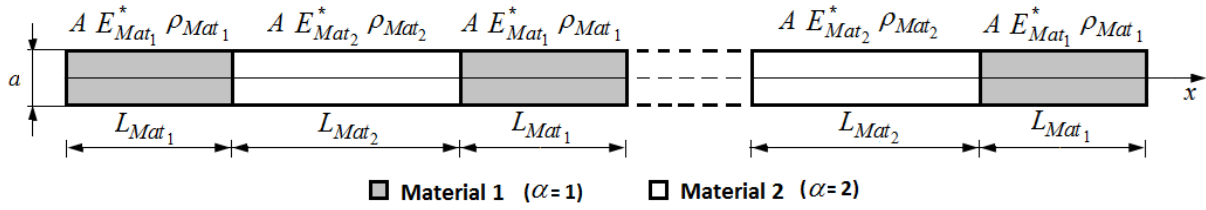
Figure 4.2 – 1D uniform periodic bar composed of two materials.

So being, the 1D forced harmonic longitudinal vibrations (where the wavelength λ of the stationary waves in the dynamically and longitudinally loaded bar is much longer than the characteristic transverse dimension h of the bar, see sub-chapter 2.5.2.4 and [104], [121] and [122] for more details) Eq. (2.41) may be rewritten for each material layer Mat_α, where α is layer's type number, as

$$E^*_{Mat_\alpha} A \frac{\partial^2 u_{Mat_\alpha}(x,t)}{\partial x^2} - \rho_{Mat_\alpha} A \frac{\partial^2 u_{Mat_\alpha}(x,t)}{\partial t^2} = 0 \qquad \alpha = 1,2. \tag{4.2}$$

where, $E^*_{\mathrm{Mat}_\alpha}$ is the corresponding longitudinal dynamic modulus of elasticity, $\rho_{\mathrm{Mat}_\alpha}$ is the corresponding mass density and $u_{\mathrm{Mat}_\alpha}(x,t)$ is the corresponding displacement response at the longitudinal coordinate x and time t.

4.3.1. Infinite periodic two-material layer bar

From the *Bloch* wave theory [53] it is known that due to the periodicity of the infinite structure, the natural modes of such structure may be characterized by using wave number k and assuming that displacement in the cell is expressed by

$$u_n(x) = u_0(x - nL) e^{i(knL)}, \qquad n = 1, 2, \quad i = \sqrt{-1}, \tag{4.3}$$

where n is the total number of the cells, $L = L_{\text{Mat}_1} + L_{\text{Mat}_2}$ is the length of the cell and u_0 is the periodic solution, i.e., $k = 0$. Thus, the dispersion equation is a function of the wave number and may be expressed as [56]

$$k = \frac{1}{L} \arccos \left[\cos\left(k_{\text{Mat}_1} L_{\text{Mat}_1}\right) \cos\left(k_{\text{Mat}_2} L_{\text{Mat}_2}\right) \right.$$
$$\left. - \frac{1}{2} \left(\frac{k_{\text{Mat}_1}}{k_{\text{Mat}_2}} + \frac{k_{\text{Mat}_2}}{k_{\text{Mat}_1}} \right) \sin\left(k_{\text{Mat}_1} L_{\text{Mat}_1}\right) \sin\left(k_{\text{Mat}_2} L_{\text{Mat}_2}\right) \right], \tag{4.4}$$

where k_{Mat_1} and k_{Mat_2} are the wave numbers in the respective materials expressed as $k_{\text{Mat}_\alpha} = \omega \, c_{\text{Mat}_\alpha}^{-1}$ where $c_{\text{Mat}_\alpha} = \left(E_{\text{Mat}_\alpha}' \rho_{\text{Mat}_\alpha}^{-1} \right)^{1/2}$ is the wave phase velocity and α is the type of material.

From Eq. (4.4) it is possible to determine for the infinite layer bar the wave number k versus frequency ω. For frequency values ω that make the wave number k complex, the amplitude of the displacements is exponentially attenuated. Thus, the frequency ranges where k is complex are bandgaps (stopbands) while the frequency ranges where k is real bands are passbands.

It is common to plot the frequency versus wavenumber as illustrated by Figure 4.3, in which the respective dispersion curves for the (k, ω) domain are presented.
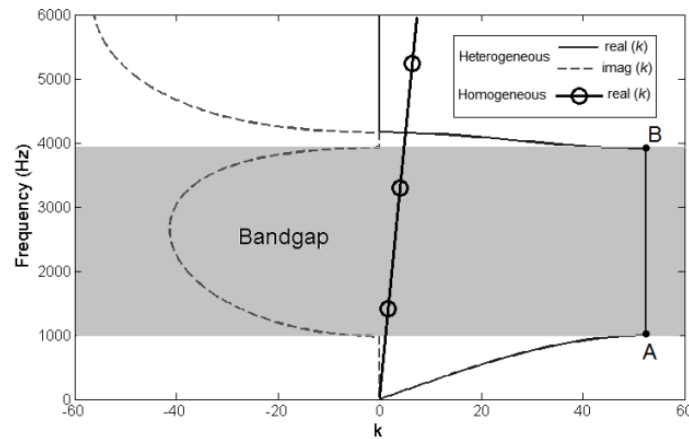
Figure 4.3 – Dispersion curves obtained from homogeneous Eq. (4.1) and heterogeneous Eq. (4.4).

From Figure 4.3 it is possible to observe that the heterogeneous two-material layer structure presents a bandgap (the grey shaded area corresponds to the first bandgap) when the wave number, k, is complex. On the other hand, for the homogeneous structure the wave number is always real, i.e, no bandgap exists.

For an intuitive understanding of how bandgaps exist, consider a 1D periodic bar, as illustrated by Figure 4.2, composed of infinite alternating layers of two different materials with longitudinal storage moduli of elasticity E'_{Mat_1} and E'_{Mat_2}, mass densities ρ_{Mat_1} and ρ_{Mat_2} and lengths L_{Mat_1} and L_{Mat_2}. At every interface, an incoming wave transfers part of its energy into secondary, reflected waves, which then interfere with each other [134]. If this interference is destructive, all the energy of the original wave is reflected back and the wave cannot propagate through the crystal resulting in the creation of a bandgap (stopband). On the other hand, if the interference is constructive, then all energy of the original wave is transmitted through the crystal leading to the formation of propagation bands (passbands).

4.3.2. Finite periodic two-material layer bar

For the finite repetitive structure, consider the 1D finite two-material layer bar model (identical to that presented in sub-chapter 3.3.1 and here summarized for presentation ease) with uniform transversal sectional area A, as illustrated in Figure 4.4, with parallel alternating layers of two materials, with longitudinal storage moduli of elasticity $E^*_{\mathrm{Mat}_1}$ and $E^*_{\mathrm{Mat}_2}$, mass densities ρ_{Mat_1} and ρ_{Mat_2} and lengths L_{Mat_1} and L_{Mat_2}.
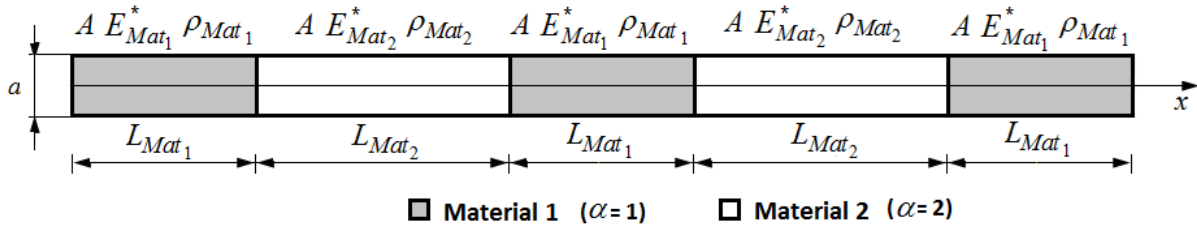
Figure 4.4 – 1D Finite uniform periodic bar composed of two materials.

So being, the 1D forced harmonic longitudinal vibrations, see Eq. (2.41), of a piecewise heterogeneous bar, see Eq. (4.2), may be expressed, when damping is not considered (which is only valid for frequency independent or weakly frequency dependent materials [88]) by Eq. (3.3).

The analytical FRF curve may be obtained by solving the forced harmonic vibration problem expressed by Eq. (3.3). Using the dynamic stiffness matrix $\mathbf{Z}$ expressed by Eq. (3.10), one obtains for each applied frequency ω_{ap} the following system of linear equations

$$\mathbf{Z}(\omega_{\mathrm{ap}})\ \mathbf{U} = \mathbf{F}_0, \tag{4.5}$$

where $\mathbf{F}_0$ is the amplitude vector of the nodal applied harmonic force (at same excitation frequency) and $\mathbf{U}$ is the vector that defines the nodal displacement response.

4.4. Finite element model

In terms of FEs, the finite repetitive structure is modeled using a two node bar finite FE (see sub-chapter 2.5.2.4). The dynamic stiffness $\mathbf{K}_{el}^*$, and mass $\mathbf{M}_{el}$ matrices and force vector $\mathbf{F}_{el}$ of a FE with length L are

$$\mathbf{K}_{el}^* = \frac{E_{el}^* A}{L}\begin{bmatrix} 1 & -1 \\ -1 & 1 \end{bmatrix}, \quad \mathbf{M}_{el} = \frac{\rho_{el} A L}{6}\begin{bmatrix} 2 & 1 \\ 1 & 2 \end{bmatrix}, \quad \mathbf{F}_{el} = \begin{Bmatrix} F_1 \\ F_2 \end{Bmatrix} e^{i\omega_{ap}t}, \tag{4.6}$$

where F_1 and F_2 are the amplitude of the nodal forces attributed to the respective element. Then, the element dynamic stiffness matrix is expressed as

$$\mathbf{Z}_{el} = \mathbf{K}_{el}^* - \omega^2 \mathbf{M}_{el}. \tag{4.7}$$

4.5. Prototypes

The experimental models, also referred to as prototypes along this chapter (see Figure 4.5), are composed of alternate layers of two materials (each pair of layers is called a cell). The prototypes may differ depending on: the type of materials used in the cell; the lengths of each material and; the number of cells.
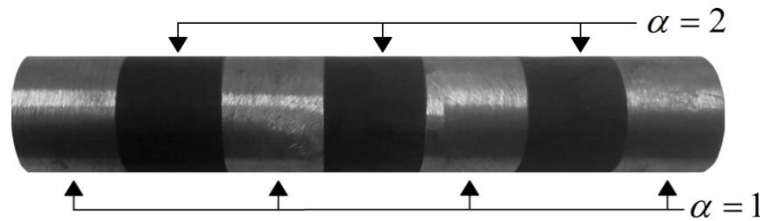
Figure 4.5 – Photograph of a prototype with 3.5 cells and $L_{Mat_1} = L_{Mat_2} = 20\,\text{mm}$, where $\alpha = 1$ indicates steel and $\alpha = 2$ indicates the resilient material.

A two component epoxy adhesive, with a cure time of approximately five minutes is used to join the material layers along the structure (see procedure in Appendix A.5). A study to determine the effect of the adhesive layer in the structure was conducted concluding that the adhesive layer has negligible influence for thicknesses less than about 50 microns [44]. Note that no special care is needed to ensure the thickness of the adhesive, just a minimum amount of adhesive is used to uniformly fill the surfaces to be joined.

Each prototype is subject to experimental modal analysis from which the respective FRF curves are obtained and subject to analysis.

4.6. The experimental setups to obtain the frequency response function curves

The experimental setup used to obtain the receptance FRF curves from the prototypes follows that presented in subchapter 3.3.7 and illustrated by Figure 3.7 where the only difference is the prototype.

Regarding the experimental setup used to obtain the force transmissibility curves of the prototypes, there are two configurations that essentially differ in the number of prototypes (i.e., one or three as illustrated by Figure 4.6 and Figure 4.7, respectively) that are used to support a load mass. The load mass is a portion of a cylindrical aluminum rod with a diameter of 150 mm, a length of 65 mm and a mass of approximately 3.2 kg. This value is similar to the mass of the motor of the hermetic compressor that is later addressed when considering these devices in a real industrial application. Furthermore, note that the supporting configurations may vary between helical springs, PIVI and a combination of both, which is the case illustrated in Figure 4.7.

In either case it may be described as: a signal is generated and transmitted to the vibration exciter (Brüel&Kjaer 4808) which is suspended from a fix support by metallic chains. The force effectively applied to a load mass (input signal) is measured through a force transducer (PCB 208C01). The dynamical deformation propagates throughout the prototype and, at the opposite extremity, force transducer(s) (PCB 208C01) measures the force effectively transmitted to the foundation (output signal).

The input and output signals are acquired using a data acquisition unit (Brüel&Kjaer 3560D) and analyzed (Bruel&Kjær analysis software PULSE® LabShop Version 6.1.5.65).
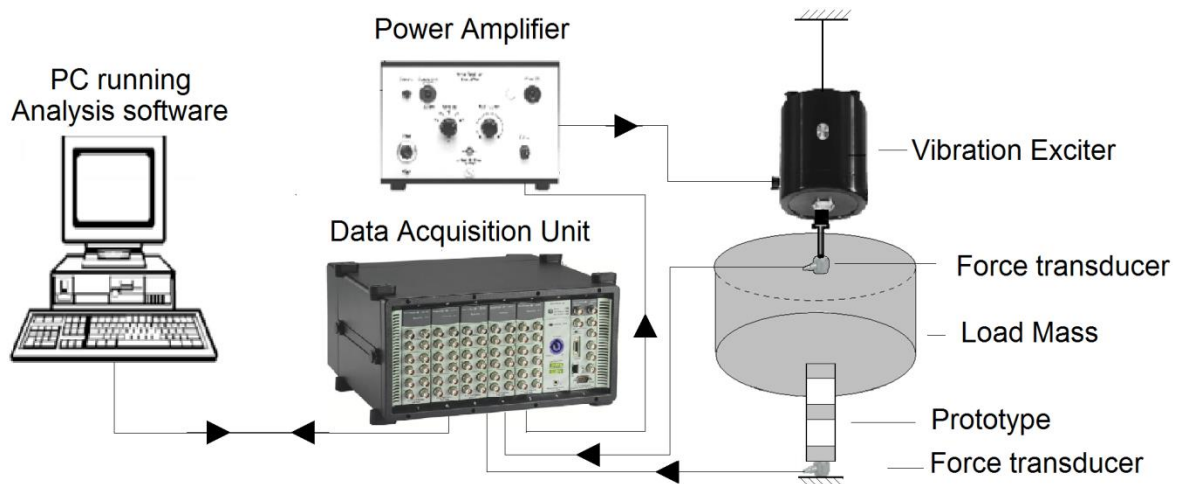
Figure 4.6 – Basic layout of the experimental setup to obtain the force transmissibility curves using one prototype.
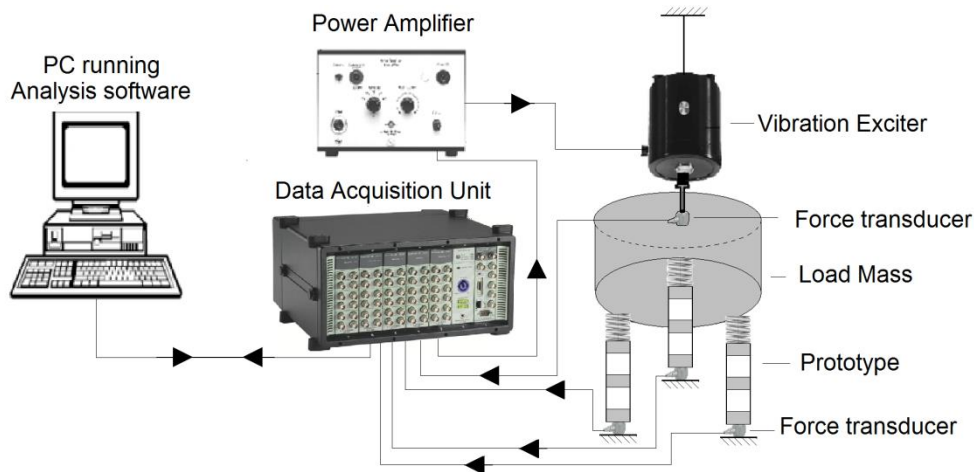
Figure 4.7 – Basic layout of the experimental setup to obtain the force transmissibility curves using three prototypes to support the load mass.

4.7. Selection of materials

The material selection is considered essential to this study since one is targeting as low as possible frequency ranges of practical interest. In [40], the author has studied four materials, namely aluminum, epoxy and a CCMs, that were individually combined with steel. Note that previous to this work, the results presented in the literature regard ARs in frequency ranges which are considered high, see e.g., Jensen and Sigmund [145] in which the first AR of interest starts at ≈80 kHz. A rare exception is the work of Jensen and Pedersen [144]), that tested a steel-Polymethyl Methacrylate (PMMA) periodic rod with approximately 1.5 m long and obtained a considerable AR initiating at approximately 1840 Hz. Anyway, note that these authors were only interested in showing the presence of ARs at elastic solids under stress wave propagation.

The choice of CCMs combined with steel was a novelty proposed, by the author of this thesis, with which was possible to have a high enough contrast in the wave phase velocity of the materials such that the first AR of interest initiates at frequencies bellow 1 kHz for prototypes with lengths less than 0.2 m.

As previously discussed, the widths and locations of the ARs are determined by the materials layout and the contrasting ratio of the material properties used. Among the materials studied in [40] and in this study, steel and CCMs present the highest contrasting ratio in wave phase velocity thus, the most suitable to target the design of ARs in the low frequency ranges, which are of interest in this study.

4.8. Design, structural improvement and optimization of phononic-inspired vibration isolators

4.8.1. Design and structural improvement

To target a desired AR, both in width and location in the frequency range, the design of a unit cell may be considered as one of the most important steps in the design stage of the two-material layer periodic bar.

Hence, consider a unit cell as illustrated in Figure 4.8 a) made of two materials with high contrast in their elastic properties (E'_{Mat_α} and $\rho_{\mathrm{Mat}_\alpha}$), e.g. steel and CCM. The length of each material layer, i.e. L_{Mat_1} and L_{Mat_2} , is the design parameter. The improvement problem is subject to several length constraints, namely, minimum $L_{\mathrm{Mat}_{\alpha\,\min}}$ and maximum $L_{\mathrm{Mat}_{\alpha\,\max}}$ length of the layer of material α as well as the minimum $L_{\mathrm{T}_{\min}}$ and maximum $L_{\mathrm{T}_{\max}}$ total length of the unit cell.

a)   b)
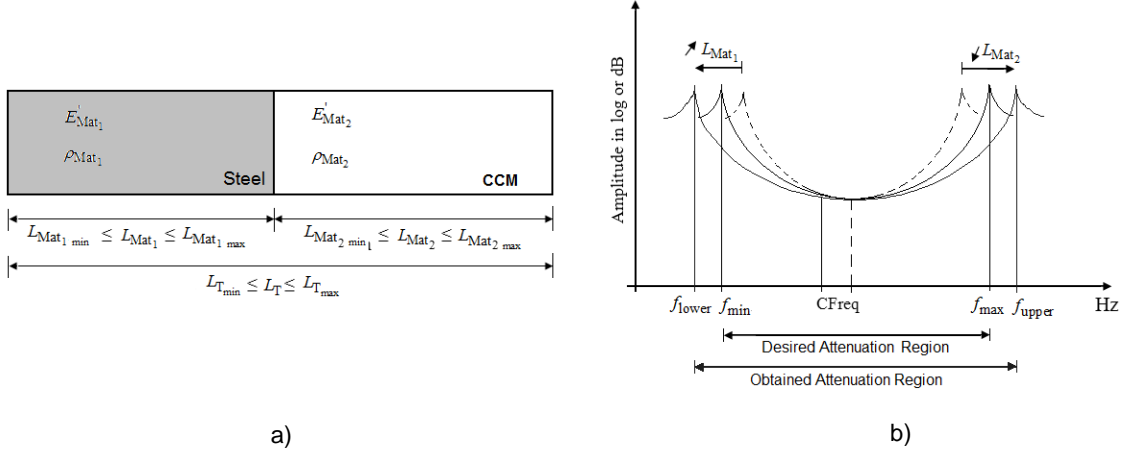
Figure 4.8 – a) Unit cell; b) Frequency response curves illustrating $f_{\min}$, $f_{\max}$, f_{lower} , f_{upper} , and AR.

As previously introduced in sub-chapter 4.3.1, the dispersion equation allows computing and plotting the frequency as an implicit function of the quasi-wave number k obtaining the dispersion curves where the stopband and passband regions may be identified (see Figure 4.3). Solving the dispersion equation, see Eq. (4.4), would be an alternative to the numerical FE model for the design of a unit cell if it were differentiable in a specific domain. Figure 4.3 illustrates the dispersion curves where points A and B represent the initial and final frequency points, respectively, of the stopband. In these points, the dispersion equation is not differentiable. The numerical identification of these non-differentiable points is not an easy task and is not considered in this study.

Alternatively, the numerical FE model was introduced in sub-chapter 4.4. This is based on the relation between the curves obtained as will be shown. The modal and/or harmonic problems, see subchapter 2.2, are solved in this case (e.g., with a total of 5.5 unit cells), although three unit cells has shown to be enough for the steady-state dynamic behavior of a finite periodic structure to qualitatively match that of the infinite periodic structure [54]. In addition, 16 FEs per wavelength are used as it shown to be enough in this study [44].

The desired AR may be defined by the minimum $\left(f_{\min}\right)$ and maximum $\left(f_{\max}\right)$ AR frequencies, that are equivalent to points A and B, respectively, as illustrated in Figure 4.3.

The main concept introduced in [44] and illustrated by Figure 4.8 b) is that: 1) the maximum frequency of the AR ($f_{\max}$) increases when the length of material 2 (L_{Mat_2}) is decreased and; 2) increasing the length of material layer 1 (L_{Mat_1}) the minimum frequency of the AR ($f_{\min}$) decreases.

A design procedure for these types of cells is developed here based on this concept, considering L_{Mat_1} and L_{Mat_2} as the design parameters subject to the following constraints: minimum $L_{\text{Mat}_{\alpha\ \text{min}}}$ and maximum $L_{\text{Mat}_{\alpha\ \text{max}}}$ length of the layer of material α as well as the minimum $L_{\text{T}_{\text{min}}}$ and maximum $L_{\text{T}_{\text{max}}}$ total length of the cell, and applied as illustrated in the diagram of Figure 4.9.
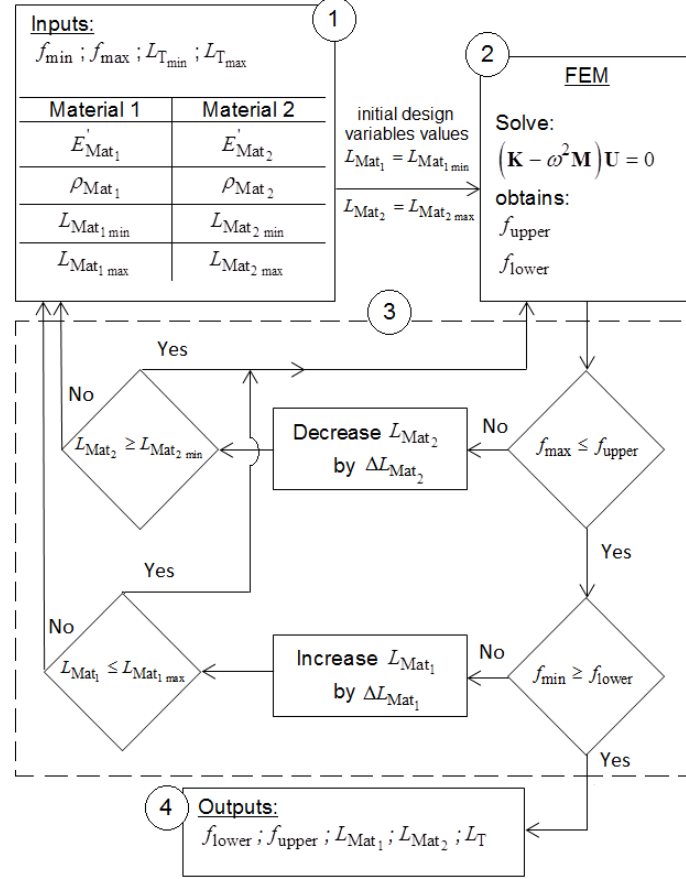
Figure 4.9 – Diagram of the design procedure applied to the design of a unit cell. The numbers within circles from 1 to 4 underline the steps of the procedure.

Figure 4.9 illustrates the main steps of the developed design procedure, which is here described as:

1. Start by defining the minimum f_{min} and maximum f_{max} AR frequencies, minimum $L_{\text{T}_{\text{min}}}$ and maximum $L_{\text{T}_{\text{max}}}$ total length of the cell, the properties of the materials (E'_{Mat_α} and ρ_{Mat_α}), and the minimum $L_{\text{Mat}_{\alpha\ \text{min}}}$ and maximum $L_{\text{Mat}_{\alpha\ \text{max}}}$ length of the layer of material α. The length of each material layer, i.e. L_{Mat_1} and L_{Mat_2}, are the design parameters, which initially assume the values of $L_{\text{Mat}_{1\ \text{min}}}$ and $L_{\text{Mat}_{2\ \text{max}}}$, respectively. The improvement problem is subject to several length constraints, namely, minimum $L_{\text{Mat}_{\alpha\ \text{min}}}$ and maximum $L_{\text{Mat}_{\alpha\ \text{max}}}$ length of the layer of material α as well as the minimum $L_{\text{T}_{\text{min}}}$ and maximum $L_{\text{T}_{\text{max}}}$ total length of the cell.

2. The free vibration analysis, see sub-chapter 2.2.2, is solved from which, the lower (f_{lower}) and upper (f_{upper}) AR frequencies are computed.

3. The upper (f_{upper}) and maximum (f_{max}) AR frequencies are compared. While $f_{max} > f_{upper}$ the length of material 2 (L_{Mat_2}) is decreased by ΔL_{Mat_2} (e.g., 10%) until $L_{Mat_2} < L_{Mat_2 \, min}$. Once this constraint is satisfied the lower (f_{lower}) and minimum (f_{min}) AR frequencies are then compared. While $f_{min} < f_{lower}$ the length of material layer 1 (L_{Mat_1}) is increased by ΔL_{Mat_1} (e.g., 10%) until $L_{Mat_1} \leq L_{Mat_1 \, max}$. The order in which the material lengths change is important, since an increase in the length of material 1 (L_{Mat_1}) will not significantly affect the value of the upper (f_{upper}) AR frequency previously obtained, as it will be shown.

4. If no constraint is violated, a feasible solution is found and the lower and upper frequencies of the AR (f_{lower} and f_{upper}) as well as the lengths of the materials (L_{Mat_1} and L_{Mat_2}) and the total length of the structure L_T are presented.

Note that in this study, the value of 10% is used to increase/decrease lengths as it shown to be a good compromise between computational speed and results convergence.

An alternative to this iterative method is a structural optimization procedure.

4.8.2. Structural optimization

A structural optimization procedure, see sub-chapter 2.7, that avoids including the upper and/or the lower design regions in the objective function can be obtained by defining a mass ratio cost function. The lengths of the material layer L_{Mat_1} and L_{Mat_2} are the design parameters subject to a set of frequency and length constraints. Hence, the optimization problem is formulated as

$$
\min_{L_{Mat_1}, L_{Mat_2}} \left(\frac{\rho_{Mat_1} L_{Mat_1}}{\rho_{Mat_2} L_{Mat_2}} \right)
$$
$$
s.t.
$$
$$
\left([K] - \omega^2 [M] \right) \{ \Phi \} = \{ 0 \},
$$
$$
f_{lower} \leq f_{min}
$$
$$
f_{max} \leq f_{upper}
$$
$$
L_{Mat_1 \, min} \leq L_{Mat_1} \leq L_{Mat_1 \, max}
$$
$$
L_{Mat_2 \, min} \leq L_{Mat_2} \leq L_{Mat_2 max}
$$

(4.8)

where ρ_{Mat_1} is the mass density of material 1, ρ_{Mat_2} is the mass density of material 2, f_{min} and f_{max} are the minimum and maximum frequencies of the AR, respectively, and f_{lower} and f_{upper} are the respective lower and upper frequencies of the AR obtained after optimization.

For the numerical optimizations a SQP algorithm (see e.g., [113] for more details) and an iterative procedure with the following steps are implemented: 1) Initialize by giving initial design values; 2) Run a modal analysis for the initial design; 3) Start the optimization loop. After writing the values of the current iteration design variables (L_{Mat_1} and L_{Mat_2}) to a file, it will call the FE analysis in batch mode and will return to the optimization routine the current calculated values of the design variables and; 4) After satisfying the stopping criteria (constraints or predefined stopping parameters), run a modal analysis for the final design.

4.9. Phononic-inspired vibration isolators for mechanical applications

Looking back at one of the first experimental prototypes, developed and tested by the author (based on the work of Jensen and Pedersen [144]), it consisted of a steel-Polymethyl Methacrylate (PMMA) periodic structure with approximately 1.5 m long and a considerable AR initiating at approximately 1840 Hz as illustrated by Figure 4.11. However, the objective with that experiment was to validate the FE model and obtain the experimental evidence of the existence of a significant AR associated with the respective phononic bandgap in periodic structures.

Figure 4.10 – Photograph of the experimental setup used to test a 5.5 cell steel-PMMA periodic cylindrical bar with a diameter of 0.020m, composed of six steel and five PMMA half-cells each with a length of 0.135m [44].
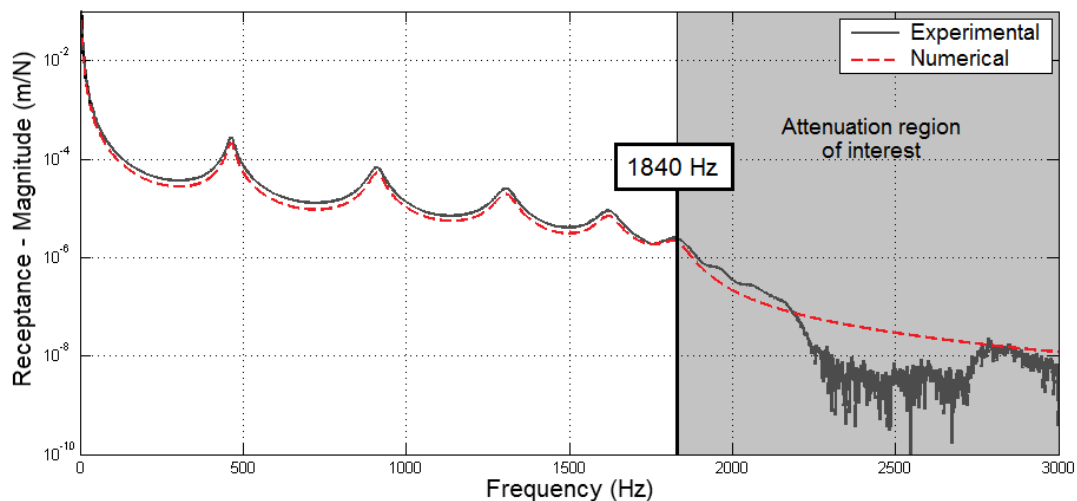
Figure 4.11 – Magnitude of the experimental and numerical FRF curves of a 5.5 cell steel-PMMA cylindrical bar with a diameter of 0.020m, composed of six steel and five PMMA half-cells each with a length of 0.135m [44].

With the knowledge that solid materials with high contrast in wave phase velocity are necessary to have a structure with acceptable dimension (in the centimeters range) as well as an AR in a frequency range of practical use for several mechanical applications, steel and CCMs were the selected materials for further analyses.

That next step, revealed to be a considerable challenge. It consisted in characterizing the dynamic properties of CCMs that allow matching simulation and experimental values, since their properties were unavailable. The author explored different approaches, starting from the standardized tests and ending by proposing a hybrid analytical-experimental methodology that revels to be simple and rigorous (see sub-chapter 3.3).

Once the dynamic properties of the CCMs are accurately known, then the location and width of the bandgap is all about design. In this sense, the first two-material periodic layer structure with steel and a CCM (referenced as 8123 by a cork composite producer - Amorim Cork Composites [132]) was built and tested using the experimental setup illustrated by Figure 4.12, to determine its AR.
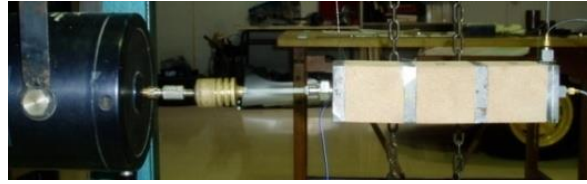
Figure 4.12 – Photograph of the experimental test prototype periodic bar with square cross-section with a side length of 0.050m, composed of 3.5 unit cells, i.e., four steel and three CCM (ref.8123) half-cells each with a length of L_{Mat_1} =0.010m and L_{Mat_2} =0.050m, respectively [44].

Then, to lower the frequency range of the AR (maintaining a total of 3.5 repetitive cells for comparison purposes with the previous example) the length of the CCM L_{Mat_2} was increased by a factor of two since, it was the largest dimension available by the producer at the time.
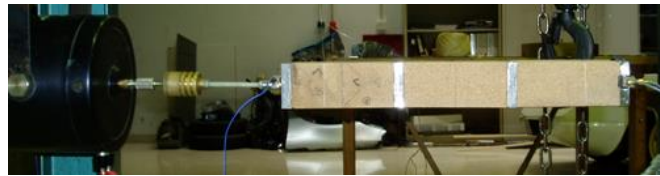
Figure 4.13 – Photograph of the experimental test prototype periodic bar with square cross-section with a side length of 0.050m, composed of 3.5 unit cells, i.e., four steel and three CCM ref.8123 half-cells each with a length of L_{Mat_1} =0.010m and L_{Mat_2} =0.100m, respectively [44].

These two steel-CCM periodic devices may be considered as presenting acceptable dimensions as well as considerable ARs in a frequency range of interest for several mechanical applications as will be shown.

Form what has been presented, it is quite reasonable to consider that with an analysis of the repetitive structure one could increase the capacity of the devices by reallocating the AR to a frequency range of interest, at least for certain frequency ranges.

4.10. On commercial and proposed phononic-inspired vibration isolators

Nowadays, besides the common rubber mount, illustrated by Figure 4.14 a), there are others, e.g., two-material vibration isolators illustrated by Figure 4.14 b) and Figure 4.14 c). The two materials are stacked up in a pile where one is best suited for damping and the other for rigidity of the isolator.
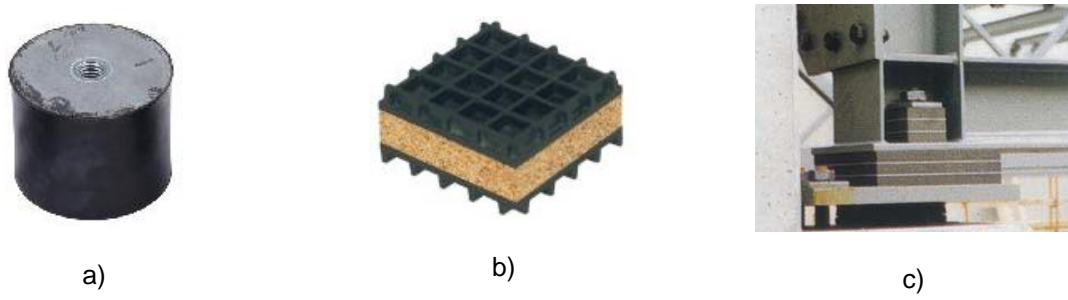
Figure 4.14 – Vibration isolators for machine application: a) rubber mount; b) neoprene waffle and cork sandwich; c) steel and CCM layer structure (Image reproduced from [146]).

The performance of vibration isolators is usually accounted for in terms of force transmissibility, i.e., the ratio between the force that is effectively transmitted to the target from the source, see sub-chapter 2.8. In this study, this concept is used to evaluate the performance of two commercial vibration isolators (previously designated as CVIs), illustrated by Figure 4.14 a) and Figure 4.14 b), and five PIVIs, illustrated by Figure 4.15. These PIVIs are compared using the experimental setup described in sub-chapter 4.6 and illustrated by Figure 4.6, where one prototype is tested between the force transducer fixed to the floor and the load mass on the other side.
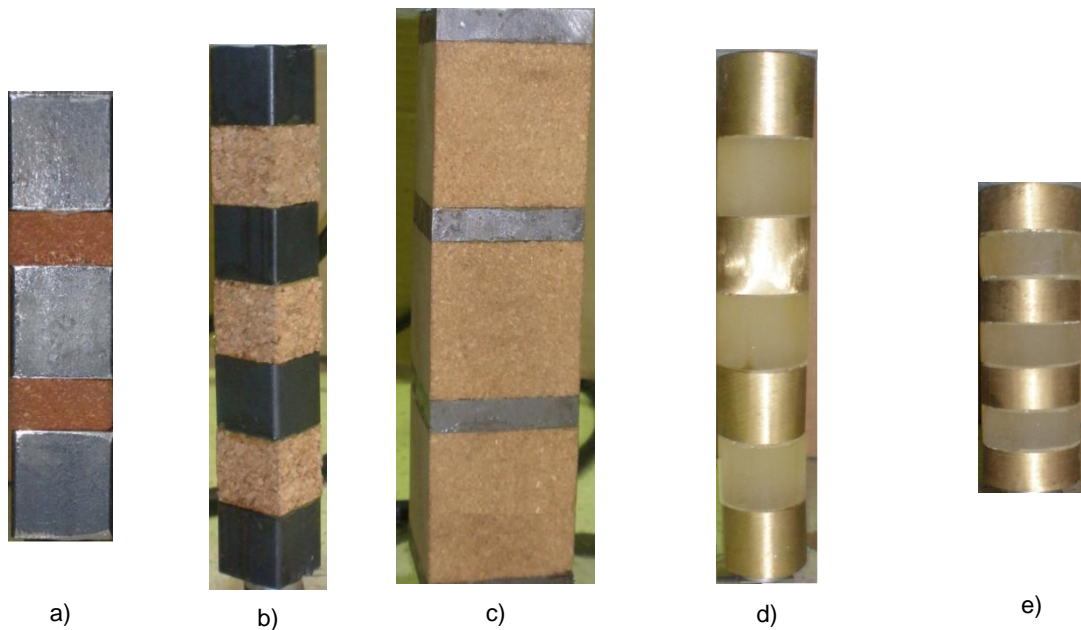
Figure 4.15 – Phononic-inspired vibration isolators tested with different resilient layers: a) cork-rubber ref. VC5200 (SIPVI–1); b) cork agglomerate ref. NL20 (SIPVI–2); c) cork agglomerate ref. 8123 (SIPVI–3); d) urethane with 20mm (SIPVI–4); e) urethane with 10mm (SIPVI–5).

Hence, the two CVIs tested, see Figure 4.14 a) and Figure 4.14 b), consist of a typical rubber mount (designated as CVI–1) and neoprene waffle cork sandwich (designated as CVI–2), respectively, which are commonly used in the support of machinery. The five PIVIs tested are illustrated in Figure 4.15. At Figure 4.15 a) is illustrated a steel-cork rubber (ref. VC5200) prototype with 2.5 cells and a total length of approximately 80 mm. At Figure 4.15 b) is illustrated a steel-cork agglomerate

(ref. NL 20) prototype with 3.5 cells and a total length of approximately 140 mm. At Figure 4.15 c) is illustrated a steel-cork agglomerate (ref. 8123) prototype with 3.5 cells and a total length of approximately 190 mm. At Figure 4.15 d) is illustrated a steel-urethane prototype with 3.5 cells and a total length of approximately 140 mm. The last prototype is illustrated by Figure 4.15 e) and consists of a steel-urethane prototype with 3.5 cells and a total length of approximately 70 mm.

Note that urethane, being a resilient material, is only used in this study for comparison purposes with the CCMs.

4.11. Phononic-inspired vibration isolators and spring tested using a load mass approximation

In this sub-chapter is presented an initial study on the dynamic behavior, in terms of force transmissibility (see sub-chapter 2.8), of three different devices used to support a load mass of approximately 3.2 kg (previously referred in sub-chapter 4.6), which is similar to the mass of the motor of the hermetic compressor that is further addressed when considering these devices in a real industrial application.

The three elastic support devices used to support the load mass are illustrated by Figure 4.16, and consist of: helical springs (with a height of 20.4 mm, a diameter of the wire of 1.5 mm, an inner diameter of 12 mm, 4 active coils and 2 close plain coils at each end [147]), PIVI prototypes and the combination of the previous two (PIVIs and helical springs). The experimental setup used is that described in sub-chapter 4.6 and illustrated by Figure 4.7.

a)   b)   c)
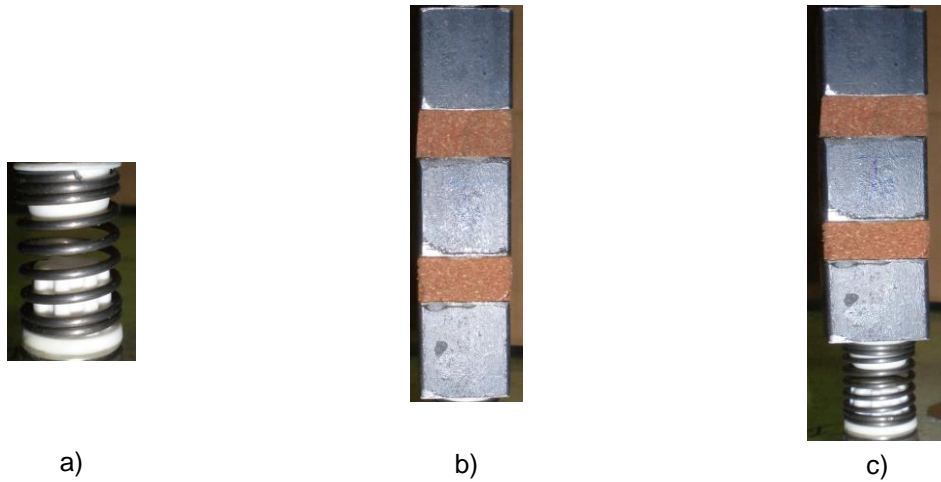
Figure 4.16 – Supporting devices: a) helical spring (the white terminations are plastic connection devices); b) PIVI steel-VC 5200; c) PIVI steel-VC 5200 + helical spring.

The load mass is supported by three similar devices (of the type previously referred) as illustrated by Figure 4.17.

An excitation force $\mathbf{F}_{\omega_{ap}}$ with excitation frequency ω_{ap} is applied to the load mass at the center of

the top surface. Then, by measuring the force effectively transmitted to the foundation $\left(\mathrm{F_T}\right)$ one uses

the concept of force transmissibility, i.e., the ratio between the magnitude of the force that is transmitted to the foundation and the magnitude of the applied force, see sub-chapter 2.8.
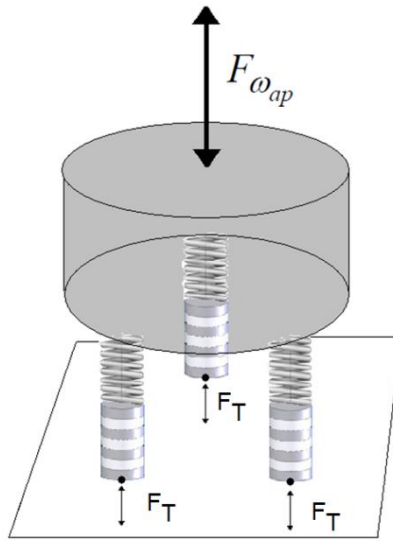
Figure 4.17 – Load mass supported by three devices.

4.12. Phononic-inspired vibration isolators tested supporting a motor of hermetic compressor

This sub-chapter is in fact a continuation of the previous where the load mass, see Figure 4.17, is replaced by a working motor of a hermetic compressor, see Figure 4.18.
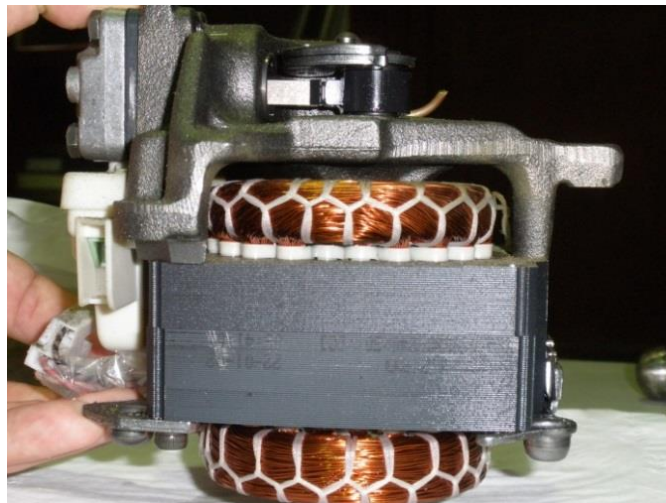
Figure 4.18 – Photograph of a motor of a hermetic compressor.

Similarly, the objective is to evaluate the performance of the supporting devices in terms of force transmissibility (see sub-chapter 2.8). In this particular case, two types supporting devices are considered. The first type are the original helical springs that equip the hermetic compressor and the second type are the PIVI prototypes combined with these springs.

4.13. Results and discussion

In this sub-chapter are presented and discussed the main results obtained in the framework of PIVIs.

4.13.1. Structural improvement of the attenuation regions bandwidth

As previously referred, the design of a unit cell, see Figure 4.8 a), is perhaps one of the most important steps in the design stage of the two-material layer periodic bar intended to target a specific AR frequency range.

In this sense, consider a structural improvement problem that consists of varying the axial length of the resilient layer (L_{Mat_2}) of each unit cell while maintaining the total length of the repetitive cell ($L_{\text{Mat}_1} + L_{\text{Mat}_2}$), see Figure 4.8 a) to obtain the maximum amplitude of the AR.

It was assumed that the bar has a total length of L_T =0.036 m, the minimum length of the resilient layer $L_{\text{Mat}_{2\,\text{min}}} = 0.0012$ m, the two material properties are those presented in Table 4.1 and that the initial design consisted of $L_{\text{Mat}_1} = L_{\text{Mat}_2} = L_T/(2Ncel)$ with $Ncel = 3$.

	E'_{Mat_α} (Pa)	ρ_{Mat_α} (kg m^{-3})
Material 1 ($\alpha = 1$)	205×10^9	7860
Material 2 ($\alpha = 2$)	3×10^6	1140

Table 4.1 – Storage modulus and mass density of the materials.

By applying the developed design procedure described in sub-chapter 4.8.1 and illustrated by Figure 4.9, improvement in the separation of two adjacent frequencies (j and $j+1$) relative to the initial design, i.e. from initial separation to improved final value, were obtained as illustrated Figure 4.19 and shown by the values presented in Table 4.2, for j =3.
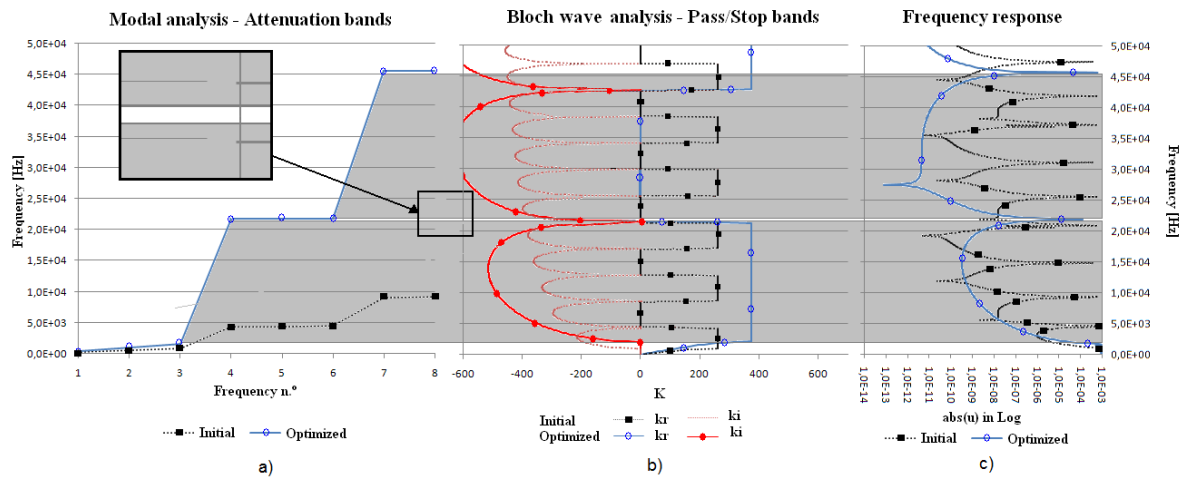
Figure 4.19 – Results for $j = Ncel = 3$: a) eigenfrequencies curve plot; b) dispersion curves and c) FRF plot.

Note that $j=3$, means that f_4 will be put apart from f_3 as far as possible originating the grey areas illustrated in Figure 4.19.
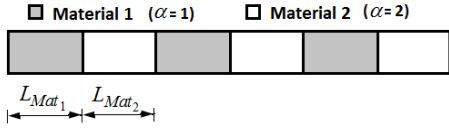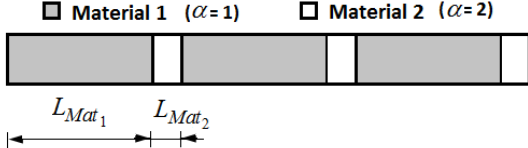
	L_{Mat_2} (m)		$\Delta f = f_{j+1} - f_j$ (Hz)
Initial	6.00×10^{-3}	☐ Material 1 ($\alpha=1$) ☐ Material 2 ($\alpha=2$)	3440
Improved	1.20×10^{-3}	☐ Material 1 ($\alpha=1$) ☐ Material 2 ($\alpha=2$)	20160

Table 4.2 – Output results from the structural improvement case with $j = 3$.

In Figure 4.19 a) is presented the solution obtained by solving the eigenvalue problem presented in Eq. (2.19) where in the abscissa is represents the number of the natural frequency and in the ordinate is the corresponding frequency value in Hz.

The dispersion curves obtained as described in sub-chapter 4.3.1 are presented in Figure 4.19 b).

The frequency response of displacement at node $x = \left(L_T - \left(L_T / Ncel \right) \right)$ is presented in Figure 4.19 c) for an applied axial harmonic force with 200 N of magnitude at x=0 m. The ARs are identified (by the gray areas) and related with the stopbands given by the dispersion curves.

The separations of the adjacent eigenvalues, expressed by Δf, are evident (see Table 4.2) when comparing the initial design curves with corresponding curves of the improved design.

4.13.2. Structural improvement considering minimum and maximum bounds for the attenuation region

In this second case, consider a prototype with a total number of 3.5 cells, see e.g. Figure 4.5, in which the cell is designed to have an AR with a minimum ($f_{\min}$) and maximum ($f_{\max}$) frequency bounds of 1000 Hz and 4100 Hz, respectively. It was assumed that material 1 is steel and material 2 is a CCM. The respective material properties are the presented in Table 4.3.

	E'_{Mat_α} (Pa)	ρ_{Mat_α} (kg m^{-3})
Material 1 ($\alpha = 1$)	205×10^9	7860
Material 2 ($\alpha = 2$)	40×10^6	260

Table 4.3 – Storage modulus and mass density of the materials.

By applying the design procedure described in sub-chapter 4.8.1 and illustrated by Figure 4.9, the results presented in Table 4.4 and illustrated by Figure 4.20 are obtained.

	Target	Design (obtained)
f (Hz)	$f_{\min} < 1000$	$f_{\text{lower}} = 980$
f (Hz)	$f_{\max} > 4100$	$f_{\text{upper}} = 4139$
L_{Mat_1} (m)	$0.01 \leq L_{\text{Mat}_1} \leq 0.05$	0.01
L_{Mat_2} (m)	$0.01 \leq L_{\text{Mat}_2} \leq 0.05$	0.05
L_T (m)	$0.02 \leq L_T \leq 0.10$	0.06

Table 4.4 – Target and design values of frequency and material lengths.
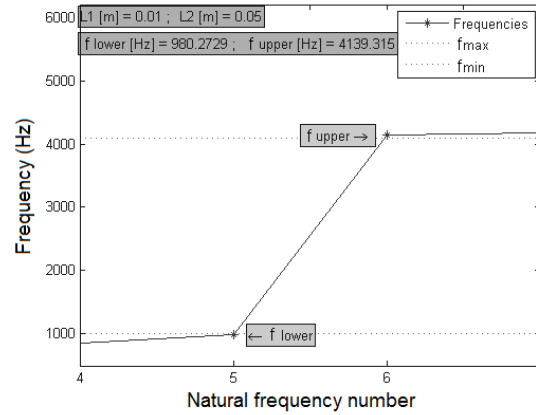
Figure 4.20 – Attenuation region obtained considering $f_{\min} < 1000$ Hz and $f_{\max} > 4100$ Hz.

Figure 4.20 illustrates the AR obtained where the dotted lines represent the desired minimum ($f_{\min}$) and maximum ($f_{\max}$) bounds of the AR. The solid asterisk line represent the obtained design lower (f_{lower}) and upper (f_{upper}) bounds of the AR. Table 4.4 indicates the target and the obtained values.

The lower bound of the AR (f_{lower}) is 20 Hz lower than the minimum required ($f_{\min}$), see Table 4.4, leaving room for some optimization of the length of material 1 (L_{Mat_1}) which can be decreased in order to approximate the lower and minimum bounds of the AR.

A decrease in L_{Mat_1} may be seen as advantageous since the total size of the structure will decrease, and if the weight of the structure and/or the cost of the material are to be accounted for, these will decrease.

4.13.3. Structural improvement considering new minimum and maximum bounds for material lengths

In this third structural improvement case, continue to consider that material 1 is steel and material 2 is a CCM with the properties presented in Table 4.3 and a desired AR with minimum ($f_{\min}$) and maximum ($f_{\max}$) bounds of 1000 Hz and 4100 Hz, respectively. The length of each material, which

differs from the previous case, are now $0.001 \le L_{\mathrm{Mat}_1} \le 0.05$ m and $0.01 \le L_{\mathrm{Mat}_2} \le 0.05$ m. By applying the design procedure described in sub-chapter 4.8.1, Figure 4.21 and Table 4.5 which illustrate and indicate the results determined are obtained.

a)   b)
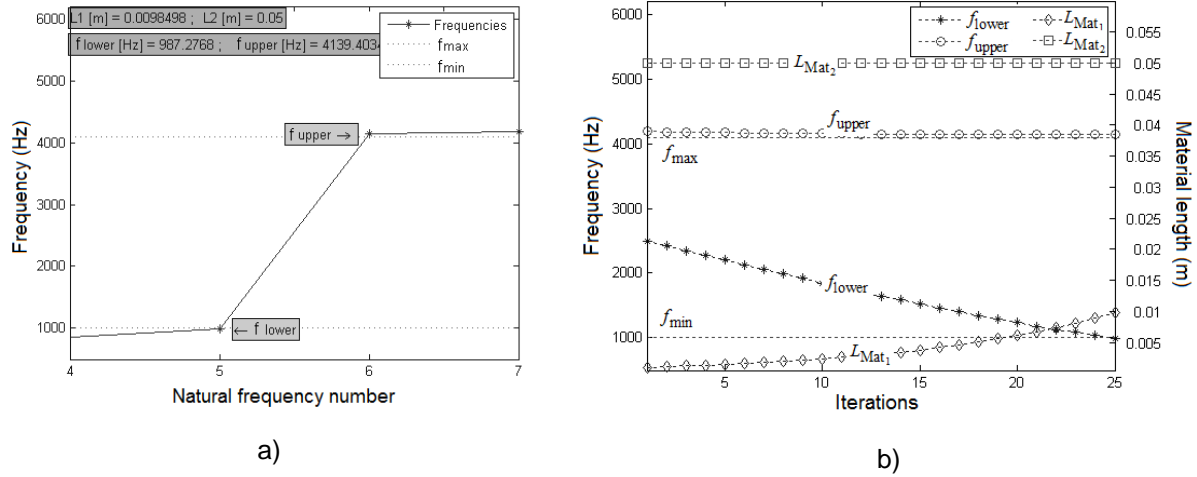
Figure 4.21 – Case 3: a) Attenuation region obtained; b) Frequencies and material length convergence history.

Figure 4.21 a) illustrates the AR obtained between the lower (f_{lower}) and upper (f_{upper}) frequencies. Figure 4.21 b) illustrates the convergence history for the frequencies and material length where the asterisk line represent the obtained design lower (f_{lower}), the circle line represent the obtained upper (f_{upper}) bounds of the AR, the diamond line represent the obtained length for material 1 (L_{Mat_1}) and the square line represent the obtained length for material 2 (L_{Mat_2}).

	Target	Design (obtained)
f (Hz)	$f_{\mathrm{min}} < 1000$	$f_{\mathrm{lower}} = 987$
	$f_{\mathrm{max}} > 4100$	$f_{\mathrm{upper}} = 4139$
L_{Mat_1} (m)	$0.001 \le L_{\mathrm{Mat}_1} \le 0.05$	0.0098498
L_{Mat_2} (m)	$0.01 \le L_{\mathrm{Mat}_2} \le 0.05$	0.05
L_T (m)	$0.02 \le L_T \le 0.10$	≈0.05985

Table 4.5 – Target and design values obtained for the frequency and material lengths.

In this case, the obtained design length of material 1 (L_{Mat_1}) is 0.0098 m, which is less than the value of 0.01 m obtained in example 2 due to the inputted length of material layer 1 which was of 0.001 m. So being, it is noticed that the input length of material 1 (L_{Mat_1}) should be the minimum length allowed, i.e., $L_{\mathrm{Mat}_1} = L_{\mathrm{Mat}_1 \mathrm{min}}$, in order to obtain a solution that presents a lower length of material 1 which is advantageous, as previously stated in the second case (see sub-chapter 4.13.2). For this case, an approximate reduction, in terms of mass density, of 1.6 kg/m^3 is obtained.

It is also confirmed that as the length of material 1 (L_{Mat_1}) increases the lower bound frequency of the AR (f_{lower}) decreases and the upper bound frequency of the AR (f_{upper}) is not significantly affected, being nearly constant.

4.13.4. Structural improvement with new minimum and maximum frequency bounds

In this fourth structural improvement case, continue to consider that material 1 is steel and material 2 is CCM with the properties presented in Table 4.3. The desired AR minimum and maximum bounds to be considered are now of f_{min} =1000 Hz and f_{max} =10 kHz, respectively.

The length of each material, are the same as in the previous case, i.e., 0.001 m ≤ L_{Mat_1} ≤ 0.05 m and 0.01 m ≤ L_{Mat_2} ≤ 0.05 m. By applying the design procedure described in sub-chapter 4.8.1 (see Figure 4.9) Figure 4.22 and Table 4.6 are obtained.

Similarly to the previous case, Figure 4.22 a) illustrates the AR obtained defined by f_{lower} and f_{upper} , Figure 4.22 b) illustrates the convergence history for the AR frequencies and material lengths L_{Mat_α} and Table 4.6 indicates the target values and the values obtained.

a)   b)
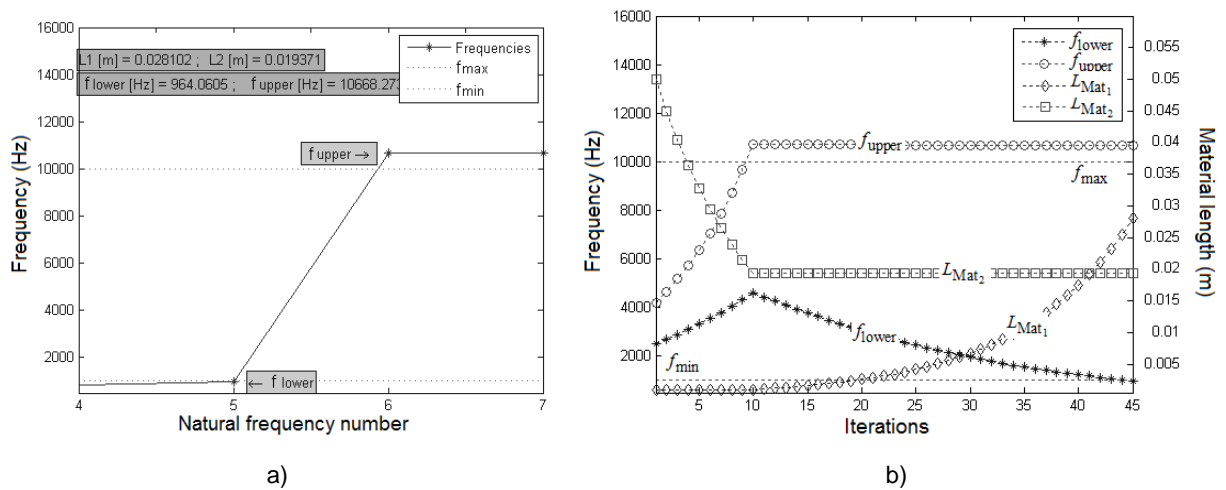
Figure 4.22 – Case 4: a) Attenuation region obtained; b) Frequencies and material length convergence history.

	Target	Design (obtained)
f (Hz)	f_{min} < 1000	f_{lower} =964
	f_{max} > 10000	f_{upper} =10668
L_{Mat_1} (m)	0.001 ≤ L_{Mat_1} ≤ 0.05	0.028102
L_{Mat_2} (m)	0.01 ≤ L_{Mat_2} ≤ 0.05	0.019
L_T (m)	0.02 ≤ L_T ≤ 0.10	≈ 0.0471

Table 4.6 – Target and design values obtained for the frequency and material lengths.

As in the previous case (see sub-chapter 4.13.3), a similar line of though may be applied to the length of material layer 2, i.e., it should be inputted as the maximum length allowed $L_{\mathrm{Mat}_2} = L_{\mathrm{Mat}_2 \max}$, in order to obtain a solution that presents a minimum length of material 2 which is advantageous as previously stated, see e.g., sub-chapter 4.8.1.

It is confirmed that as the length of material 2 (L_{Mat_2}) decreases the upper bound frequency of the AR (f_{upper}) increases and the lower bound frequency of the AR (f_{lower}) also increases. It is re-confirmed that as the length of material 1(L_{Mat_1}) increases the lower bound frequency of the AR (f_{lower}) decreases and the upper bound frequency of the AR (f_{upper}) is not significantly affected, being nearly constant.

In this example, there is also room for some optimization of the length of material 1 (L_{Mat_1}) which can be decreased in order to approximate the lower and minimum bounds of the AR.

The upper bound frequency of the AR (f_{upper}) is slightly higher than the maximum required ($f_{\max}$), leaving room for some optimization of the length of material 2 (L_{Mat_2}) which can be increased in order to minimize the difference between the two values. An increase in length of material 2 (L_{Mat_2}) may be seen as disadvantageous since the optimized AR would present a smaller bandwidth then the obtained AR, the total size of the structure will increase, and if the weight of the structure and/or the cost of the material are to be accounted for, these will increase.

On the other hand, one may be led to maximize the AR by maximizing the difference between the upper bound and the maximum required frequency ($f_{\max}$) of the AR. But in contrast to the insignificant effects that an increase in the length of material 1 (L_{Mat_1}) have in the upper bound frequency (f_{upper}), a decrease in the length of material 2 (L_{Mat_2}) leads to an increase of the lower bound frequency of the AR ($\mathrm{f}_{\mathrm{lower}}$). Consequently this would have to lead to an increase of the length of material 1 (L_{Mat_1}) to decrease the lower bound frequency of the AR (f_{lower}) below the minimum required ($f_{\max}$) and to all the disadvantages previously referred of a longer, heavier and possible more expensive structure.

4.13.5. Structural optimization results

An alternative to the structural improvement design procedure, presented in sub-chapter 4.8.1, is the structural constrained nonlinear optimization methodology, described in sub-chapter 4.8.2 and expressed by Eq. (4.8), in which a mass ratio cost objective function is minimized in order to obtain the optimal material lengths (L_{Mat_1} and L_{Mat_2}) subject to several frequency and length constraints (see the Target column of Table 4.7 and Table 4.8).

For this, was considered a structure with a total number of 3.5 cells, see e.g. Figure 4.5, composed of steel (material 1) and a CCM (material 2) with the respective material properties presented in Table 4.3.

Similarly to the third and fourth improvement cases, presented in sub-chapter 4.13.3 and sub-chapter 4.13.4, respectively, consider that the ARs should present a minimum ($f_{\min}$) frequency bound inferior to 1000 Hz and maximum ($f_{\max}$) frequency bounds greater than: i) 4100 Hz and; ii) 10 kHz.

The results obtained are presented for case i) and ii) in Table 4.7 and Table 4.8, respectively.

	Target	Design procedure (sub-chapter 4.13.3)	Design (Optimization) (sub-chapter 4.13.5)
f (Hz)	$f_{\min}$ < 1000	f_{lower} =987	f_{lower} =999.57
	$f_{\max}$ > 4100	f_{upper} =4139	f_{upper} =4135
L_{Mat_1} (m)	$0.001 \leq L_{\text{Mat}_1} \leq 0.05$	0.0098	0.0097
L_{Mat_2} (m)	$0.01 \leq L_{\text{Mat}_2} \leq 0.05$	0.0500	0.0499
L_T (m)	$0.02 \leq L_T \leq 0.10$	≈0.0598	≈ 0.0596

Table 4.7 – Target, design and optimized values considering $f_{\max}$ > 4100 Hz.

	Target	Design procedure (sub-chapter 4.13.4)	Design (Optimization) (sub-chapter 4.13.5)
f (Hz)	$f_{\min}$ < 1000	f_{lower} =964	f_{lower} =998
	$f_{\max}$ > 10000	f_{upper} =10668	f_{upper} =10185
L_{Mat_1} (m)	$0.001 \leq L_{\text{Mat}_1} \leq 0.05$	0.0281	0.0253
L_{Mat_2} (m)	$0.01 \leq L_{\text{Mat}_2} \leq 0.05$	0.0190	0.0203
L_T (m)	$0.02 \leq L_T \leq 0.10$	≈ 0.0471	≈ 0.0457

Table 4.8 – Target, design and optimized values considering $f_{\max}$ > 10 kHz.

The structural optimization results present lower values for the upper frequency bound (f_{upper}) which is more evident in the second case (see Table 4.8) due to an increase in the length of material 2 (L_{Mat_2}). Furthermore, and for both cases, see Table 4.7 and Table 4.8, higher values for the lower frequency bound (f_{lower}) are obtained due to the decrease of the length of material 1 (L_{Mat_1}), as intended. So being, the disadvantage of a heavier structure previously referred (due to the high mass density of material 1 which, in these cases are steel) is now minimized.

4.13.6. Phononic-inspired vibration isolators for mechanical applications

Having presented the numerical results obtained using the structural improvement and optimization methodologies for the design of the unit cell and the PIVI itself, in this sub-chapter are presented the experimental modal analysis results of PIVIs prototypes composed of steel and CCMs.

Figure 4.23 illustrates the experimental setup (see subchapter 3.3.7 for more details) used to determine the AR of a two-material periodic structure with steel and CCM layers.

Figure 4.23 – Photograph of the experimental test prototype periodic bar with square cross-section with a side length of 0.050m, composed of 3.5 unit cells, i.e., four steel and three CCM (ref. 8123) half-cells each with a length of L_{Mat_1} =0.010m and L_{Mat_2} =0.050m, respectively [44].

The FRF curves obtained are presented in Figure 4.22 where the filled and dashed curves represent the experimental and the numerical (FEM) results, respectively.
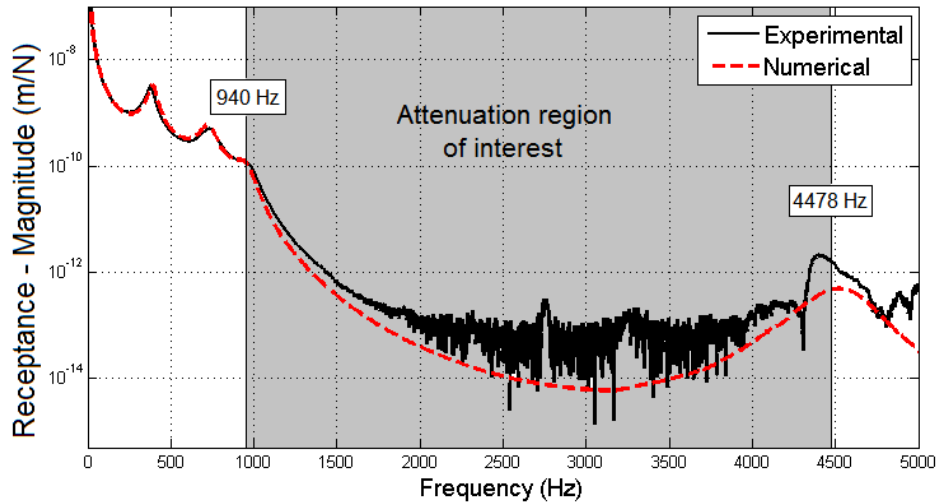
Figure 4.24 – Experimental and numerical FRF curves of the periodic bar with lengths L_{Mat_1} =0.010m and

$$L_{\mathrm{Mat}_2} =0.050\text{m.}$$

As illustrated in Figure 4.22, the first AR of interest starts at approximately 940 Hz. It presents a width of approximately 3500 Hz and was obtained with the two-material periodic structure illustrated by Figure 4.23.

To lower the starting frequency of the AR (maintaining a total of 3.5 repetitive cells for comparison purposes with the previous example) the length of the CCM (L_{Mat_2}) was increased by a factor of two as illustrated by Figure 4.25.

Figure 4.25 – Photograph of the experimental test prototype periodic bar with square cross-section with a side length of 0.050m, composed of 3.5 unit cells, i.e., four steel and three CCM ref. 8123 half-cells each with a length of L_{Mat_1} =0.010m and L_{Mat_2} =0.100m, respectively. The half-cells are bonded with a structural adhesive creating a prototype with a total length of 0.340m [44].

The FRF curves obtained are presented in Figure 4.26 where the filled and dashed curves represent the experimental and the numerical (FEM) results, respectively.
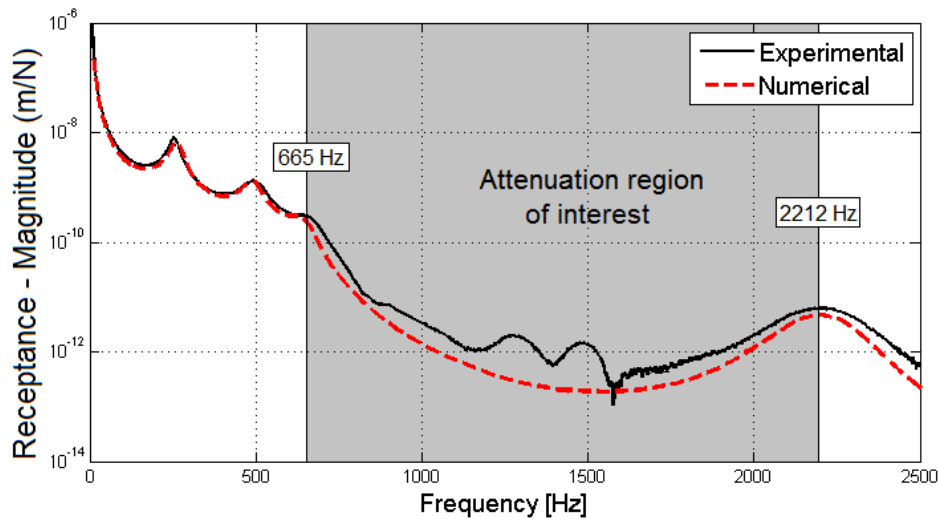
Figure 4.26 – Experimental and numerical FRF curves of the periodic bar with lengths L_{Mat_1} =0.010m and L_{Mat_2} =0.100m.

As illustrated in Figure 4.26, the first AR of interest starts at a lower frequency of approximately 665 Hz presenting a width of approximately 1550 Hz was obtained with the two-material periodic structure illustrated by Figure 4.25.

From the author's point of view, these steel-CCM PIVIs present acceptable dimensions as well as a substantial AR in a frequency range of interest for several mechanical applications. However, lower lengths of the structures and AR situated at lower frequency ranges are desirable. But remember, that one of the initial objectives was simple and prompt fabrication of the prototypes allowing for uncomplicated experimental setups leading to quick validation of the results obtained. And as presented, that was successfully achieved.

With this study, for a given set of: dimensions, AR location and width it is up to a simple optimization procedure, presented in sub-chapter 4.8.2, to verify the feasibility of such requirements and considering different material for these types of periodic structures.

Nowadays, numerous types of vibration isolators are being commercialized and used in industrial applications and some of which, are composed of two materials as illustrated by Figure 4.14 b) and c), which are stacked up in a pile where one material is best suited for damping and the other for rigidity of the isolator.

The AR aspects do not appear to be explored in the commercial solutions, which in the author's opinion might be due to the fact that only recently, and with the work of the author that studies the use of CCMs combined with steel, has been shown evidence of ARs in a low frequency range that are useful for several mechanical applications.

4.13.7. Brief comparison between two commercial and five phononic-inspired vibration isolators

In this sub-chapter are presented the force transmissibility results obtained using the experimental setups described in sub-chapter 4.6 and illustrated by Figure 4.27 and Figure 4.28 for some of the isolators presented in sub-chapter 4.10.

More specifically, two CVIs, i.e., CVI–1 and CVI–2 illustrated by Figure 4.14 a) and Figure 4.14 b), respectively (for which no technical specifications are available), and the five PIVIs illustrated by Figure 4.15.

| a) | b) |

Figure 4.27 – Photograph of the experimental setup used to test the commercial vibration isolators: a) rubber mount (CVI–1); b) neoprene waffle and cork sandwich (CVI–2).

The properties of the materials that are used in the five PIVIs tested are presented in Table 4.9, whereas, some of the properties, e.g., $E_{\mathrm{Mat_1}}'$, have been determined by the author in [44] as indicated in Table 4.9. The remaining material properties, e.g., $E_{\mathrm{Mat_2}}'$, were determined using the hybrid analytical-experimental methodology presented in sub-chapter 3.3.
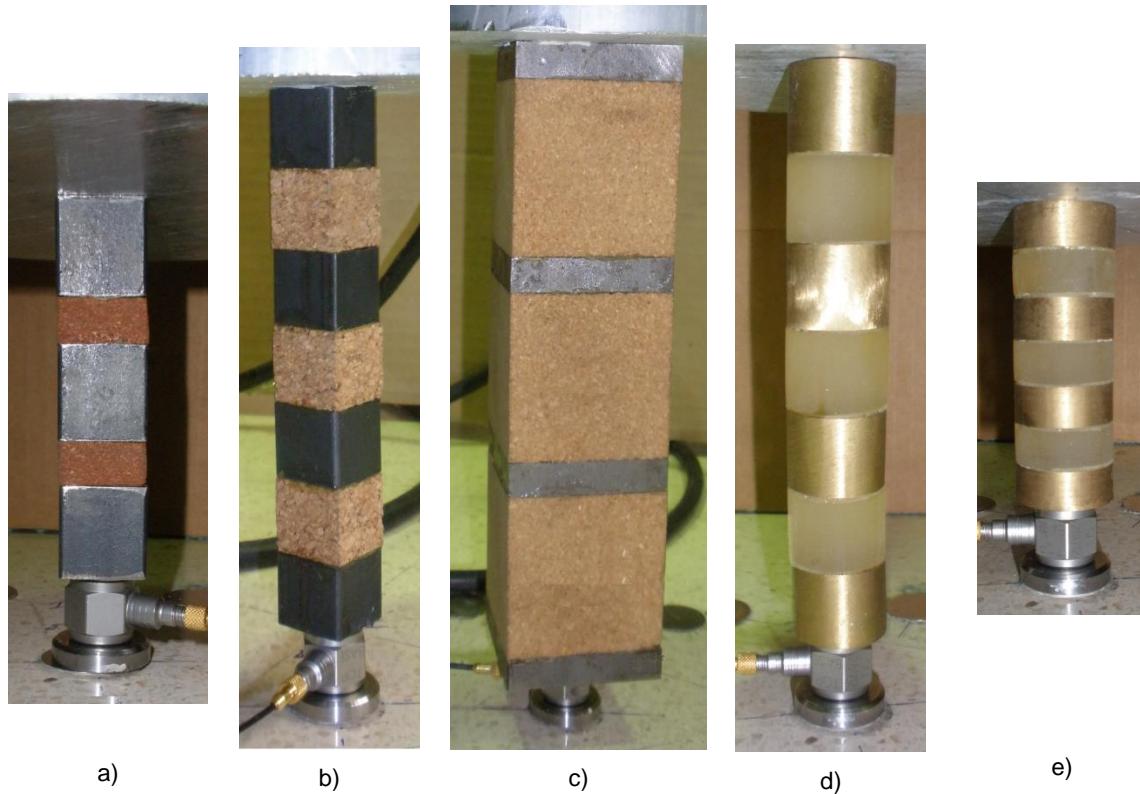
Figure 4.28 – Photograph of the experimental setup (between the floor and the load mass) used to test the PIVIs with different resilient layers: a) cork-rubber ref. VC5200 (PIVI–1); b) cork agglomerate ref. NL20 (PIVI–2); c) cork agglomerate ref. 8123 (PIVI–3); d) urethane with 20mm (PIVI–4); e) urethane with 10mm (PIVI–5).

Prototype	Ncel	Mat_α		L_{Mat_α} (mm)		E'_{Mat_α} (MPa)		$\rho_{\mathrm{Mat}_\alpha}$ (kg m^{-3})		η_{Mat_2}	
Material type	-	$\alpha{=}1$	$\alpha{=}2$	$\alpha{=}1$	$\alpha{=}2$	$\alpha{=}1$ [44]	$\alpha{=}2$	$\alpha{=}1$ [44]	$\alpha{=}2$	$\alpha{=}1$ [44]	$\alpha{=}2$
PIVI–1	2.5	Steel	VC 5200	20.5	10.1	205×10³	26.2	7640	836	≈0.001	0.244
PIVI–2	3.5	Steel	NL 20	20.5	20.5	205×10³	17.9	7640	210	≈0.001	0.130
PIVI–3	3.5	Steel	8123	10.0	45.0	200×10³	43 [44]	7860	256 [44]	≈0.001	-
PIVI–4	3.5	Brass	Urethane	10.0	10.0	115×10³	-	8011	-	≈0.001	-
PIVI–5	3.5	Brass	Urethane	20.0	20.0	115×10³	-	8011	-	≈0.001	-

Table 4.9 – Properties of the PIVIs: number of cells; material type; material length; material storage modulus, material mass density and material loss factor.

This study is restricted to the experimental modal analysis and suited for comparing the performance of the different isolators in terms of force transmissibility. Numerical FE analyses were not addressed here and the main reason is that no properties are available for the CVIs.

At Figure 4.29, are illustrated the force transmissibility FRFs for the different vibration isolators tested. Furthermore, in Table 4.10 are presented the frequencies after which the PIVIs are advantageous when compared to the CVIs and the respective attenuation reduction at 1600Hz.
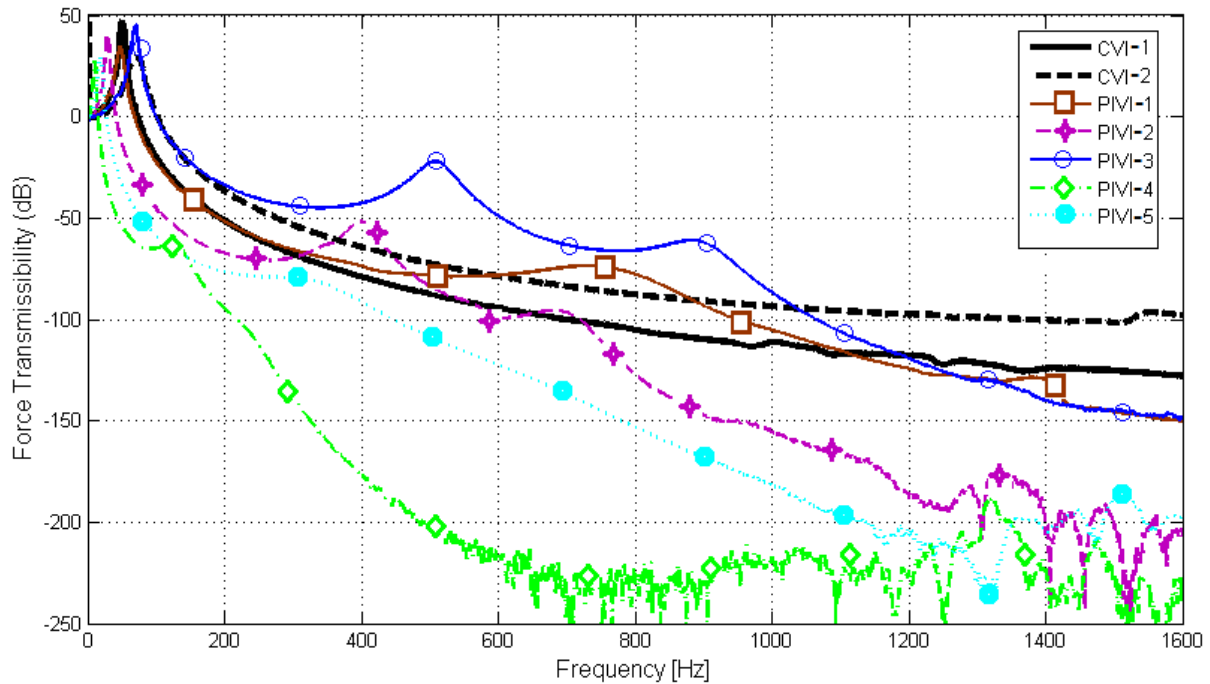
Figure 4.29 – Experimental force transmissibility results for different vibration isolators.

	CVI–1		CVI–2	
PIVI	Frequency (Hz)	Attenuation reduction (dB) at 1600 Hz	Frequency (Hz)	Attenuation reduction (dB) at 1600 Hz
1	1110	25	885	50
2	723	75	445	100
3	1180	25	1040	50
4	15	75	14	100
5	26	100	25	125

Table 4.10 – Frequency after which the PIVIs are advantageous when compared to the CVIs and the respective attenuation reduction at 1600Hz.

From Figure 4.29 it is evident that after specific frequencies, see Table 4.10, the PIVIs are more advantageous in terms of isolation then the CVIs, see Table 4.10. As an example, consider PIVI–1, which corresponds to the line with the square marker in Figure 4.29. PIVI–1 revels to be more advantageous after 1110 Hz relative to CVI–1 and after 885 Hz relative to CVI–2 presenting an attenuation reduction of 25 dB and 50 dB at 1600Hz relative to CVI–1 and CVI–2, respectively. However, when considering PIVI–4, which corresponds to the line with the diamond shape marker in Figure 4.29, one obtains after 14-15 Hz attenuation reduction of 75 dB and 100 dB at 1600Hz relative to CVI–1 and CVI–2, respectively. Furthermore, when compared to the other PIVIs it presents higher attenuation reductions from approximately 150 Hz to 1400 Hz.

Thus, and based on these results alone one may momentarily question the use of CCMs for the resilient layer. Nevertheless, it should be noted that e.g., this specific type of urethane presents a hardness of 30 in the Shore A hardness scale, meaning that it is a relatively soft and flexible material. Hence, its use in PIVIs is not recommended in the sense that the longitudinal stability of the device is not assured unless some sort of guiding mechanism is used. For this reason alone, CCMs are still used in the resilient layer of PIVIs.

4.13.8. Test with load mass supported by springs, by phononic-inspired vibration isolators (PIVIs) and by the combined structure (PIVI-1 and spring)

In the following are presented the main experimental results obtained, using the experimental setup described in sub-chapter 4.6 and illustrated by Figure 4.7, to study the dynamic behavior, in terms of force transmissibility (see sub-chapter 2.8), of three different devices, i.e., helical springs, PIVI-1 prototypes and the combination of the previous two (PIVIs and springs). These devices are used to support a load mass of approximately 3.2 kg, which is similar to the mass of the motor of the hermetic compressor that is then addressed when considering these devices in a real industrial application.

Thus, consider that: i) the load mass is supported by three helical springs; ii) the load mass is supported by three PIVI (VC5200) prototypes; and iii) the load mass is supported by three prototypes that combine the PIVI (VC5200) and the spring.

a)   b)
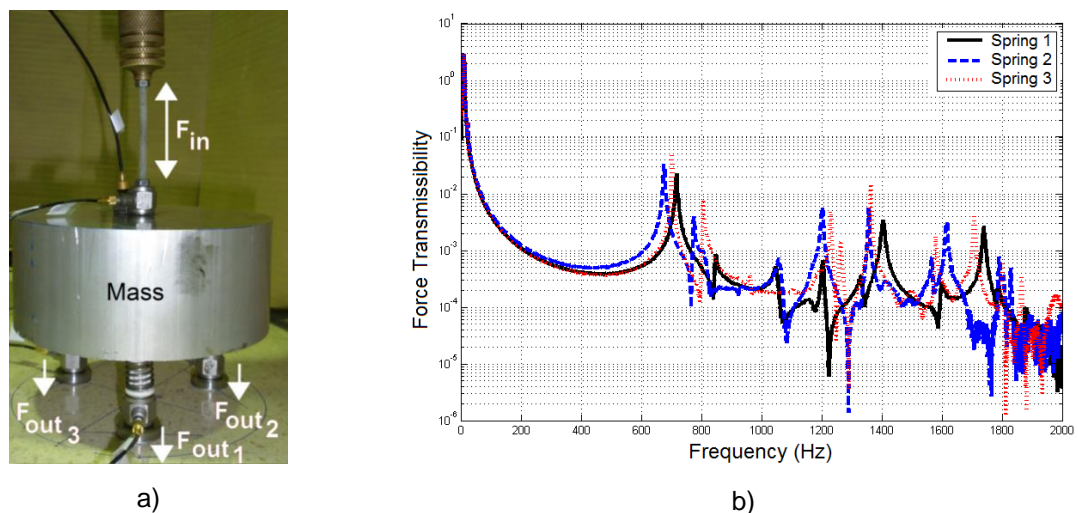
Figure 4.30 – Case i): Load mass supported by helical springs: a) experimental setup; b) force transmissibility curves.

For case i), it was verified that the dynamical behavior, with emphasis on the natural frequencies, of the three helical springs are not equal, as expected. However, it may be considered similar and located within a small enough bound that allows identification.
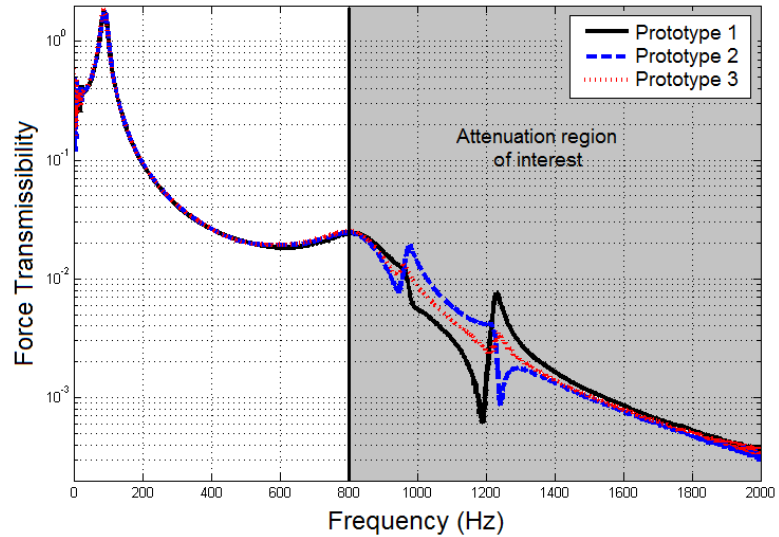
Figure 4.31 – Case ii): Load mass supported by PIVI-1: a) experimental setup; b) force transmissibility curves.

In case ii), it is verified that the PIVI-1prototypes present a similar dynamic behavior presenting an AR of interest after approximately 800 Hz. Note that even though two flexural modes are present nearby 1 kHz and 1.23 kHz, with more significance for prototypes 1 and 2, these do not influence the longitudinal AR of interest.
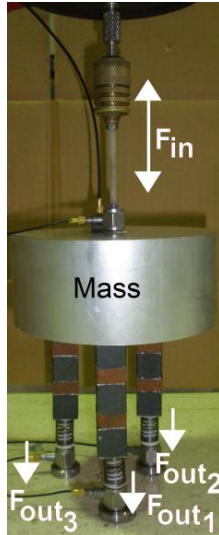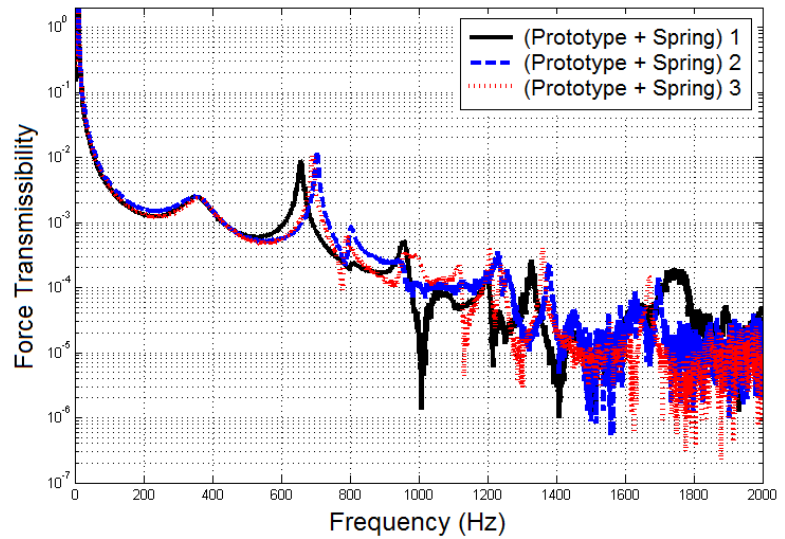
Figure 4.32 – Case iii): Load mass supported by the combined structures (prototype + spring): a) experimental setup; b) force transmissibility curves.

In case iii), the combined structures (prototype + spring) present a similar dynamic behavior even though, the combined structure 1 (solid curve) presents a lower natural frequency relative to the other two combined structures. Similarly to case i), it is considered to be located within a small enough bound that allows identification.

To compare the relative performance, in terms of force transmissibility, of each type of supporting device, i.e., spring, prototype and the combined structure (prototype + spring) the force transmissibility curves of each of device (in this case position 3 was chosen) are illustrated in Figure 4.33.
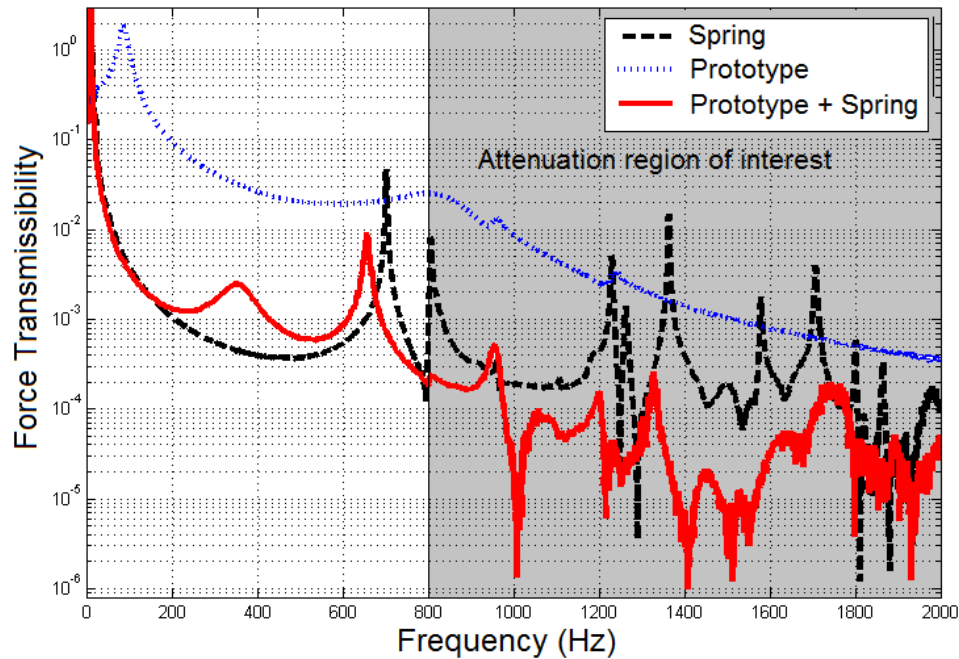
Figure 4.33 – Force transmissibility curves of the helical spring, the PIVI-1 prototype; and the combined structure (PIVI-1 prototype + spring).

From Figure 4.33, it is verified that the combined structure (solid line) is capable of effectively reducing the amplitude of the springs responses (dashed line) with emphasis at the natural frequency within the prototypes AR (shaded area), i.e., after approximately 800 Hz.

Thus, with the combined structure it is possible to improve isolation of a source of vibration, in terms of force, with a PIVI device that has an AR in a specific frequency range, which acts as a "filter", and still maintains the flexibility of the support due to the combined spring. That flexibility is important for shock absorption but is out of the scope of this study.

This conception can be useful and applied in several mechanical applications.

4.13.9. Test with motor of hermetic compressor supported by springs and the combined structure (PIVI-1 and spring)

Instead of a load mass, consider that the working motor of a hermetic compressor, illustrated by Figure 4.18, is supported by: i) the original helical springs that equip the hermetic compressor and; ii) the combined structure consisting of PIVI-1 and the springs.

To study the dynamic behavior, in terms of force transmissibility (see sub-chapter 2.8), of the two supporting device cases, consider the experimental setup (based on the one presented sub-chapter 4.6) and illustrated by Figure 4.34, that may be summarized as follows.
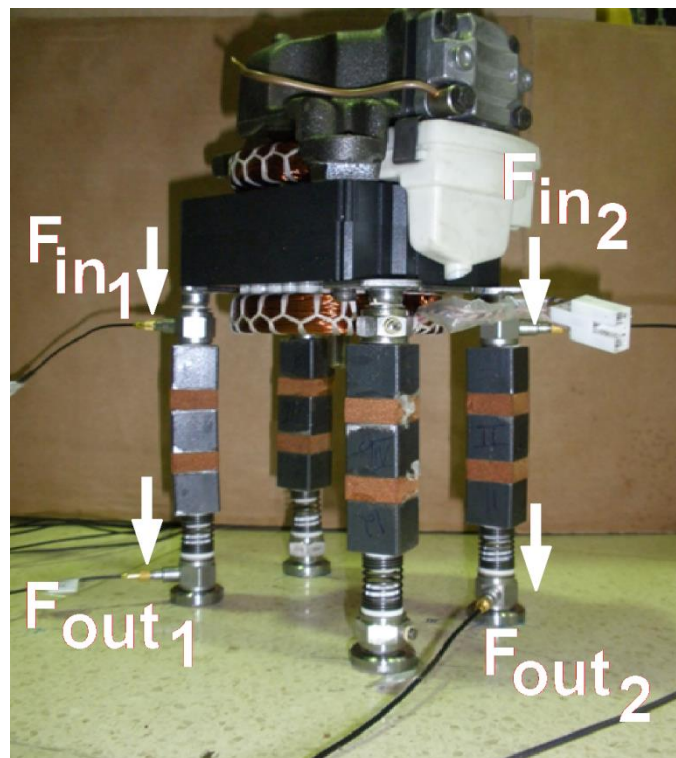
Figure 4.34 – Photograph of a motor of a hermetic compressor.

The source of vibration is the motor itself that at the time of the experiment is working (as it was directly connected to the electricity net), so no vibration exciter is used. During the experiment, the piston and cylinder are manually lubrified to avoid overheating and consequently damage to the motor. Furthermore and as a precaution, the motor runs for approximately 1 minute and then rests at least 5 minutes before the next experiment.

This specific motor has four support points thus, it requires four supporting devices and consequently it would require eight force transducers to measure the input and output forces at all four support points. However, only four force transducers (PCB 208C01) were available and it was decided to used them to measure the force transmissibility at two of the four support points, see Figure 4.35 a) and Figure 4.36 a). On the other two support points, "dummy" force transducers (simulating the presence of functional force transducers from which no data was obtained, see sub-chapter 2.4.2) were used, see Figure 4.35 b) and Figure 4.36 b).

First, the original springs that equip the hermetic compressor are tested (see Figure 4.35).

a)

"Dummy" force transducers (not connected)

b)
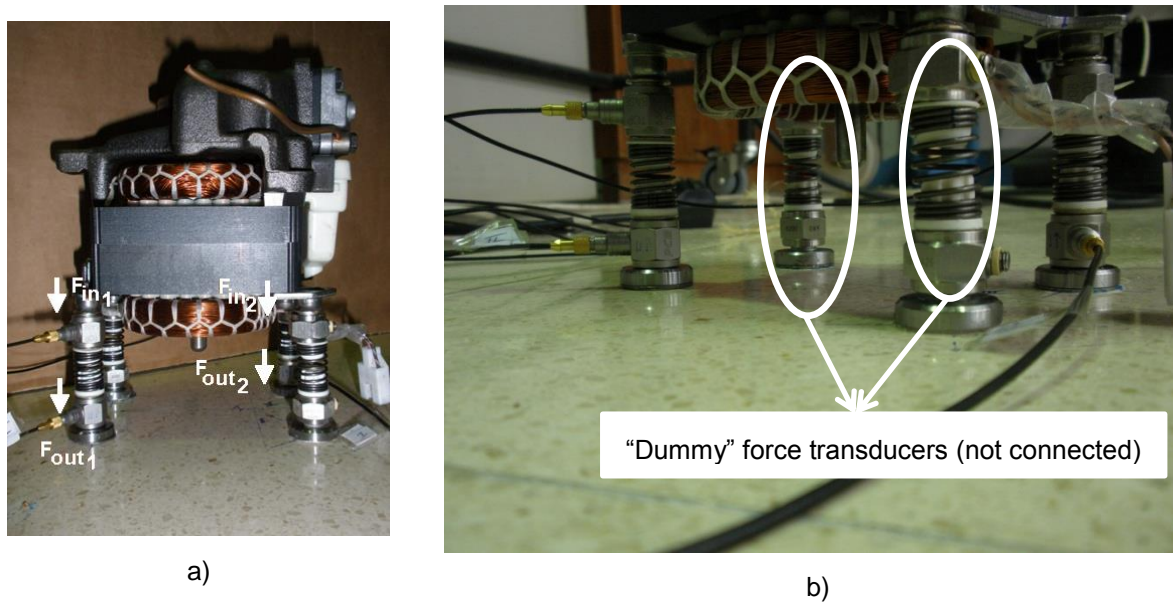
Figure 4.35 – Experimental setup of the motor of a hermetic compressor supported by helical springs: a) input-output points; b) force transducers not connected.

Then, the original helical springs that equip the hermetic compressor are combined with the PIVI-1 prototypes (see Table 4.9) and tested, see Figure 4.36.

a)

Force transducers

b)
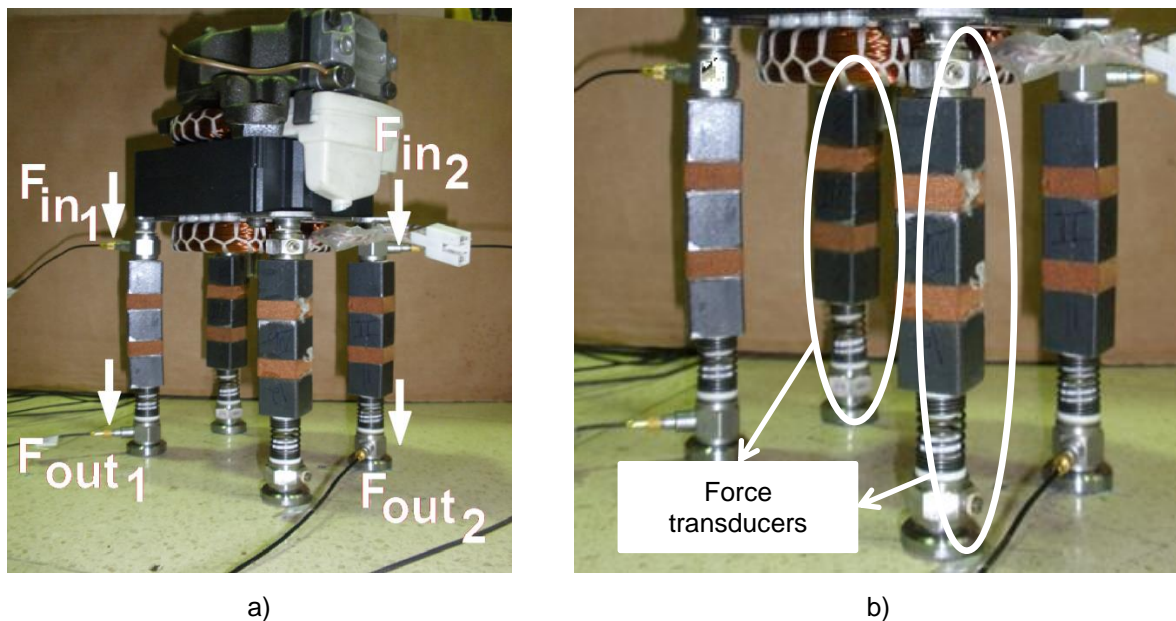
Figure 4.36 – Experimental setup of the motor of a hermetic compressor supported by the combined structure (PIVI-1 + spring): a) input-output points; b) force transducers not connected.

Figure 4.37 illustrates the force transmissibility curves obtained for the two supporting device cases previously referred, i.e.: i) the original helical springs that equip the hermetic compressor and; ii) the PIVI-1 prototypes combined with the springs.
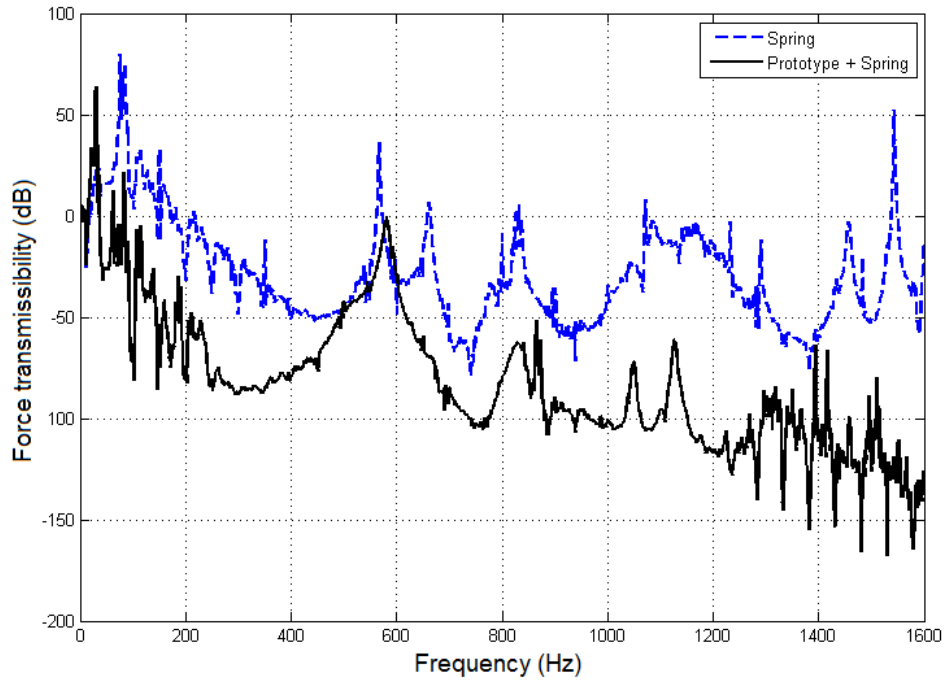
Figure 4.37 – Force transmissibility for the helical spring and combined structure (PIVI-1 + spring).

From Figure 4.37 it is evident that when the combined structure (solid line) is used (instead of the original helical springs (dashed line)) to support the working motor of hermetic compressor, in general the force transmissibility is lower. Even between 500-600 Hz it is not worst. This becomes more evident in the AR of interest (defined by the PIVI) that starts at approximately 800 Hz. Hence, it is possible to isolate vibration, in terms of force, with a PIVI that has an AR in a specific frequency range functioning as a "filter", and still maintaining the flexibility due to the spring.

At least from this point of view, the concept, design and application of PIVIs are sought to have a significant impact in the development of better vibration isolation devices as it presents a real isolation improved alternative and/or solution for several mechanical applications.

4.14. Conclusions on phononic-inspired vibration isolator

In this sub-chapter are presented the original contributions and main conclusions regarding a new concept of 1D vibration isolators that were inspired on phononic structures hence, its designation of PIVI.

This works shows that combining PIVIs with springs has considerable effects in the reduction of the force transmissibility. The combined structure achieves at certain points 50dB of reduction and practically never present worst transmissibility than the original spring by itself.

The author proposes in this chapter methodologies to perform analytical and numerical simulations/predictions as well as experimental methodologies to confirm the values with the prototypes built for this effect.

The original contributions regarding the PIVIs, consists of the design, development and application of PIVIs that consists of a periodic bar with alternating layers of two materials with a significant

contrast in their wave phase velocities that together with the proper length of the cell (thickness of the layers) define the ARs widths and location in frequency ranges that are of interest for several mechanical applications. Recall that prior to this study, these type of phononic structures were not intended to function as mechanical vibrations isolators (presenting total lengths > 1 m) and with ARs in the kHz range.

Thus, a solution that contemplates the use of different pairs of steel and CCMs was adopted in this study. Even though several other material pair combinations and cell lengths were used, e.g., brass-urethane, the longitudinal stability of the isolator was a significant problem in those cases. For that reason, at this study these were not considered as an interesting and feasible solution from the application point-of-view.

Another aspect is that the hybrid analytical-experimental methodology (presented in chapter 3) was fundamental to characterize, in terms of dynamic modulus, the different CCMs used in the development of these PIVIs. Without that development many of these achievements would not have been possible at the modeling level.

Furthermore, structural design procedures, FE analysis, optimization techniques, prototyping and modal testing were essential for the development of both numerical and experimental models of PIVIs that present significantly wide ARs in frequency ranges of interest for several mechanical applications.

Modal testing was conducted on:

i) two CVIs and on five PIVIs to assess the performance of these devices, in terms of force transmissibility. Results evidentiated the presence of greater attenuation reduction (between 25 dB and 100 dB at e.g., 1600 Hz) for the steel-CCMs PIVIs relatively to the CVIs;

ii) on a load mass (that simulates the mass of the motor of a hermetic compressor) that was supported first by springs and then by combined structures consisting of PIVIs and springs. Results show that the combined structure is capable of effectively reducing the amplitude of the force transmitted by the helical springs within the AR of the PIVI (i.e., after approximately 800 Hz);

iii) a working motor of a hermetic compressor (excitation source) that was supported first by springs and then by combined structures consisting of PIVIs and springs. As in case ii) results evidentiate the capability of the combined structure in isolating vibrations. The PIVI has an AR in a specific frequency range operating as a "filter" and the spring maintain the flexibility of the combined supporting device.

Further criteria such as: fatigue, durability, effect of temperature and humidity, etc. were not considered in this study. Additionally, protecting these devices from fluids e.g., oil, and the redesign of the connections to the motor are also topics that should be addressed in future work.

In the author's opinion, this study demonstrates the capability, relevance and impact that these PIVIs present for noise and vibration reduction applications as they can be design to suite a specific AR in the frequency range, its width, and level of attenuation. Unfortunately, and as far as the author knowledge, this aspect does not appear to be addressed by actual producers of isolation systems.

Chapter 5

Surface Damping Treatments

5.1. Introduction

Surface damping treatments (SDTs) are a way for vibration reduction, usually associated to sheet metal structure vibration reduction, by means of passive techniques [1]. Such treatments are classified according to whether the damping material is subjected to predominant extensional or shear deformation and are referred to as extensional or FLD or unconstrained and as shear or CLD treatments, respectively.

Due to an increasing concern on the vibro-acoustic comfort of the passengers, several studies on the performance of the SDTs have been conducted for different transportation areas, such as: automotive [65]-[67], railway [68], and aerospace [65] and [69]. Usually the vibrations are transmitted along different paths to the components (e.g., panels) causing discomfort to the passengers.

To improve it, FLD and CLD treatments are currently available and being applied in the industry. Generally, the FLD treatments are applied using solid polymeric viscoelastic material sheets, e.g., asphaltic melt sheet (with a mass density varying between 1200 kg m^{-3} and 1600 kg m^{-3} [70]) or liquid polymeric damping sprays designated as liquid applied sprayable damper (with a mass density of approximately 1000 kg m^{-3} [70]). The CLD treatments, in most cases, involve the addition of a damping layer (similarly to the FLD treatments) and an additional metallic constraining layer [71].

However, for applications subjected to a wide range of temperatures like near of engine parts, exhaust systems, automotive panels, etc., the use of CCMs may be seen as an alternative low mass density, thermal and acoustic insulation solution which provides a damping capacity [30] over a wide temperature range, e.g., -60ºC to 150ºC.

It is clear that the benefits of the SDTs must be paid at least in terms of additional mass, resulting in additional fuel consumption. Thus, the challenge is to balance the comfort of passengers with the need to reduce mass and cost. Hence, in this chapter, the author studies the use of CCM sheets, which have a mass density of approximately 200 kg m^{-3}, in both FLD and CLD treatments. Note that with the exception of the author's works ([81], [148] and [149]) no reference to the use of CCMs in SDTs was found by the author in the researched literature.

Even though in general, the CLD treatment is more efficient than the FLD treatment, for a given weight of damping material, it presents greater complication in both analysis and application [69]. In

this context, numerous reported approaches to fully automate optimization of SDTs may be found in the literature [72]-[80].

For example, Eschenauer and Wodtke [72], Yildiz and Stevens [73] and Lumsdaine and Scott [74] studied the optimal design of the damping layer distribution with variable thickness on thin walled structures using different optimization methods. Bandini et al. [75] considered a constant thickness of the damping layer and used a genetic algorithm to control the evolution and a FEM to evaluate the performance of the configurations. In [76], Lin and Scott studied the FLD and CLD treatments in beams and optimized the shape of a damping layer for both. To find optimal and "allowable" positions of damping materials Alvelid [77] proposed a modified gradient method. To design optimal SDTs Zheng et al. [78] used the topology optimization with the method of the moving asymptotes approach. In [79], the author presents a structural topology optimization scheme to evaluate the performance of a FLD treatment with constant thickness. Afterwards in [81], the author extended a similar optimization scheme to the CLD treatments and to the use of CCMs as the damping layer material.

In this study (in which, all contents are original contributions except when referenced to the respective authors) a simplified car body in white (BIW), i.e., a bare body after welding but before painting, FE model is developed for optimization of the FLD and CLD treatments applied to the inside floor of the car. For this, the author developed a structural topology optimization scheme (in which commercial FEM software is used) to evaluate the performance and the use of CCM as the damping layer material in SDTs with constant thickness. The SIMP idea [80] (previously introduced as solid isotropic material with penalization) is used to model the properties of the material used in the SDTs. The properties are assumed constant within each element used to discretize the design domain in which the stiffness is proportional to density in the power n (>1). The optimization results are mostly "black-and-white", i.e., either additional damping material is present in that element or it is not.

The results obtained with the implemented method illustrate the capability of the developed methodology for improving the efficiency of the SDTs within a predefined range of frequencies.

To conclude this introductory sub-chapter, the respective chapters layout follows.

This chapter, is composed of eight sub-chapters. This first introductory sub-chapter is followed by a second sub-chapter where the FLD and CLD SDTs are briefly introduced. In the third sub-chapter is presented the FE parameterization adopted. This is followed by a fourth sub-chapter in which the formulation for the structural optimization problem solved here is presented. In the fifth sub-chapter are presented the FE models developed and used in this study for structural analysis. The sixth chapter regards the experimental setup used to obtain the modal test data to validate the numerical models. The seventh sub-chapter contains the main results and their discussion. To conclude, the main contributions and conclusions regarding this chapter are presented in the eighth sub-chapter.

5.2. Unconstrained and constrained surface damping treatments

SDTs are usually designated according to whether the damping material is subjected to predominant extensional or shear deformation and are referred to as FLD or CLD treatments, respectively.

In this study, it is assumed that there is no slipping between the elastic and viscoelastic layers at their interfaces (see Figure 5.1, and Figure 5.2). Thus, the analyses assume rigid connections between the various layers of the system. However, in practice and because in general most damping materials are not self-adhesive, an additional adhesive layer is used. In this case, the thickness of the adhesive layer must be kept to a minimum [9].

For a detailed discussion of SDTs, such as effects of temperature, frequency, wavelengths, bonding techniques, etc., see Mead [2], Nashif et al. [9] and Jones [29].

5.2.1. Unconstrained surface damping treatments

The extensional, unconstrained or free layer damping treatment (FLD) consists of coating one or both sides of the structure with a damping material [2]. So, whenever the structure is subjected to cyclic flexure, the damping material is predominantly subjected to tension-compression deformation parallel to the plane of the structure (see Figure 5.1 where e_1 and e_2 are the thicknesses of the structure and of the damping material, respectively).
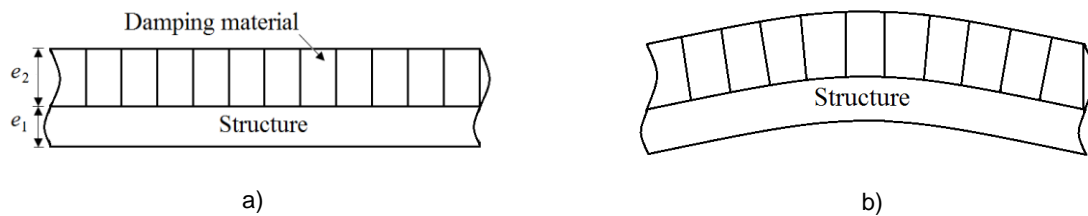
Figure 5.1 – FLD treatment – a) undeformed structure; b) deformed structure in flexure.

5.2.2. Constrained surface damping treatments

In the constrained damping treatment (CLD) the viscoelastic layer is constrained between two elastic layers [2], e.g., the structure and the metal sheet cover (see Figure 5.2 where e_1, e_2 and e_3 are the thicknesses of the structure, the damping material and the elastic layer, respectively). So, whenever the structure is subjected to flexure, the damping material layer is predominantly subjected to shear deformation, rather than tension-compression deformation. A generally accepted fact is that the CLD is more efficient in terms of dissipating energy in comparison with the FLD, see Mead [2], Nashif et al. [9] and Jones [29].
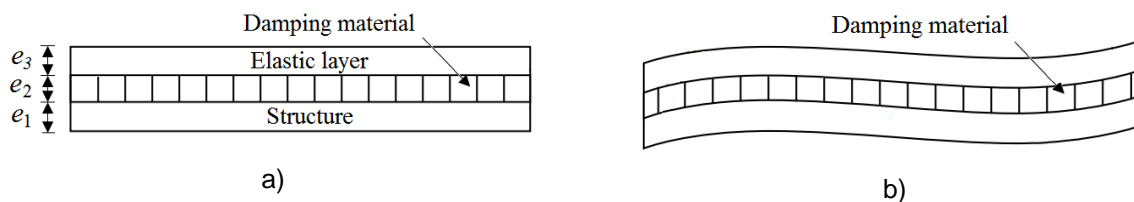
Figure 5.2 – CLD treatment – a) undeformed structure; b) deformed structure in flexure.

In engineering practice, simple structures are rarely encountered, but simplicity is helpful in understanding and developing the basic principles. For FLD, approximate equations (e.g., Oberst's

equation [29]) and various graphical information are available (see e.g. Jones [29]). For the CLD, several types of approximate equations are known, e.g., the Ross-Kerwin-Ungar (RKU) equation, which applies accurately only to beam like structures with pinned-pinned boundary conditions, even though being often applied to other boundary conditions, see, e.g. Jones [29]. More complicated structures with CLD treatment can be properly addressed, e.g., by FE analysis [29].

5.3. Finite element modeling

In this study, it is assumed the RM plate taking into account an approximate shear stress distribution over the thickness, see sub-chapter 2.5.2.5.

The FE models of the structures are built considering a number of FEs (N_{elem}) in the X and Y directions as illustrated by Figure 5.3. Even though one could allow several elements throughout the thickness of the damping layer, such an approach would require a significantly larger number of elements. Furthermore, as the optimization process may involve many FE runs, the time required would be computationally larger. Thus, only one element was used for the damping layer through the thickness. It is verified that this captures the essential features of the FLD and CLD behaviors.

The base structures, illustrated by the dark gray areas in Figure 5.3, are modeled with RM plate elements defined by four nodes and having six degrees of freedom at each node (translations in the nodal x, y, and z directions, and rotations about the x, y, and z axes), see SHELL181 element in [150] for more details).

The damping layer and the constraining elastic layer, see Figure 5.3, are modeled using solid FEs defined by eight nodes and having three degrees of freedom at each node, translations in the nodal x, y, and z directions, (see SOLID45 element in [150] for more details).
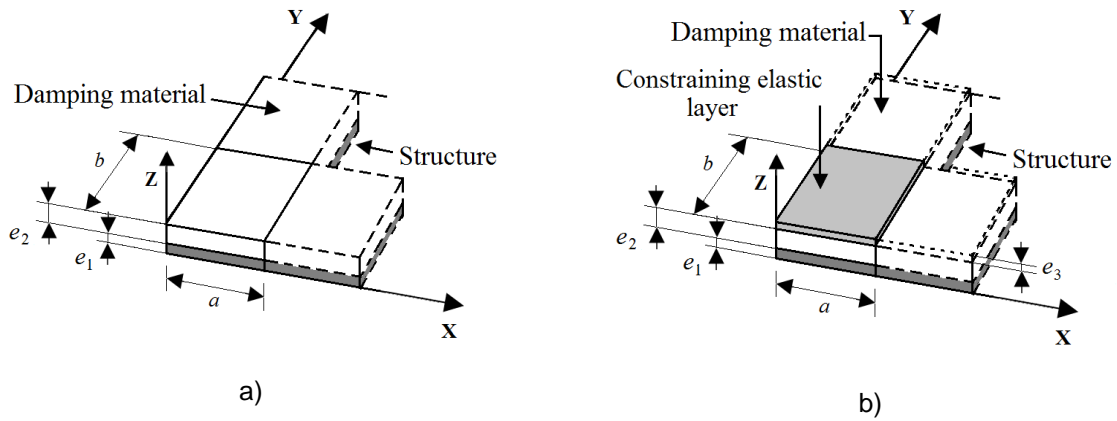
Figure 5.3 – Parameterization of the structure – a) unconstrained damping treatment; b) constrained damping treatment.

The geometric parameters of the elements are their lengths a and b, and the thicknesses e_1, e_2 and e_3 of the structure, the damping material and the elastic constraining layer, respectively.

As previously referred, and with more emphasis in the transportation industry, a compromise has to be made between the performance of the SDTs and the additional weight inherent to its use. One

obvious way of minimizing the SDT additional weight is to use lighter damping materials, e.g., CCMs, as previously referred. Furthermore, it is common practice to use topology optimization techniques (see e.g., [78], [79] and [81]) to determine the optimal layout distribution of the SDT over the structure.

5.4. Structural optimization method

In this study, the structural optimization problem (see sub-chapter 2.7) consists of finding an optimized layout of the uniform thickness for both FLD and CLD treatments that are spatially distributed over the vibrating structure.

For this, a topology optimization problem is formulated as

$$\min_{p_i} \left[\sum_{j=1}^{N} \left(\max_{\omega \in [\omega_{\min}, \omega_{\max}]} |u(\omega)| \right)_j^2 \Big/ N \right]^{1/2} ,$$

$$s.t.$$

$$\sum_{i=1}^{N_{elem}} p_i \leq \text{Value defining the total area subject to SDT}$$

$$0 < p_i \leq 1,$$

(5.1)

where N_{elem} is the total number of elements to which the SDTs are applied.

The objective function consists of the root mean square of the maximum harmonic vibration response displacement $u(\omega)$ of one or more response points, N, of the structure for a specific frequency range $[\omega_{\min}, \omega_{\max}]$ from an initial value ($\omega_{\min}$) to a final value ($\omega_{\max}$), which contains one or more natural frequencies.

The design variable $p(x)$ indicates the existence (p = 1) or absence (p = 0) of the added damping layer in each point x, as it is characteristic of structural topology optimization problems. To relax the 0-1 problem to a continuum problem in]0,1], p can be relaxed to a "material relative density" value instead of the two extreme values.

By relaxing the problem, intermediate values of p_i (piecewise constant parameter of each element) are allowed which can be understood as a "porous" material, which properties can be computed by

$$E_i^{'} = p_i^n E^{'}; \qquad \eta_i = p_i^{n-1} \eta; \qquad \rho_i = p_i^{n-2} \rho.$$

(5.2)

To preserve the mesh and avoid computational problems, a value close to zero (e.g., $p_{\min} = 10^{-6}$) is used instead of zero. These properties follow the SIMP idea [80], where the stiffness is proportional to density in the power n (greater than one). This penalizes intermediate values of p_i and for $n \geq 3$ the result of the optimization is mostly "black-and-white" ($p = 1$ and $p = 0$, respectively).

For the numerical optimizations a SQP algorithm (see e.g., [113] for more details) and an iterative procedure with the following steps are implemented: 1) Initialize by giving initial design values; 2) Run a harmonic analysis for the initial design; 3) Start the optimization loop. After writing the values of the current iteration design variables to a file, it will call the FE analysis in batch mode and will return to the optimization routine the current calculated values of the design variables and; 4) After satisfying the stopping criteria (constraints or predefined stopping parameters), run a harmonic analysis for the final design.

5.5. Finite element models for structural analysis

In this study, and before applying the structural optimization procedure (described in sub-chapter 5.4) it is first considered the case of a FE model of a rectangular panel, see Figure 5.4, which is subject to FLD and CLD treatments. The objective is to obtain validated FE models for both types of SDTs, based on experimental modal tests which are addressed in the following sub-chapter. An introduction on the model validation can be found in sub-chapter 2.6, on the plate FE model in sub-chapter 2.5.2.5 and on the experimental model tests in sub-chapter 2.4.
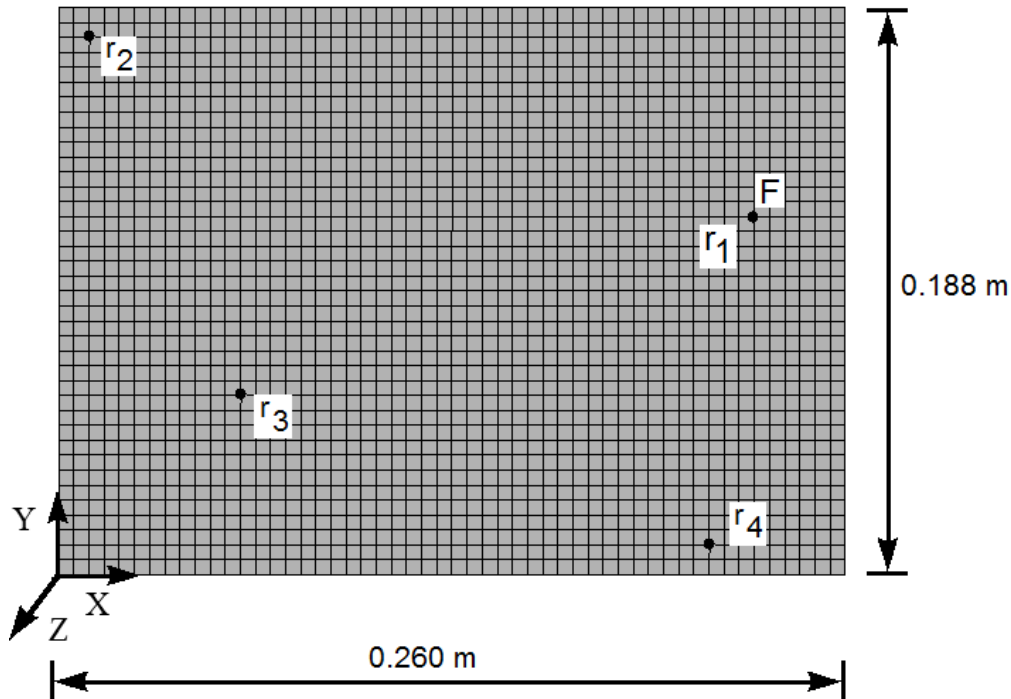
Figure 5.4 – FE model and discretization of the panel (coordinates of points F and r_1: X=230 mm and Y=125 mm; r_2: X=10 mm and Y=175 mm; r_3: X=60 mm and Y=70 mm; r_4: X=220 mm and Y=98 mm).

The panel has a thickness of 0.6 mm and is discretized using 52 FEs in the X direction and 38 FEs in the Y direction, see Figure 5.4 and Table 5.1 for additional parameterization details.

Once this FE model is validated, two other FE models of a cantilever plate, see Figure 5.5 a), and a simplified car BIW, see Figure 5.5 b), are developed and introduced to study the optimization of the material layout for both SDTs considering the procedure previously described in sub-chapter 5.4.

For each of the case, a steady-state (harmonic) force is applied at point (F) and the displacements are determined at points r, see Figure 5.4, Figure 5.5 a) and Figure 5.5 b). Note that point r is not visible in Figure 5.5 b) since it is located on the floor of the car FE model. However, its location is presented along with the respective results.
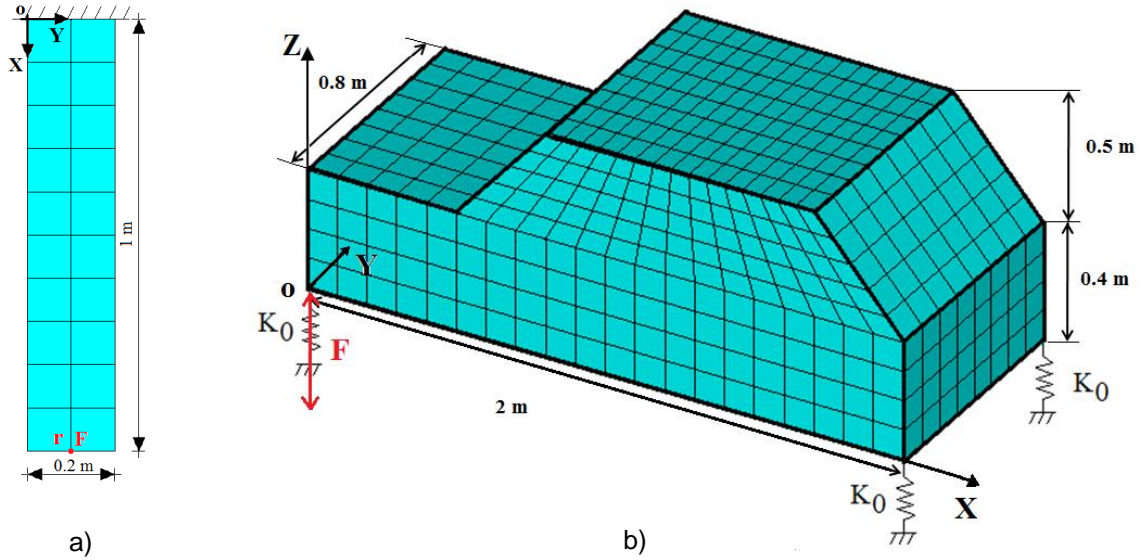
Figure 5.5 – Finite element discretization of the structures oriented according to the indicated coordinate axis OXYZ indicated: a) cantilever plate; b) simplified model of a car.

The dimensions and FE discretization of the models is as follows:

i) the cantilever beam with dimensions 1 m by 0.2 m is discretized using 10 FEs in the X direction and 2 FEs in the Y direction, see Figure 5.5 a) and Table 5.1. In this case, points F and r are coincident.

ii) the floor of the simplified car BIW FE model with dimensions 2 m by 0.8 m is discretized using 20 FEs in the X direction and 8 FEs in the Y direction, see Figure 5.5 b) and Table 5.1. Additionally, a uniform steel plate with a thickness of 10 mm was adopted for the shell of the car and was modeled using the RM plate element (see sub-chapter 2.5.2.5). Furthermore, to simulate the suspension (no dampers were included), four tension-compression springs (see sub-chapter 2.5.2.2) with a spring constant $K_0=30$ kN/m are applied. A steady-state (harmonic) force is applied at one of those corners (point F), as indicated in Figure 5.5 b).

Steel is considered for the structure and elastic layer (in the CLD treatment) while a CCM (NL20) is used as the damping layer. The material properties and geometric parameters of these materials (e_1, e_2 and e_3 illustrated in Figure 5.3) are presented in Table 5.1, and Table 5.2.

Note that the dynamic properties of the damping material used in this study (CCM - NL20) were determined using the hybrid analytical-experimental methodology based on a three-layer specimen with metallic extremities and an intermediate resilient layer of the CCMs developed and presented by the author in sub-chapter 3.3.

	N_{elem} in X	N_{elem} in Y	a (m)	b (m)	e_1 (m)	e_2 (m)	e_3 (m)
Panel	52	38	0.005	≈0.005	0.0006	0.002	0.0006
Plate	10	2	0.1	0.1	0.01	0.002	0.001
Car	20	8	0.1	0.1	0.01	0.002	0.001

Table 5.1 – Values of the geometric parameters.

	$E^{'}$ (MPa)	$G^{'}$ (MPa)	ν	ρ (kg/m^3)	η
Stainless steel (panel) [151]	220×10^3	-	0.33	7700	0.001
Steel (cantilever plate and car)	210×10^3	-	0.33	7850	0.001
NL 20 (see Table 3.6)	17.9	7.5	0.23	210	0.135

Table 5.2 – Material properties: longitudinal storage $E^{'}$ and shear storage $G^{'}$ moduli, and *Poisson's* ratio ν, mass density ρ and modal damping factor η.

Configuration	e_1 (mm)	e_2 (mm)	e_3 (mm)
1 – No treatment	0.6	-	-
2 - FLD	0.6	2.0	-
3 - CLD	0.6	2.0	0.6

Table 5.3 – Thickness , e_1, e_2 and e_3 for the different SDTs configurations.

5.6. Experimental setup and test panels for surface damping treatment

In this sub-chapter are presented the three experimental test panel configurations subject to experimental modal analysis, see Figure 5.6, and the respective experimental setup used for the purposes, illustrated by Figure 5.7.

Thus: i) first it is considered the panel without treatment; ii) second, the panel is subjected to a FLD treatment using a CCM as the damping material layer and; iii) the panel is subject to a CLD treatment in which a CCM is used as the damping layer and a similar steel panel is used as the elastic constraining layer (see Table 5.1 and Table 5.2 for material and geometric properties).

A high performance commercial adhesive tape (reference 3M$^{®}$ 467MP [152]) with a thickness of 50 μm is used to bond the damping material to the structure as well as to the elastic constraining layer.

<div style="text-align: center;">a)   b)</div>
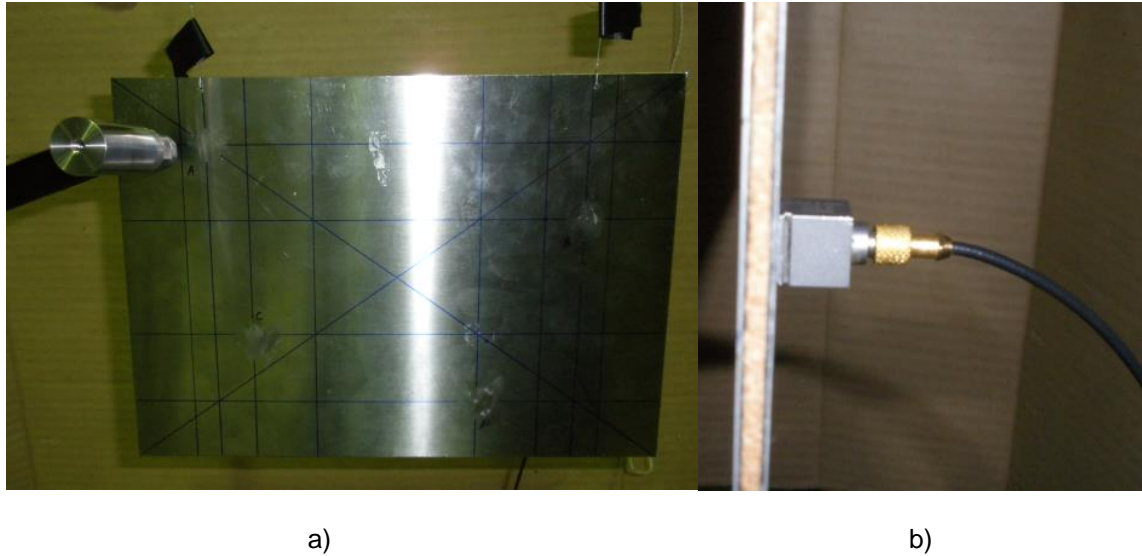
Figure 5.6 – Photographs of the experimental test panels: a) steel panel; b) constrained layer panel (side view).

To obtain the experimental FRF curves, one uses the experimental setup illustrated in Figure 5.7, i.e., with an impact hammer one applies to the panel a perpendicular force at point F, see Figure 5.4, that is measured through a force transducer (input signal). The dynamical deformation propagates throughout the panel and, on the back side of the panel, four accelerometers at points r, see Figure 5.4, measure the accelerations (output signals). The panel is suspended from a fix support by two thin elastic nylon strings.
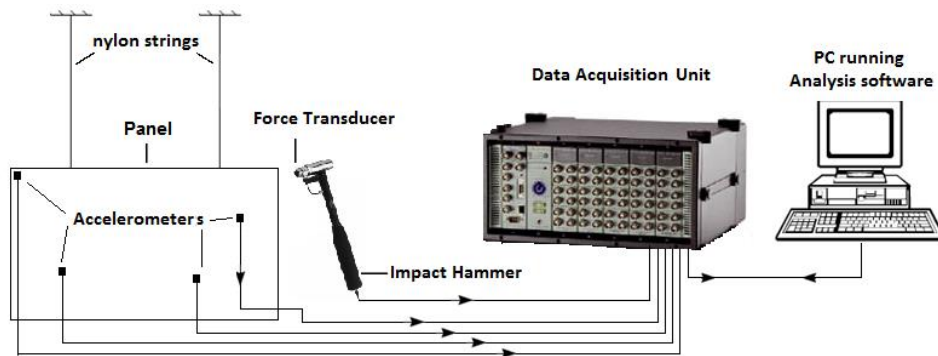
Figure 5.7 – Basic layout of the experimental setup to obtain the experimental FRFs.

The input and output signals are acquired by a data acquisition unit and analyzed using appropriate software. The FRF curve is recorded and compared with the one obtained numerically to validate the numerical model.

5.7. Results and discussion

In this subchapter are presented and discussed the main results obtained in the framework of the SDTs presented in this study.

5.7.1. Surface damping treatments on a metallic panel

The experimental FRF curves were obtained using the experimental prototypes and setup previously described in sub-chapter 5.6. Tests were conducted at an approximately constant temperature of 20.5ºC and a relative humidity of 39.9%. Even though FRFs were obtained at four points r, see Figure 5.4, next are only illustrated the FRF curves obtained at point r_1 as it present the main characteristics found in all and avoiding by this way an extensive illustrated sub-chapter. Nevertheless, the remaining illustrations regarding the other points are presented in Appendices A.8 and A.9.

Hence, Figure 5.8 illustrates the results obtained at point r_1 considering the panel without damping treatment (solid line), with FLD treatment (dot line) and with CLD treatment (dashed line).
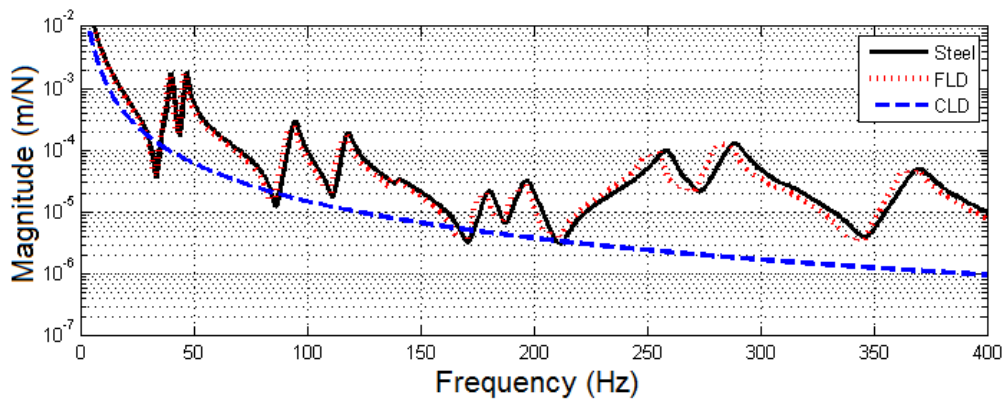
Figure 5.8 – Experimental FRF curves of a steel plate without treatment, with free layer damping treatment, and with constrained layer damping treatment (response at point r_1: X=230 mm and Y=125 mm).

From Figure 5.8, it is possible to see that the response of the panel with the CLD treatment (dashed line) presents a significantly lower magnitude relatively to the FLD treatment (dot line), which is similar in terms of magnitude to the case without treatment (solid line), confirming (as expected) the higher capability of the CLD in terms of SDT. When comparing the FLD treatment (dot line) to the case without treatment (solid line) there is a slight decrease of the magnitude at the resonances (damping effect) and as well as a shift of the resonances to lower frequencies due to the added mass of the damping layer.

Thus, from these experimental tests one can conclude that the use of this type of CCM in CLD treatments is capable of a significantly reducing the magnitude of the resonances.

These experimental FRF curves are compared with the numerical FRF curves which were obtained by conducting a harmonic response analysis, see Eq. (2.58), using FE models of the three panel configurations, as described in sub-chapter 5.5, before and after model updating (see sub-chapter 2.6.3).

The experimental (solid line), numerical (dotted line) and numerical after model updating (dashed line) for each case are illustrated in Figure 5.9 for the case without treatment, in Figure 5.11 for the

case with FLD treatment and in Figure 5.13 for the case with CLD treatment at point r_1. The remaining illustrations regarding the other points are presented in Appendix A.9.

Furthermore, the experimental and numerical updated FRF curves were then correlated using the FRAC, Eq. (2.59), and the FAAC, Eq. (2.60), assurance criteria and are illustrated by Figure 5.10 a) and Figure 5.10 b), before and after updating, respectively.
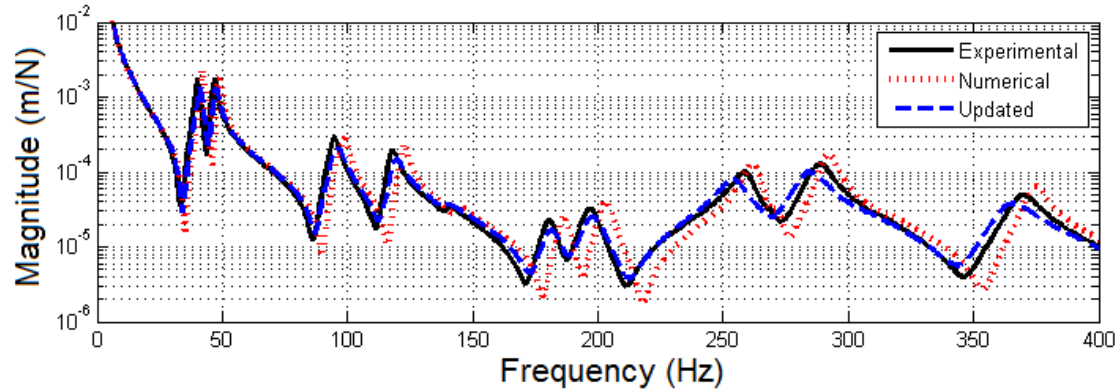
Figure 5.9 – Experimental and numerical FRF curves of a steel plate without treatment (response at point r_1: X=230 mm and Y=125 mm).
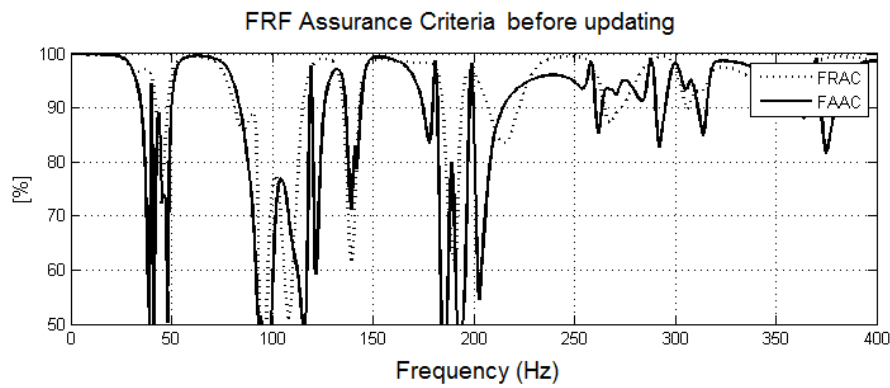
a)
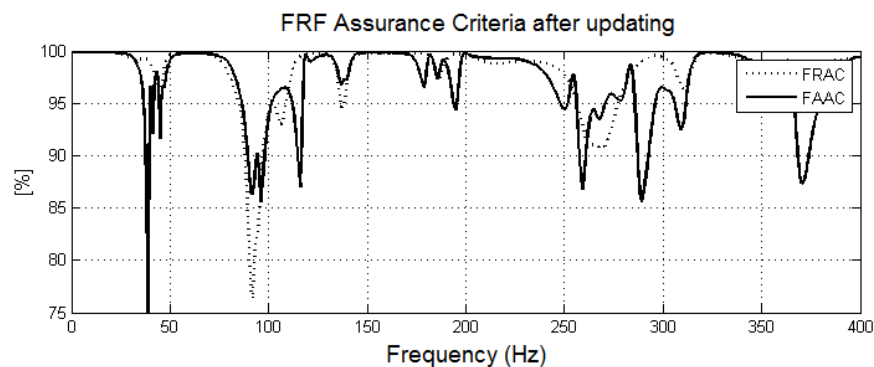
b)

Figure 5.10 – FRF correlation functions curves of a steel plate without treatment: a) before updating; b) after updating (response at point r_1: X=230 mm and Y=125 mm).

For the case of the panel without treatment, the experimental and numerical results obtained, see Table 5.4, present a maximum relative error in the first natural frequency of 4.76%. However after model updating, this value decreases to 2.5%. The FRF curves illustrated in Figure 5.9, namely the experimental (solid line) and numerical (dotted line) updated (dashed line) show a satisfactory agreement as also indicated by the FRF assurance criteria curves illustrated in Figure 5.10 b). In general, the FRAC and FAAC curves present values above 75% after updating.
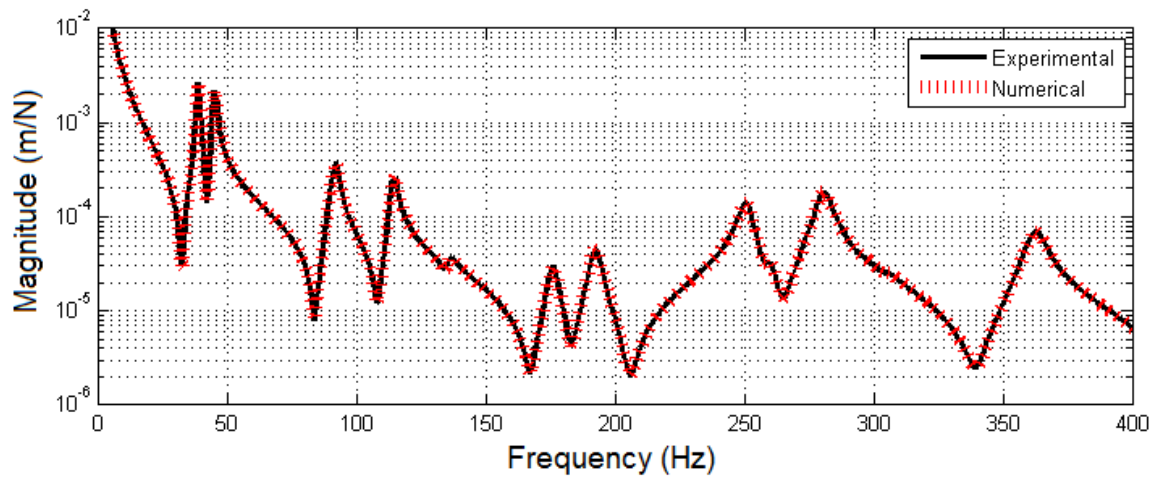
Figure 5.11 – Experimental and numerical FRF curves of a steel plate with free layer damping treatment.
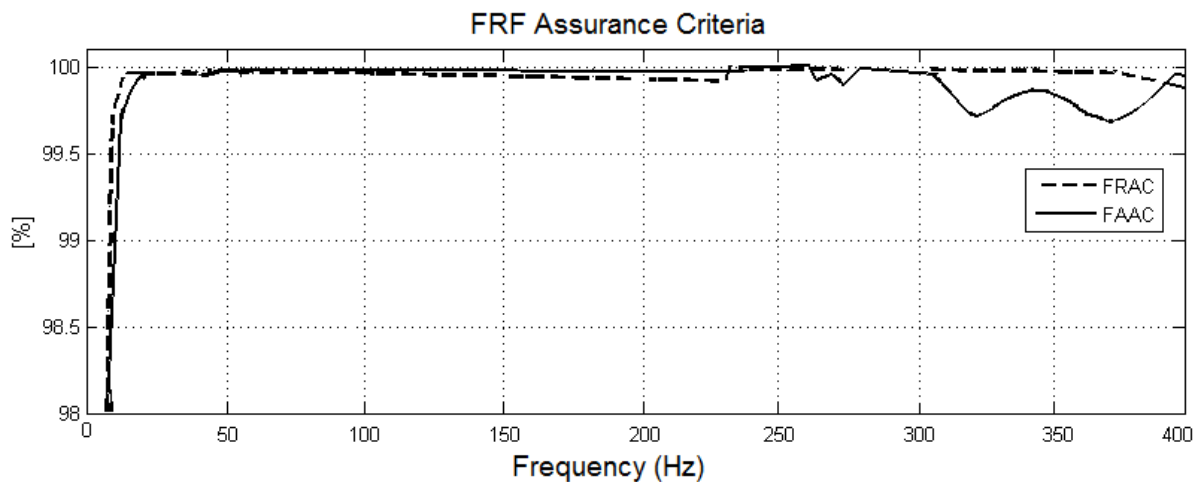
Figure 5.12 – FRF correlation functions curves of a steel plate with free layer damping treatment.

For the case of the panel with FLD treatment, the experimental and numerical results obtained, see Table 5.5, present a maximum relative deviation in the sixth natural frequency of 0.80%. Thus, no updating was conducted for the FLD treatment. The FRF curves illustrated in Figure 5.11, namely the experimental (solid line) and numerical (dotted line) show a satisfactory agreement as also indicated by the FRF assurance criterions curves illustrated in Figure 5.12. Beyond 10 Hz, the FRAC and FAAC curves present values above 99.5%.
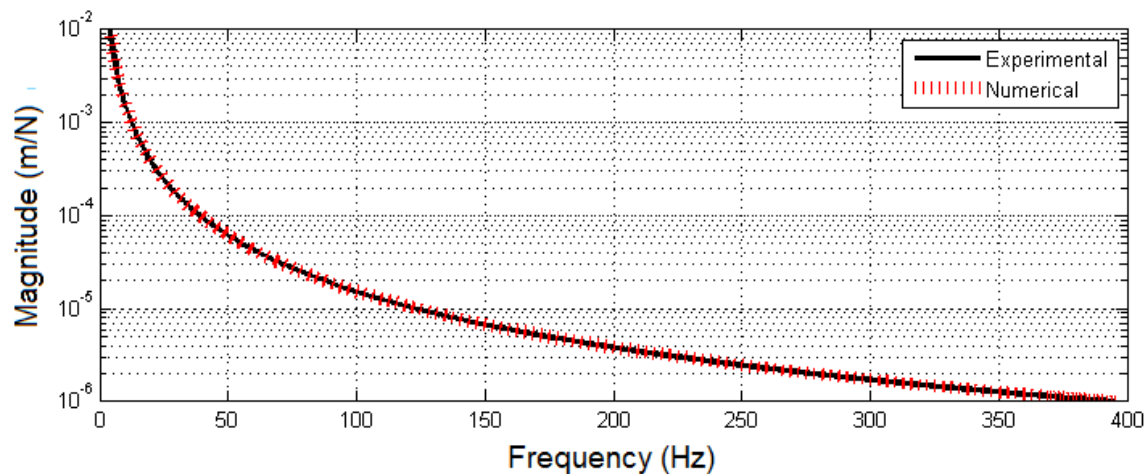
Figure 5.13 – Experimental and numerical FRF curves of a steel plate with constrained layer damping treatment.
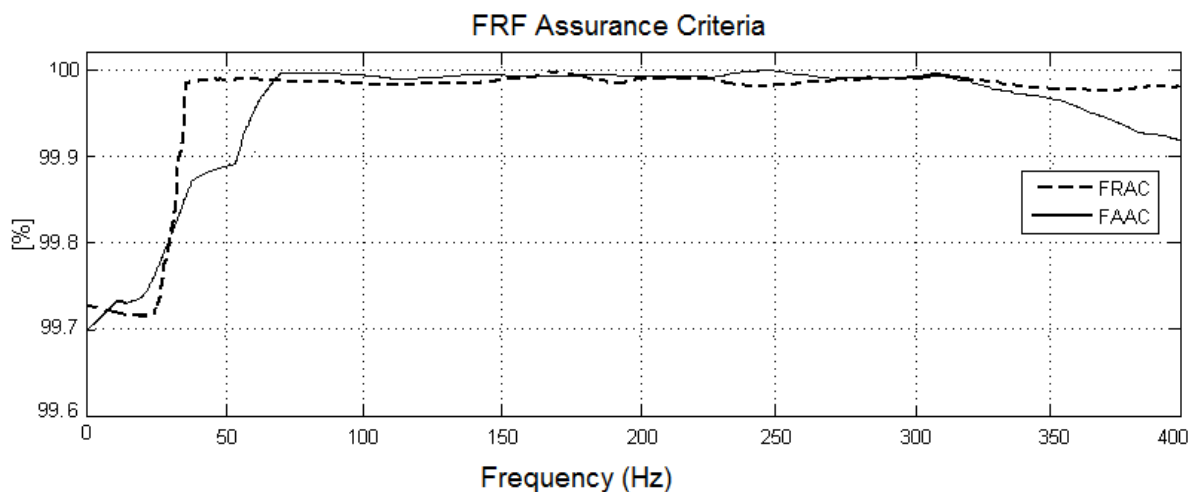
Figure 5.14 – FRF correlation functions curves of a steel plate with constrained layer damping treatment.

For the CLD treatment, see Figure 5.8 (dashed line) and Figure 5.13, the values of the natural frequencies are not identifiable just by looking at the curves. Even though, the FEM results are known, the experimental values would have to be estimated using, e.g., an adequate modal analysis identification method, which is not always as simple to implement. Nevertheless, it is consensual to say that the FRF curves illustrated in Figure 5.13, namely the experimental (solid line) and numerical (dotted line) show a satisfactory agreement as also indicated by the FRF assurance criteria curves illustrated in Figure 5.14. Beyond 20 Hz, the FRAC and FAAC curves present values above 99.9%.

The experimental and numerical results obtained in terms of the values of the natural frequencies and respective relative deviations for the panel without and with FLD treatment are presented in Table 5.4. and Table 5.5, respectively.

Natural frequency	Configuration 1 - Panel without surface damping treatment				
	Experimental	FEM	FEM Updated	Relative deviation FEM	Relative deviation FEM Updated
1	40 Hz	42 Hz	41 Hz	4.76%	2.50%
2	47 Hz	49 Hz	48 Hz	4.08%	2.13%
3	95 Hz	99 Hz	96 Hz	4.04%	1.05%
4	118 Hz	122 Hz	119 Hz	3.28%	0.85%
5	180 Hz	186 Hz	180 Hz	3.23%	0.00%
6	197 Hz	203 Hz	197 Hz	2.96%	0.00%
7	289 Hz	292 Hz	288 Hz	1.03%	0.35%
8	370 Hz	375 Hz	369 Hz	1.33%	0.27%

Table 5.4 – Experimental, numerical and numerical updated natural frequencies for the panel without treatment.

| Natural frequency	Configuration 2 - Panel with FLD treatment		
	Experimental	FEM	Relative deviation FEM
1	39 Hz	39 Hz	0.00%
2	45 Hz	45 Hz	0.00%
3	92 Hz	92 Hz	0.00%
4	115 Hz	115 Hz	0.00%
5	176 Hz	176 Hz	0.00%
6	253 Hz	251 Hz	0.80%
7	283 Hz	282 Hz	0.35%
8	366 Hz	365 Hz	0.27%

Table 5.5 – Experimental and numerical natural frequencies for the panel with free layer damping treatment.

In Table 5.6 are indicated the model parameters subject to updating and the respective values before and after the updating.

Model parameters	Before updating [151]	After updating
$E^{'}$ (MPa)	220×10^3	216×10^3
ρ (kg/m^3)	7700	7760
η	0.005	0.015
e_1 (m)	0.0006	0.000597

Table 5.6 – Model parameters used in updating.

Note that it was not necessary to update the parameters of the CCM to obtain a satisfactory agreement between the experimental and numerically updated models. This is due to the rigorous proposed methodology previously presented (see sub-chapter 3.3) and used in this study to

characterize the dynamic modulus of the CCM used as the damping layer for both FLD and CLD treatments.

As previously referred, the experimental and numerical updated FRF curves show a satisfactory agreement among each other and the FRAC and FAAC curve values further justify this agreement. In this sense, the numerical updated model is validated. Hence, it is considered suitable for further analyses.

5.7.2. Structural optimization results

The structural optimization formulation, previously described in sub-chapter 5.4, is first applied to the FE model of the cantilever plate illustrated by Figure 5.5 a). The cantilever plate is harmonically excited at point F with the displacements determined at point r, see Figure 5.5 a). The goal is to minimize the objective function (root mean square of a certain point over the frequency range of interest) expressed in Eq. (5.1) in a frequency range that contains the first natural vibration mode [1-20 Hz], subjected to a 30% of the total damping treatment area (considering a constant thickness). The material and geometric properties are presented in Table 5.1 and Table 5.2.

The results obtained are presented in Table 5.7 and are illustrated in Figure 5.15 and Figure 5.16.

Type of damping treatment →	FLD		CLD	
	Displacement	Mass	Displacement	Mass
Initial (without damping)	240.00 mm	15.700 kg	240.00 mm	15.700 kg
Before optimization (p_i =0.5)	30.83 mm	15.742 kg	20.52 mm	16.527 kg
Optimized	20.32 mm	15.742 kg	1.06 mm	16. 527 kg
Optimized variation relative to the initial design	90.33%	+0.16%	99.56%	+3.06%

Table 5.7 – Cantilever plate results.

a)

Damping material

b)

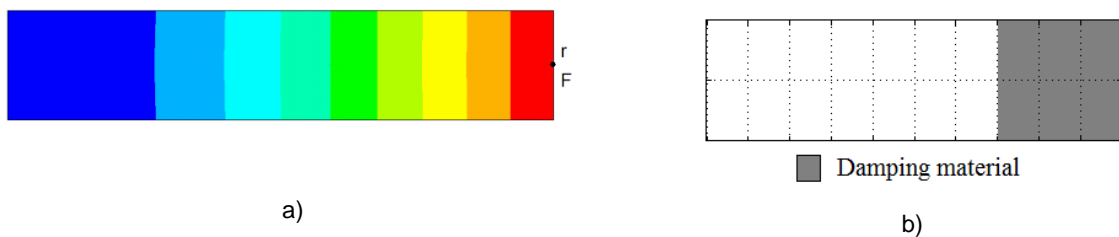Figure 5.15 – Cantilever plate clamped at left extremity: a) 1st natural vibration mode (with indication of points r and F); b) optimized material distribution.

After application and optimization of the SDTs, see Figure 5.15 b), the displacements were minimized by approximately 90.3% (see Table 5.7 and Figure 5.16 a)) and by approximately 99.5% (see Table 5.7 and Figure 5.16 b)) for the FLD and CLD treatments, respectively.

Figure 5.16 – Displacement curves of cantilever plate with no damping treatment, before and after optimization considering: a) free layer damping treatment; b) constrained damping treatment.

This was achieved with approximately 0.16% and 3.06% of additional mass for the FLD and CLD treatments, respectively. In this case, it can be observed that the optimized material layout, see Figure 5.15 b), is similar for both FLD and CLD treatments (due to the added mass at the tip while shear is constant along all the beam).

In a similar way, the structural optimization formulation, previously described in sub-chapter 5.4, is applied only to the inside floor of a simplified car BIW FE model illustrated by Figure 5.5 b) keeping the other panels without damping treatment. A steady-state (harmonic) force is applied at one of those corners, as indicated in Figure 5.5 b) and the respective response displacements determined at point r, which is not visible in the same figure since it is located on the floor of the car FE model. However, its location is presented along with the results. Once more, the goal is to minimize the objective function expressed in Eq. (5.1) in a frequency range that contains the first vibration mode of the floor [20-60 Hz] subjected to a maximum of 30% of the total damping treatment area (considering a constant thickness). The material and geometric properties are presented in Table 5.1, and Table 5.2. An initial distribution of SDT with $p = 0.5$ is considered over the entire floor panel.

The results obtained are presented in Table 5.8 and are illustrated in Figure 5.17 and Figure 5.18.

Type of damping treatment →	FLD		CLD	
	Displacement	Mass	Displacement	Mass
Initial (without damping)	15.78 mm	1256.00 kg	15.78 mm	1256.00 kg
Before optimization (p_i =0.5)	14.55 mm	1256.34 kg	1.76 mm	1259.97 kg
Optimized	5.03 mm	1256.20 kg	0.15 mm	1259.97 kg
Optimized variation relative to the initial design	68.12%	+0.02%	99.05%	+0.32%

Table 5.8 – Simplified car model results.

a)

b)
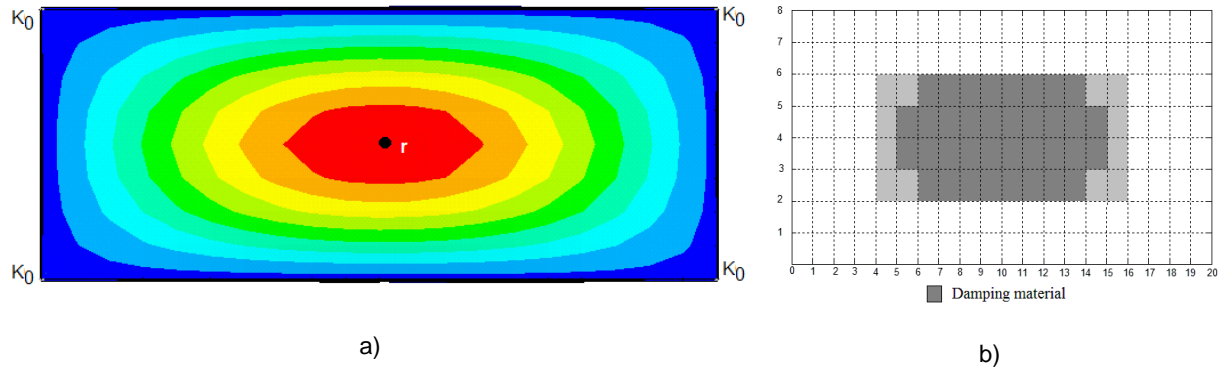
Figure 5.17 – Floor of the simplified BIW car model: a) 1st natural vibration mode (with indication of point r); b) optimized material distribution.

a)

b)
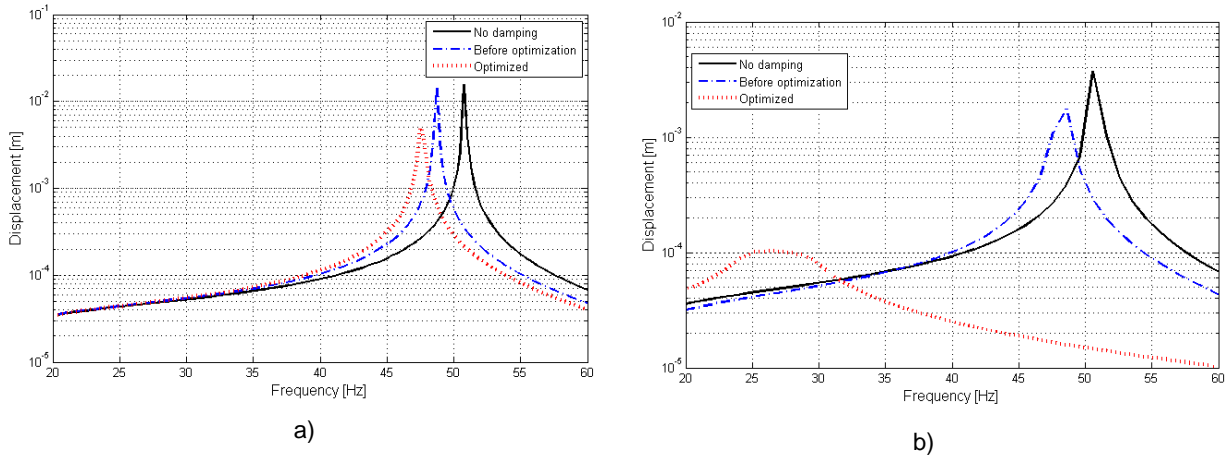
Figure 5.18 – Frequency response function curves of the floor of the simplified BIW car model with no damping treatment, before and after optimization considering: a) free layer damping treatment; b) constrained layer damping treatment.

After application and optimization of the SDTs, see Figure 5.17 b), the displacements were minimized by approximately 68% (see Table 5.8 and Figure 5.18 a)) and by approximately 99% (see Table 5.8 and Fi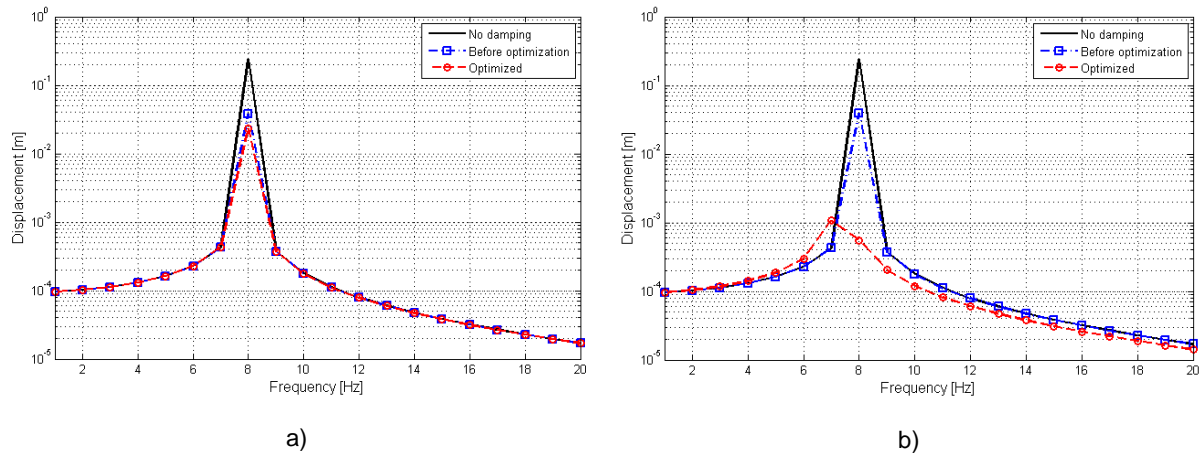gure 5.18 b)) for the FLD and CLD treatments, respectively. This was achieved with approximately 0.02% and 0.32% of additional mass for the FLD and CLD treatments, respectively. As in the cantilever beam, it can be observed that the optimized material layout, Figure 5.17 b), is similar in both FLD and CLD treatments.

5.8.   Conclusions on surface damping treatments

The original contributions of this sub-chapter regarding the use of CCMs in SDTs consist of the demonstrated capability of using CCMs in SDTs. Furthermore, and with it arises an alternative low mass density solution ($\approx$ 200 kg m^{-3}, whereas asphaltic melt sheet mass density varies between 1200 kg m^{-3} and 1600 kg m^{-3} [70] and liquid polymeric damping sprays mass density is $\approx$ 1000 kg m^{-3} [70]) with the additional advantage of providing a damping capacity over a wide temperature range, e.g., -60ºC to 150ºC.

Additionally, FE models that simulate the dynamic behavior of metallic panels subject to FLD and CLD treatments were updated and validated using experimental data. Note that due to the rigorous proposed hybrid analytical-experimental methodology presented in chapter 3, which was used in this study to characterize the dynamic modulus of the CCM used as the damping layer for both FLD and CLD treatments, it was not necessary to update the parameters of the CCM to obtain a satisfactory correlation agreement between the experimental and numerically updated models.

With the topology optimization procedure developed it was possible to improve the efficiency of the SDTs within a predefined frequency range. As expected, the CLD treatments revealed to be more efficient than the FLD treatment, for a given weight of damping material.

Even though this chapter is somewhat shorter in contents relatively to the previous ones, in the author's opinion it contains the initial and fundamental steps as well as the novelty that allows for the use of CCMs in several future new applications and for different areas of engineering.

Chapter 6

Contributions, conclusions and future works

In this thesis, theoretical, numerical and experimental models were formulated and developed allowing for characterization of the dynamic modulus of resilient materials and its application in dynamic analysis. This characterization, or material property identification, revealed to be essential for validating the numerical models that simulate the dynamic behavior of the two types of layer structures studied here, for a given frequency range and under steady-state conditions.

The main four original contributions of this study are:

i) A novel hybrid analytical-experimental methodology to determine the longitudinal dynamic modulus of resilient materials, with emphasis on cork composite material (CCMs);

ii) Perhaps still part of i) is the development/adaptation of the hybrid analytical-experimental methodology to determine the shear dynamic modulus of resilient materials, again with emphasis on CCMs;

iii) The design, development and application of phononic-inspired vibration isolators (PIVIs) that contemplates the use of different pairs of steel and CCMs presenting attenuation regions (ARs) that allow for vibration isolation in a frequency ranges of interest for several mechanical applications. With this is presented a novel perspective on the design of vibration isolators;

iv) Experimental and validated numerical models as well as a topology optimization methodology illustrating the potential use of CCMs in surface damping treatments (SDTs) which in the author's perspective presents an interesting alternative low mass density damping solution to the conventional polymeric materials.

Based on the work conducted to achieve these original contributions, one may list the principal conclusions of this study as:

a) The proposed hybrid methodology referred in i) revealed to be simpler (avoiding specific geometric and boundary constraints) and more rigorous (when compared to other methods), presenting a more accurate on hand alternative solution. Furthermore, the modal test consists of a simple setup and requires only the common equipment found in a vibration laboratory (i.e., impact hammer with force transducer, one accelerometer, data acquisition equipment and cables).

b) Even though the experimental setup of the proposed hybrid methodology, referred in ii) for the shear complex modulus is not as simple as the one referred in i), it still provides a rigorous on hand solution for which does not exist (to the author's knowledge) any simple and/or similar low cost alternatives.

c) Thus, with the proposed hybrid methodologies referred in i) and ii) one obtains a rigorous and prompt characterization of both the longitudinal and shear dynamic moduli, and with it, the bulk modulus and *Poisson's* ratio (under the assumption of the homogeneous isotropic linear elastic material behavior), of resilient materials.

d) The results obtained using the proposed hybrid methodology referred in i) were verified using dynamic mechanical analysis (DMA) and suggest for the tested CCMs a low frequency dependence for both the storage modulus $E^{'}$ and loss factor η in a frequency range between 1 Hz and 10^4 Hz.

e) Regarding the PIVIs, the numerical and experimental results obtained present a satisfactory agreement and evidentiate the significant ARs of interest in a frequency ranges of interest for several mechanical applications.

f) When comparing the performance (in terms of force transmissibility) of PIVIs with commercial vibration isolators (CVI) it is verified that the PIVIs present interesting attenuation reduction (e.g., for the cases tested it varies between 25 dB and 100 dB at 1600 Hz).

g) Furthermore, when the PIVI is combined in series with a spring it is verified that the combined structure is capable of effectively reducing the amplitude of the longitudinal force transmitted within the AR of the PIVI.

h) In this sense, it is demonstrated the capability, relevance and impact that these PIVIs present for noise and vibration reduction applications as they can be design to suite a specific AR in the frequency range, its width, and level of attenuation.

i) Regarding the SDTs, by using the topology optimization procedure developed it was possible to improve the efficiency of the SDTs within a predefined frequency range.

j) In this sense, one may conclude that the use of CCM presents an interesting alternative low mass density solution, to the synthetic viscoelastic materials commonly used, with the additional advantage of providing a damping capacity and thermal insulation over a wide temperature range.

For future works and among others, one may consider:

- How the changes in the temperature, humidity, age of the materials, amount of overload among other parameters, influence the dynamic modulus of the materials;

- Other criteria as fatigue, aging, etc., in the design of PIVIs;

- How to protect the PIVI from fluids (e.g., oil) by guiding and encapsulating;

- The redesign of the connections points in the case of the motor of the hermetic compressor ;

- The development of guiding devices, to be used in the presence of flexible PIVIs, in order to guarantee the longitudinal stability of the isolator;

- Search and develop new materials that allow for ARs in lower frequency ranges and/or that allow to keep the length of the cell while designing by phase velocity contrast;
- The development of PIVIs for multiaxial vibration isolation;
- Development of liquid cork sprays for SDT.

To conclude, the author would like to remark that this thesis relates different areas of science and engineering such as: numerical methods, symbolic computation, structural analysis, theoretical and experimental modal analysis of vibrations, rheology, materials characterization, prototyping and more recent areas such as phononics.

It should be noted that in the author's opinion, this thesis enhances both value and knowledge to CCMs applications, whose significance for the Portuguese industry has been evidenced though pioneering international projects, e.g., Amorim Cork Composites LIFE project [97]. Apart from the quality of the scientific component, the use of CCMs is a supplementary contribute to the expansion of the cork sector of which Portugal is considered a leader in production, processing, research, development and innovation.

It is expected that this study creates impact, especially amongst the cork and CCMs environments, manufactures and research and development institutes and groups, since these materials are capable of novel and innovative applications even when subject to dynamic solicitations, where both the longitudinal and shear dynamic moduli of elasticity are now of simpler determination by using the proposed hybrid analytical-experimental methodology here presented.

REFERENCES

[1] Chu S.Y. and Soong T.T., Reinhorn A.M., Active, Hybrid and Semi-Active Structural Control. John Wiley & Sons (2005).

[2] Mead D.J., Passive Vibration Control. John Wiley & Sons, New York (1999).

[3] Olhoff N., A Survey of the Optimal Design of Vibrating Structural Elements, Part I: Theory, Shock Vib. Dig., **8** (8) 3-10 (1976).

[4] Ormondroy J. and Hartog J.P. Den, The theory of dynamic absorber, Transactions of the American society of mechanical engineers APM-50-7 (1928).

[5] Ross D., Ungar E.E. and Kerwin Jr E.M., Damping of plate flexural vibrations means of viscoelastic laminae. Structural Damping, ASME, New York (1959).

[6] Snowdon J.C., Vibration isolation on rigid and non-rigid foundations. Report No. TM 79-137, Applied Research Laboratory, Pennsylvania State University, PA 16801, July (1979).

[7] International Organization for Standardization ISO 18437-2, Mechanical vibration and shock – Characterization of the dynamic mechanical properties of visco-elastic materials, part 2: resonance method (2005).

[8] Ferry J.D., Viscoelastic Properties of Polymers. Wiley, New York, 3rd ed. (1980).

[9] Nashif A.D., Jones D.I.G. and Henderson J.P., Vibration Damping. Wiley-Interscience, New York, (1985).

[10] Tarantola A., Inverse problem theory, methods for data fitting and model parameter estimation. SIAM: Society for Industrial and Applied Mathematics (2004).

[11] Schlägel A., Measurements of Modulus of Elasticity and Loss Factor for Solid Materials, Brüel&Kjær Technical Review, No.4 (1957).

[12] Norris Jr. D.M. and Young W.C., Complex modulus measurements by longitudinal vibration testing, Experimental Mechanics **10** 93-96 (1970).

[13] Madigosky W.M. and Lee G.F., Improved resonance technique for material characterization, Journal of the Acoustical Society of America **73** 1374-1377 (1983).

[14] Pritz T., Transfer function method for investigating the complex modulus of acoustic materials: Rod-like specimen, Journal of Sound and Vibration **81** (3) 359–376 (1982).

[15] Pritz T., Transfer function method for investigating the complex modulus of acoustic materials: Spring-like specimen, Journal of Sound and Vibration **72** (3) 317–341 (1980).

[16] Pritz T., Dynamic strain of a longitudinally vibrating viscoelastic rod with an end mass, Journal of Sound and Vibration **85** (2) 151–167 (1982).

[17] Oberst H. and Frankenfeld K., On the damping of bending vibrations on thin sheet metal by firmly bonded coatings, Acustica **2** 181–194 (1952). (In German)

[18] Liao Y. and Wells V., Estimation of complex Young's modulus of non-stiff materials using a modified Oberst beam technique, Journal of Sound and Vibration **316** 87-100 (2008).

[19] Gade S., Zaveri K., Konstantin-Hansen H. and Herlufsen H., Complex Modulus and Damping Measurements using Resonant and Non-Resonant Methods, Brüel&Kjær Technical Review, No.2 (1994).

[20] Foreman J., Dynamic mechanical analysis of polymers. Reprinted from American Laboratory January (1997).

[21] Riande E., Diaz-Calleja R., Prolongo M.G., Masegosa R.M. and Salom C., Polymer viscoelasticity. Stress and strain in practice. Marcel Dekker Inc., New York (2000).

[22] Theocaris P.S. and Papadopoulou N., Propagation of stress waves in viscoelastic media, Polymer **19** (2) 215-219 (1978).

[23] Blanc R.H., Transient wave propagation methods for determining the viscoelastic properties of solids, Journal of Applied Mechanics **60** (3) 763-768 (1993).

[24] Lundberg B. and Blanc R.H., Determination of mechanical material properties from the two-point response of an impacted linearly viscoelastic rod specimen, Journal of Sound and Vibration **126** (1) 97-108 (1988).

[25] Odeen S. and Lundberg B., Determination of complex modulus from measured end-point accelerations of an impacted rod specimen, Journal of Sound and Vibration **165** (1) 1-8 (1993).

[26] Lundberg B. and Odeen S., In situ determination of the complex modulus from strain measurements on an impacted structure, Journal of Sound and Vibration **167** (3) 413-419 (1993).

[27] Soula M., Vinh T., Chevalier Y., Beda T. and Esteoule C., Measurements of isothermal complex moduli of viscoelastic materials over a large range of frequencies, Journal of Sound and Vibration **205** (2) 167-184 (1997).

[28] Lakes R.S., Viscoelastic measurement techniques, Rev. Sci. Instrum. **75** 797 (2004).

[29] Jones D.I.G., Handbook of viscoelastic vibration damping, John Wiley & Sons, New York (2001).

[30] Dickinson R.C., Monterastelli M.R., and Vydra E.J., Development of materials for noise and temperature control, Society of Automotive Engineers, Paper No. 950621 (1995).

[31] Fortes M.A., Rosa M.E. and Pereira H., A Cortiça, IST Press, Lisboa (2004). (In Portuguese)

[32] Gil L., Cork Composites: A Review, Materials **2** (3) 776-789 (2009).

[33] Pereira H., Cork: biology, production and uses, Elsevier Science, 1st ed. (2007).

[34] Gil P., Fernandes J., Neves M.M., Reis L., Suitability of corkrubber gaskets in gasoline-ethanol blens, Materials Science Forum **636-637** 266-272 (2010).

[35] Gil P., Selagem de Motores com Juntas Planas de Cortiça-Borracha: Influência da Percentagem de Etanol em Misturas com Gasolina (Engine Static Sealing with CorkRubber Flat Gaskets Influence of the Ethanol Percentage in Blends with Gasoline). MSc Thesis, Instituto Superior Técnico, Universidade Técnica de Lisboa, Portugal (2008). (In Portuguese)

[36] Pritz T., Dynamic Young's modulus and loss factor of floor covering materials, Applied Acoustics **49** (2) 179-190 (1996).

[37] Diogo A.C., Análise dinâmico-mecânica de sólidos poliméricos. Aplicação ao estudo do comportamento de diversos polímeros de origem biológica. Novos Materiais, Que Futuro?, Sociedade Portuguesa de Materiais, Coimbra, **1** 249-258 (1989). (In Portuguese)

[38] Mano J.F., The viscoelastic properties of cork, Journal of Materials Science **37** (2) 257-263 (2002).

[39] Moreira R.A.S., Melo F.J.Q., and J.F. Dias Rodrigues Static and dynamic characterization of composition cork for sandwich beam cores, Journal of Materials Science **45** 3350-3366 (2010).

[40] Policarpo H., Neves M.M. and Ribeiro A.M.R., Dynamical response of a multi-laminated periodic bar: Analytical, numerical and experimental study, Shock and Vibration **17** (4-5) 521-535 (2010).

[41] Policarpo H., Neves M.M. and Ribeiro A.R., An Experimental Characterization of Cork Storage Modulus for Cork-Steel Applications in Vibration Attenuation, Materials Science Forum **636-637** 1199-1205 (2010).

[42] Marburg S., Six boundary elements per wavelength. Is that enough?, Journal of Computational Acoustics **10** 25-51 (2002).

[43] Policarpo H., Neves M.M. and Maia N.M.M., A simple method for the determination of the complex modulus of resilient materials using a longitudinally vibrating three-layer specimen, Journal of Sound and Vibration **332** (2) 246-263 (2013).

[44] Policarpo H., Analytical, Numerical and Experimental Study of the Dynamical Response of Helicoidal Springs and Periodic Bars. MSc Thesis, Instituto Superior Técnico, Universidade Técnica de Lisboa, Portugal (2008).

[45] Benabid F., Hollow-core photonic bandgap fibre: new light guidance for new science and technology, Phil. Trans. R. Soc. A **364** 3439-3462 (2006).

[46] Kinematic sculpture by Eusebio Sempere. Available at: http://francisthemulenews.wordpress. com/2009/12/. (Accessed on April 29, 2013).

[47] Martínez-Sala R., Sancho J., Sánchez J. V., Gómez V., Llinares J. and Meseguer F., Sound attenuation by sculpture, Nature **378** 241 (1995).

[48] Sánchez-Pérez J. V., Caballero D., Martínez-Sala R., Rubio C., Sánchez-Dehesa J., Meseguer F., Llinares J., and Gálvez F., Sound attenuation by a two-dimensional array of rigid cylinders, Phys. Rev. Lett., **80** (24) 5325-5329 (1998).

[49] Cartaxo A., Caracterização de Filtros Acústicos Baseada no Método dos Elementos Finitos (Acoustic Filters Characterization Based on Finite Elements Models. MSc Thesis, Instituto Superior Técnico, Universidade Técnica de Lisboa, Portugal (2007). (In Portuguese)

[50] Cartaxo A., Almeida J., Silva O., Neves M. and Bento Coelho J., Numerical Study of Finite Periodic Structures and Validation of Results Obtained with Bloch Wave Techniques, International Conference on Engineering Dynamics, Carvoeiro, Portugal (2007).

[51] Cartaxo A., Neves M. Gerges S.N.Y. and Bento Coelho J., Verification and validation of a fluid-structure interaction model used to characterize sound attenuation by a periodically spaced array

of cylinder elements, ICSV 17- International Conference on Sound and Vibration, Kraków, Poland, 5-9 of July (2009).

[52] Meseguer F., Holgad M., Caballero D., Benaches N., Lopez C., Sanchez-Dehesa J., and Llinares J., Two-Dimensional Elastic Bandgap Crystal to Attenuate Surface Waves, J. Lightwave Technol. **17** 2196 (1999).

[53] Ashcrofat N. W., and Mermin N. D., Solid State Physics. Wiley, New York (1976).

[54] Hussein M.I., Hulbert G.M., and Scott R.A., Dispersive elastodynamics of 1D banded materials and structures: analysis, Journal of Sound and Vibration **289** 779-806 (2006).

[55] Hussein M.I., Hulbert G.M., and Scott R.A., Dispersive elastodynamics of 1D banded materials and structures: design, Journal of Sound and Vibration **307** 865-893 (2007).

[56] Kosevich M. A., On a simple model of the photonic or phononic crystal, JEPT Letters **74** 633-637 (2001). (In Russian).

[57] Brillouin L., Wave Propagation in Periodic Structures. Dover Phoenix Editions, New York, 2nd ed. (1946).

[58] Mead D.J., Wave Propagation in Continuous Periodic Structures: Research Contributions from Southampton, 1964-1995, Journal of Sound and Vibration **190** 495-524 (1996).

[59] Sigmund O. and Jensen J.S., Systematic design of phononic band-gap materials and structures by topology optimization, Phil. Trans. R. Soc. Lond. A **361** 1001–1019 (2003).

[60] Bloch wave techniques applied to design periodic structures. Research and Development project with reference POCTI/EME/44728/2002 funded by the Portuguese government namely to the Ministry of Education and Science, through the Fundação para a Ciência e Tecnologia (FCT). http://www.fct.pt/apoios/projectos/consulta/vglobal_projecto.phtml.en?idProjecto=44728&sapiens= 2002. (Accessed on 16 July 2013).

[61] Patent PT103969, Atenuador de vibrações multicamada (Multi-layer vibration attenuator), Boletim de Propriedade Industrial Nº. 2009/04/23, pp.6. (In Portuguese)

[62] Neves M.M., Silva O.M.J., Policarpo H. and Cartaxo A.G., Using classical FEM to predict the dynamical response of periodic devices in acoustic and vibration applications, Phononics 2011: First International Conference on Phononic Crystals, Metamaterials and Optomechanics, Santa Fe, New Mexico, USA (2011).

[63] Jensen J.S., Optimal Design of Nonlinear Wave Devices, Phononics 2011: First International Conference on Phononic Crystals, Metamaterials and Optomechanics, Santa Fe, New Mexico, USA (2011).

[64] Hulbert G.M., Meaud J. and Ma Z.D., Structurally-Inspired Phononic Metamaterials, Phononics 2011: First International Conference on Phononic Crystals, Metamaterials and Optomechanics, Santa Fe, New Mexico, USA (2011).

[65] Rao M.D., Recent applications of viscoelastic damping for noise control in automobiles and commercial airplanes, Journal of Sound and Vibration **262** (3) 457-474 (2003).

[66] Furukava M., Gerges S., Neves M.M. and Coelho B.J.L., Analysis of structural damping performance in passenger vehicles chasis, J. Acoust. Soc. Am. **126** 22–80 (2009).

[67] Danti M., Vigè D. and Nierop G.V., Modal Methodology for the Simulation and Optimization of the Free-Layer Damping Treatment of a Car Body, Journal of Vibration and Acoustics **132** (2) (2010).

[68] Fan R., Meng G., Yang J. and He C., Experimental study of the effect of viscoelastic damping materials on noise and vibration reduction within railway vehicles, Journal of Sound and Vibration **319** 58–76 (2009).

[69] Mead D.J., The effect of certain damping treatments on the response of idealized airplane structures excited by noise, Air Force Materials Lab. AFML-TR-65-284,WPAFB, August (1965).

[70] Furukava M., Uma metodologia de avaliação de desempenho de material viscoelástico aplicado a uma estrutura de um veículo de passeio. MSc Thesis, Universidade Federal de Santa Catarina, Brazil (2009). (In Portuguese).

[71] MSC - CAFE Standards Weighing You Down? Lower The Weight, Noise And Cost. Available at: http://www.matsci.com/wp-content/themes/MSC/PDFs/MSC_QS_Canton.pdf. (Accessed on February 22 2013).

[72] Eschenauer H.A. and Wodtke H.W., Optimal design with damping materials for vibration reduction, Research Center for Multidisciplinary Analyses and Applied Structural Optimization, University of Siegen, Germany.

[73] Yildiz A. and Stevens K., Optimum thickness distribution of unconstrained viscoelastic damping layer treatment for plates, Journal of Sound and Vibration **103** 183–199 (1985).

[74] Lumsdaine A. and Scott R.A., Shape optimization of unconstrained viscoelastic layers using continuum finite elements, Journal of Sound and Vibration **216** 29–52 (1988).

[75] Bandini, M., Governi, L. and Pierini, M., Optimal Design of Damping Material Distribution in Dynamically Excited Panels, Proceedings of ISMA 2002 **1** 441-449 (2002).

[76] Lin T.C. and Scott R.A., Shape optimization of damping layers, Proceedings of the 58th Shock and Vibration Symposium, Huntsville, Alabama **1** 395-409 (1987).

[77] Alvelid M., Optimal position and shape of applied damping material, Journal of Sound and Vibration **310** 947-965 (2008).

[78] Zheng L., Xie R., Wang Y. and Adel E.S., Topology optimization of constrained layerdamping on plates using Method of Moving Asymptote (MMA) approach, Shock and Vibration **18** 221-244 (2011).

[79] Maia N.M.M., Policarpo H., Neves M.M., Furukava M., Silva O.M., Gerges S.N.Y and Carli S., A Finite Element Model to Improve Unconstrained Layer Damping Treatments on a Simplified Passenger Car Body in White Model, 18th International Congress on Sound and Vibration, Rio de Janeiro, Brazil, July 10-14 (2011).

[80] Bendsøe M.P. and Sigmund O., Topology Optimization - Theory, Methods and Applications, Springer Verlag, Berlin Heidelberg (2003).

[81] Policarpo, H., Neves, M.M., Maia, N.M.M. and Urgueira, A.P.V., On using composition cork damping layer for surface damping treatments, ISMA 2012 – International conference on Noise & Vibration Engineering, Leuven, Belgium, September 17-19 (2012).

[82] Bathe K.J., Finite Element Procedures in Engineering Analysis, Prentice-Hall (1982).

[83] Zienkiewicz O.C. and Taylor R.L. , The Finite Element Method: The Basis. Volume I, Butterworth-Heinemann, Oxford, W.H Press el al. teds1, 5th ed. (2000).

[84] Zienkiewicz O.C. and Taylor R.L., The Finite Element Method: The Basis. Volume II, Butterworth-Heinemann, Oxford, W.H Press el al. teds1, 5th ed. (2000).

[85] Zienkiewicz O.C. and Taylor R.L., The Finite Element Method: The Basis. Volume III, Butterworth-Heinemann, Oxford, W.H Press el al. teds1, 5th ed. (2000).

[86] Cook R.D., Malkus D.S., Plesha M.E. and Witt R.J., Concepts and Applications of Finite Element Analysis, 4th ed. (2001).

[87] Reddy J.N., An Introduction to the Finite Element Method, McGraw-Hill Education, 3rd ed. (2005).

[88] Maia N.M.M., Silva J.M.M., He J., Lieven N.A.J., Lin R.M., Skingle G.W., To W.-M. and Urgueira A.P.V., Theoretical and Experimental Modal Analysis, Eds. Maia & Silva, Research Studies Press Ltd., Baldock, Hertfordshire, England (1997).

[89] Broch J.T., Mechanical vibration and shock measurements. Brüel & Kjaer, 2nd ed. (1980).

[90] Ewins D.J., Modal Testing: Theory and Practice. Research Studies Press (1984).

[91] McConnell K.G., Vibration testing: Theory and Practice. Wiley Interscience (1995).

[92] Mottershead J.E. and Friswell M.I., Model updating in structural dynamics: a survey, Journal of Sound and Vibration **167** (2) 347–375 (1993).

[93] Friswell M.I. and Mottershead J.E., Finite element model Updating in Structural Dynamics. Kluwer Academic Publishers, Dordrecht (1995).

[94] Mottershead J.E., Link M. and Friswell M.I., The sensitivity method in finite element model updating: A tutorial, Mechanical Systems and Signal Processing **25** (7) 2275-2296 (2011).

[95] Hatke H.G., Updating computational models in the frequency domain based on measured data: a survey, Probabilistic Engineering Mechanics **3** (1988).

[96] Imregun M. and Visser W.J., A review of model updating techniques, The Shock Vibration Digest, **23** (1) (1991).

[97] Amorim Cork Composites LIFE project. Available from: http://life.inegi.up.pt/Project-Life_2011.pdf (Accessed 10 February 2013).

[98] Thimoshenko S.P. and Goodier J.N., Theory of Elasticity. McGraw-Hill, 2nd ed. (1951).

[99] Kikuchi, N., Finite Element Methods in Mechanics. Cambridge University Press (1986).

[100] Saad, Y., Numerical Methods for Large Eigenvalue Problems. SIAM, 2nd ed. (2011).

[101] Pedersen N.L., Design of cantilever probes for atomic force microscopy (AFM), Engineering Optimization, **32** (3) 373-392 (2000).

[102] Richardson M.H. and Formenti D.L., Parameter Estimation from Frequency Response Measurements using Rational Fraction Polynomials, Proceedings of the 1st International Modal Analysis Conference, Orlando, Florida, November 8-10 (1982).

[103] Acuna C.G. and Friswell M., Rational Fraction Polynomial method implemented in MATLAB®, http://www.mathworks.com/matlabcentral/fileexchange/3805-rational-fraction-polynomial-method. (Accessed 7 March 2011).

[104] Gomes J.F.S., Longitudinal stress wave propagation in a finite length bar with variable cross section, and fracture of brittle solids of revolution due to stress wave interaction, Dissertation submitted for obtain the degree of Master of Science, to the Victoria University of Manchester, (1974). http://hdl.handle.net/10216/12260

[105] Reddy, J.N., Theory and analysis of elastic plates and shells. CRC Press, Taylor and Francis (2007).

[106] American Institute of Aeronautics and Astronautics, Guide for the Verification and Validation of Computational Fluid Dynamics Simulations, AIAA-G-077-1998, Reston, VA (1998).

[107] Carson II S.J., Model Verification and Validation, Proceedings of the 34th conference on Winter simulation (2002).

[108] Thacker B.H., Doebling, S.W., Hemez F.M., Anderson M.C., Pepin J.E. and Rodriguez E.A., Concepts of Model Verification and Validation, Los Alamos National Lab. (2004).

[109] Heylen W. and Avitabile P., Correlation considerations - Part 5, Proceedings of IMAC VI, 16 207-214 (1988).

[110] Nefske D.J. and Sung S.H., Correlation of a coarse-mesh FE model using structural system identification and a frequency response assurance criterion, Proceedings of IMAC **14** 597-602 (1996).

[111] Lieven N.A. and Ewins D.J., Spatial correlation of mode shapes, the co-ordinate modal assurance criterion (COMAC), Proceedings of IMAC VI **6** 690-695 (1988).

[112] Hemez M.F. and Doebling W.S., Model Validation and uncertainty Quantification, 19th International Modal Analysis Conference, Kissimmee, Florida (2001).

[113] Arora, J.S., Introduction to optimum design. Academic Press, 2nd ed. (2004).

[114] Ungar, E.E., Equality of Force and Motion Transmissibilities, Journal of Acoustical Societies of America 596–597 (1991).

[115] Maia N.M.M., Lage Y.E. and Neves M.M., Recent Advances on Force Identification in Structural Dynamics, Advances in Vibration Engineering and Structural Dynamics, Dr. Francisco Beltran-Carbajal Ed. InTech (2012). Available from: http://www.intechopen.com/books/advances-in-vibration-engineering-and-structural-dynamics/recent-advances-on-force-identification-in-structural-dynamics. (Accessed 10 July 2013).

[116] Lage Y.E., Neves M.M., Maia N.M.M., Tcherniak D., Force transmissibility versus displacement transmissibility, (submitted 2013).

[117] Kubo S., Classification of inverse problems arising in field problems and their treatments, Proceedings of 1st IUTAM Symposium on Inverse Problems in Engineering Mechanics, Tokyo, Japan (1992).

[118] Pritz T., Frequency dependences of the complex moduli and complex Poisson's ratio of real solid materials, Journal of Sound and Vibration **214** (1) 83-104 (1998).

[119] Read B.E., and Dean G.D., The Determination of Dynamic Properties of Polymers and Composites, Bristol, Hilger (1978).

[120] Policarpo H., Diogo A.C., Neves M.M., Maia N.M.M., A note on the estimation of cork composite elasto-dynamic properties and their frequency dependence, ICEDyn'2013 – International Conference on Structural Engineering Dynamics, Ericeira, Portugal, June 17-18 (2013).

[121] Love A.E.H., A Treatise on the Mathematical Theory of Elasticity. (1944) New York, Dover Publications, republished in (2007).

[122] Pritz T., Apparent complex Young's modulus of a longitudinally vibrating viscoelastic rod, Journal of Sound and Vibration **77** 93-100 (1981).

[123] Policarpo H, Neves MM and Maia NMM, On a hybrid analytical-experimental technique to assess the storage modulus of resilient materials using symbolic computation. First National Conference on Symbolic Computation in Education and Research - CSEI2012, Lisbon, Portugal, April 2-3 (2012).

[124] Policarpo H., Neves M.M., Maia N.M.M., On a hybrid analytical-experimental technique to assess the storage modulus of resilient materials using symbolic computation. Journal of Symbolic Computation **61-62** 31-52 (2014) (Available online on 16/10/2013).

[125] MATLAB$^{®}$ Version 7.10 (R2010) help documentation manual.

[126] http://www.mathworks.com/help/techdoc/ref/fzero.html (Accessed 7 March 2011).

[127] Policarpo H., Neves M.M., Maia N.M.M and Urgueira A.P.V., Estimation of Complex Longitudinal and Shear Moduli of Composition Cork Materials, ICEM15 – 15th International Conference on Experimental Mechanics, Porto, Portugal, July 22-27 (2012).

[128] Fesko, D.G. and Tschoegl, N.W., Time–temperature superposition in thermorheologically complex materials, J. Polym. Sci. **35** 51–69 (1971).

[129] Schapery, R.A., Viscoelastic behavior and analysis of composite materials, in Mechanics of Composite Materials. Academic Press, New York (1974).

[130] TA Instrument Universal Analysis 2000 part of TA Thermal Advantage software Available from: http://www.tainstruments.com/product.aspx?siteid=11&id=110&n=1 (Accessed on 10 February 2013).

[131] TA Instrument Rheology Advantage Data Analysis part of TA Thermal Advantage software Available from: http://www.tainstruments.com/product.aspx?siteid=11&id=110&n=1 (Accessed on 10 February 2013).

[132] Amorim Cork Composites. Available at: http://www.amorimcorkcomposites.com/ (Accessed on 30 May 2013).

[133] Renault A., Jaouen L. and Sgard F., Characterization of elastic parameters of acoustical porous materials from beam bending vibrations, Journal of Sound and Vibration **330** 1950-1963 (2011).

---

[134] Joannopoulos J.D., Johnson S.G., Meade R.D., and Winn J.N., Photonic Crystals: Molding the Flow of Light. Princeton Univ. Press, 2nd ed. (2008).

[135] Kuo N. and Piazza G., Demonstration of Ultra High Frequency Fractal Air/Aluminum Phononic Crystals, Phononics 2011: First International Conference on Phononic Crystals, Metamaterials and Optomechanics, Santa Fe, New Mexico, USA (2011).

[136] Cahill D.G., Ford W.K., Goodson K.E., Mahan G.D., Majumdar A., Maris H.J., Merlin R. and Phillpot S.R., Nanoscale Thermal Transport, J. Appl. Phys. **93** 793 (2003).

[137] Maldovan M., Understanding and Controlling High-Frequency Phonon Thermal Energy Transport in Nanostructures, Phononic Crystals for Communication, Sensing, and Energy Management, Phononics 2011: First International Conference on Phononic Crystals, Metamaterials and Optomechanics, Santa Fe, New Mexico, USA (2011).

[138] Hsu F.C., Hsu J.C., Huang T.C., Wang C.H. and Chang P., Reducing Support Loss in Micromechanical Ring Resonators Using Phononic Band-gap Structures, J. Phys. D: Appl. Phys. **44** (2011).

[139] Meseguer F., Holgado M., Caballero D., Benaches N., Lopez C., Sanchez-Dehesa J. and Llinares J., Two-Dimensional Elastic Bandgap Crystal to Attenuate Surface Waves, J. Lightwave Technol. **17** (1999).

[140] Cummer S.A., Popa B., Schurig D., Smith D.R., Pendry J., Rahm M. and Starr A., Scattering Theory Derivation of a 3D Acoustic Cloaking Shell, Phys. Rev. Lett. **100** (2008).

[141] Papanikolaou N., Psarobas I. E. and Stefanou N., Absolute Spectral Gaps for Infrared Light and Hypersound in Three-Dimensional Metallodielectric Phoxonic Crystals, Appl. Phys. Lett. **96** (2010).

[142] Hussein M.I., Hulbert G.M. and Scott R.A. Dispersive elastodynamics of 1D banded materials and structures: analysis, Journal of Sound and Vibration **289** 779-806 (2006).

[143] Hussein M.I., Hulbert G.M., Scott R.A., Hamza K., and Saitou, K., Multiobjective evolutionary optimization of periodic layered materials for desire wave dispersion characteristics, Structural and Multidisciplinary Optimization **31** 60-75 (2006).

[144] Jensen J.S. and Pedersen N.L., On maximal eigenfrequency separation in two-material structures: the 1D and 2D scalar cases, Journal of Sound and Vibration **269** 967-986 (2006).

[145] Jensen J.S. and Sigmund O., Phononic band gap structures as optimal designs, in IUTAM Symposium on Asymptotics, Singularities and Homogenisation in Problems of Mechanics. Kluwer Academic Publishers, Dordrecht, 71-81 (2003).

[146] CDM – Resilient fixations for machines. Available at: http://www.cdmca.com /CDM-ISO-MACHINE-FIX.page (Accessed on March 19, 2012).

[147] Shigley J.E., Mischke C.R. and Budynas R.G., Mechanical Engineering Design. Mc Graw Hill, 7th ed. (2004)

[148] Policarpo H., Neves M.M. and Maia N.M.M, Cork Composition Damping Layer to Reduce Vibrations in Metallic Plates, ICEM15: 15th International Conference on Experimental Mechanics, , Porto, Portugal, July 22-27 (2012).

[149] Policarpo H., Furukava M., Neves M.M., Maia N.M.M., Silva O.M. and Gerges S.N.Y., A methodology for the performance evaluation of diferent surface damping treatments, IRF'2013 – 4th International Conference on Integrity, Reliability and Failure, Funchal, Portugal, June 23-27 (2013).

[150] ANSYS V.11.0, Documentation for Ansys.

[151] Outokumpu steel EN 1.4012 ASTM 430. Available at: http://www.outokumpu.com/Site CollectionDocuments/Ferritic_Stainless_Steel_1.4300_1.4512_1.4016_1.4510_1.4509_1.4521_D atasheet.pdf (Accessed 3 February 2013).

[152] Adhesive tape reference 3M[®] 467MP. Available at: http://multimedia.3m.com/mws/mediaweb server?mwsId=66666UF6EVsSyXTtIXTyLxfyEVtQEVs6EVs6EVs6E666666-&fn=70070938587.P DF (Accessed 25 February 2013).

APPENDICES

A.1 – A MATLAB® Code for obtaining Eq. (3.16) using symbolic computation

This code can be selected and past to the MATLAB® command window. It has all symbolic computations done to obtain Eq. (3.16).

```
% MATLAB 7.10 R(2010a)
% This script obtains the scalar nonlinear equation Eq.(3.16) of  the
inverse problem that solves the identification problem.
clc; clear all;
% Construct symbolic objects
syms  w w1 x c cmat1 cmat2 B1 B2 Lmat Lmat1 Lmat2 kmat kmat1 kmat2 A
Emat...,
      Emat1 Emat2 rhomat1 rhomat2 D1 D2
% The above entities are, respectively:
% w - angular frequency (rad s^-1)
% w1 - first natural frequency (rad s^-1)
% x - Coordinate along the length of the bar
% c - wave phase velocity (m s^-1)
% A - cross sectional area of the specimen (m^2)
% Lmat - Material length (m)
% Lmat1 - Length of material 1  (m)
% Lmat2 - Length of material 2  (m)
% kmat - Wave number
% kmat1 - Wave number in material 1
% kmat2 - Wave number in material 2
% Emat - Storage modulus (Pa)
% Emat1 - Storage modulus of material 1 (Pa) first and last layer
% Emat2 - Storage modulus of material 2 (Pa)
% cmat1 - wave phase velocity in material 1 (m s^-1)
% cmat2 - wave phase velocity in material 2 (m s^-1)
% rhomat1 - Mass density of material 1 (kg m^-3)
% rhomat2 - Mass density of material 2 (kg m^-3)
%
% Solution of differential equation (5) considering harmonic motion
u=D1*sin(kmat*x)+D2*cos(kmat*x)
%Neumman Boundary conditions  B.C. - Free : du/dx=0 <=> Stress=0
x0=0; xLmat=Lmat;
ux0=subs(u,{x},{x0});
uxL=subs(u,{x},{xLmat});
%Displacement matrix [UD]: U=[UD]D
%========================================================
% Extract coefficients of D1 and D2 from these 2 equations
%========================================================
UD(1,1)=subs(ux0,{D1},{1}); UD(1,1)=subs(UD(1,1),{D2},{0});
UD(1,2)=subs(ux0,{D1},{0});UD(1,2)=subs(UD(1,2),{D2},{1});
UD(2,1)=subs(uxL,{D1},{1}); UD(2,1)=subs(UD(2,1),{D2},{0});
UD(2,2)=subs(uxL,{D1},{0});UD(2,2)=subs(UD(2,2),{D2},{1});
UD
%Derivative of the displacement u with respect to the coordinate x
dudx=diff(u,x);
dudx0=subs(dudx,{x},{x0});
dudxL=subs(dudx,{x},{xLmat});
% Derivative of displacement matrix [dU]
%========================================================
% Extract coefficients of D1 and D2 from these 2 equations
%========================================================
dU(1,1)=subs(-dudx0,{D1,D2},{1,0});
```

```
dU(1,2)=subs(-dudx0,{D1,D2},{0,1});
dU(2,1)=subs(dudxL,{D1,D2},{1,0});
dU(2,2)=subs(dudxL,{D1,D2},{0,1});
% matrix [FD]: F=[FD]D where F is Force
FD= Emat*A*dU;
% U=[UD]D and F=[FD]D  ==> F=[FD]*inv([UD])*U ==> F=ZU
% Obtain Z=[FD]*inv([UD])
Zz=FD/UD;
Z=simplify(Zz) % Dynamic Stiffness matrix [Z]
% Symbolic variables substitution
% Generate matrix for each layer Lmat1=Lmat3 e Lmat2
Zmat1=subs(Z,{Emat,kmat,Lmat},{Emat1,kmat1,Lmat1});
Zmat2=subs(Z,{Emat,kmat,Lmat},{Emat2,kmat2,Lmat2});
% Global dynamic stiffness matrix for a two-material three layer bar
ZG(1,1)=Zmat1(1,1);
ZG(1,2)=Zmat1(1,2);
ZG(2,1)=Zmat1(1,2);
ZG(2,2)=Zmat1(2,2)+Zmat2(1,1);
ZG(2,3)=Zmat2(1,2);
ZG(3,2)=Zmat2(1,2);
ZG(3,3)=Zmat2(2,2)+Zmat1(1,1);
ZG(3,4)=Zmat1(1,2);
ZG(4,4)=Zmat1(2,2);
ZG(4,3)=Zmat1(1,2);
kkmat1=w/cmat1;
kkmat2=w/cmat2;
% Symbolic variables substitution
ZZG=subs(ZG,{kmat1,kmat2},{kkmat1,kkmat2});
% Determinant of ZG gives the Characteristic Polynomial of the system
DETZZG=det(ZZG)
% Symbolic simplifications
[NDet DDet]=numden(DETZZG); %Get numerator and denominator of  DETZZG
AA=simplify(NDet); % Simplify numerator
AAA=collect(AA, [A w Emat1])
P2=subs(AAA,{Emat1^3,Emat1^4},{0,0})
P3=subs(AAA,{Emat1^2,Emat1^4},{0,0})
P4=subs(AAA,{Emat1^2,Emat1^3},{0,0})
% Simplify previous symbolic expressions
PP2=simplify(P2/DDet);
PP3=simplify(P3/DDet);
PP4=simplify(P4/DDet);
% Introduce the c2 in terms of Emat2
ccmat2=sqrt(Emat2/rhomat2);
PPP2=subs(PP2,{cmat2},{ccmat2});
PPP3=subs(PP3,{cmat2},{ccmat2});
PPP4=subs(PP4,{cmat2},{ccmat2});
% Simplify previous symbolic expressions
%% Automatic replacement of a group of factors: divide by the factors and
%% multiply by the variable LAM and others that represents that group of
factors
syms LAM1 LAM2 LAM3 LAM4 C B1 B2 B3
C=A^4*Emat1^2*w^4;
B1=cos(w*Lmat1/cmat1);
B2=sin(w*Lmat1/cmat1);
B3=tan(w*Lmat2/ccmat2);
% LAM1=(-C*rhomat2*cmat1^-2*B1^2*B2^-2))
TERM1=simplify(PPP2/(-C*rhomat2*cmat1^-2*B1^2*B2^-2))*LAM1;
```

```
% LAM2=(-2*C*Emat1*cmat1^-3*rhomat2^(1/2)*B1*B2^-1))
[TERM2_NUM TERM2_DEN]=numden(simplify(PPP3/(-2*C*Emat1*cmat1^-
3*rhomat2^(1/2)*B1*B2^-1))*LAM2);
TERM2_NUM =simple(simple(TERM2_NUM)*tan((Lmat2*w)/(Emat2/rhomat2)^(1/2)));
% LAM3=(Emat2)^(1/2) ?????
TERM2_DEN =simple(TERM2_DEN)*tan(LAM3/(Emat2)^(1/2));
% The rhomat2^(1/2) should cancel in the denominator
TERM2_DEN=subs(TERM2_DEN,rhomat2,1);  %%To simplify the expression
% LAM4=(C*Emat1^2*cmat1^-4))
TERM3=simplify(PPP4/(C*Emat1^2*cmat1^-4))*LAM4;
%% Group the compacted terms
FF=TERM1+TERM2_NUM/TERM2_DEN+TERM3
FF=collect(FF,[LAM1 LAM2 LAM3 LAM4])
pretty(FF)
```

A.2 – A note on the two DOF discrete layer bar model

The two-material three layer bar illustrated by Figure 3.3, may alternatively be modeled using two infinitely rigid point masses M_{Mat_1} (see, sub-chapter 2.5.2.1) and one massless spring k_{Mat_2} (see sub-chapter 2.5.2.2.) as illustrated in Figure A.2.1.
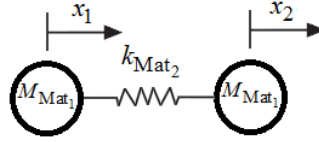
Figure A.2.1 – Two DOF discrete model.

For this system, Eq. (2.19), i.e., $\det\left(\mathbf{K} - \omega^2 \mathbf{M}\right) = \mathbf{0}$ may be rewritten as

$$\det\left(\begin{bmatrix} k_{\text{Mat}_2} & -k_{\text{Mat}_2} \\ -k_{\text{Mat}_2} & k_{\text{Mat}_2} \end{bmatrix} - \omega^2 \begin{bmatrix} M_{\text{Mat}_1} & 0 \\ 0 & M_{\text{Mat}_1} \end{bmatrix}\right) = 0, \tag{A.2.1}$$

leading to

$$\begin{vmatrix} k_{\text{Mat}_2} - \omega^2 M_{\text{Mat}_1} & -k_{\text{Mat}_2} \\ -k_{\text{Mat}_2} & k_{\text{Mat}_2} - \omega^2 M_{\text{Mat}_1} \end{vmatrix} = \left(k_{\text{Mat}_2} - \omega^2 M_{\text{Mat}_1}\right)^2 - k_{\text{Mat}_2}^2 = 0. \tag{A.2.2}$$

After simplification one obtains

$$\omega^2\left(-2k_{\text{Mat}_2} M_{\text{Mat}_1} + \omega^2 M_{\text{Mat}_1}^2\right) = 0. \tag{A.2.3}$$

The solutions of Eq. (A.2.3) are

$$\omega^2 = 0 \quad and \quad \omega^2 = \frac{2k_{\text{Mat}_2}}{M_{\text{Mat}_1}}. \tag{A.2.4}$$

Thus, the first non-zero natural frequency of the 2 DoF discrete model may be expressed as

$$\left(f_1\right)_{2\text{DoF}} = \left(2\pi\right)^{-1}\sqrt{2k_{\text{Mat}_2}/M_{\text{Mat}_1}}, \tag{A.2.5}$$

where $\omega_1 = 2\pi f_1$, $M_{\text{Mat}_1} = \rho_{\text{Mat}_1} A_{\text{Mat}_1} L_{\text{Mat}_1}$ and $k_{\text{Mat}_2} = E'_{\text{Mat}_2} A_{\text{Mat}_2}/L_{\text{Mat}_2}$ which, when solved in order to the unknown E'_{Mat_2} and considering that $A_{\text{Mat}_1} = A_{\text{Mat}_2} = A$ leads to

$$\left(E'_{\text{Mat}_2}\right)_{2\text{DoF}} = \left(2\pi^2 \rho_{\text{Mat}_1} M_{\text{Mat}_1} L_{\text{Mat}_1} L_{\text{Mat}_2}\right)\left(f_1^2\right)_{2\text{DoF}}. \tag{A.2.6}$$

A.3 – A MATLAB® Code for solving Eq.(3.16) using the solution of Eq. (3.17) as the initial guess

This code can be selected and past to the MATLAB® command window. It has all computations to

estimate E'_{Mat_2} for the data introduced (at line where is the comment: %Values of the variables).

```
% MATLAB 7.10 R(2010a)
% This script initializes the parameters, builds and solves the
% scalar nonlinear function Eq. (3.16) of the identification problem
% Knowing:
% Emat1 - Storage modulus of material 1 (Pa) first and last layer;
% rhomat1 - density of material 1 (kg m^-3);  rhomat2 - density of
% material 2 (kg m^-3) intermediate resilient layer;
% Lmat1 - length of material 1 (m); Lmat2 - length of material 2 (m);
% A - cross sectional area of the specimen (m^2);
% w1 - the first natural frequency of the specimen (rad s^-1)
% obtained  experimentally on a three layer
% specimen where w1=2*pi*f1 with f1 the frequency in Hz;
%
% Furthermore, this script obtains the solutions of the scalar nonlinear
% equation of the inverse problem that solves the identification problem.
% The fzero function is used to find the roots of the nonlinear equation
% corresponding to the Emat2 parameter.
% An appropriate initial guess (initial_guess) must be given to
% obtain the first positive zero.
clc; clear all;
% Values of the variables
A=0.0202*0.0202;
Lmat1=0.0202; Lmat2=0.0128;
Emat1=205E9; rhomat1=7640; rhomat2=893;
f1=1120; % cyclic frequency Hz obtained from experimental test
% Initialize the groups of factors
w1=2*pi*f1;
cmat1=sqrt(Emat1/rhomat1);  % Material 1 wave phase velocity (m/s)
C=A^4*Emat1^2*w1^4;B1=cos((Lmat1*w1)/cmat1); B2=sin((Lmat1*w1)/cmat1);
LAM1=-C*rhomat2*cmat1^-2*B1^2*B2^-2;LAM2=-2*C*Emat1*cmat1^-
3*rhomat2^(1/2)*B1*B2^-1;
LAM3=rhomat2^(1/2)*Lmat2*w1;LAM4=C*Emat1^2*cmat1^-4;
% Rescale the equation FF(x)=0
maxLAM=max([abs(LAM1),abs(LAM2),abs(LAM4)]);
LAM1=LAM1/maxLAM; LAM2=LAM2/maxLAM; LAM4=LAM4/maxLAM;
LAM1;LAM2;LAM3;
% Build the expression for the Eq.(3.16)
FF=horzcat(num2str(LAM1),'*x+(',num2str(LAM2),'*tan((',num2str(LAM3),...
    '*x^-0.5))^-1*x^0.5)+',num2str(LAM4));
%% Solve for x the FF(x)=0
% a good initial_guess can be obtained from the k-m 2 DOFs model approach
initial_guess=2*pi^2*rhomat1*Lmat1*Lmat2*f1^2; %Eq.(3.16)
Emat2=fzero(FF,initial_guess); % Emat2 (Pa)
% Outputs
[s,errmsg]=sprintf('Emat1= %f GPa and rhomat1 %f kg/m3',Emat1/1e9,
rhomat1);disp(s)
[s,errmsg]=sprintf('Emat2= %f MPa and rhomat2 %f kg/m3',Emat2/1e6,
rhomat2);disp(s)
[s,errmsg]=sprintf('A= %f m2, L1= %f m and L2= %f m  ',A, Lmat1,
Lmat2);disp(s)
[s,errmsg]=sprintf('Emat2 obtained with f1= %f Hz',f1);disp(s)
```

A.4 – A note on the total modal loss factor of a two-material uniform bar

This note shows why η_t is given by η_{Mat_2} when η_{Mat_1} can be neglected. For it, a MATLAB® code that can be selected and past to the command window is appended at the end of this appendix.

Consider an one-dimensional bar (rod) with uniform transversal sectional area A, as illustrated in Figure A.4.1, with two parallel layers of different materials, with longitudinal dynamic moduli of elasticity $E^*_{\text{Mat}_1}$ and $E^*_{\text{Mat}_2}$, modal loss factors η_{Mat_1} and η_{Mat_2} and lengths L_{Mat_1} and L_{Mat_2}.
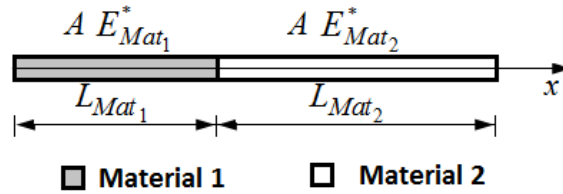
Figure A.4.1 – Two layer bar composed of two materials.

Under axial force excitation, one may assume that the longitudinal stiffness of the bar may be simulated as the stiffness of several springs that are connected in series where the total stiffness k_t is determined by $1/k_t = 1/k_{s1} + 1/k_{s2} + \cdots$. Indeed, the longitudinal stiffness of a uniform bar with uniform cross sectional area A and length L may be expressed as $k = \left(E^* A\right)/L$ and therefore, when applying for the two-material bar and as a first approximation, the total longitudinal stiffness E^*_t can be estimated like with springs connected in series as

$$\frac{E^*_t A}{L_t} = \frac{1}{\dfrac{L_{\text{Mat}_1}}{E^*_{\text{Mat}_1} A} + \dfrac{L_{\text{Mat}_2}}{E^*_{\text{Mat}_2} A}} . \tag{A.4.1}$$

Since areas A are equal and attending to $E^*_{\text{Mat}_\alpha} = E'_{\text{Mat}_\alpha}\left(1 + i\eta_{\text{Mat}_\alpha}\right)$, Eq. 4.1 may be rewritten as,

$$\frac{E^*_t}{L_t} = \frac{1}{\dfrac{L_{\text{Mat}_1}}{E'_{\text{Mat}_1}\left(1 + i\eta_{\text{Mat}_1}\right)} + \dfrac{L_{\text{Mat}_2}}{E'_{\text{Mat}_2}\left(1 + i\eta_{\text{Mat}_2}\right)}} \quad , \tag{A.4.2}$$

which when rearranged leads to

$$\frac{E^*_t}{L_t} = \frac{E'_{\text{Mat}_1}\left(1 + i\eta_{\text{Mat}_1}\right) E'_{\text{Mat}_2}\left(1 + i\eta_{\text{Mat}_2}\right)}{L_{\text{Mat}_1} E'_{\text{Mat}_2}\left(1 + i\eta_{\text{Mat}_2}\right) + L_{\text{Mat}_2} E'_{\text{Mat}_1}\left(1 + i\eta_{\text{Mat}_1}\right)} . \tag{A.4.3}$$

By expanding the denominator of Eq. (A.4.3) and considering that $L_t = L_{Mat_1} + L_{Mat_2}$ one obtains

$$E_t^* = \frac{E'_{Mat_1} E'_{Mat_2} \left(1 + i\eta_{Mat_1}\right)\left(1 + i\eta_{Mat_2}\right)\left(L_{Mat_1} + L_{Mat_2}\right)}{E'_{Mat_1} L_{Mat_2} + E'_{Mat_2} L_{Mat_1} + i\left(E'_{Mat_1} L_{Mat_2} \eta_{Mat_1} + E'_{Mat_2} L_{Mat_1} \eta_{Mat_2}\right)} . \quad (A.4.4)$$

Multiplying the numerator and denominator by the complex conjugate of the denominator one obtains

$$E_t^* = \frac{C_1 \left(E'_{Mat_1} L_{Mat_2} \eta^2_{Mat_1} + E'_{Mat_2} L_{Mat_1} \eta^2_{Mat_2} + E'_{Mat_1} L_{Mat_2} + E'_{Mat_2} L_{Mat_1}\right)}{C_2}$$
$$+ i \frac{C_1 \left(E'_{Mat_1} L_{Mat_2} \eta^2_{Mat_1} \eta_{Mat_2} + E'_{Mat_2} L_{Mat_1} \eta^2_{Mat_2} \eta_{Mat_1} + E'_{Mat_2} L_{Mat_1} \eta_{Mat_1} + E'_{Mat_1} L_{Mat_2} \eta_{Mat_2}\right)}{C_2} \quad (A.4.5)$$

where

$C_1 = E'_{Mat_1} E'_{Mat_2} \left(L_{Mat_1} + L_{Mat_2}\right)$ and

$C_2 = E'^2_{Mat_1} L^2_{Mat_2} \left(1 + \eta^2_{Mat_1}\right) + 2 E'_{Mat_1} E'_{Mat_2} L_{Mat_1} L_{Mat_2} \left(1 + \eta_{Mat_1} \eta_{Mat_2}\right) + E'^2_{Mat_2} L^2_{Mat_1} \left(1 + \eta^2_{Mat_2}\right) \eta^2_{Mat_2} .$

Separating the real and imaginary components of Eq. (A.4.5) and applying $\eta_t = \text{Im}\left(E_t^*\right) / \text{Re}\left(E_t^*\right)$ leads to

$$\eta_t = \frac{E'_{Mat_1} L_{Mat_2} \eta^2_{Mat_1} \eta_{Mat_2} + E'_{Mat_2} L_{Mat_1} \eta^2_{Mat_2} \eta_{Mat_1} + E'_{Mat_2} L_{Mat_1} \eta_{Mat_1} + E'_{Mat_1} L_{Mat_2} \eta_{Mat_2}}{E'_{Mat_1} L_{Mat_2} \eta^2_{Mat_1} + E'_{Mat_2} L_{Mat_1} \eta^2_{Mat_2} + E'_{Mat_1} L_{Mat_2} + E'_{Mat_2} L_{Mat_1}} . \quad (A.4.6)$$

Dividing the numerator and denominator of Eq. (A.4.6) by E'_{Mat_1} one obtains

$$\eta_t = \frac{L_{Mat_2} \eta^2_{Mat_1} \eta_{Mat_2} + \dfrac{E'_{Mat_2}}{E'_{Mat_1}} L_{Mat_1} \eta^2_{Mat_2} \eta_{Mat_1} + \dfrac{E'_{Mat_2}}{E'_{Mat_1}} L_{Mat_1} \eta_{Mat_1} + L_{Mat_2} \eta_{Mat_2}}{L_{Mat_2} \eta^2_{Mat_1} + \dfrac{E'_{Mat_2}}{E'_{Mat_1}} L_{Mat_1} \eta^2_{Mat_2} + L_{Mat_2} + \dfrac{E'_{Mat_2}}{E'_{Mat_1}} L_{Mat_1}} . \quad (A.4.7)$$

Assuming in Eq. (A.4.7) that $E'_{Mat_1} \gg E'_{Mat_2}$ it follows that

$$\eta_t \approx \frac{L_{Mat_2} \eta^2_{Mat_1} \eta_{Mat_2} + L_{Mat_2} \eta_{Mat_2}}{L_{Mat_2} \eta^2_{Mat_1} + L_{Mat_2}} . \quad (A.4.8)$$

Determining the limit of Eq. (A.4.8) when $\eta_{Mat_1} \to 0$ leads to

$$\lim_{\eta_{\mathrm{Mat_1}} \to 0} \eta_t = \eta_{\mathrm{Mat_2}} \ . \tag{A.4.9}$$

Thus, the modal loss factor of the intermediate resilient layer $\eta_{\mathrm{Mat_2}}$ is successfully approximated by the total modal loss factor, i.e.,

$$\eta_t \approx \eta_{\mathrm{Mat_2}} \ . \tag{A.4.10}$$

```
% MATLAB 7.10 R(2010a)
% This script was used to show that the total modal loss factor of a two
% layer bar with modal loss factors eta1 and eta2 is expressed by the
% eta2 when eta1 can be neglected
clc;clear all
syms k1 k2 k3 Keq E1 L1 E2 L2 E3 L3 eta2 eta1 A Lt 'real'
k1=(E1*(1+1i*eta1))/L1;  % Longitudinal stiffness Mat1
k2=(E2*(1+1i*eta2))/L2;  % Longitudinal stiffness Mat2
keq=(1/((1/k1)+(1/k2)));  % Equivalent stiffness Mat1-Mat2 in series
pretty(keq)    %Eq.(A.4.1)
K1=factor(keq); % Factorize keq
pretty(K1)  %Eq.(A.4.3)
[n,d] = numden(K1); % Numerator and denominator of keq
dc=conj(d); % Complex conjugate of the denominator of keq
KKn=expand(n*(L1+L2)*dc); % Multiply numerator by complex conjugate of
denominator and by Lt
pretty(KKn)
KKnr=simplify(real(KKn))
KKni=simplify(imag(KKn))
KKd=simplify(d*dc) % Multiply denominator by its complex conjugate
pretty(KKd)
KKnn=expand(KKn); % Expand the numerator
pretty(KKnn)
KKdd=expand(KKd); % Simplify the numerator
pretty(KKdd)
KKK=simplify(KKnn/KKdd); % Built equivalent keq expression - Eq.(A.4.5)
pretty(KKK)
R=real(KKK); % Real component of Eq.(A.4.5)
RR=simplify(R) % Simplify real component
pretty(RR)
I=imag(KKK); % Imaginary component
II=simplify(I)% Simplify imaginary component of Eq.(A.4.5)
pretty(II)
etaT=II/RR; % eta_total = imag/real - Eq.(A.4.6)
pretty(etaT)
[nn,dd] = numden(etaT); % Numerator and denominator of etaT
DD=(E2/E1); % factor E2/E1
KKnn=expand(nn*DD); % Multiply numerator by factor E2/E1 and expand
KKdd=expand(dd*DD); % Multiply denominator by factor E2/E1 and expand
etaTr1=KKnn/KKdd; % eta_total = imag/real
LLL=limit(etaTr1,(E2/E1),0,'right') ; % limit when E2/E1 -->0
LLLL=simplify(limit(LLL,eta1,0,'right') ); % limit when eta1 -->0
pretty(LLLL) % Expression that only depends on eta2
```

A.5 – Construction procedure of the test specimens

The construction procedure of the specimens is described in the following:

1. Start by cutting the material layers (see Figure A.5.1);

2. The steel extremities layers were polished to minimize the rugosity originated during the cutting process;

3. To remove traces of oil and grease the steel extremities layers were immersed successively in two tanks, each containing the same degreasing solvent (acetone). The first tank acts as a wash, the second as a rinse;

4. The material layers are bonded alternately using a commercial high performance, two component epoxy adhesive (*Araldite*®)[*], with a cure time of 5 minutes;

5. The adhesive's preparation consists of mixing equal portions of each of the components in a mixture recipient until a homogenized mixture is obtained;

6. When so, the adhesive is ready to be applied and the material layers are bonded alternately;

7. To minimize eventual centering deviations an L shaped beam was used to correctly align the layers as illustrated by Figure A.5.2.

[*]http://www.huntsman.com/advanced_materials/eng/Markets/Adhesives/For_Consumers/
Araldite®_Consumer_Adhesives/index.cfm?pageID=5902. (Accessed 7 March 2011).

Figure A.5.1 – Steel and CCM layers.

Figure A.5.2 – L shaped beam (side view) used to aid the centering of the cells during the cure of the adhesive.

A.6 – Further experimental and analytical FRF results determined using the proposed analytical-experimental hybrid methodology

In this appendix are presented further results obtained using the proposed hybrid analytical-experimental methodology, described in sub-chapter 3.3, to identify the dynamic modulus.

Hence, once the dynamic modulus $E^{*}_{\mathrm{Mat}_2}$ is identified, the analytical receptance FRF curves are obtained by solving the forced harmonic vibrations problem expressed by Eq. (3.13), where the dynamic stiffness matrix $\mathbf{Z}$ is in this case expressed by Eq. (3.14). The material properties ρ_{Mat_1}, ρ_{Mat_2}, $E^{'}_{\mathrm{Mat}_1}$ and η_{Mat_1} are presented in Table 3.1 whereas, L_{Mat_1}, L_{Mat_2}, $E^{'}_{\mathrm{Mat}_2}$ and η_{Mat_2} are presented in Table 3.2 and Table 3.3.

The results obtained with materials VC6400 and VC1001 are presented in sub-chapter 3.7.2 as they present the main characteristics found in all. Further results were obtained considering other resilient materials, and are here presented where the experimental and analytical receptance FRF curves are represented by the dotted-circle and filled lines, respectively, in Figure A.6.1, Figure A.6.3 and Figure A.6.5. The experimental and analytical receptance FRF curves were then correlated using the FRAC, Eq. (2.59), and the FAAC, Eq. (2.60), criteria and are illustrated by Figure A.6.2, Figure A.6.4 and Figure A.6.6, respectively.
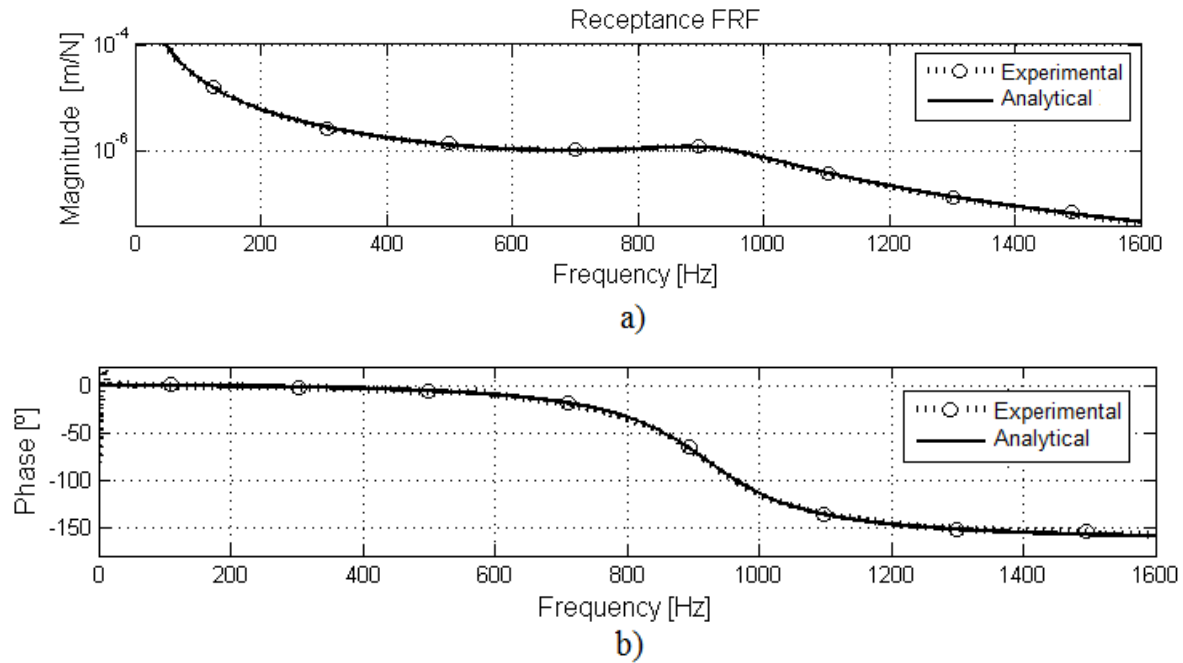
Figure A.6.1 – Experimental and analytical FRF curves of test specimen with resilient material VC 5200: a) magnitude; b) phase.
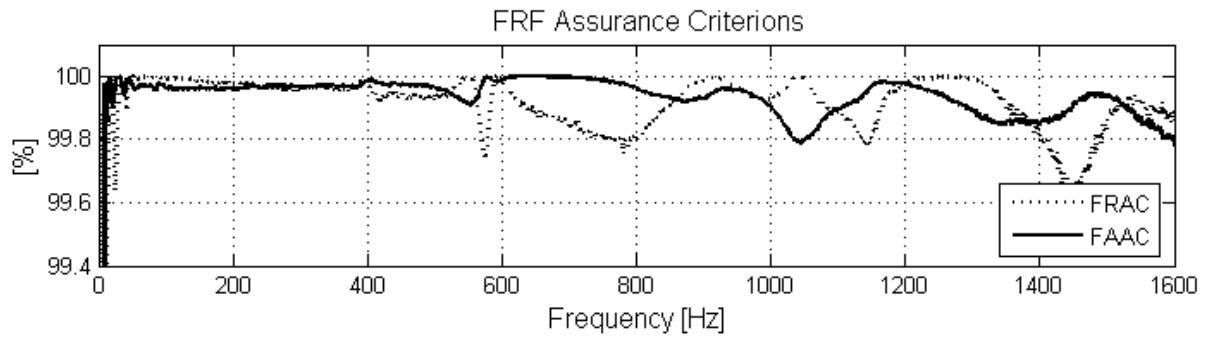
Figure A.6.2 – FRF correlation functions curves of test specimen with resilient material VC 5200.
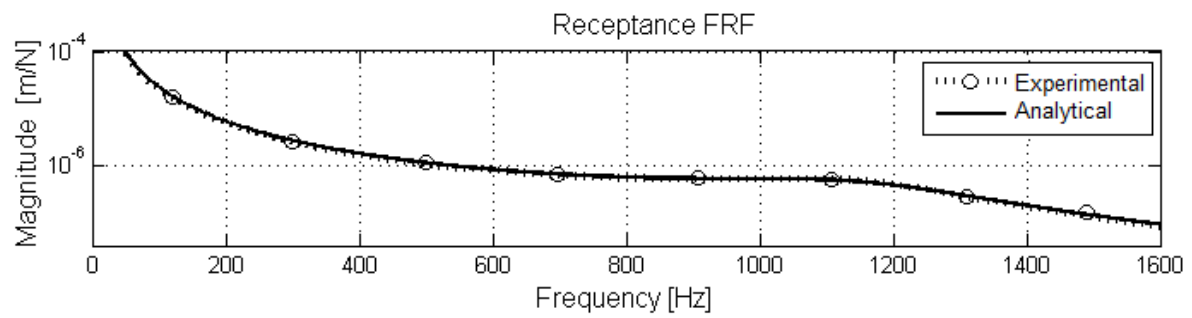
a)
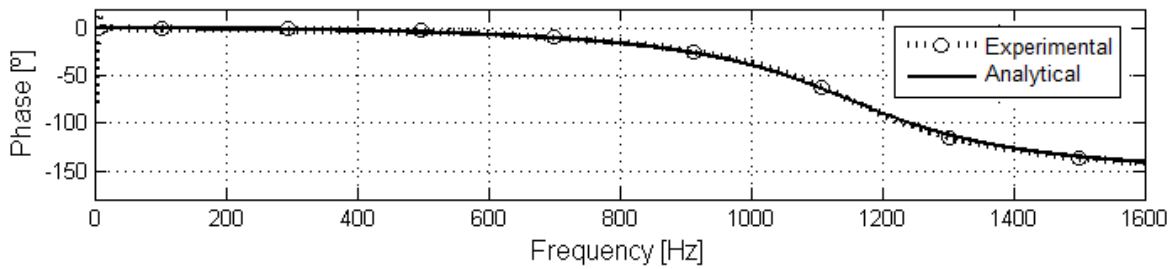
b)

Figure A.6.3 – Experimental and analytical FRF curves of test specimen with resilient material VC 2100: a) magnitude; b) phase.
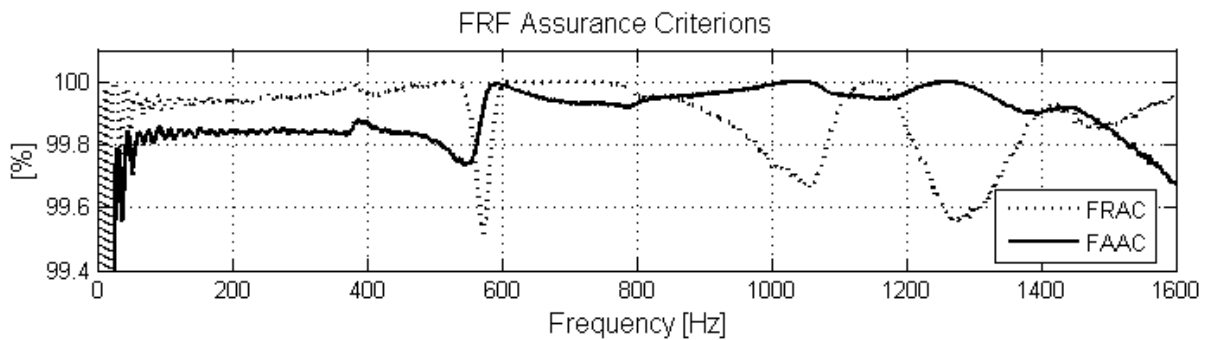
Figure A.6.4 – FRF correlation functions curves of test specimen with resilient material VC 2100.
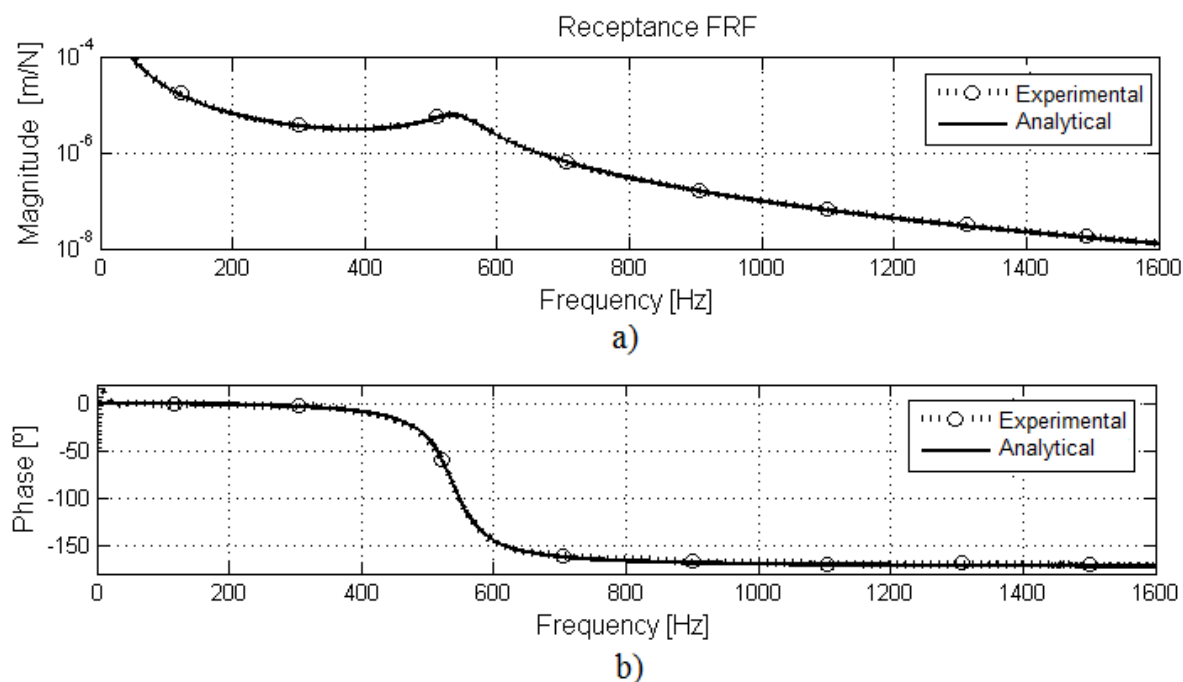
Figure A.6.5 – Experimental and analytical FRF curves of test specimen with resilient material NL 20: a) magnitude; b) phase.
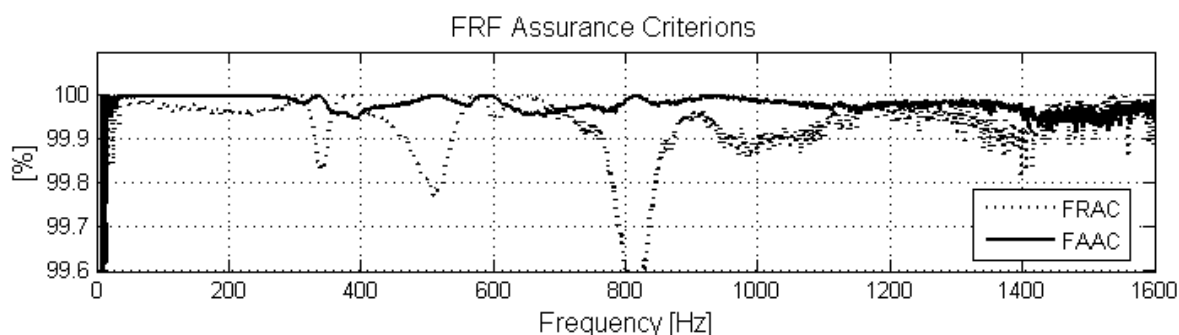
Figure A.6.6 – FRF correlation functions curves of test specimen with resilient material NL20.

The analytical and experimental FRF present a good agreement in terms of magnitude and phase as illustrated by the above figures. The results of the receptance FRF correlation criteria present values above 99% for both the FAAC and the FRAC assurance criteria, respectively. The presence of flexural modes is almost unnoticed in receptance FRF curves. However, their presence is evidentiated by the FRF assurance criteria, e.g., as seen in Figure A.6.4 near 600 Hz.

A.7 – Further experimental results obtained using DMA

In this study DMA tests were conducted on five CCMs, see Figure 3.15. However, only the results obtained for VC 6400 were presented, see sub-chapter 3.7.4, as they present the main characteristics found in all and additionally avoiding by this way a too extensive illustrated sub-chapter. In this sense, next are presented the results obtained for the other materials.

From DMA tests, one obtains the storage modulus $E^{'}$ and loss factor η curves (usually designated as tan delta or $tg\delta$ in DMA), as a function of the temperature, see Figure A.7.1, Figure A.7.5, Figure A.7.9, and Figure A.7.13 for the respective VC 5200, VC2100, VC 1001 and NL20 materials.

Using commercial software (TA Instrument Rheology Advantage Data Analysis [131]), the TTS is applied at a reference temperature of 20ºC which, is used to determine the shift factors a_T , (see Figure A.7.2, Figure A.7.6, Figure A.7.10 and Figure A.7.14 for the respective VC 5200, VC2100, VC 1001 and NL20 materials) that best fit the Arrhenius Equation, see Eq. (3.23).

This allows obtaining the master curves of the storage modulus $E^{'}$ and loss factor η as a function of frequency, as can be seen in Figure A.7.3, Figure A.7.7, Figure A.7.11 and Figure A.7.15 for the respective VC 5200, VC2100, VC 1001 and NL20 materials.

A curve fitting power law with two terms is applied to the curves in the frequency range of interest (between 1 Hz and 10 kHz) to obtain the analytical expressions, see Table 3.9 and Figure A.7.4, Figure A.7.8, Figure A.7.12 and Figure A.7.16 for the respective VC 5200, VC2100, VC 1001 and NL20 materials, that allows determining the storage modulus $E^{'}$ and loss factor η in the interval between 1Hz and 10^4Hz.
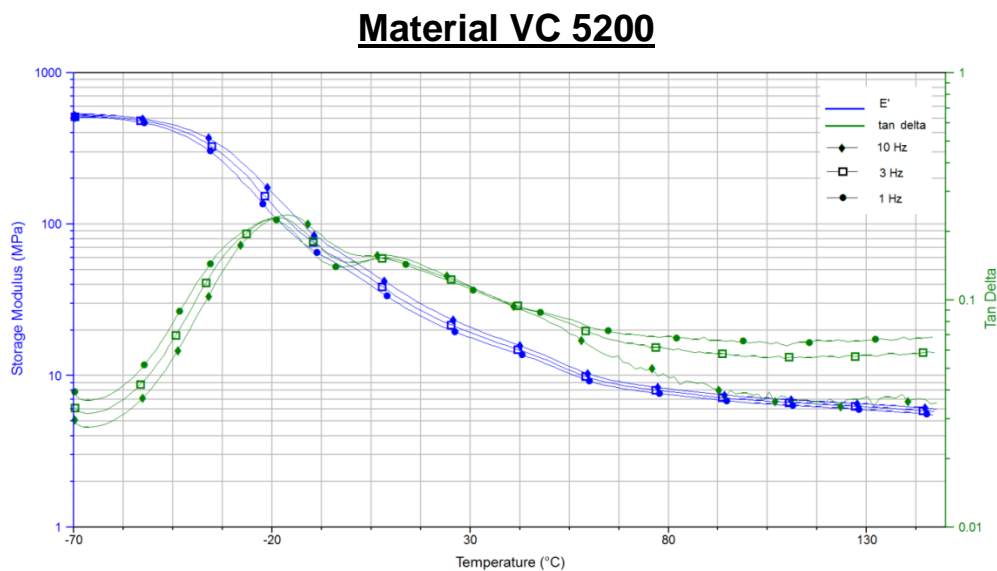
Material VC 5200

Figure A.7.1 – Storage modulus $E^{'}$ and loss factor η curves as a function of the temperature for three different frequencies for material VC 5200.
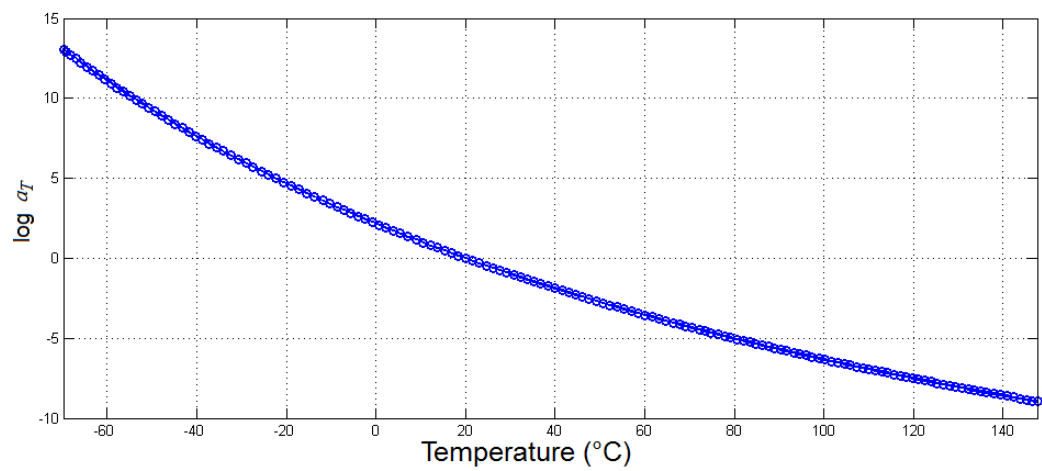
Figure A.7.2 – Shift curve at 20ºC as a function of the temperature for material VC 5200.
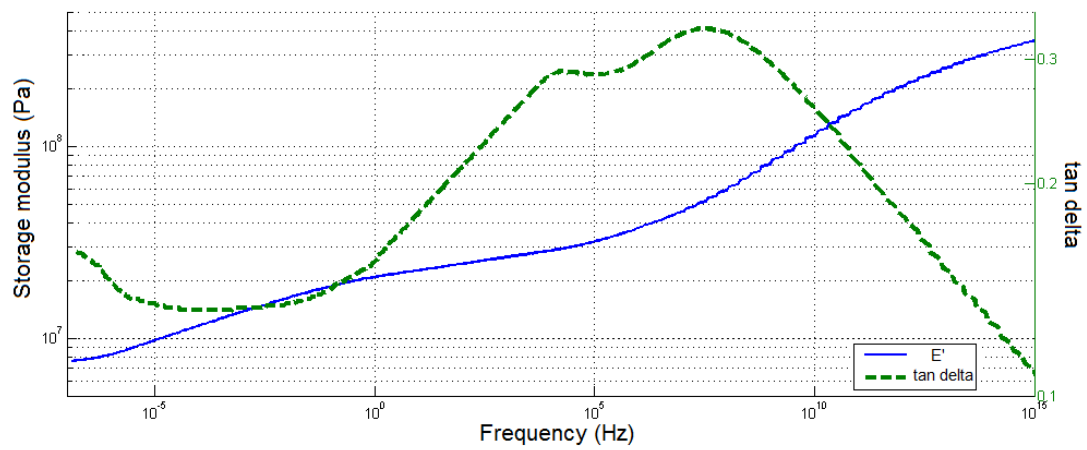
Figure A.7.3 – Master curves of the storage modulus $E^{'}$ and loss factor η as a function of the frequency for material VC 5200.
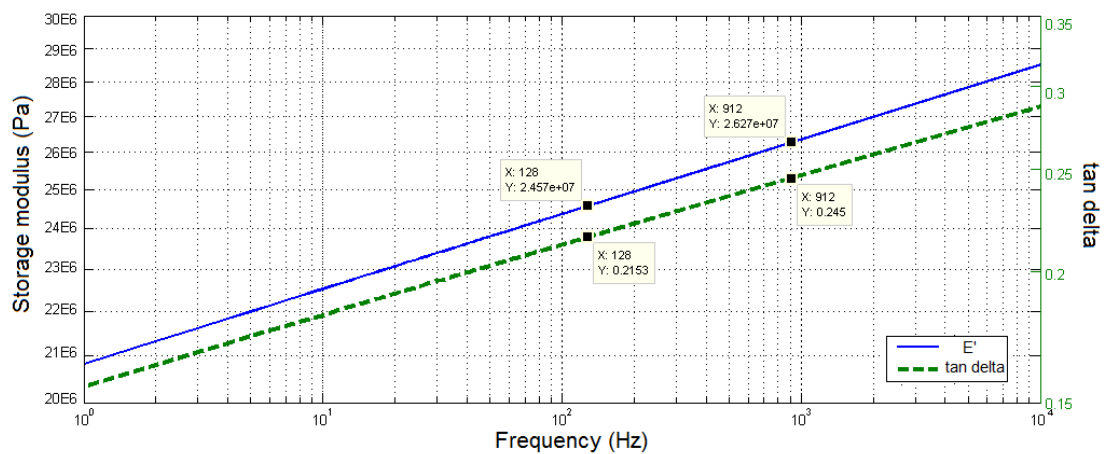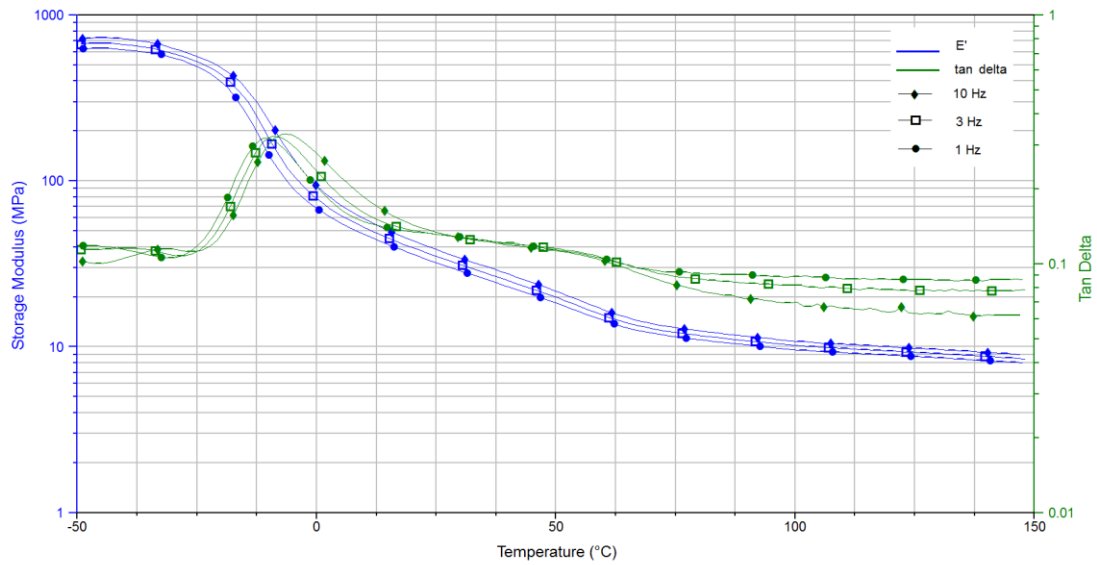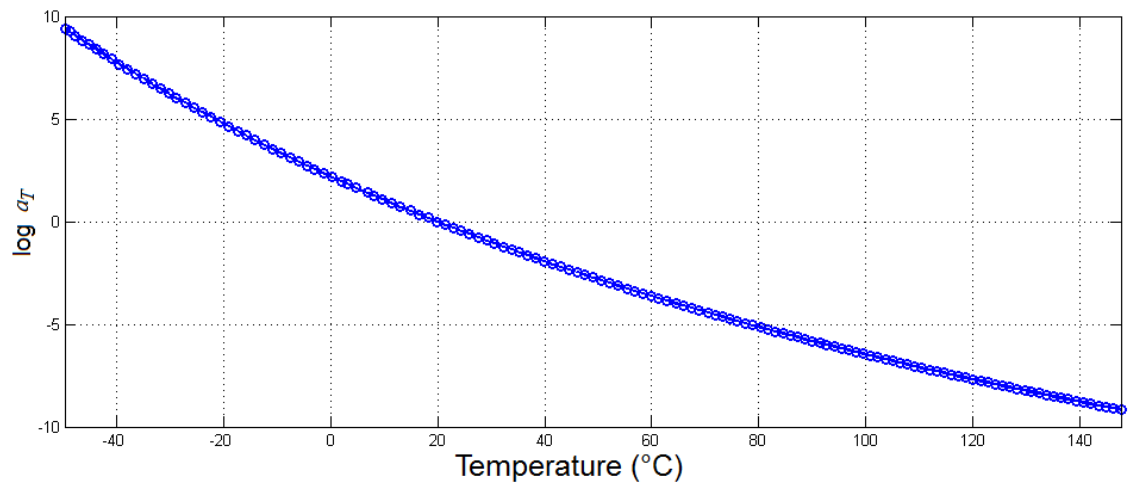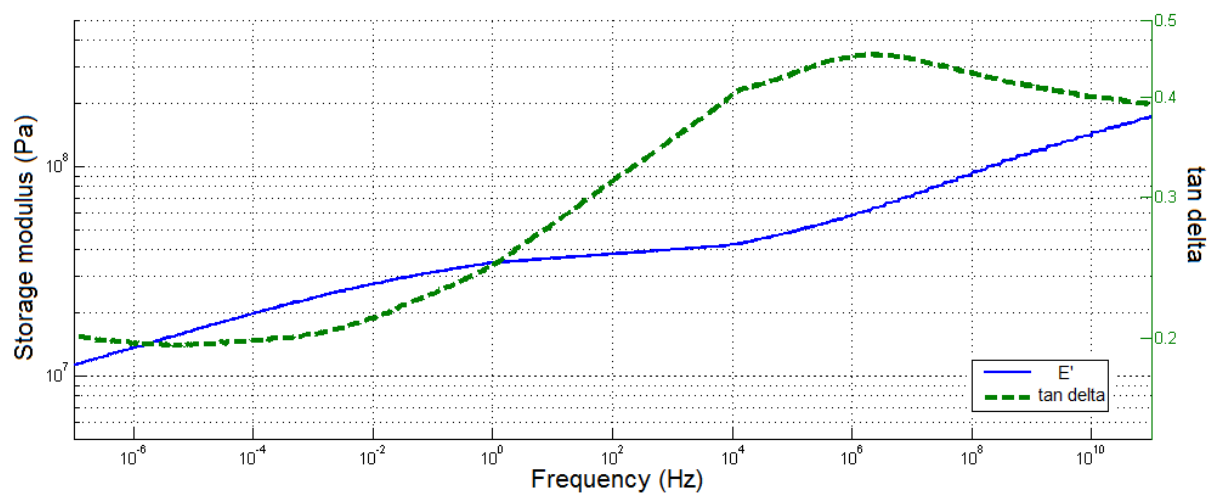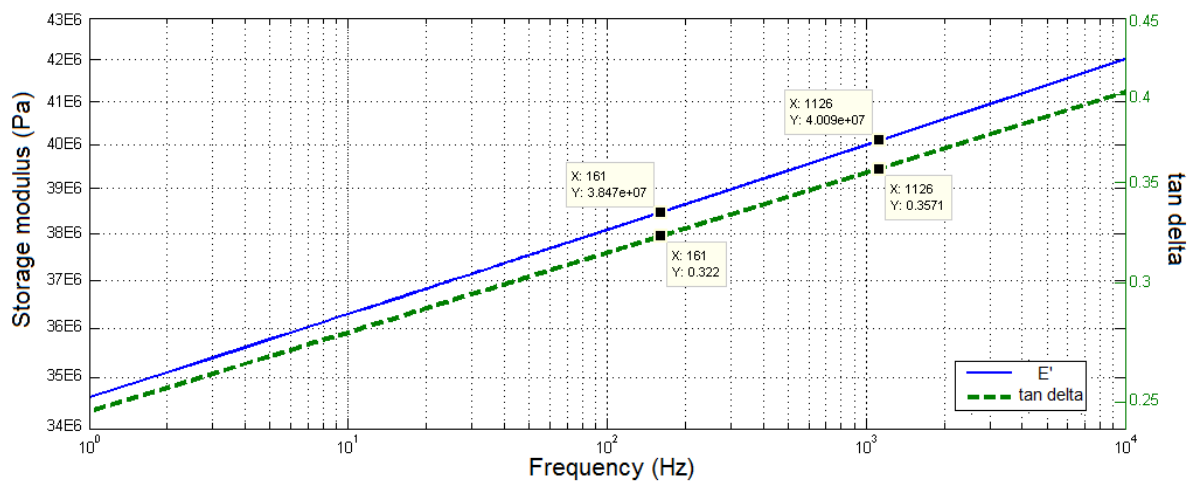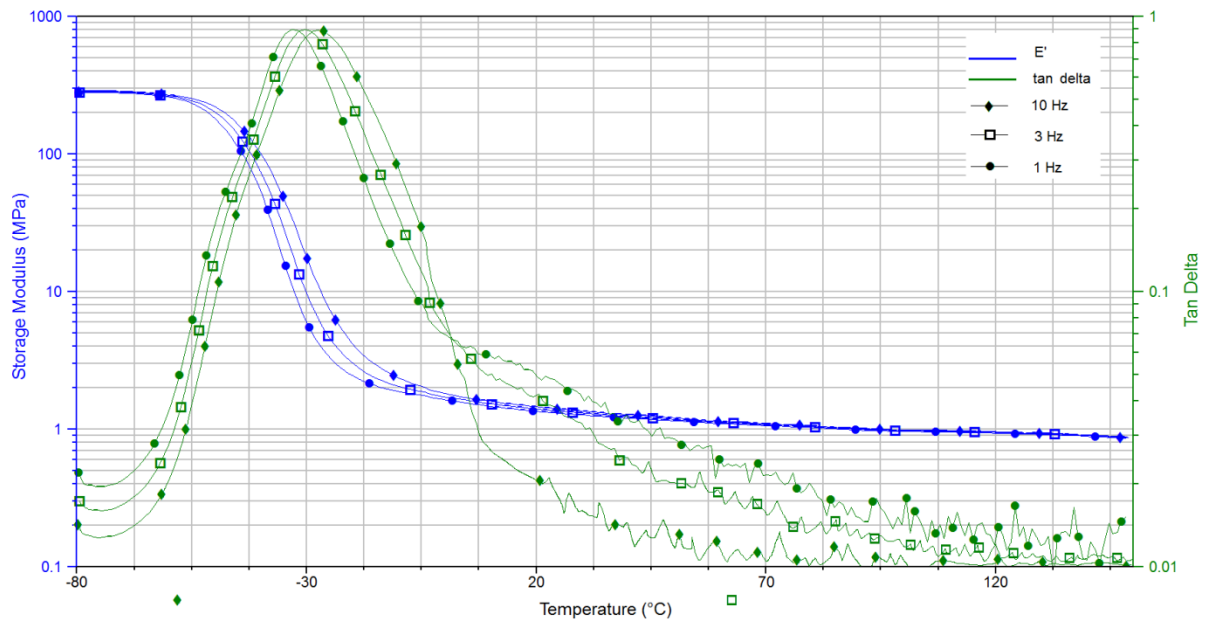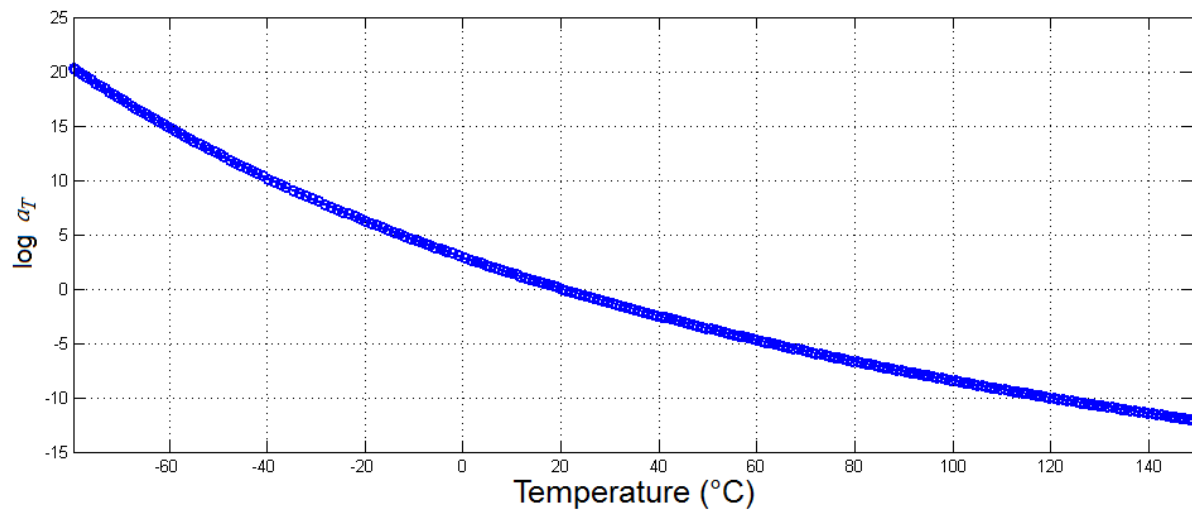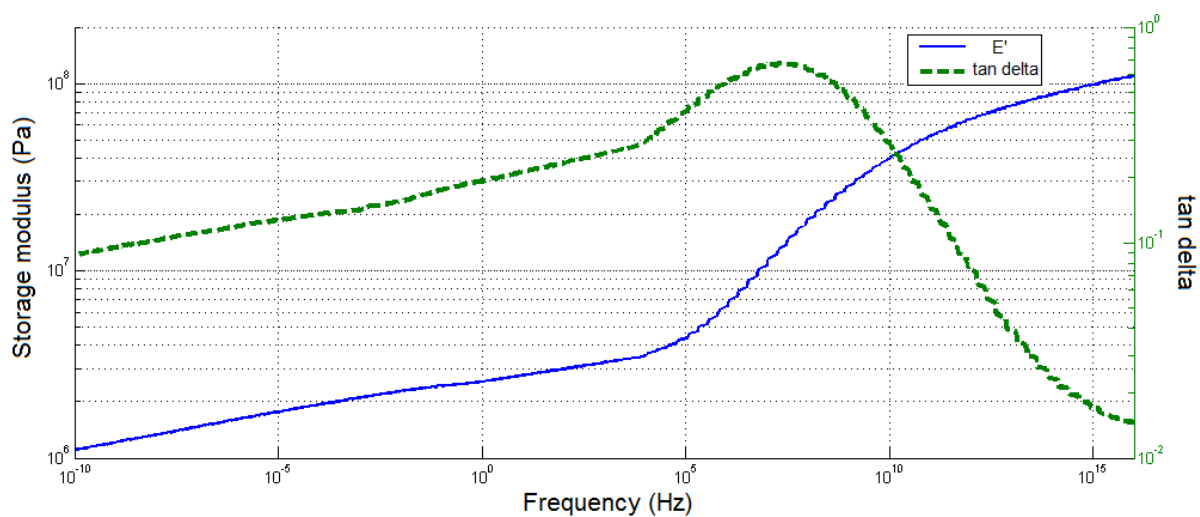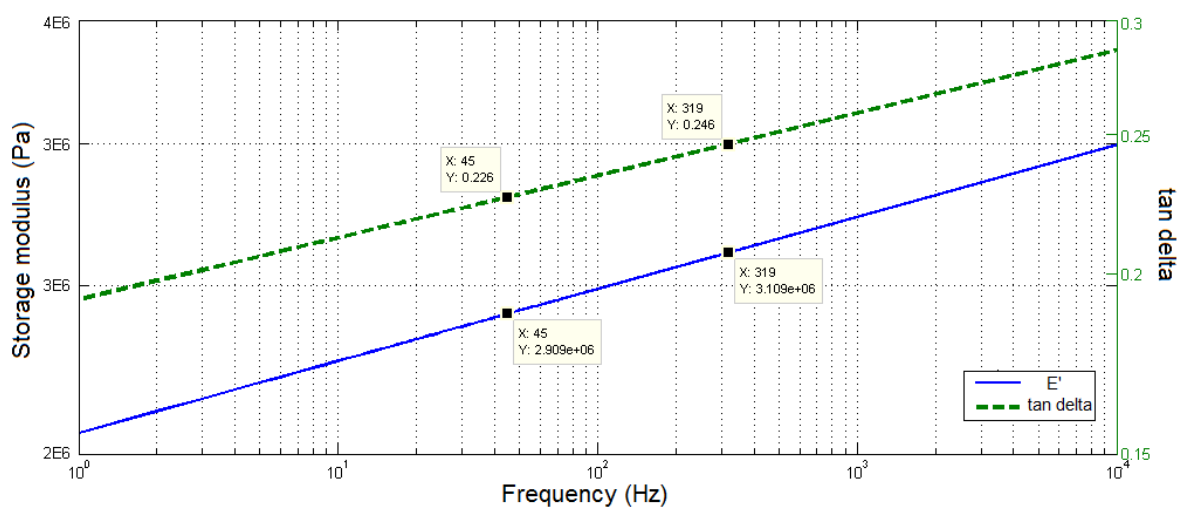

Figure A.7.4 – Curve fitting of the master curves of the storage modulus $E^{'}$ and loss factor η as a function of the frequency in the interval between 1Hz and 10^4Hz for material VC 5200.

Material VC 2100

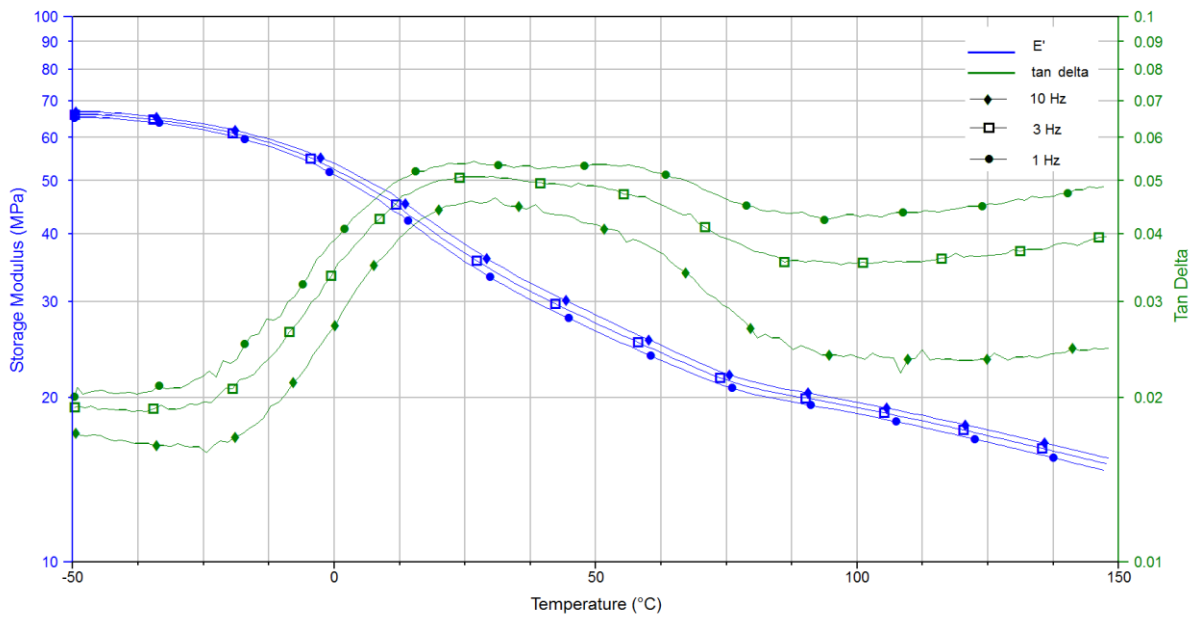
Figure A.7.5 – Storage modulus $E^{'}$ and loss factor η curves as a function of the temperature for three different frequencies for material VC 2100.

Figure A.7.6 – Shift curve at 20ºC as a function of the temperature for material VC 2100.

Figure A.7.7 – Master curves of the storage modulus $E^{'}$ and loss factor η as a function of the frequency for material VC 2100.

Figure A.7.8 – Curve fitting of the master curves of the storage modulus $E^{'}$ and loss factor η as a function of the frequency in the interval between 1Hz and 10^4Hz for material VC 2100.

Material VC 1001

Figure A.7.9 – Storage modulus $E^{'}$ and loss factor η curves as a function of the temperature for three different frequencies for material VC 1001.
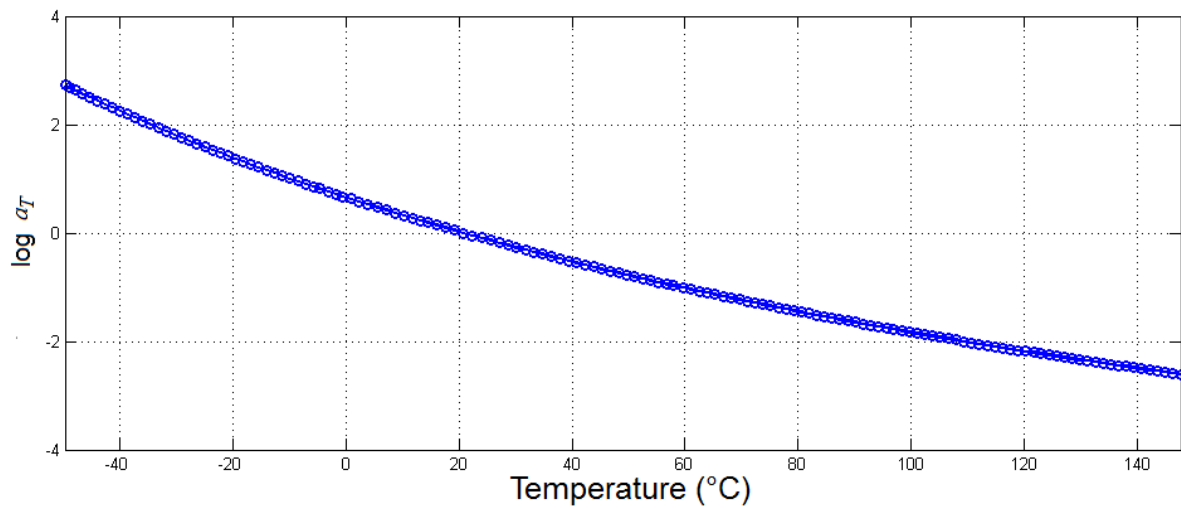

Figure A.7.10 – Shift curve at 20ºC as a function of the temperature for material VC 1001.
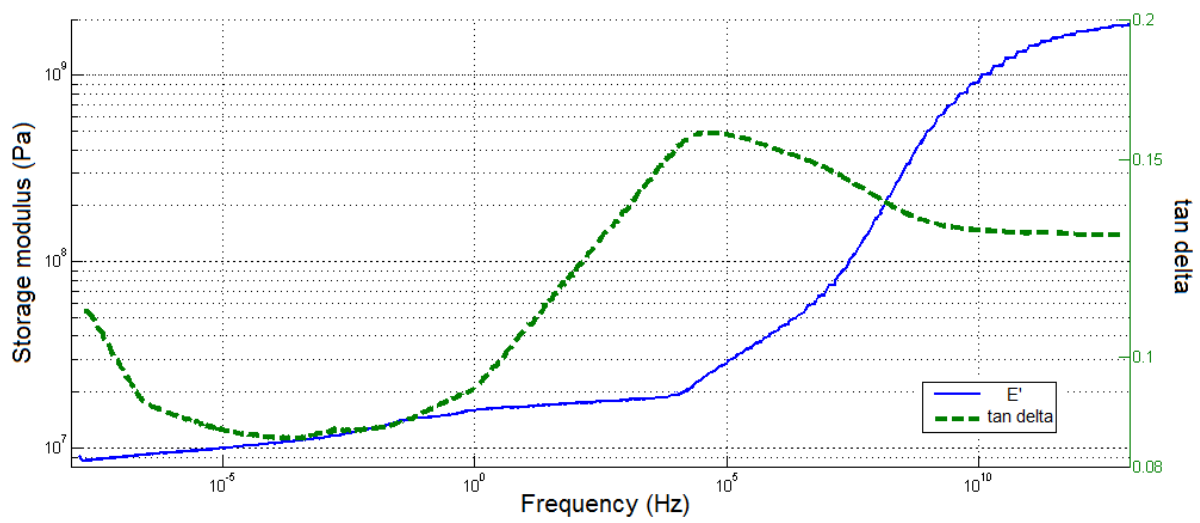
Figure A.7.11 – Master curves of the storage modulus $E^{'}$ and loss factor η as a function of the frequency for material VC 1001.
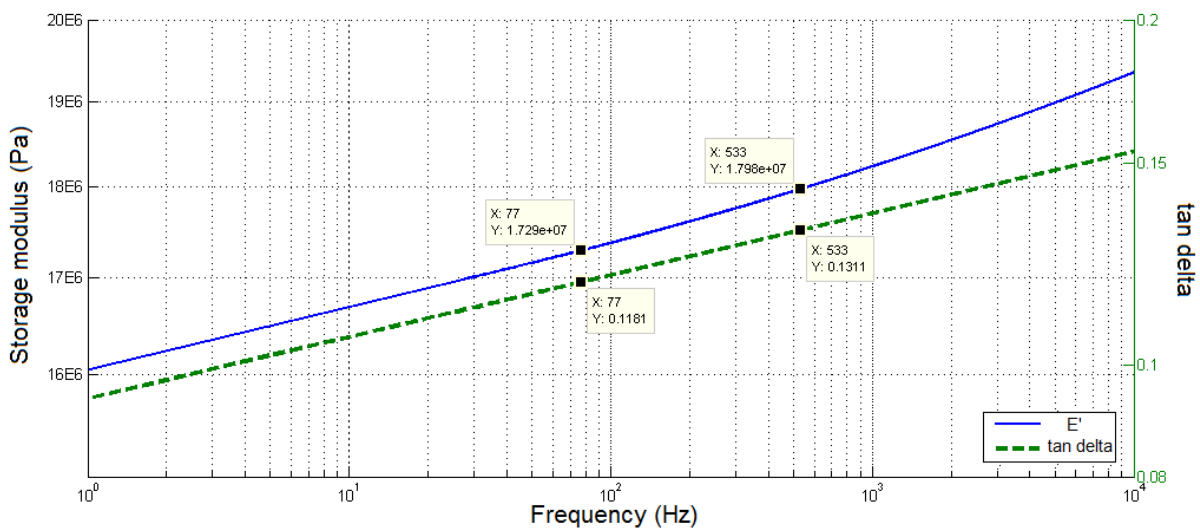

Figure A.7.12 – Curve fitting of the master curves of the storage modulus $E^{'}$ and loss factor η as a function of the frequency in the interval between 1Hz and 10^4Hz for material VC 1001.

Material NL20

Figure A.7.13 – Storage modulus $E^{'}$ and loss factor η curves as a function of the temperature for three different frequencies for material NL20.

Figure A.7.14 – Shift curve at 20ºC as a function of the temperature for material NL 20.

Figure A.7.15 – Master curves of the storage modulus $E^{'}$ and loss factor η as a function of the frequency for material NL 20.

Figure A.7.16 – Curve fitting of the master curves of the storage modulus $E^{'}$ and loss factor η as a function of the frequency in the interval between 1Hz and 10^4Hz for material NL 20.

A.8 – Further experimental results obtained for the steel plate without treatment and with FLD and CLD treatments

In this appendix are presented further results that were obtained for the steel plate considering the cases without treatment, with FLD treatment and CDL treatment. Tests were conducted using the experimental specimens and setup described in sub-chapter 5.6. FRFs were obtained at four points r, see Figure 5.4, where the results of point r_1 have already been presented in sub-chapter 5.7.1 as they present the main characteristics found.

Hence, the results obtained for points r_2, r_3 and r_4 are illustrated by Figure A.8.1, Figure A.8.2 and Figure A.8.3, respectively.
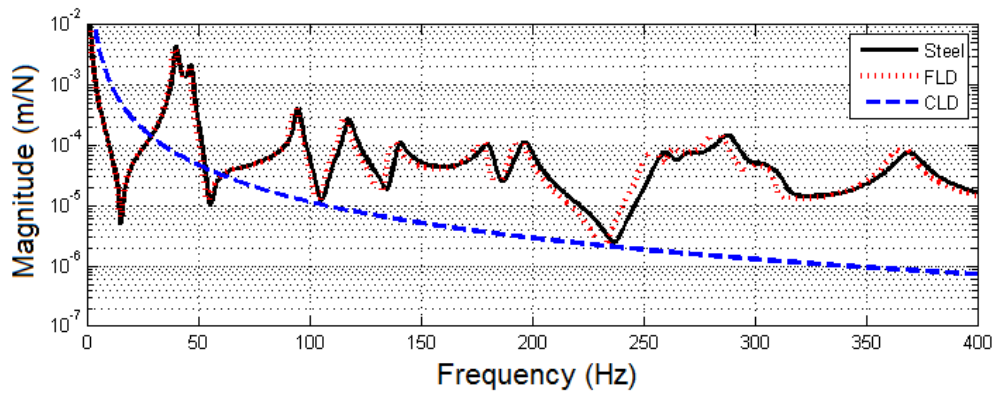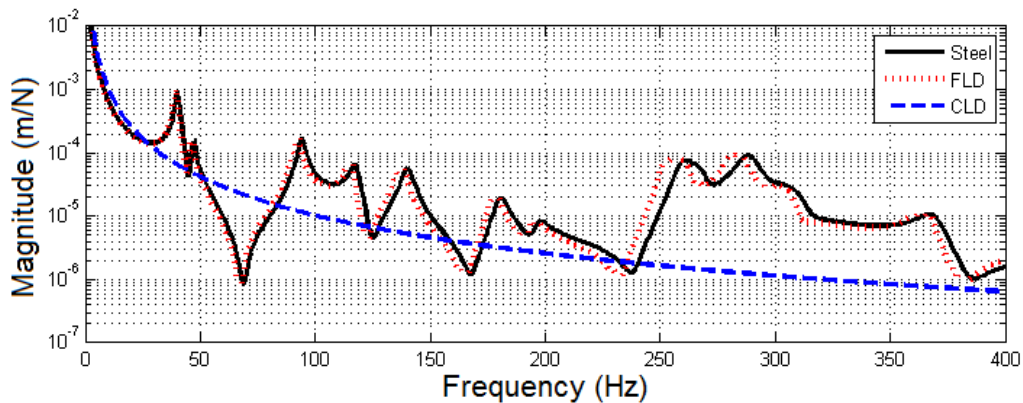

Figure A.8.1– Experimental FRF curves of a steel plate without treatment, with free layer damping treatment, and with constrained layer damping treatment (response at point r_2: X=10 mm and Y=175 mm).
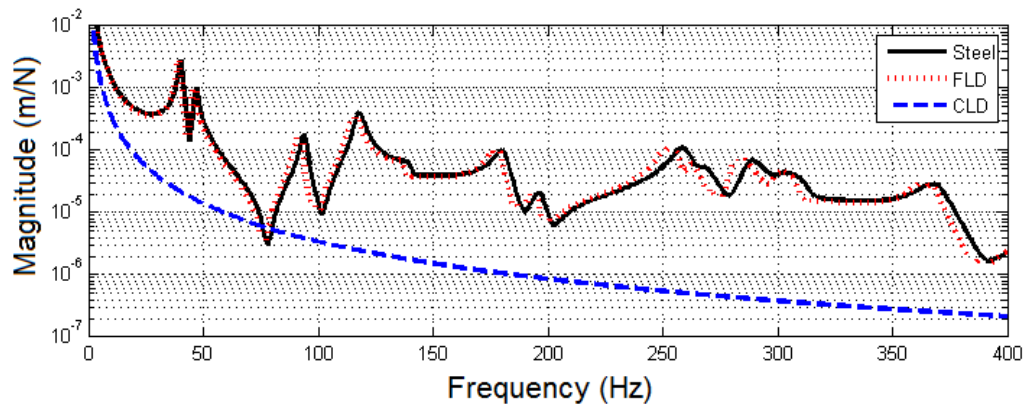

Figure A.8.2– Experimental FRF curves of a steel plate without treatment, with free layer damping treatment, and with constrained layer damping treatment (response at point ; r_3: X=60 mm and Y=70 mm).

Figure A.8.3 – Experimental FRF curves of a steel plate without treatment, with free layer damping treatment, and with constrained layer damping treatment (response at point r_4: X=220 mm and Y=98 mm).

From Figure A.8.1, Figure A.8.2 and Figure A.8.3, it is possible to observe that the response of the panel with the CLD treatment (dashed line) presents a significantly lower magnitude relatively to the FLD treatment (dot line), which is similar in terms of magnitude to the case without treatment (solid line), confirming (as expected) the higher capability of the CLD in terms of SDT.

Thus, and as expected confirming that the use of this type of CCM in CLD treatments is capable of a significantly reducing the magnitude of the resonances.

A.9 – Further experimental, numerical and updated results obtained for the steel plate without treatment.

In this appendix are presented further updated results that were obtained for the steel plate without treatment. The experimental FRF curves are compared with the numerical FRF curves that were obtained by conducting a harmonic response analysis, see Eq. (2.58), before and after model updating (see sub-chapter 2.6.3). Results were obtained at four points r, see Figure 5.4, where the results of point r_1 have already been presented in sub-chapter 5.7.1 as they present the main characteristics found.

Hence, the results obtained for points r_2, r_3 and r_4 are illustrated by Figure A.9.1, Figure A.9.2 and Figure A.9.3, respectively.
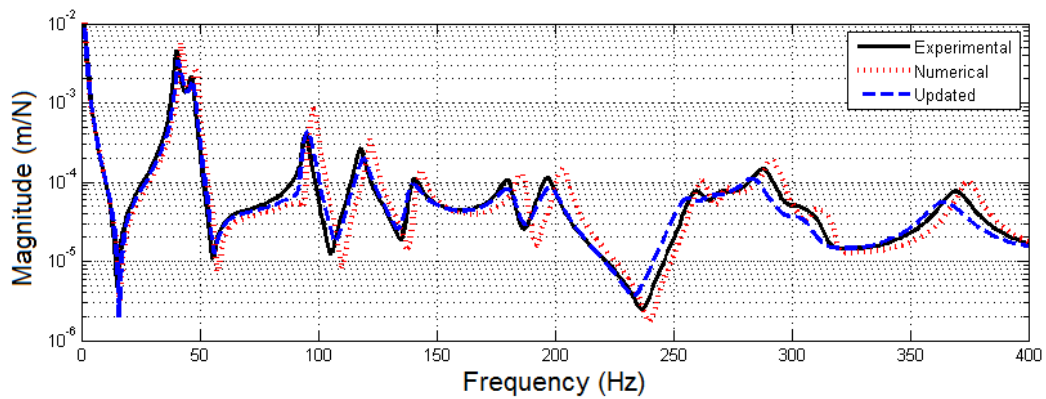

Figure A.9.1 – Experimental and numerical FRF curves of a steel plate without treatment (response at point r_2: X=10 mm and Y=175 mm).
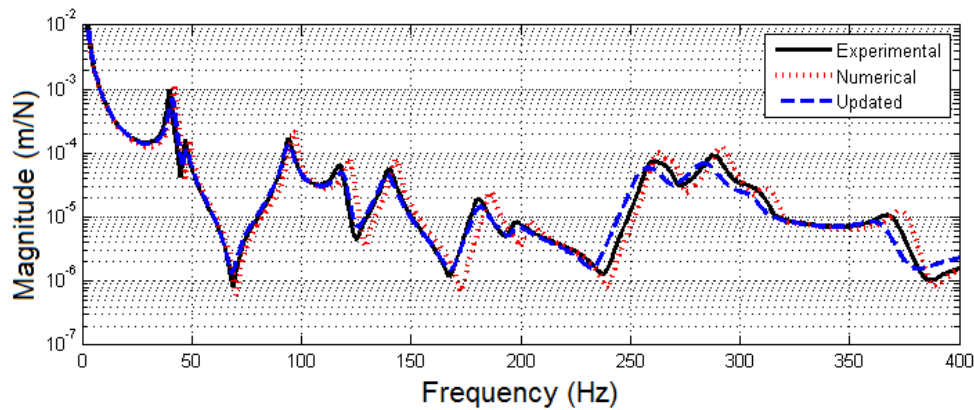

Figure A.9.2 – Experimental and numerical FRF curves of a steel plate without treatment (response at point ; r_3: X=60 mm and Y=70 mm).
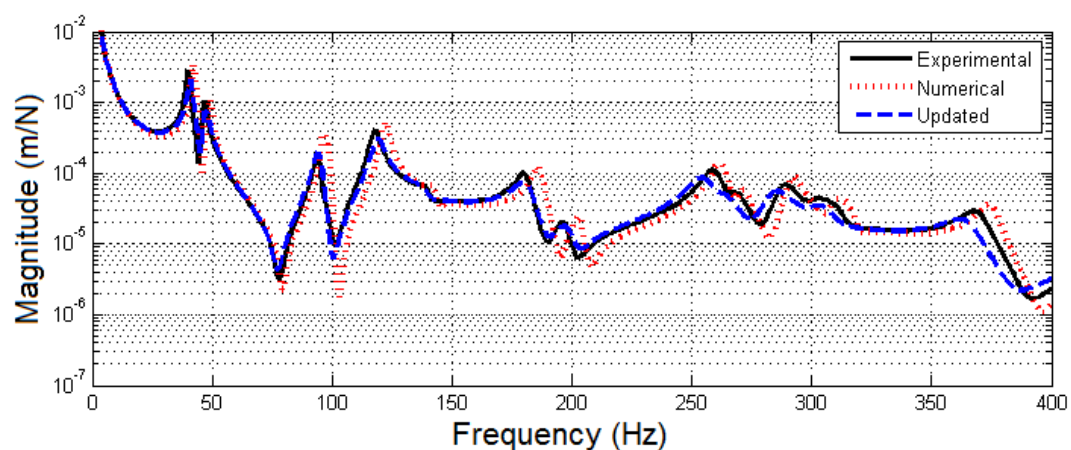
Figure A.9.3 – Experimental and numerical FRF curves of a steel plate without treatment (response at point ; r_4: X=220 mm and Y=98 mm).

Similarly to the results obtained for point r_1, see sub-chapter 5.7.1, the FRF curves for the remaining points illustrated by Figure A.9.1, Figure A.9.2 and Figure A.9.3, namely the experimental (solid line) and numerical (dotted line) updated (dashed line) show a satisfactory agreement.

This page was intentionally left blank